Universidade de Aveiro Departamento de Química
2017

Joana Carolina Quintela Carrola

Avaliação do impacto das nanopartículas de prata no metabolismo celular: um estudo *in vitro* por metabolómica de RMN

Assessing the impact of silver nanoparticles on cell metabolism: an *in vitro* NMR metabolomics study

Universidade de Aveiro Departamento de Química
2017

Joana Carolina Quintela Carrola

Avaliação do impacto das nanopartículas de prata no metabolismo celular: um estudo *in vitro* por metabolómica de RMN

Assessing the impact of silver nanoparticles on cell metabolism: an *in vitro* NMR metabolomics study

Tese apresentada à Universidade de Aveiro para cumprimento dos requisitos necessários à obtenção do grau de Doutor em Nanociências e Nanotecnologia, realizada sob a orientação científica da Doutora Iola Melissa Fernandes Duarte, Investigadora Principal do CICECO – Instituto de Materiais de Aveiro, Departamento de Química da Universidade de Aveiro e da Doutora Helena Cristina Correia de Oliveira, Investigadora em Pós-Doutoramento do CESAM e Departamento de Biologia da Universidade de Aveiro

Apoio financeiro da Fundação para a Ciência e a Tecnologia (FCT) - bolsa de investigação FCT SFRH/BD/79494/2011 no âmbito do Programa Operacional Capital Humano (POCH), comparticipado pelo Fundo Social Europeu e por fundos nacionais do Ministério da Ciência, Tecnologia e Ensino Superior, e projeto FCOMP-01-0124-FEDER-021456 (Refª. PTDC/SAU-TOX/120953/2010) financiado pelo Fundo Europeu de Desenvolvimento Regional (FEDER) através do Programa Operacional Fatores de Competitividade (COMPETE); da Universidade de Aveiro - CICECO-Instituto de Materiais de Aveiro, POCI-01-0145-FEDER-007679 (FCT UID/CTM /50011/2013) e CESAM (FCT UID/AMB/50017/2013). Agradece-se ainda à Rede Nacional de RMN (RNRMN), apoiada por fundos da FCT, e à empresa Bruker BioSpin GmbH.

o júri

presidente

Professor Doutor Rui Luís Andrade Aguiar
Professor Catedrático, Departamento de Eletrónica, Telecomunicações e Informática, Universidade de Aveiro

Professora Doutora Eduarda das Graças Rodrigues Fernandes
Professora Associada com Agregação, Departamento de Ciências Químicas, Faculdade de Farmácia, Universidade do Porto

Professor Doutor Carlos Manuel Marques Palmeira
Professor Catedrático, Departamento Ciências da Vida, Faculdade de Ciências e Tecnologia, Universidade de Coimbra

Professora Doutora Maria da Conceição Lopes Vieira dos Santos
Professora Catedrática, Departamento de Biologia, Faculdade de Ciências, Universidade do Porto

Professora Doutora Ana Maria Pissarra Coelho Gil
Professora Associada com Agregação, Departamento de Química, Universidade de Aveiro

orientadora

Doutora Iola Melissa Fernandes Duarte
Investigadora Principal, Departamento de Química, Universidade de Aveiro

agradecimentos

Quero começar por agradecer à minha orientadora, Doutora Iola Duarte, e à minha co-orientadora, Doutora Helena Oliveira, por todo o seu apoio e disponibilidade ao longo destes 4 anos. Agradeço, também, todo o conhecimento que me transmitiram e a oportunidade de realizar este trabalho.

Em segundo lugar, agradeço a toda a equipa envolvida neste projeto, em especial à Doutora Ana Daniel-da-Silva, Doutora Carmen Freire, Professora Doutora Conceição Santos, Doutor Miguel Oliveira, Eliana Malheiro, Doutora Ivana Jarak, Tiago Pedrosa e Doutora Verónica Bastos. Agradeço ainda ao Doutor Ricardo Pinto e à Mariam Nasirpour, por todo o trabalho relacionado com as nanopartículas de síntese verde.

Agradeço ao grupo de metabolómica da Universidade de Aveiro, pelos cruciais ensinamentos sobre RMN e análise multivariada, e pelas discussões críticas que tanto ajudaram ao desenvolvimento deste trabalho: à Professora Doutora Ana Gil e ao Doutor António Barros, também envolvidos neste projeto, e ao Doutor Brian Goodfelllow.

Agradeço ainda aos colegas, mas sobretudo amigos, Cláudia Rocha, Gonçalo Graça, Inês Lamego, Joana Pinto, João Rodrigues, Sílvia Diaz e Susana Aveiro, que sempre me deram motivação, com um toque de humor, para ultrapassar os momentos menos fáceis. Agradeço, também, a todos os que passaram pela “salinha”, por toda a amizade e alegria sempre presentes, Joana Marques, Lisa Sequeira, Ricardo Mendes e Sérgio Vilela.

Por fim, agradeço aos meus pais, que sempre me apoiaram e nunca mediram esforços para que eu cumprisse os meus objetivos, e restante família, a todos os amigos que se tornaram família, e ao Pedro, que tantas vezes sofreu comigo as dificuldades que encontrei e tantas vezes sorriu para tornar tudo melhor.

palavras-chave

nanopartículas de prata (AgNPs), metabolismo celular, metabolómica, espectroscopia de ressonância magnética nuclear (RMN), análise multivariada (MVA), queratinócitos (HaCaT), células de hepatoma (HepG2), macrófagos (RAW 264.7), nanotoxicologia.

resumo

Face ao uso disseminado e enorme potencial terapêutico das nanopartículas de prata (AgNPs), o estudo dos seus efeitos biológicos é um assunto relevante e atual. O trabalho apresentado nesta tese teve como objetivo aprofundar o conhecimento existente sobre o impacto das AgNPs no metabolismo celular, usando a metabolómica por espectroscopia de ressonância magnética nuclear (RMN). Os tipos celulares escolhidos para este estudo foram queratinócitos da epiderme humana, células de hepatoma humano e macrófagos sanguíneos, por serem relevantes, respetivamente, ao nível da entrada, acumulação e captação de nanopartículas no organismo.

O Capítulo 1 introduz as principais propriedades das AgNPs, a sua atividade biológica e potencial toxicidade, e descreve a abordagem metabolómica, incluindo uma breve revisão bibliográfica das suas aplicações em nanotoxicologia. O âmbito e os objetivos desta tese são, também, apresentados.

O Capítulo 2 descreve os métodos experimentais utilizados ao longo deste trabalho, incluindo a caracterização das AgNPs, os procedimentos usados na cultura celular e nos ensaios biológicos, a colheita e preparação de amostras, a análise por RMN e o tratamento estatístico dos dados.

No Capítulo 3, a atividade metabólica e a composição dos três tipos de células usados neste trabalho (queratinócitos HaCaT, células de hepatoma HepG2 e macrófagos RAW 264.7) são descritas com base na análise por RMN dos sobrenadantes dos meios de cultura (exometaboloma) e dos extratos celulares polares e lipofílicos (endometaboloma).

O Capítulo 4 apresenta a análise metabolómica das células HaCaT expostas a AgNPs de diferentes tamanhos (10, 30 ou 60 nm de diâmetro) e revestimentos (citrato, polietilenoglicol ou albumina de soro bovino). Verificou-se que o metaboloma celular foi afetado mesmo a concentrações subtóxicas de AgNPs, sugerindo: aumento da glicólise e glutaminólise, alteração na atividade do ciclo dos ácidos tricarboxílicos (TCA) e nos processos de produção e transferência de energia, degradação de proteínas, síntese de glutationa (GSH), modificações a nível das membranas e do equilíbrio osmótico. Apesar de muitas variações serem comuns a todas as nanopartículas testadas, as AgNPs de 10 nm causaram os efeitos mais distintos, nomeadamente no que diz respeito à glicólise e à síntese/utilização de GSH. Além disso, a exposição celular a prata iónica (Ag^+) confirmou o importante papel dos iões prata no mecanismo de ação das AgNPs, enquanto a comparação com o peróxido de hidrogénio (H_2O_2) permitiu destacar os efeitos relacionados com o stress oxidativo.

No Capítulo 5 são apresentadas as respostas metabólicas das células de fígado HepG2 a dois tipos de AgNPs, umas obtidas por redução química e estabilizadas em citrato e as outras obtidas por síntese verde na presença de um extrato vegetal (Cit30 e GS30, respetivamente), ambas com centros metálicos de 30 nm. Os resultados sugeriram adaptações metabólicas em

resumo (cont.)

processos de produção de energia (metabolismo da glucose e sistema da fosfocreatina), autofagia e metabolismo lipídico, refletindo possivelmente a ativação de mecanismos de proteção. Ainda que os dois tipos de AgNPs tenham induzido muitos efeitos semelhantes, as Cit30 pareceram causar um maior impacto no ciclo TCA e na degradação de proteínas, enquanto as GS30 aparentaram induzir uma diminuição mais forte na síntese de fosfolípidos. A assinatura metabólica da prata iónica foi bastante semelhante à das AgNPs, sugerindo, no entanto, uma menor capacidade das células expostas a Ag^+ extracelular para lidar com o stress oxidativo.

O Capítulo 6 descreve a avaliação do impacto das AgNPs Cit30 no metaboloma de macrófagos de murganho RAW 264.7, a concentrações subtóxicas (decréscimos de ~5 e 20% na viabilidade celular). As alterações encontradas apontaram para: estimulação da glicólise (a baixa concentração de exposição), reprogramação do ciclo TCA (resultando numa intensa produção de itaconato e succinato e numa marcada depleção de ATP, consistentes com uma resposta pro-inflamatória), ativação da gluconeogénese, promoção da síntese de GSH e acumulação de creatina/fosfocreatina. Foram, ainda, observadas variações possivelmente relacionadas com a osmorregulação e a modificação membranar. De notar que os macrófagos expostos a Ag^+ mostraram características semelhantes aos expostos a AgNPs (por ex., aumento da glucose intracelular – gluconeogénese), mas também revelaram efeitos distintos, nomeadamente em metabolitos envolvidos no ciclo TCA, em processos de transferência de energia e no metabolismo lipídico. Adicionalmente, viu-se que o metaboloma dos macrófagos respondeu de maneira diferente à exposição a H_2O_2 (por ex., tendência para diminuição da glicólise e sem efeitos observados na ativação da gluconeogénese ou da síntese de GSH), indicando que muitos dos efeitos induzidos pelas AgNPs não foram necessariamente mediados por stress oxidativo.

Finalmente, com base na integração dos resultados apresentados ao longo dos capítulos anteriores, as principais conclusões deste trabalho são apresentadas e discutidas no Capítulo 7.

keywords

silver nanoparticles (AgNPs), cell metabolism, metabolomics, nuclear magnetic resonance (NMR) spectroscopy, multivariate analysis (MVA), keratinocytes (HaCaT), hepatoma cells (HepG2), macrophages (RAW 264.7), nanotoxicology.

abstract

The wide dissemination and promising therapeutic potential of silver nanoparticles (AgNPs) make the study of their biological effects a relevant up-to-date subject. The work presented in this thesis aimed at deepening current understanding of the impact of AgNPs on cell metabolism, using NMR metabolomics of cultured mammalian cells. Epidermis keratinocytes, hepatoma cells and blood macrophages, relevant, respectively, to nanoparticle entry, accumulation and uptake, have been selected for the study.

Chapter 1 introduces the main properties of AgNPs, including their biological activity and toxicological potential, and describes the metabolomics approach, briefly reviewing its applications in the field of nanotoxicology. Also, the scope and aims of this thesis are presented.

Chapter 2 covers the experimental methods adopted during the course of this work, including the sources and characterisation of AgNPs, the procedures used in cell culture and biological assays, sample collection and preparation methods, NMR analyses and statistical data treatment.

In Chapter 3, the metabolic activity and composition of the three cell types used in this work (HaCaT keratinocytes, HepG2 hepatoma cells and RAW 264.7 macrophages) are described based on the NMR analysis of culture medium supernatants (exometabolome) and polar/lipophilic cell extracts (endometabolome).

Chapter 4 presents the metabolomic analysis of HaCaT skin cells exposed to AgNPs of different sizes (10, 30 or 60 nm in diameter) and coatings (citrate, polyethylene glycol or bovine serum albumin). The cellular metabolome was found to be affected even at sub-toxic concentrations of AgNPs, suggesting: upregulation of glycolysis and glutaminolysis, altered tricarboxylic acid (TCA) cycle activity, protein degradation, disruption of energy-producing pathways, glutathione (GSH) synthesis, membrane modification and changes in osmotic balance. Although several metabolic variations were common to all tested nanoparticles, the 10 nm AgNPs showed the most distinct effects, namely in regard to glycolysis and GSH synthesis/utilisation. Furthermore, cell exposure to ionic silver (Ag^+) confirmed the major role of silver ions in AgNPs mode of action, while comparison with hydrogen peroxide (H_2O_2) allowed the effects related to oxidative stress to be highlighted.

In Chapter 5, the metabolic responses of liver HepG2 cells to two types of 30 nm AgNPs, obtained by chemical reduction and stabilised with citrate or produced by green synthesis in the presence of a plant extract (Cit30 and GS30, respectively) are presented. Sub-toxic concentrations of AgNPs were proposed to induce metabolic adaptations in energy production processes (glucose metabolism and the phosphocreatine system), autophagy and lipid metabolism, possibly reflecting the activation of metabolism-mediated protective mechanisms. Although the two types of AgNPs induced many

abstract (cont.)

common effects, Cit30 appeared to have a greater impact on the TCA cycle and protein degradation, whereas GS30 seemed to induce stronger downregulation of phospholipid synthesis. The metabolic signature of Ag^+ was largely similar to that of AgNPs, although suggesting a lower ability of cells exposed to extracellular Ag^+ to cope with oxidative stress.
Chapter 6 addresses the impact of Cit30 AgNPs on the metabolome of murine RAW 264.7 macrophages, at concentrations causing minimal (~5 and 20%) decreases in cell viability. Exposed cells were suggested to upregulate glycolysis (at the low exposure concentration), to reprogram the TCA cycle (resulting in marked production of itaconate and succinate and in ATP depletion, consistent with a pro-inflammatory response), to activate gluconeogenesis, to promote GSH synthesis, and to increase the creatine/phosphocreatine pool. Changes putatively related to osmoregulation and membrane modification were also observed. Notably, macrophages exposed to Ag^+ showed common features to AgNPs-exposed cells (e.g. increased intracellular glucose suggesting gluconeogenesis), but also several distinct effects, for instance in metabolites involved in the TCA cycle, energy transfer processes or lipid metabolism. Furthermore, the cellular metabolome responded differently to H_2O_2 exposure (e.g. trend for downregulated glycolysis, no evidence of gluconeogenesis activation or of GSH upregulation), indicating that many of the AgNPs-induced effects were not necessarily mediated by oxidative stress.
Finally, based on the integration of the results presented along the previous chapters, the main conclusions of this work are presented and discussed in Chapter 7.

Publications resulting from the work carried out within this thesis

Full paper: Carrola, J., Bastos, V., Jarak, I., Oliveira-Silva, R., Malheiro, E., Daniel-Da-Silva, A.L., Oliveira, H., Santos, C., Gil, A.M., Duarte, I.F. Metabolomics of silver nanoparticles toxicity in HaCaT cells: structure-activity relationships and role of ionic silver and oxidative stress. *Nanotoxicology* 2016, 10(8): 1105-17.

Full paper: Carrola, J., Bastos, V., Ferreira De Oliveira, J.M., Oliveira, H., Santos, C., Gil, A.M., Duarte, I.F. Insights into the impact of silver nanoparticles on human keratinocytes metabolism through NMR metabolomics. *Archives of Biochemistry and Biophysics* 2016, 589: 53-61.

Abstract: Carrola J., Gil A.M., Daniel-Da-Silva A.L., Bastos V., Oliveira H., Oliveira J., Santos C., Duarte I.F. Metabolic response of human keratinocytes to silver nanoparticles: A metabolomics study. *Toxicology Letters* 2013, 221: S242-S3.

Manuscripts in preparation:

Carrola J., Pinto R.J.B., Nasirpour M., Freire C.S.R., Gil A.M., Santos C., Oliveira H., Duarte I.F. Metabolic profiling of liver (HepG2) cells exposed to silver nanoparticles suggests activation of metabolism-mediated protective mechanisms.

Carrola J., Oliveira H., Gil A.M., Santos C., Duarte I.F. Differential effects of silver nanoparticles, ionic silver and hydrogen peroxide on the metabolome of RAW 264.7 macrophages.

Other publications related to this work

Book Chapter: Pinto R.J.B., Nasirpour M., Carrola J., Oliveira H., Freire C.S.R., Duarte I.F. Antimicrobial properties and therapeutic applications of silver nanoparticles and nanocomposites. *In:* Grumezescu, A.M. (ed.) *Antimicrobial Nanoarchitectonics.* 2017. Elsevier.

Full paper: Bastos V., Ferreira-De-Oliveira J.M.P., Carrola J., Daniel-Da-Silva A.L., Duarte I.F., Santos C. and Oliveira H. Coating independent cytotoxicity of citrate- and PEG-coated silver nanoparticles on a human hepatoma cell line. *Journal of Environmental Sciences* 2016 (in press).

Full paper: Jarak I., Carrola J., Barros A.S., Gil A.M., Pereira M.L., Corvo M.L., Duarte I.F. Metabolism modulation in different organs by silver nanoparticles: an NMR metabolomics study of a mouse model. *Submitted*.

Abstract: Bastos V., Carrola J., Duarte I.F., Santos C., Oliveira H. Comparative *in vitro* cytotoxicity of citrate-coated silver nanoparticles on skin, liver and blood cell lines. *Toxicology Letters* 2016, 258(Supplement): S262.

Abstract: Marçal R., Carrola J., Jarak I., Corvo M.L., Duarte I.F., Pereira, M.D.L. Microscopic studies of liver and kidney in mice exposed to silver nanoparticles. *Microscopy and Microanalysis* 2016, 22(S4): 18-9.

Contents

List of abbreviations and symbols

1D	one-dimensional
2D	two-dimensional
Abs	absorbance
ADP	adenosine diphosphate
AgNPs	silver nanoparticles
Ag^+	ionic silver
AMP	adenosine monophosphate
ATP	adenosine triphosphate
BSA	bovine serum albumin
BSA30	30 nm BSA-stabilised silver nanoparticles
Cho	choline
Cit10	10 nm citrate-stabilised silver nanoparticles
Cit30	30 nm citrate-stabilised silver nanoparticles
Cit60	60 nm citrate-stabilised silver nanoparticles
CK	choline kinase
CoA	coenzyme A
Cr	creatine
CR	classification rate
DMEM	Dulbecco's modified Eagle's medium
DMSO	dimethyl sulfoxide
DNA	deoxyribonucleic acid
EDTA	ethylenediaminetetraacetic acid
EG	*Eucaliptus globulus* Labill.
FAD^+	flavin adenine dinucleotide
FBP-1	fructose-1,6-bisphosphatase
FBS	foetal bovine serum
GC	gas chromatography
GDP	guanosine diphosphate
GPC	glycerophosphocholine
GSH	reduced glutathione
GSSG	oxidised glutathione
GTP	guanosine triphosphate
GS30	30 nm biogenic silver nanoparticles
HMDB	human metabolome database

HRMAS	high resolution magic angle spinning
HSQC	heteronuclear single-quantum coherence
IC_5	5% inhibitory concentration
IC_{20}	20% inhibitory concentration
IC_{50}	half maximal inhibitory concentration
IDH	isocitrate dehydrogenase
J-res	*J*-resolved
LC	liquid chromatography
LDH	lactate dehydrogenase
LV	latent variable
MCCV	Monte Carlo cross-validation
m-Ino	*myo*-inositol
MALDI	matrix-assisted laser desorption/ionisation
MIC	minimum inhibitory concentration
MS	mass spectrometry
MTT	3-(4,5-dimethylthiazol-2-yl)-2,5-diphenyltetrazolium bromide
MVA	multivariate analysis
NAA	*N*-acetylaspartate
NAD^+	nicotinamide adenine dinucleotide
$NADP^+$	nicotinamide adenine dinucleotide phosphate
NMR	nuclear magnetic resonance
NPs	nanoparticles
PBS	phosphate buffer saline
PC	phosphocholine
PCA	principle component analysis
PEG	polyethylene glycol
PEG10	10 nm PEG-stabilised silver nanoparticles
PEG30	30 nm PEG-stabilised silver nanoparticles
PTC	phosphatidylcholine
PTE	phosphatidylethanolamine
PLS-DA	partial least squares-discriminant analysis
PUFA	polyunsaturated fatty acyl
PVP	polyvinylpyrrolidone
r	Pearson's correlation coefficient
RNA	ribonucleic acid

ROC	receiver operating characteristic
ROS	reactive oxygen species
RSPA	recursive segment-wise peak alignment
SDH	succinate dehydrogenase
STOCSY	statistical total correlation spectroscopy
SW	spectral window
TCA	tricarboxylic acid
TEM	transmission electron microscopy
TMS	tetramethylsilane
TOCSY	total correlation spectroscopy
TSP	3-trimethylsilylpropionic acid
UDP	uridine diphosphate
UTP	uridine triphosphate
UV	unit variance
UV-Vis	UV-visible spectroscopy
VIP	variable importance to the projection

Chapter 1. Introduction

1.1. Silver nanoparticles (AgNPs)

Silver has been used throughout history for a large variety of applications, including the manufacture of currency coins, ornaments, jewellery, tableware and utensils. Furthermore, its healing and preservative properties have been known since primordial civilisations, as attested by the use of silver films for water preservation by the Phoenicians, or of silver powders as anti-disease agents by ancient Egyptians (Murphy *et al.*, 2015). Over the last century, the engineering of silver into nanoparticles has further extended the myriad of applications for this noble metal. Today, silver nanoparticles (AgNPs) represent one of the classes of nanomaterials with largest production and commercialisation (Tran *et al.*, 2013). In particular, their well-documented antimicrobial properties has propelled their incorporation into numerous consumer goods, including plastics, textiles, cosmetics and food packaging materials, as well as in medical products, such as wound dressings, implants and catheters (Ge *et al.*, 2014). Moreover, new therapeutic applications are increasingly being explored with a view to take advantage of other interesting biological properties of AgNPs, such as the antiviral or anticancer activities (Wei *et al.*, 2015). On the other hand, given the high propensity for human exposure, there is a recognised need to better define the potential adverse effects of AgNPs to human health, and to understand their mechanisms of action in eukaryotic cells and higher organisms. In the following sections, the main physicochemical and biological properties of AgNPs as well as the current knowledge on their toxicity will be reviewed, aiming at establishing a sound and informed background that will aid in the interpretation of the results presented in this thesis.

1.1.1. Synthesis and physicochemical properties of AgNPs

AgNPs are nanoscale clusters of metallic silver (20-15000 atoms), with sizes typically below 100 nm in at least one dimension. They can be synthesised by numerous methods, usually divided into three main categories: chemical, physical and biological methods (Wei *et al.*, 2015; Pinto *et al.*, 2017). Chemical methods comprise the reduction of silver ions (Ag^{+}) in aqueous or organic solutions, forming metallic silver (Ag^{0}) atoms that subsequently form clusters, yielding colloidal silver in the nanometric range. In particular, the chemical synthesis of AgNPs can be achieved through chemical or electrochemical reduction, hydrothermal, microemulsion and photochemical methods (Pinto *et al.*, 2017).

Physical methods include, among others, laser ablation, whereby AgNPs are synthesised through the ablation of metallic bulk materials by laser pulses, evaporation-condensation, and arc discharge between titanium electrodes in a silver nitrate solution (Pinto *et al.*, 2017). Finally, biological synthetic routes for AgNPs make use of different organisms like bacteria, fungi, algae, yeasts or plants. These are generally safer and more economic than chemical or physical methods, since the solvent medium is preferably water, and the reducing and stabilising agents are non-toxic and environmentally friendly (Rajan *et al.*, 2015; Rauwel *et al.*, 2015).

Depending on the fabrication method, AgNPs can present different shapes, including spheres, rods, wires and plates (Figure 1.1a), as well as various sizes. For instance, strong reducing agents usually produce small monodisperse particles, while weak reductants tend to generate larger polydisperse particles (Galdiero *et al.*, 2011).

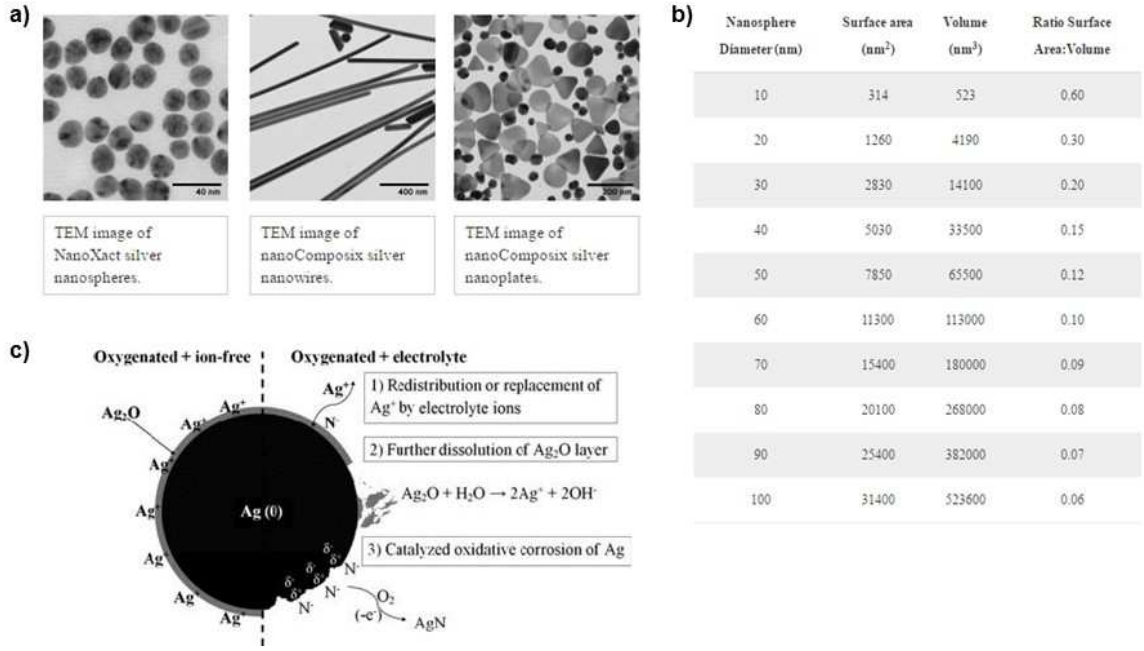

Nanosphere Diameter (nm)	Surface area (nm^2)	Volume (nm^3)	Ratio Surface Area:Volume
10	314	523	0.60
20	1260	4190	0.30
30	2830	14100	0.20
40	5030	33500	0.15
50	7850	65500	0.12
60	11300	113000	0.10
70	15400	180000	0.09
80	20100	268000	0.08
90	25400	382000	0.07
100	31400	523600	0.06

Figure 1.1. a) Differently shaped AgNPs (nanoComposix, 2016a). b) Surface area:volume ratios of nanospheres, according to their diameter (nanoComposix, 2016a). c) Schematic representation of surface oxidation and dissolution of the oxide layer in AgNPs; reprinted with permission from (Li *et al.*, 2012), Copyright © 2012 American Chemical Society.

Since nanosized materials have a significant number of atoms on the surface, they are characterised by high surface area to volume ratio, which increases with decreasing nanoparticle size (Fig 1.1b). Consequently, the chemical reactivity and many of the physical properties of the nanoparticles, such as solubility and tendency to aggregate, are dominated

by the nature of the nanoparticle surface. Silver nanoparticles are characterised by the presence of an oxide layer (Ag_2O) on the surface of the metallic core (Ag^0) (Figure 1.1c), which dissolves under certain conditions to release silver ions (Ag^+) (Li *et al.*, 2010; Li *et al.*, 2012). Thus, it is not surprising that surface coating affects the dissolution behaviour of AgNPs (Li *et al.*, 2012). The coating agent is also determinant for nanoparticle stabilisation and prevention of agglomeration, either through electrostatic (e.g. citrate coating) or steric interactions (e.g. polyvinylpyrrolidone (PVP) or polyethylene glycol (PEG) coating). Furthermore, it is important to stress that the surface of most nanoparticles is dynamic and strongly influenced by the local environment.

Another size-dependent property of AgNPs is their ability to absorb and scatter light with great efficiency. This is due to the collective oscillation of conduction electrons on the metal surface when they are excited by incident light at specific wavelengths, producing the so called surface plasmon resonance (SPR). These unique optical properties allow AgNPs stability to be accurately monitored using UV-Vis spectroscopy (Zook *et al.*, 2011).

1.1.2. Biological properties of AgNPs

Antibacterial activity

Silver has been used as a bactericidal agent since ancient times, especially until the appearance of antibiotics. Then, the evolution of antibiotic-resistant strains of bacteria (Rai *et al.*, 2012), led to a renewed interest in the antibacterial properties of silver, namely in the nanoparticulate form. AgNPs have shown high efficacy against a vast range of bacteria, including Gram negative bacteria, such as *Escherichia*, *Vibrio* or *Pseudomonas*, and Gram positive bacteria, such as *Staphylococcus*, *Enterococcus* or *Bacillus*, with reported minimum inhibitory concentrations (MIC) typically varying in the range 1-100 µg/mL (Tran *et al.*, 2013). Moreover, the efficacy of AgNPs alone or in combination with antibiotics against several multidrug-resistant (MDR) strains (Rai *et al.*, 2012) and the ability of AgNPs to prevent and disrupt bacterial biofilms (Franci *et al.*, 2015), which can be responsible for serious infections, present a gateway for the development of new antibacterial therapies.

The bactericidal activity of AgNPs is greatly influenced by their physicochemical properties, namely size, surface charge and shape. Smaller nanoparticles have been shown to possess stronger antibacterial activity than larger nanoparticles (Morones *et al.*, 2005; Choi and Hu, 2008; Agnihotri *et al.*, 2014), possibly due to their higher surface area and reactivity. In terms of surface charge, the strong electrostatic interactions between the

bacterial membrane and positively-charged AgNPs are probably responsible for the higher efficacy of these nanoparticles against *Bacillus* species, when comparing to negatively charged ones (El Badawy *et al.*, 2011). The influence of shape has also been tested, revealing that silver nanoplates present higher bactericidal activity than spherical or rod-shaped AgNPs (Pal *et al.*, 2007; Sadeghi *et al.*, 2012); this was proposed to be related to the NPs crystallographic surface structure, since the top basal plane of a truncated triangular nanoplate is a {111} facet, which is a high-atom-density surface that favours silver reactivity, whereas spherical and rod-shaped AgNPs are known to predominantly have {100} facets with a small percentage of {111} facets.

Some works have attributed the antibacterial activity of AgNPs to intrinsic properties (Morones *et al.*, 2005; Choi and Hu, 2008), while silver ions (Ag^+), formed by oxidative dissolution of AgNPs or through the release of chemisorbed ions at the particles surface (Le Ouay and Stellacci, 2015), have been shown to play a key role in AgNPs toxicity (Xiu *et al.*, 2012). Indeed, Xiu and co-workers found that the viability of *E. coli* was not affected under anaerobic conditions, in which dissolution to Ag^+ did not occur, even when the concentration of AgNPs was much higher than the minimum lethal concentration measured under aerobic conditions.

Even though the mechanism of silver interaction with bacterial cells is not fully understood, several processes are thought to be involved (Eckhardt *et al.*, 2013), as illustrated in Figure 1.2. The direct physical damage to the cell membrane, resulting from attachment and penetration of AgNPs and Ag^+ into the bacterial cell wall, can lead to increased cell permeability and subsequent cell death. In particular, it was proposed that membrane destabilisation could result in collapsed membrane potential, dissipation of proton motive force and depletion of intracellular ATP levels (Dibrov *et al.*, 2002; Lok *et al.*, 2006). Furthermore, the uptake and intracellular accumulation of AgNPs and Ag^+ (facilitated by membrane poration) enables their interaction with vital enzymes and phosphorous-containing nucleobases, affecting major cell functions, such as cell division and DNA replication (Li et al., 2013b), resulting in bacterial apoptosis (Bao et al., 2015). Oxidative stress, with consequent damage to proteins, lipids and DNA, is another possible mechanism of AgNPs toxicity; high levels of reactive oxygen species (ROS) have been found in bacteria exposed to AgNPs (Kim *et al.*, 2007; Park *et al.*, 2009; Xu *et al.*, 2012), and have been suggested to arise either from over-production, or from disruption of ROS-scavenging enzymatic and non-enzymatic systems, as recently reviewed (Rizzello and Pompa, 2014).

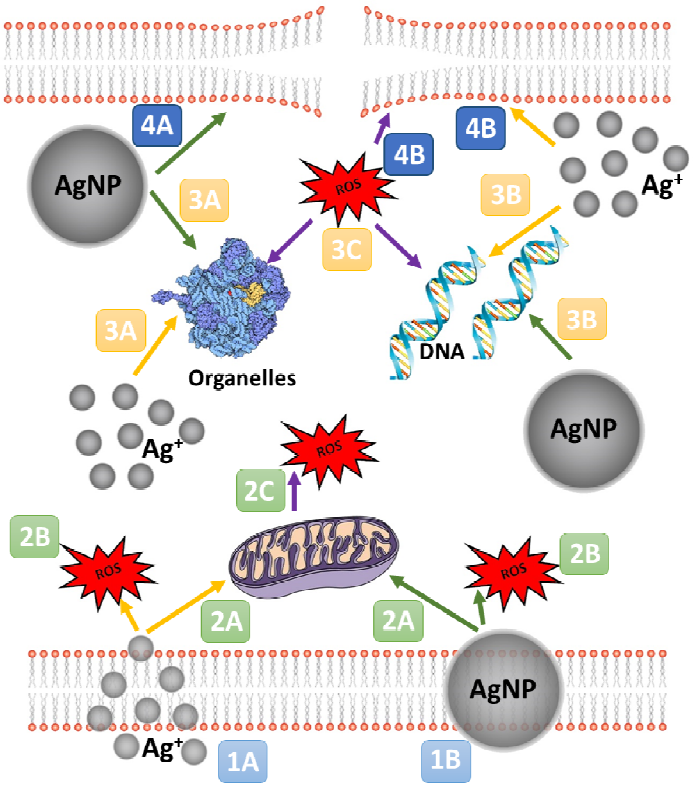

Figure 1.2. Scheme illustrating the proposed mechanisms of action on AgNPs on bacteria: 1A, diffusion; 1B, endocytosis; 2A, mitochondrial damage; 2B, direct generation of ROS; 2C, generation of ROS by damaged mitochondria; 3A, organelle damage via interaction with sulphur and phosphor groups; 3B, DNA damage via nucleotide oxidation; 3C, DNA and organelle damage via oxidative stress; 4A, electrostatic interaction of AgNPs with cell membrane; 4B, membrane damage (lipid oxidation) by Ag^+ and ROS (Pinto *et al.*, 2017).

Antifungal activity

The application of many antifungal medicines is often accompanied by toxicity and development of resistance (Sardi *et al.*, 2013). Thus, AgNPs have appeared as alternative fungicidal agents, especially against *Candida* species, which are opportunistic pathogens in humans. The high anticandidal activity of AgNPs has been reported in several studies, with MIC values in approximately the same range as that of conventional antifungal agents (0.05 – 2 µg/mL) (Kim *et al.*, 2009a; Panacek *et al.*, 2009; Selvaraj *et al.*, 2014; Bonilla *et al.*, 2015). Moreover, AgNPs have been shown to inhibit the formation and bioactivity of *Candida albicans* biofilms (Li *et al.*, 2014b; Lara *et al.*, 2015; Longhi *et al.*, 2015). It has been proposed that the antifungal mode of action of AgNPs against *C. albicans* involves the disruption of the cell membrane, with pore formation and subsequent inhibition of the normal budding process (Kim *et al.*, 2009a). Nonetheless, the ultrastructural analysis of *C. albicans*, exposed to AgNPs and fluconazole, through high-resolution transmission electron

microscopy (HRTEM), did not show severe damage to cell membranes (Vazquez-Munoz *et al.*, 2014). It showed, however, high extracellular accumulation of AgNPs, with release of Ag^+, and intracellular biosynthesis of smaller AgNPs (through reduction by cell organic compounds). In another study, the increased ROS production in AgNPs-exposed *C. albicans* was related with mitochondria-dependent apoptosis and DNA fragmentation (Hwang *et al.*, 2012).

Antiviral activity

Several works have demonstrated the activity of AgNPs against different viruses (Galdiero *et al.*, 2011), such as those causing human immunodeficiency (Elechiguerra *et al.*, 2005), herpes simplex (Baram-Pinto *et al.*, 2009), hepatitis B (Lu *et al.*, 2008), Dengue (Sujitha *et al.*, 2015) and influenza (Xiang *et al.*, 2011; Mori *et al.*, 2013; Xiang *et al.*, 2013). It has been suggested that the inhibition of viral infections by AgNPs could be due to an impaired attachment of viruses to host cells, resulting from the interaction of AgNPs with outer proteins in the viral envelope (Elechiguerra *et al.*, 2005; Sun *et al.*, 2008; Lara *et al.*, 2010). Nonetheless, in the presence of AgNPs, the *Vaccinia virus* was capable of adsorbing to cells but was prevented from entering (Trefry and Wooley, 2013). On the other hand, AgNP-treated tacaribe virus (TCRV) was more efficiently internalised into Vero cells than untreated TCVR (Speshock *et al.*, 2010); in that work, viral RNA production (and thus virus replication) was found to be inhibited upon AgNPs treatment, leading the authors to suggest the potential use of AgNPs in vaccine products.

Anti-inflammatory activity

The anti-inflammatory properties of AgNPs have been demonstrated both *in vitro* and *in vivo*. Recently, biosynthesised AgNPs with antibacterial activity were shown to have a cytoprotective effect towards hydrogen peroxide (H_2O_2)-induced inflammation in murine macrophages (Manikandan *et al.*, 2015). PVP-coated AgNPs also helped controlling inflammation triggered by a *Chlamydia trachomatis* infection in macrophages, through the regulation of several upstream surface receptors and downstream inflammatory pathway genes (Yilma *et al.*, 2013). In another study, composites of AgNPs and dendrimers were shown to have synergistic anti-inflammatory activity in lipopolysaccharide-stimulated murine macrophages (Liu *et al.*, 2014). Furthermore, in the presence of biogenic AgNPs, the production of pro-inflammatory cytokines by human keratinocytes exposed to UVB

radiation was decreased (David *et al.*, 2014). Regarding *in vivo* studies, AgNPs were shown to reduce inflammation and/or accelerate healing in murine models of allergic airway diseases (Jang *et al.*, 2012; Shin and Ye, 2012), a porcine model of contact dermatitis (Nadworny *et al.*, 2008), postoperative peritoneal adhesion models (Wong *et al.*, 2009; Zhang *et al.*, 2014a) and a burn wound mouse model (Liu *et al.*, 2014).

Anticancer activity

A recent review thoroughly describes the potential therapeutic applications of AgNPs in cancer (Wei *et al.*, 2015). Angiogenesis, the formation of new blood vessels, is a critical process for tumour growth and spreading. It has been shown that AgNPs and a natural anti-angiogenesis molecule, contributed almost equally to the inhibition of the formation of new blood microvessels induced by vascular endothelial growth factor (VEGF) (Gurunathan *et al.*, 2009). Moreover, several studies have demonstrated the ability of AgNPs to directly kill tumour cells. As described in the following section, AgNPs can cause dose-dependent toxicity in mammalian cells, including oxidative stress and DNA damage, ultimately leading to cell death. In particular, apoptosis has been often highlighted as a main mechanism through which AgNPs exert their cytotoxic action against tumour cells (Gurunathan *et al.*, 2009; Krishnasamy *et al.*, 2015; Gurunathan *et al.*, 2015; Satapathy *et al.*, 2015). Other potential applications of AgNPs in cancer treatment are based on their ability to sensitise tumour cells to radiation therapy (Lu *et al.*, 2012; Swanner *et al.*, 2015), and to show phototherapeutic properties under near-infrared (NIR) radiation (Boca *et al.*, 2011; Mfouo-Tynga *et al.*, 2014).

1.1.3. Toxicity of AgNPs towards mammalian cells

While in some applications the cytotoxicity of AgNPs is a desirable feature, e.g. when envisaging the killing of tumour cells, the successful use of AgNPs, e.g. as antimicrobial agents, often requires low toxicity towards human cells. Therefore, there is a great need to understand the mechanisms of AgNPs toxicity and the influencing factors that modulate toxic effects. In recent years, numerous studies have been carried out to address the toxicological potential of AgNPs towards mammalian cultured cells, as will be briefly reviewed below.

Several works have demonstrated that AgNPs can be readily taken up by various human-derived cell types, such as normal bronchial cells (Gliga *et al.*, 2014), liver cells

(Song *et al.*, 2012), epidermal keratinocytes (Monteiro-Riviere *et al.*, 2013), mesenchymal stem cells (Greulich *et al.*, 2011) and various tumour cell lines (Liu *et al.*, 2010; Yu *et al.*, 2013b). Similarly to other nanomaterials (Zhao *et al.*, 2011), the uptake of AgNPs has been shown to occur mainly through active pathways, namely clathrin- and caveolin-dependent endocytosis, macropinocytosis and phagocytosis, although involvement of energy-independent uptake pathways has also been suggested (Jiang *et al.*, 2014). Inside cells, AgNPs were often found to localise within membrane-bound structures, namely endosomes and lysosomes (Jiang *et al.*, 2013; Milic *et al.*, 2015; Gliga *et al.*, 2014). Less frequently, AgNPs have also been found in the cell nuclei (AshaRani *et al.*, 2009; Cronholm *et al.*, 2013).

Silver nanoparticles have been found to negatively affect the viability of many cell types in a concentration- and time-dependent manner. Based mainly on mitochondrial metabolic activity (e.g. formazan-based MTT assay) or membrane leakage (e.g. LDH assay) endpoints, several studies have reported significant decreases in cell viability upon AgNPs exposure. Reported IC_{50} values (concentrations causing a 50% decrease in cell viability) typically ranged from a few µg/mL (e.g. HepG2 cells exposed to 5 nm AgNPs (Avalos *et al.*, 2014)) to over 50 µg/mL (e.g. HaCaT cells exposed to 30 nm AgNPs (Mukherjee *et al.*, 2012)). This variability likely reflects not only the diverse susceptibility of the different cell types to AgNPs, but also the variable physicochemical properties of the AgNPs tested. For instance, the size of AgNPs was often shown to have a major influence on biological outcomes. In the majority of cases, smaller particles were more cytotoxic than larger ones, with AgNPs sized below 40 nm generally causing much higher toxicity (Liu *et al.*, 2010; Park *et al.*, 2011; Prasad *et al.*, 2013; Avalos *et al.*, 2014; Wang *et al.*, 2014; Gliga *et al.*, 2014; Butler *et al.*, 2015). The surface chemistry and shape of AgNPs were also highlighted as determinant to particle toxicity (Stoehr *et al.*, 2011).

DNA damage and chromosomal aberrations are other commonly reported outcomes of AgNPs exposure. In particular, DNA strand breaks and/or micronuclei formation have been observed in several AgNPs-exposed human cells, such as fibroblasts and glioblastoma cells (AshaRani *et al.*, 2009), epidermal keratinocytes (Austin *et al.*, 2011; Szmyd *et al.*, 2012), renal cells (Kang *et al.*, 2012), and white blood cells (Butler *et al.*, 2015). Induction of bulky DNA adducts (Foldbjerg *et al.*, 2011) and increased levels of 8-oxo-2'-deoxyguanosine (Jiang *et al.*, 2013), a marker of oxidative DNA damage, have also been reported, summing up to recent alerting evidence on the mutagenic potential of AgNPs (Huk *et al.*, 2014). Consistently with DNA damage, cell cycle arrest at the G2/M phase, to repair damaged DNA, has often been reported (AshaRani *et al.*, 2009; Kang *et al.*, 2012;

Song *et al.*, 2012; Foldbjerg *et al.*, 2012; Jiang *et al.*, 2013; Xue *et al.*, 2016). When cellular genetic material is damaged beyond repair, cells may initiate apoptotic cell death. Indeed, AgNPs have been shown to induce apoptosis in several human-derived cells (Piao *et al.*, 2011; Szmyd *et al.*, 2012; Xue *et al.*, 2016). Necrosis has also been reported to occur in a few studies with AgNPs, to an extent which depended on the cell type (Kim *et al.*, 2012), as well as on the time of exposure, size and concentration of AgNPs (Kumar *et al.*, 2015).

The cells inability to cope with high levels of ROS and to counteract their harmful effects leads to oxidative stress. Many studies have proposed this condition to be the main mechanism underlying the cytotoxicity and genotoxicity of AgNPs. Indeed, ROS have been found to be significantly increased in several types of human cells exposed to AgNPs (Suliman *et al.*, 2015; Avalos *et al.*, 2014; Ahlberg *et al.*, 2014; De Matteis *et al.*, 2015). Additionally, exposure to AgNPs has been related to other markers of oxidative stress, namely lipid peroxidation, protein carbonylation, altered levels of reduced glutathione (GSH) and upregulated transcription of stress-related genes (Kim and Ryu, 2013). Together with studies showing that ROS scavengers could strongly reduce or eliminate AgNPs toxic effects (Hsin *et al.*, 2008; Foldbjerg *et al.*, 2011; Kim *et al.*, 2011a; Kang *et al.*, 2012), there is thus strong evidence for a major role of oxidative stress in AgNP-mediated toxicity. The causal relationship between AgNPs exposure and increased ROS is thought to be explained through multiple events (Foldbjerg *et al.*, 2015): i) the AgNPs themselves and their oxidative dissolution to silver ions can directly generate free radicals (He *et al.*, 2012; Ahlberg *et al.*, 2014), ii) AgNPs (and/or liberated ions) can enhance ROS production by disrupting the mitochondrial electron transport chain, whereby escaped electrons are accepted by molecular oxygen and give rise to radical species, iii) antioxidant molecules may be depleted and antioxidant enzymes impaired by AgNPs (and/or liberated ions). On the other hand, a few studies have underlined the possible additional role of ROS-independent mechanisms. For instance, Gliga and co-authors found no evidence of ROS production preceding DNA damage and postulated that this could be due to direct interaction of AgNPs with DNA repair pathways (Gliga *et al.*, 2014). In another work, pre-treatment of lung cells with a ROS scavenger prevented reduction of cell viability upon AgNPs administration but did not stop cell cycle changes, which appeared to be ROS-independent (Chairuangkitti *et al.*, 2013).

The contribution of the particles *per se* and of released silver ions to AgNPs-mediated toxicity has been a matter of controversy. While some studies attributed toxicity solely to Ag^+ (Bouwmeester *et al.*, 2011; Prasad *et al.*, 2013), others suggested that Ag^+ could not entirely account for the effects produced (Foldbjerg *et al.*, 2011; Foldbjerg *et al.*,

2012; Grosse *et al.*, 2013; Sambale *et al.*, 2015). Moreover, it has been reported that the influence of Ag^+ on nanosilver toxicity decreased with increasing particle size (Pratsinis *et al.*, 2013) and varied with the silver ion fraction in the AgNPs suspensions (Beer *et al.*, 2012). Recent works have provided key data to understand this interplay, by clearly distinguishing between the effects caused by extracellular and intracellular Ag^+ (Cronholm *et al.*, 2013; Gliga *et al.*, 2014; De Matteis *et al.*, 2015). Silver ions present in the external cell medium showed very low internalisation by cells and induced cell death through membrane damage (Cronholm *et al.*, 2013; De Matteis *et al.*, 2015). On the other hand, AgNPs were shown to be readily taken up by cells and to release Ag^+ intracellularly, in a so called 'Trojan horse' effect. Indeed, by taking advantage of a recently developed chemosensor, De Matteis and co-authors could experimentally demonstrate the gradual release of Ag^+ inside living cells (De Matteis *et al.*, 2015). Thus, the intracellular dissolution of AgNPs, favoured by the acidic environment in the lysosomes and influenced by the physicochemical properties of the particles, appears to be a main driver of the AgNPs toxic effects on cells.

While many reports have addressed the acute toxic effects of AgNPs towards various cultured cells, there is still insufficient knowledge on possible sub-toxic alterations of cell function, more representative of real exposure scenarios. Omics technologies, namely genomics, transcriptomics, proteomics and metabolomics, constitute a valuable approach in this respect, as they offer the possibility to detect unsuspected subtle changes in genes, transcripts, proteins or metabolites before cytotoxic events are detectable by conventional methods. In this thesis, metabolomics has been the approach elected to detect and aid interpreting biochemical events triggered by exposure to low concentration of AgNPs. Thus, the principles of this approach and the state-of-the-art concerning its applications in the field of nanotoxicology will be presented in subsequent sections of this chapter. Before that, a brief overview of cell metabolism is presented, focusing on some major metabolic pathways, as this information is relevant to interpret the results and metabolic hypotheses generated within this work.

1.2. Brief overview of major cellular metabolic pathways

Cellular metabolism can be viewed as a complex network of chemical reactions, catalysed by enzymes and strictly regulated, which allow organisms to grow and reproduce, maintain their structures, and respond to environmental changes (Nelson and Cox, 2004).

As represented in Figure 1.3, these reactions are organised into many inter-dependent metabolic pathways (Kanehisa *et al.*, 2016). Some of those pathways are briefly reviewed below, due not only to their central importance to animal cells, but also to their particular relevance in the context of the results presented in this thesis.

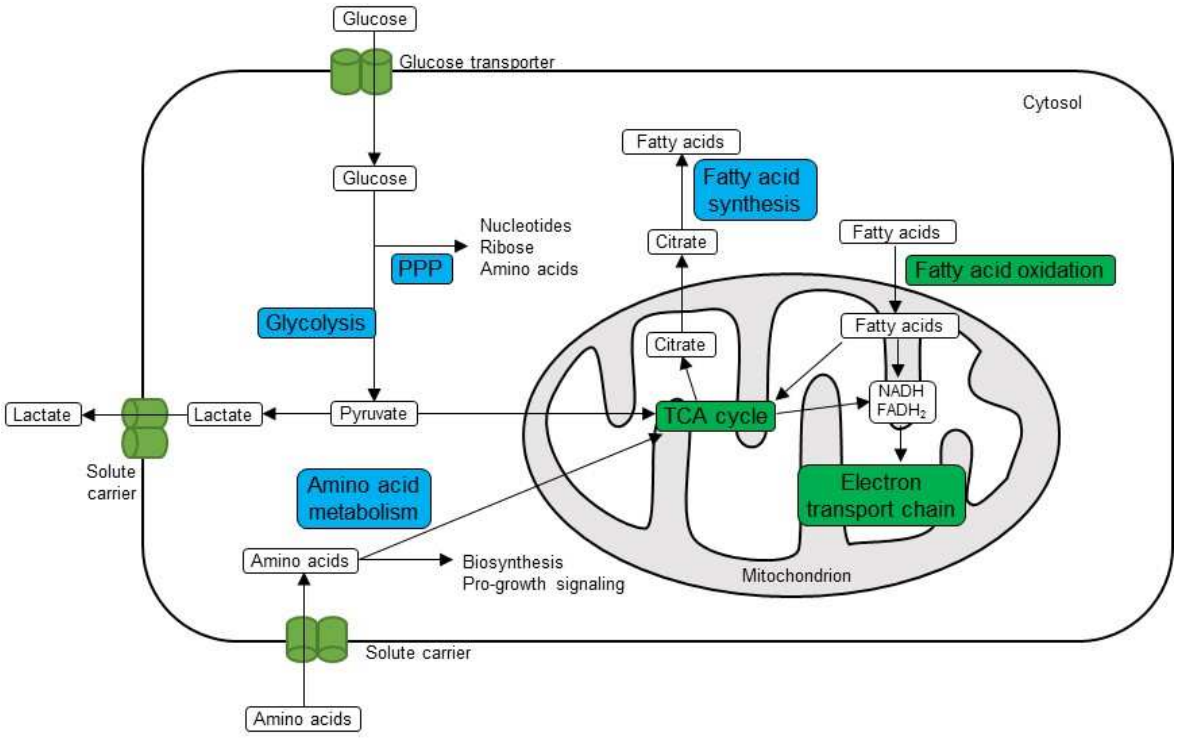

Figure 1.3. Diagram illustrating the integration of major metabolic pathways in animal cells. Pyruvate, from glycolysis, is either converted into lactate and released, or used to fuel the tricarboxylic acid (TCA) cycle. The TCA cycle can also be fuelled by several amino acids, which originate acetyl-CoA, pyruvate or cycle intermediates, or by acetyl-CoA resulting from fatty acid oxidation. Citrate, generated in the TCA cycle, and NADPH, from the pentose phosphate pathway (PPP), are then used for fatty acid synthesis. Finally, NADH and $FADH_2$, produced in the TCA cycle and during fatty acid oxidation, contribute for ATP production from the electron transport chain. Green boxes, oxygen-dependent pathways; blue boxes, oxygen-independent pathways. Adapted from (O'Neill *et al.*, 2016).

1.2.1. Glycolysis and gluconeogenesis

Glycolysis is a ten-step process by which cells split one glucose molecule into two pyruvate molecules, yielding also two ATP and two NADH molecules (Figure 1.4a, left, green). It starts with the uptake of extracellular glucose and proceeds within the cell's cytosol. At an initial phase, the six-carbon glucose molecule is phosphorylated to glucose-6-phosphate, which is converted to fructose-6-phosphate; then, another phosphorylation occurs, forming fructose-1,6-bisphosphate, which is split in two three-carbon molecules,

glyceraldehyde-3-phosphate and dihydroxyacetone phosphate (later isomerised to glyceraldehyde-3-phosphate). In these steps, two molecules of ATP are consumed. Then, each molecule of glyceraldehyde-3-phosphate is oxidised and phosphorylated by inorganic phosphate (P_i) to form 1,3-bisphosphoglycerate. This reaction is accompanied by the reduction of NAD^+ to NADH. The two molecules of 1,3-bisphosphoglycerate are then dephosphorylated in successive steps, with formation of four ATP molecules (substrate-level phosphorylation), yielding two molecules of pyruvate. Pyruvate can subsequently be oxidised to yield the acetyl group of acetyl-coenzyme A, which enters the tricarboxylic acid (TCA) cycle, as part of cellular respiration (section 1.2.2).

The glycolytic pathway is under tight enzymatic control, phosphofructokinase (PFK-1) acting as the key regulatory and rate-limiting point of glycolysis (Berg *et al.*, 2002). PFK-1 is inhibited by ATP and activated by AMP, thus making glycolytic activity dependent on the cell energetic status. PFK-1 is also regulated by metabolites which signal the availability of building blocks for biosynthesis, being inhibited by citrate (generated in the TCA cycle) and long-chain fatty acids. On the other hand, fructose-2,6-bisphosphate is the most potent allosteric activator of PFK-1, being able to elevate enzymatic activity even when ATP levels are high.

Although glycolysis is not highly efficient in energetic terms (net production of two ATP molecules per each glucose molecule oxidised), it plays essential roles in generating NADH molecules, used as electron carriers in multiple biochemical reactions, and in providing intermediates for biosynthetic purposes. Accordingly, rapidly proliferating cells (such as tumour cells) are often characterised by intense glycolytic activity (Mazurek, 2007). To maintain the glycolytic flux, cells must regenerate NAD^+ from NADH. This can be accomplished in the mitochondria through the electron transport chain, or, especially when oxygen is in short supply, through the reduction of pyruvate into lactate, catalysed by the enzyme lactate dehydrogenase (LDH) – lactic acid fermentation (Figure 1.4a, bottom, purple).

Another important pathway of glucose metabolism is gluconeogenesis, defined as the endogenous production of glucose from non-carbohydrate precursors, mainly lactate, certain amino acids and glycerol. These precursors are first converted into pyruvate, either directly (e.g. lactate and alanine) or through TCA cycle intermediates (e.g. oxaloacetate from aspartate), or enter the pathway at later stages (e.g. glycerol converted to dihydroxyacetone phosphate). Although many reactions in gluconeogenesis are the reverse of glycolytic steps, specific enzymes are needed to bypass the three irreversible reactions

of glycolysis (Figure 1.4a, right, blue). These are pyruvate carboxylase and phosphoenolpyruvate carboxykinase, required to form phosphoenolpyruvate from pyruvate, fructose-1,6-bisphosphatase, needed to hydrolyse the phosphate ester of fructose-1,6-bisphosphate and form fructose-6-phosphate, and glucose-6-phosphatase, which catalyses the hydrolysis of glucose-6-phosphate into glucose. Gluconeogenesis and glycolysis are usually reciprocally regulated so that one pathway is minimally active while the other is highly active (Berg *et al.*, 2002).

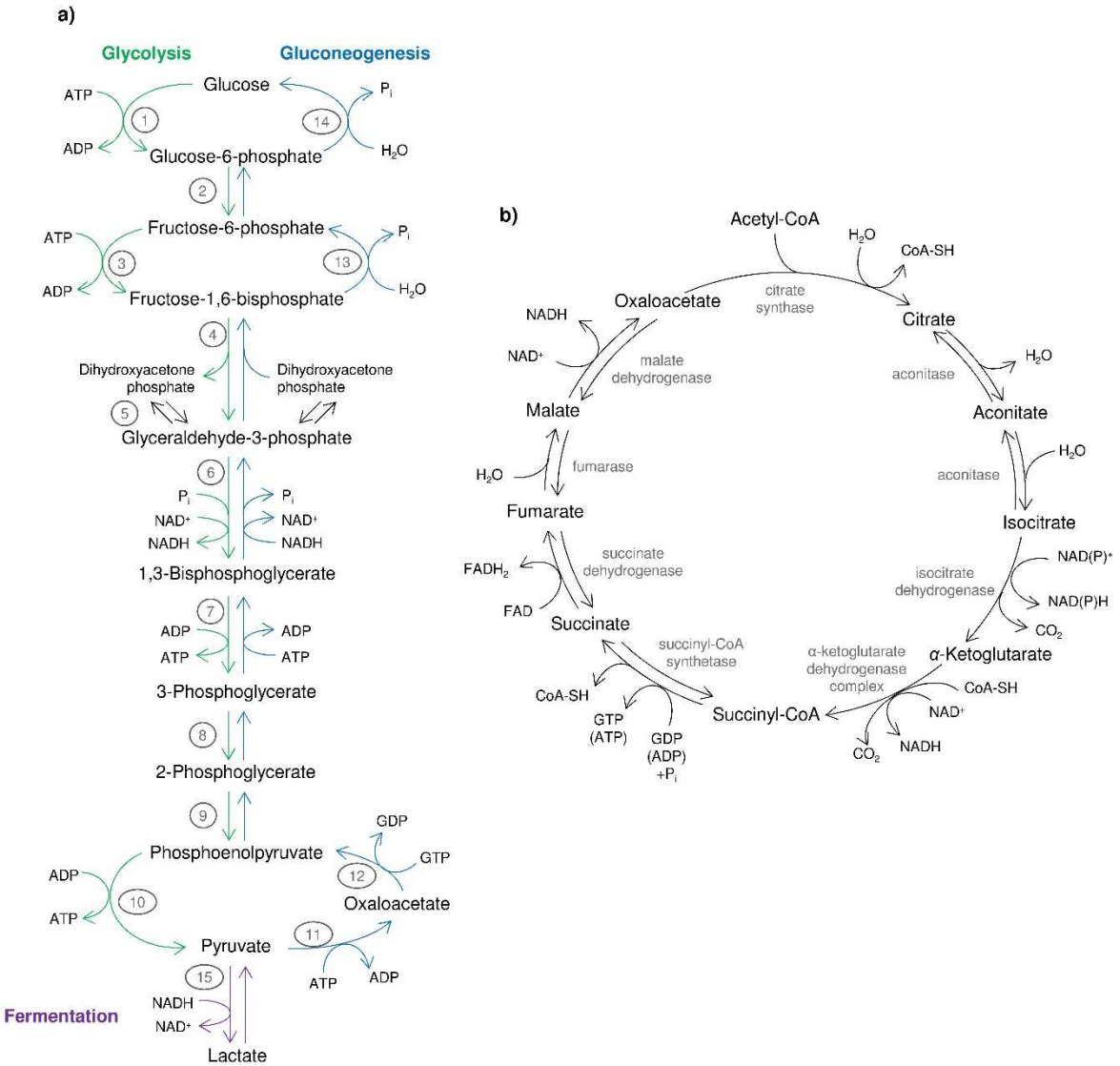

Figure 1.4. a) Opposing pathways of glycolysis (left, green) and gluconeogenesis (right, blue), and lactic acid fermentation (bottom, purple). Circled grey numbers represent the enzymes catalysing each reaction: 1, hexokinase; 2, phosphohexose isomerase; 3, phosphofructokinase-1; 4, aldolase; 5, triose phosphate isomerase; 6, glyceraldehyde-3-phosphate dehydrogenase; 7, phosphoglycerate kinase; 8, phosphoglycerate mutase; 9, enolase; 10, pyruvate kinase; 11, pyruvate carboxylase; 12, phosphoenolpyruvate carboxykinase; 13, fructose-1,6-bisphosphatase; 14, glucose-6-phosphatase; 15, lactate dehydrogenase. b) Reactions of the TCA cycle. Enzymes are represented in grey. Adapted from (Nelson and Cox, 2004).

1.2.2. The TCA cycle and oxidative phosphorylation

The TCA cycle is a series of eight enzyme-catalysed reactions which take place in the mitochondria and form a key part of cellular aerobic respiration (Figure 1.4b). Acetyl-CoA from glycolysis-derived pyruvate, fatty acid oxidation, or amino acid metabolism, enters the TCA cycle by donating its acetyl group to the four-carbon oxaloacetate, forming the six-carbon citrate, in a condensation reaction. Next, in reversible steps, citrate is dehydrated yielding *cis*-aconitate, which is hydrated to form isocitrate. The oxidative decarboxylation of isocitrate, requiring $NAD(P)^+$ as the electron acceptor, then forms *α*-ketoglutarate, NAD(P)H and CO_2. Another oxidative decarboxylation follows, in which *α*-ketoglutarate is converted to succinyl-CoA and CO_2. In this step, NAD^+ also acts as the electron acceptor. Then, succinate is reversibly formed through the hydrolysis of the thioester bond in succinyl-CoA. This reaction has intermediate steps where the enzyme is phosphorylated, and then the phosphoryl group is transferred to ADP/GDP to form ATP/GTP (substrate-level phosphorylation). Succinate is then reversibly oxidised to fumarate, and $FADH_2$ is formed from FAD. Following the reversible hydration of fumarate to malate, the latter is finally oxidised to oxaloacetate, with production of NADH, in a reversible step.

NADH and $FADH_2$ are two major products of the TCA cycle, which transfer electrons to molecular oxygen (reducing it to water) in a set of membrane proteins known as the electron transport chain. This leads to the formation of a proton gradient across the inner mitochondrial membrane, which powers the synthesis of ATP. Overall, this process of oxidative phosphorylation generates 26 (or 28) of the 30 (or 32) ATP molecules formed when one glucose molecule is completely oxidised to carbon dioxide and water. Notably, the tight coupling between electron transfer (with recycling of electron donors back to the TCA cycle) and ADP phosphorylation to ATP ensures that the rate of the TCA cycle matches the need for ATP (Berg *et al.*, 2002).

The TCA cycle also has a role in anabolism, as it provides intermediates for biosynthesis, such as succinyl-CoA for the formation of porphyrins, *α*-ketoglutarate or oxaloacetate for the synthesis of amino acids, and citrate for the formation of fatty acids. This anabolic role is usually sustained by replenishment of TCA cycle intermediates by anaplerosis, mainly using amino acids as substrates, in order to keep the cycle operating.

1.2.3. The pentose phosphate pathway (PPP)

The pentose phosphate pathway occurs in the cytosol, as a parallel branch of glycolysis, and comprises a linear oxidative portion and a cyclic non-oxidative phase (Figure 1.5). The first step is the oxidative decarboxylation of glucose-6-phosphate, ultimately leading to: i) the formation of ribose-5-phosphate, used in the synthesis of nucleotides, coenzymes and nucleic acids, and ii) the generation of NADPH. This dinucleotide provides reducing equivalents for biosynthetic reactions (e.g. synthesis of fatty acids and sterols), as well as for regeneration of reduced glutathione (GSH) from its oxidised form (GSSG), in order to maintain an adequate cellular redox environment. The non-oxidative branch of the PPP consists of the reversible metabolism of five-carbon phosphosugars into phosphorylated three- and six-carbon sugars, which can be utilised by glycolysis.

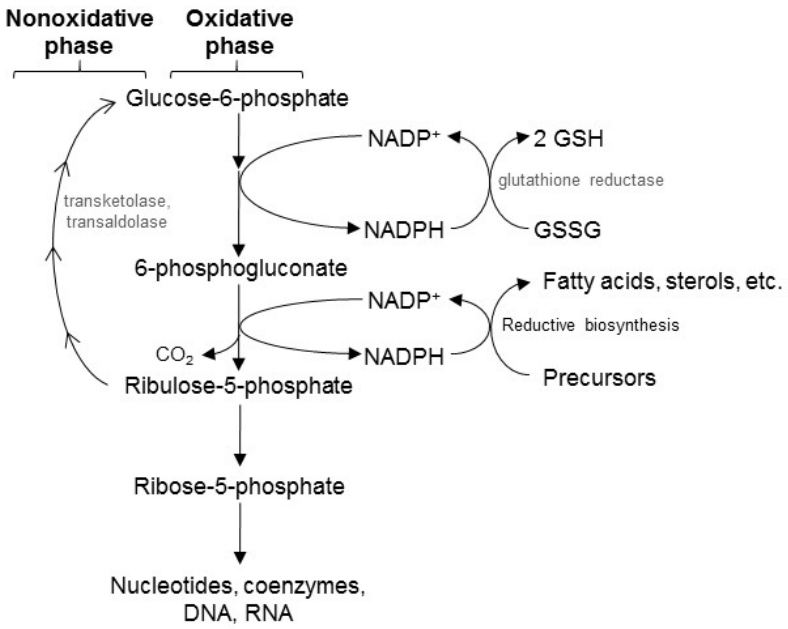

Figure 1.5 Schematic representation of the pentose phosphate pathway (PPP): in the oxidative phase, glucose-6-phosphate is dehydrogenated and decarboxylated by NADP-dependent enzymes, yielding NADPH and ribulose-5-phosphate which is then converted to ribose-5-phosphate, the precursor for nucleotides, coenzymes and nucleic acids; in the nonoxidative phase, ribulose 5-phosphate is converted back to glucose 6-phosphate by a series of reactions catalysed mainly by transketolase and transaldolase. NADPH formed in the oxidative phase is used to recycle GSH from GSSG and to support reductive biosynthesis. Adapted from (Nelson and Cox, 2004).

1.2.4. Fatty acid synthesis and degradation

Fatty acids are synthesised in the cytosol from acetyl-CoA and NADPH, in a series of reactions catalysed by fatty acid synthases. The precursors in fatty acid synthesis may derive from glycolysis, the TCA cycle and the pentose phosphate pathway. In particular, for the synthesis of straight chain fatty acids, citrate originated in the TCA cycle passes through the mitochondrial inner membrane, through the citrate-malate shuttle, into the cytosol where it is cleaved, regenerating acetyl-CoA along with oxaloacetate in an ATP-dependent reaction. Acetyl-CoA is then carboxylated to form malonyl-CoA, the committed step in fatty acid synthesis, catalysed by acetyl-CoA carboxylase and allosterically regulated (through activation by citrate and feedback inhibition by palmitoyl-CoA). Elongation of fatty acyl chains proceeds with condensation of an acyl group (e.g. from acetyl-CoA) activated by fatty acid synthase and two carbons derived from malonyl-CoA, with elimination of CO_2. The nascent fatty acid chain is then reduced to an alcohol, dehydrated to create a double bond, and reduced to form a saturated product. The last four steps are repeated until, for example, palmitate, which is the precursor of other long-chain fatty acids, is synthesised. In the case of branched-chain fatty acid synthesis, branched-chain amino acids are used as substrates for elongation. Fatty acids are then used to generate lipids essential for cellular growth and proliferation, namely triacylglycerols and phospholipids.

Fatty acid degradation takes place in the mitochondria and involves three stages: in the first, named β-oxidation, fatty acids are transported into the mitochondria, either by diffusion (short-chain fatty acids) or through conjugation with carnitine (medium- and long-chain fatty acids), where they are oxidised to two-carbon fragments, yielding large amounts of acetyl-CoA, NADH and $FADH_2$; then, if the supply of oxaloacetate is sufficient, the resulting acetyl-CoA is oxidised to CO_2 in the TCA cycle. Alternatively, acetyl-CoA can give rise to ketone bodies; finally, the reduced electron carriers $FADH_2$ and NADH produced during β-oxidation transfer electrons to O_2 through the electron transport chain, for ATP generation (oxidative phosphorylation). The rate of fatty acid degradation is coupled to the need for ATP, as β-oxidation can continue only if NAD^+ and FAD are regenerated, and is inhibited by malonyl-CoA, which prevents the translocation of fatty acids into mitochondria by inhibiting the formation of acyl carnitine.

1.3. Metabolomics in nanotoxicology

1.3.1. The metabolomics approach

Metabolomics entails the comprehensive analysis of the inventory of endogenous small molecules (molecular mass < 1000 Da) present in a biological system as a result of intermediary cellular metabolism (Nicholson *et al.*, 1999; Fiehn, 2002). The general aim is to detect/quantify fluctuations in this inventory, the so called metabolome, upon a given stimulus/perturbation, such as a disease, a toxicant, a pharmaceutical drug or a nanomaterial. Being modulated by the complex interplay between gene expression, enzymatic activities and fluctuations in metabolic fluxes, the metabolome closely reflects the cell's functional status. Hence, the comprehensive description of metabolite changes, through metabolomics, has the potential to reveal unforeseen deviations from homeostasis and to identify new endpoint markers of effect. Moreover, since a metabolite is the same chemical entity irrespective of its origin, metabolic profiles of cultured cells can potentially be correlated to those of animal tissues/biofluids, thus enabling *in vitro-in vivo* correlations to be proposed.

The main analytical platforms used in metabolomic studies are nuclear magnetic resonance (NMR) spectroscopy and mass spectrometry (MS), the latter being usually coupled to liquid (LC) or gas chromatography (GC). These techniques enable the simultaneous detection of tens to hundreds of metabolites in complex mixtures like biofluids and tissue/cell extracts, providing a holistic approach which is clearly more powerful than the measurement of a few pre-established metabolites by classical biochemical methods (Lindon and Nicholson, 2008). Data treatment by multivariate statistics is then typically employed to deal with data complexity and search for consistent variation patterns or build classification models.

MS-based methods are generally more sensitive than NMR, enabling the detection of metabolites present at sub-nanomolar concentrations (Wishart *et al.*, 2013). However, the wider view of the metabolome offered by MS methods does not always translate into a significant gain in biochemical information, as the resulting data may be extremely complex and difficult to interpret. On the other hand, despite inherent sensitivity limitations, high resolution NMR shows unparalleled analytical reproducibility and the ability to provide unequivocal structural and quantitative information on a wide range of metabolites, present in the micromolar-milimolar range. In this work, metabolic profiling of cultured cells has been performed through NMR metabolomics. Thus, the basic principles of NMR spectroscopy,

as well as of the multivariate analysis and univariate statistical methods employed, will be reviewed below.

NMR spectroscopy

The theory of NMR is thoroughly covered in the literature (Ross *et al.*, 2007; Keeler, 2010; Zerbe and Jurt, 2014) and the aim of this subsection is not to provide an in depth account of NMR fundamentals and methods, but rather to briefly describe the basic principles underlying this technique.

NMR is a phenomenon which occurs when the nuclei of certain atoms are immersed in a static magnetic field (B_0) and exposed to a second oscillating magnetic field (B_1). Not all nuclei experience this phenomenon, it depends on whether they possess a property called spin (I). Some nuclei carry a total spin (e.g. ^{1}H, ^{2}H, ^{13}C, ^{15}N, ^{19}F, ^{31}P) resulting in a magnetic moment $\mu = \gamma I h / 2\pi$ (where γ is the gyromagnetic ratio of the atomic nucleus), while others, with even number of protons and neutrons (e.g. ^{12}C, ^{14}C, ^{16}O), do not, thus being undetectable by NMR spectroscopy.

When nuclear spins with $I = ½$ (such as protons) are exposed to an external homogenous magnetic field B_0, usually defined along z, the magnetic moments align parallel or anti-parallel with respect to B_0, resulting in two spin states α and β with an energy difference ΔE. The α and β states are filled according to the Boltzmann distribution, resulting in a slight excess of α states at equilibrium ($N\alpha/N\beta = e^{\Delta E/kT}$). This excess of α states gives rise to a macroscopic magnetic moment, the so called net magnetisation M_0, aligned with the z axis.

To detect an NMR signal, M_0 is flipped into the xy plane by applying a radiofrequency (RF) magnetic field B_1, orthogonal to z, for a defined time period (RF pulse). The magnetisation M will align along the x-direction and precess with a resonance frequency $f_0 = \gamma B_0 / 2\pi$. As soon as the RF pulse is turned off, the nuclear spins relax back to equilibrium according to two processes: i) the recovery of the magnetization along the z axis (longitudinal relaxation characterised by the time constant T_1) and ii) the loss of phase coherence of spins precessing at different rates in the xy plane (transverse relaxation occurring with the time constant T_2). Precession of magnetization in the xy plane induces an oscillating signal in the detection coil, the so called free induction decay (FID), which is then converted into a frequency domain signal by Fourier transformation (FT) (Figure 1.6).

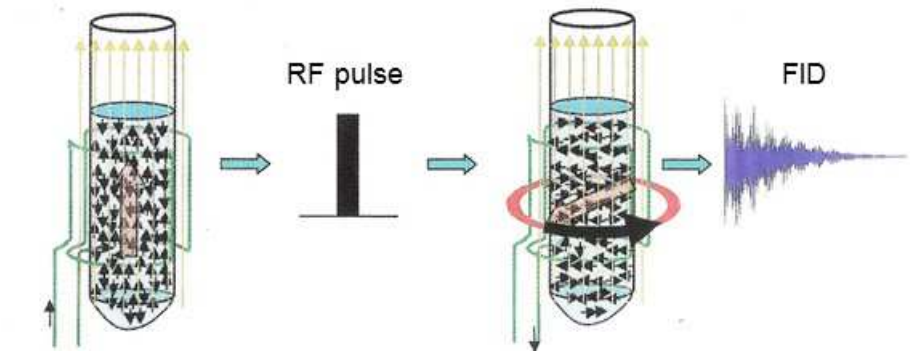

Figure 1.6. Detection of an NMR signal: (left) a sample with many spins (>10^{12}) is placed inside a strong external magnetic field B_0 (orange) oriented along the *z*-direction. The sample is enclosed in a detection coil (green). At thermal equilibrium about one spin in every 10,000 contributes to a macroscopic magnetisation M_0 shown in transparent red. After short application of a high-frequency B_1 field (90º pulse, black bar at the left panel) the magnetisation is aligned along the *x*-axis of the rotating B_1 field, and starts to precess around B_0. Adapted from (Ross *et al.*, 2007).

Nuclei with different chemical environments (electronic cloud/chemical neighbourhood) will resonate at slightly different frequencies, giving rise to signals in different positions of the NMR spectrum. The frequency values are converted into chemical shifts (in parts per million), based on the frequency of a reference compound, so that chemical shifts are independent of B_0 and data acquired at different field strength can be directly compared.

The ^{1}H chemical shifts of some characteristic functional groups are comprised within the relatively narrow range of 0-15 ppm: saturated hydrocarbons generally resonate between 1.0 and 4.0 ppm, whereas the olefinic protons appear in the region of 5.0-6.5 ppm and the resonances of aromatic protons are in the region of 6.5-10 ppm.

Another important property of NMR signals is their splitting pattern, which reflects the interactions between neighbouring spins, via the electrons in the chemical bond – scalar or *J* coupling. For nuclei with $I = ½$, the multiplicity of the line splitting equals n + 1, where n is the number of non-equivalent nuclei in the neighbouring group. The line separation (in Hz) corresponds to the coupling constant (*J*) between the nuclei, which generally decreases as the number of bonds between the coupled nuclei increases.

^{1}H NMR is inherently quantitative, as the area under each signal is proportional to the number of protons that originate that signal. However, some conditions must be obeyed to perform absolute quantification, namely a sufficiently long delay between repetitions (scans) to allow the full relaxation of nuclear spins. In particular, a perfect linearity between the NMR signal and analyte concentration requires that the inter-scan delay (recycle time)

is larger than five times the longest T_1 in the sample (Bharti and Roy, 2012). For most metabolites, T_1 relaxation times are in the range 1-3 s (Ross *et al.*, 2007), hence quantitative conditions require long acquisition times. This is often impractical due to time constraints and metabolomic studies typically rely on relative quantification of metabolites.

The unambiguous identification of resonances in the ^{1}H NMR spectrum of a biological sample, usually characterised by a rich, complex composition, requires the use of two-dimensional (2D) NMR methods. In general, these methods are based on the acquisition of a set of 1D spectra under incrementation of a t_1 evolution delay (Figure 1.7a). Performing FT in respect to both t_1 and t_2 (acquisition time of each FID) produces a 2D map where the spectral amplitude is plotted as a function of two frequency dimensions. Among the most commonly employed 2D methods are homonuclear shift-correlation experiments (Figure 1.7b), namely correlation and total correlation spectroscopy (COSY and TOCSY, respectively). In ^{1}H-^{1}H TOCSY, additional cross peaks show up for pairs of spins which have a common coupling to another spin, through multistep transfer of the magnetization over a network of nuclei in a molecule. If the correlation is between different nuclei e.g. ^{1}H and ^{13}C, the experiment is called heteronuclear (Figure 1.7c). For instance, in a ^{1}H-^{13}C heteronuclear single quantum coherence (HSQC) spectrum, one dimension shows the chemical shift of ^{13}C and the other the chemical shift of the directly bound ^{1}H (correlated via the $^1J_{CH}$ coupling constant). Another frequently used 2D experiment is the *J* resolved (*J*-res), where *J*-coupling information is separated into a second dimension from the chemical shifts (Ross *et al.*, 2007).

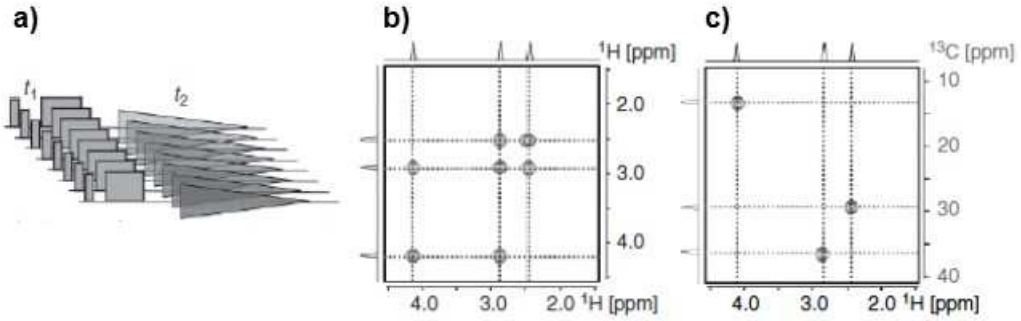

Figure 1.7 a) Diagram illustrating a basic 2D NMR experiment: a set of 1D spectra are acquired under incrementation of a t_1 evolution delay, and FT is performed with respect to t_1 and t_2; b) 2D homonuclear correlation spectrum, where the off-diagonal cross peaks code for magnetization which was transferred by a selected interaction mechanism between two spins; c) 2D heteronuclear correlation spectrum, where proton magnetization was transferred to carbons (evolution along t_1) and back to protons for detection along t_2. Adapted from (Ross *et al.*, 2007).

Multivariate analysis (MVA)

Since each 1D NMR spectrum comprises a wide range of variables (metabolites) and numerous spectra are often acquired within a study, multivariate analysis (MVA) is required to reduce data complexity and extract meaningful biochemical information.

Multivariate analysis (MVA) enables the multi-parametric evaluation of complex datasets, such as ^{1}H NMR spectra from multiple samples, thus helping to unveil consistent differences between sample groups. A typical MVA workflow, similar to that used in this work, is shown in Figure 1.8. After appropriate data pre-treatment, which commonly includes signal alignment, normalisation and scaling procedures (Veselkov *et al.*, 2009), the data are initially explored through unsupervised methods, such as principal component analysis (PCA), whereby no *a priori* information on sample groups is included.

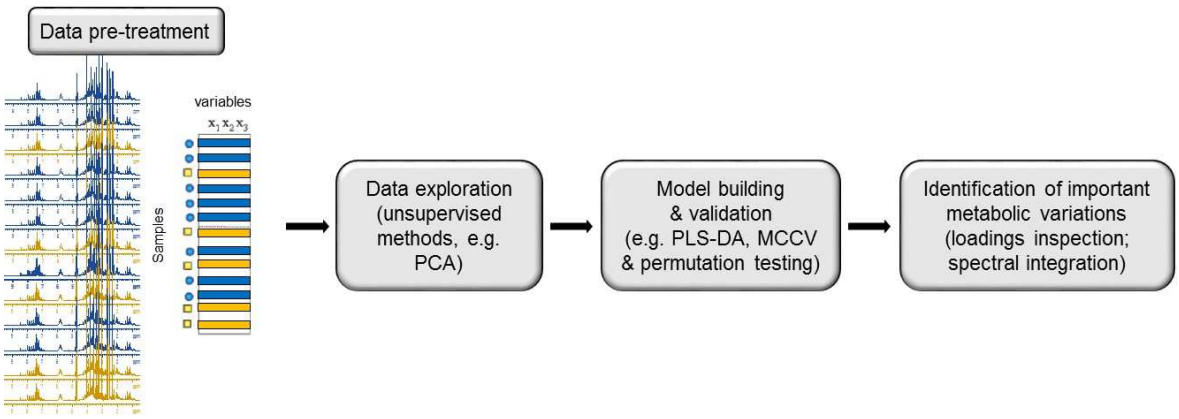

Figure 1.8. Typical workflow for the multivariate analysis of NMR data in metabolomic studies.

PCA is a projection-based method which converts the multidimensional data table (in this case, a spectral matrix composed of samples or observations and variables) into a lower-dimensional matrix. In PCA, the original variables are converted into a set of uncorrelated (orthogonal) variables, called principal components (PCs: PC1, PC2,…PCn), thereby defining a lower n-dimensional space to represent the data. The PCs are linear combinations of the original variables computed so that PC1 accounts for most of the variance, PC2 for the 2nd largest variance and so on, always obeying the constraint that all PCs are orthogonal to each other. Hence, PCA allows samples (observations) to be distributed in a scores scatter plot according to the similarities and differences in their profiles. The influence (weight, w) of each variable on sample clustering is then given by

the loadings projection, knowing that the disposition of the observations in the scores plot is related to the disposition of the variables in the loadings plot (Figure 1.9).

After initial data exploration, supervised methods (i.e. methods whereby information on class membership is included) may follow to build classification models and provide improved information on the variables accounting for sample separation. Partial least squares discriminant analysis (PLS-DA) is the most commonly used method for this purpose. PLS-DA assesses the relationship between the original data matrix X and a second matrix Y containing qualitative values which relate to sample class. The goal is to define new variables (latent variables, LVs) which model both the data matrix X and the correlation with Y, i.e. which maximise class discrimination. Similarly to PCA, the results of PLS-DA can be visualised through scores and loadings plots. Additionally, the loadings may be coloured as a function of variable importance to the projection (VIP) to highlight the most discriminant metabolites (with VIP > 1).

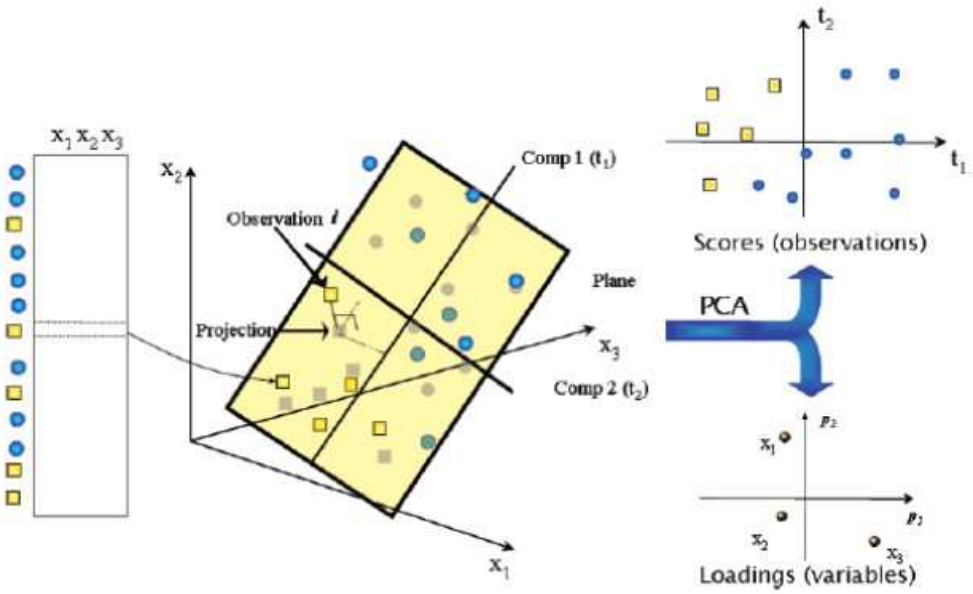

Figure 1.9. Scheme representing principal component analysis (PCA), whereby the observations are projected into the space defined by the new reduced set of variables (principal components) obtained by linear combination of the original variables. Reprinted with permission from (Trygg *et al.*, 2007), Copyright © 2007 American Chemical Society.

Given the very high ratio of variables to samples typically characterising the matrices used in metabolomic studies, PLS-DA models are prone to over-fitting and sample separation in the scores plot does not always correspond to consistent differences between the groups. A way to assess model robustness is through cross validation methods and permutation testing (Westerhuis *et al.*, 2008). For instance, in Monte Carlo cross validation

(MCCV), used in this work, the data is randomly divided into calibration and validation sets, and internal cross validation of the calibration set is followed by prediction of class membership in the validation set (Xu and Liang, 2001). This process is repeated for a number of iterations (500-1000), each time with a randomly changed composition of the calibration and validation sets. The resulting confusion matrix can then be used to calculate sensitivity and specificity, which may be plotted in a receiver operating characteristic (ROC) space. Also, a chiefly important parameter to assess model robustness is the cross-validated explained variance or predictive power (Q^2), which represents the fraction of total variation of X and Y matrices that can be predicted by the extracted components; the closer Q^2 is to 1 the more robust is the model.

Univariate analysis

Measurement of signal integrals to quantify the extent of specific metabolic variations is often performed in NMR metabolomics as a complement to MVA. The most simple and straightforward way to evaluate such extent is to calculate the percentage of variation (%var) between two groups (Equation 1.1, where $\bar{X}$ is the average value in a given group). This value should be accompanied by its respective error, which takes into account the standard deviation (s) and the number of samples (n) in each group (Equation 1.2).

$$\%var = \frac{\bar{X}_1 - \bar{X}_2}{\bar{X}_2} \times 100 \qquad \textbf{Equation 1.1.}$$

$$error\ (\%) = \frac{\sqrt{\frac{s_1^2}{n_1} + \frac{s_2^2}{n_2}}}{\frac{(n_1 \times \bar{X}_1 + n_2 \times \bar{X}_2)}{(n_1 + n_2)}} \times 100 \qquad \textbf{Equation 1.2.}$$

Another way to express the magnitude of variation between groups is through the calculation of the standardised mean difference or effect size (*ES*) (Berben *et al.*, 2012). This parameter accounts for the standard deviations (s_1 and s_2) associated with the means compared ($\bar{X}_1$ and $\bar{X}_2$) and the number of samples (n_1 and n_2). As shown in equation 1.3, the difference between the average of each group is divided by their pooled standard

deviation; *df* stands for degrees of freedom and corresponds to $n_1 + n_2 - 2$. The standard error (*SE*) of the standardised mean difference is then calculated according to Equation 1.4. In order to avoid a biased *ES* due to small sample numbers, a correction (*J*) can be applied by multiplying *J* (Equation 1.5) by the *ES* value. The same correction should also be applied to the *SE*.

$$ES = \frac{\bar{X}_1 - \bar{X}_2}{\sqrt{\frac{(n_1-1)\times s_1^2 + (n_2-1)\times s_2^2}{df}}} \qquad \textbf{Equation 1.3.}$$

$$SE = \sqrt{\frac{n_1+n_2}{n_1\times n_2} + \frac{ES^2}{2(n_1+n_2)}} \qquad \textbf{Equation 1.4.}$$

$$J = 1 - \frac{3}{4\times df - 1} \qquad \textbf{Equation 1.5.}$$

Using the *ES* as a measure of the magnitude of variations is advantageous because not only it accounts for intra-group dispersion, as it is reasonably insensitive to sample size, thus providing more reliable comparison of small sample sets. According to Cohen and colleagues absolute effect sizes around 0.2, 0.5 and larger than 0.8 correspond to small, medium and large variations, respectively (Cohen, 1988). Thus, in this work, the criterion for considering a variation to be relevant was absolute $ES > 0.8$.

Additionally, the *p*-value determined through the student t-test (or a non-parametric analogue like the Wilcoxon test) provides information on the statistical significance of the difference between the two means compared. The *p*-value expresses the probability of rejecting the null hypothesis (no difference between the means compared) at a pre-established significance level. However, *p*-values are greatly influenced by sample size (Kalinowski and Fidler, 2010), decreasing with increasing number of samples compared. This means that an effect can be large, but fail to meet the often used $p < 0.05$ criterion if the sample size is small.

Correlation analysis

The statistical correlation between two metabolites can be very helpful in identifying biochemical relationships. The Pearson correlation coefficient, *r*, gives an estimate of the degree of linear association between normally distributed variables, and is calculated through Equation 1.6, where *x* and *y* are metabolites, forming *n* pairs. Inverse correlation between variables is demonstrated through negative *r* values, -1 being the value for the maximum inverse association; conversely positive *r* values indicate positive correlations, with maximum at *r* = 1.

$$r = \frac{\sum_{i=1}^{n}(x_i-\bar{x})(y_i-\bar{y})}{\sqrt{\sum_{i=1}^{n}(x_i-\bar{x})^2 \sum_{i=1}^{n}(y_i-\bar{y})^2}} \qquad \textbf{Equation 1.6.}$$

It is also possible to correlate a single variable with all variables in a NMR spectral matrix, through statistical total correlation spectroscopy (STOCSY) (Cloarec *et al.*, 2005). In NMR studies, this procedure is particularly helpful for the assignment of unknown resonances. Here, the correlation matrix *C* is computed from a set of sample spectra according to Equation 1.7, where X_1 and X_2 designate the autoscaled experimental matrices and *n* is the number of spectra.

$$C = \frac{1}{n-1} X_1^t X_2 \qquad \textbf{Equation 1.7.}$$

1.3.2. Considerations about NMR metabolomics of cultured mammalian cells

Metabolomic studies of cultured mammalian cells have been growing exponentially over the last years, with applications reported in diverse areas like toxicology, drug testing, mechanistic understanding of diseases and pharmaceutical research (León *et al.*, 2013).

Compared to metabolomics of animal models or human subjects, *in vitro* cell metabolomics offers several advantages, such as a high control over experimental variables, less stringent ethical issues, lower costs and potentially lower biological variability (Čuperlović-Culf *et al.*, 2010). On the other hand, the metabolomic analysis of cultured cells involves specific requirements that can be quite challenging. One critical issue is the

number of cells needed to obtain detailed metabolic information. Under common NMR acquisition conditions (500-600 MHz field strength, regular high resolution probe), a minimum of ~3-5 million cells per sample is typically required to detect a few tens of metabolites (Khoo and Al-Rubeai, 2007; Duarte *et al.*, 2009a). Thus, in a study involving several experimental conditions and biological replicates of each condition, growing sufficiently high cell numbers can be a demanding task. This is probably one of the reasons why cell lines are more extensively used than primary cultures, as the first are much easier to grow and present nearly unlimited lifespan. Moreover, cell lines tend to have stable phenotypes which do not depend on donor characteristics, unlike primary cells, particularly those of human origin, which are characterised by high phenotypic variability (León *et al.*, 2013).

Another important aspect when culturing adherent cells, is the method of detachment from the culture surface. A commonly used method consists of using trypsin, to cleave cell adhesion proteins, together with ethylenediaminetetraacetic acid (EDTA) to chelate calcium ions needed for integrin-mediated cell attachment. Although trypsinization is extensively used in routine cell culture, it has been argued that it alters the physiological state of cells, changing their metabolic profile (Teng *et al.*, 2008). Moreover, depending on the cell type and the time required for trypsinization, this procedure has been shown to cause significant metabolite leakage by increasing cell membrane permeability (Dettmer *et al.*, 2011). Another inconvenience regards the time-consuming steps that follow trypsin addition (washing and centrifugation), which can lead to metabolite modifications and further losses. An alternative approach consists of mechanically scraping the cells of the culture surface, after medium removal. In particular, direct scraping in the presence of the extraction solvent has been recommended as the harvesting procedure that maximises overall metabolite yield and enables rapid metabolism quenching (Teng *et al.*, 2008; Dettmer *et al.*, 2011; Garcia-Canaveras *et al.*, 2011).

The quenching (deactivation) of cellular metabolic activity at the time of sampling is critical to avoid fluctuations in metabolite levels during sample collection and processing, which could lead to misleading results. There are several ways to halt enzymatic activity, such as liquid nitrogen freezing, addition of ice-cold organic solvents or of quenching buffers (León *et al.*, 2013). If cell integrity is to be preserved, the use of a cold isotonic saline solution (0.9% NaCl, 0.5ºC) is favoured (Dietmair *et al.*, 2010).

When using NMR spectroscopy, cells can either be analysed directly or subjected to solvent extraction to obtain liquid metabolite mixtures. Direct analysis of whole cells can involve tube NMR (with inherent disadvantages of poor resolution and sample deposition over time) or high resolution magic angle spinning (HRMAS) NMR. This latter method allows well-resolved spectra of whole cells to be recorded (especially if cells have been lysed), providing simultaneous information on both small metabolites and macromolecular components (Duarte *et al.*, 2009b). Also, it avoids losses or modifications possibly associated with extraction procedures, offering a closer representation of the real cellular composition and environment. On the other hand, quantification of metabolites from HRMAS spectra presents additional complexity, as the visibility of signals is not only dependent on metabolite abundance but also on their molecular mobility. For instance, while the lipid signals detected by HRMAS ^{1}H NMR of cell pellets/suspensions correspond mainly to highly mobile neutral lipids in cytosolic droplets (Lutz *et al.*, 2005), lipid extracts have a better chance to represent the entire cellular lipid pool, including membrane lipids. In addition, given the possibility of using an automatic sample changer for liquid samples, the NMR analysis of cell extracts is much faster than HRMAS of whole cells, which is especially important when high sample numbers are to be analysed.

Cell extraction protocols reported in the literature vary in conditions like type of solvent and volume proportion, number of extraction cycles, duration of each cycle, temperature and homogenisation method (León *et al.*, 2013). Given the diverse chemical nature of intracellular metabolites, there is no universal method capable of extracting the whole cellular content. Nevertheless, efforts have been made to establish the most efficient and reproducible extraction procedures which are compatible with the analytical platform to be used. In particular, different solvent mixtures have been extensively tested, including different proportions of water, acids and organic solvents (Dettmer *et al.*, 2011; Martineau *et al.*, 2011). Among the solvent mixtures compared, the one based on methanol, chloroform and water was highlighted as the most suitable for retrieving a higher number of metabolites from adherent mammalian cells and for achieving reliable and robust NMR metabolic profiles (Martineau *et al.*, 2011). Also, this mixture allows the dual-phase extraction of both polar and lipophilic compounds, allowing their composition to be characterised separately.

In this work, after a careful literature review and some experimental tests (results not shown), we have decided to perform cell metabolomics by solution state NMR of cellular polar and lipophilic extracts, together with NMR of culture medium supernatants. The experimental details of sample collection and preparation are presented in Chapter 2.

1.3.3. State-of-the-art of metabolomics applications in nanotoxicology

Assessing the metabolic changes induced by nanomaterials on cellular or animal models, through NMR or MS-based metabolomics, is increasingly proving its value for revealing unforeseen biological effects and helping to understand the mechanisms of nanomaterials toxicity (Duarte, 2011; Lv *et al.*, 2015). Indeed, the number of scientific papers reporting metabolomic applications in nanotoxicology has been continuously growing over the last years (Figure 1.10a). The earliest reports date back to 2008-2010 and used NMR analysis of animal (rats) biofluids to assess the systemic responses to the administration of copper (Lei *et al.*, 2008), titanium dioxide (Bu *et al.*, 2010) or iron oxide (Feng *et al.*, 2010) nanoparticles. Subsequently, in 2011, the first papers describing the metabolic responses of cultured mammalian cells to nanomaterials were published (Figure 1.10b). Both NMR spectroscopy and MS-based analytical platforms have been used in those studies (Figure 1.10c) and the complementarity of the various methods in revealing different aspects of the metabolome has often been highlighted.

Among the nanomaterials addressed by metabolomics, titanium dioxide and silica nanoparticles were the ones most extensively studied (Figure 1.10d). This was probably due to their widespread industrial uses and incorporation into consumer products (thus causing increased occupational exposure), together with emerging biomedical applications. For similar reasons, the interest in AgNPs has intensified over the last years, as largely reflected by the work produced within this thesis (Carrola *et al.*, 2016a; Carrola *et al.*, 2016b).

Note, however, that before the commencement of this work, the information about the impact of silver nanoparticles on cell metabolism was very scarce. A preliminary study published in 2011 by Kim and co-authors examined the metabolic effects of AgNPs on cultured liver cells and suggested that the changes observed were mediated by oxidative stress and glutathione metabolism (Kim *et al.*, 2011c). However, the lack of information on nanoparticle properties and exposure conditions, as well as of proper validation of metabolic changes, hampered solid conclusions from that work. As for *in vivo* metabolomics of AgNPs,

studies have focused on the environmental impact of these particles, using a terrestrial invertebrate earthworm (Li *et al.*, 2015b) and a freshwater invertebrate (Li *et al.*, 2015a) as model organisms. On the other hand, the investigation of mammalian models with a view to assess putative effects of AgNPs on human health, has been addressed in two studies, one confined to the analysis of rat urine (Hadrup *et al.*, 2012) and the other, published by our group, comprehensively describing the metabolic effects of AgNPs on mice serum and several organ tissues (paper submitted).

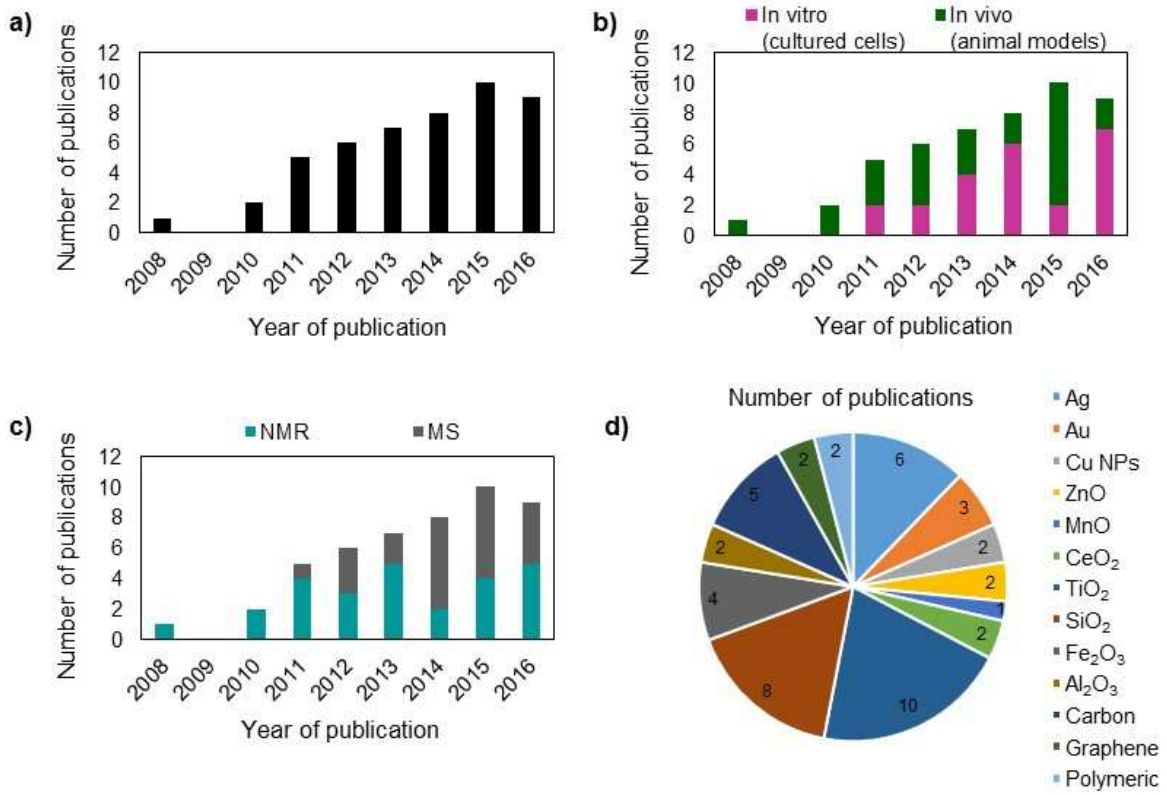

Figure 1.10. Published papers reporting metabolomic applications in nanotoxicology: a) total number of published papers, by year; b) distribution according to the model in study; c) distribution according to the analytical platform used; d) distribution according to the nanomaterial tested. Source: Web of Science, September 2016 (ThomsonReuters™, 2016); search terms: (metabolomics or metabonomics) and (nanoparticles or nanomaterials).

Other nanoparticles investigated through metabolomics included gold nanorods, several metal oxide nanoparticles, carbon nanotubes and graphene nanosheets (Figure 1.10d). A summary list of metabolomic applications in nanotoxicology, using *in vitro* or *in vivo* animal models, is presented in Table 1.1. The biochemical findings of some of these works will be discussed, when pertinent, along with the results presented through Chapters 4 to 6 of this thesis.

Table 1.1. List of metabolomic studies addressing the effects of different nanoparticles on cellular or animal models. n. a., not available.

NP type	Size (nm)	Cell model	Animal model	Sample type	Analysis method	Perturbed metabolic pathways	Reference
Ag	30	human keratinocytes (HaCaT)		cell extracts and medium supernatants	^{1}H NMR	glutathione-based antioxidant protection; glutaminolysis; TCA cycle; energy depletion; cell membrane modification	(Carrola *et al.*, 2016a)
	10, 30, 60	human keratinocytes (HaCaT)		cell extracts and medium supernatants	^{1}H NMR	glutathione-based antioxidant protection; glutaminolysis; TCA cycle; energy depletion; cell membrane modification	(Carrola *et al.*, 2016b)
	10, 40		*Daphnia magna* planktonic crustaceans	extracts	^{1}H NMR	energy metabolism; oxidative stress; anaerobic metabolism	(Li *et al.*, 2015a)
	10, 40		*Eisenia fetida* earthworms	extracts	^{1}H NMR	energy metabolism; protein synthesis; osmoregulation	(Li *et al.*, 2015b)
	14		male and female Wistar rats	urine	HPLC-MS	purine metabolism	(Hadrup *et al.*, 2012)
	n. a.	human Chang liver cells		intact cells	HRMAS NMR	glycolysis; amino acid and phospholipid metabolism; GSH synthesis	(Kim *et al.*, 2011c)
Au	5, 30	human colon adenocarcinoma (Caco-2)		cell lysates	LC-MS	carbohydrate metabolism; stress response	(Gioria *et al.*, 2016)
	10	spermatocyte-derived /GC-2) and Sertoli (TM-4)		cell extracts	GC-MS	glycine, serine and threonine metabolism	(Xu *et al.*, 2014)
	58×15 nanorods	human lung epithelial (A549) and bronchial epithelial (16HBE)		cell extracts	^{1}H NMR	glycolysis; glutathione synthesis; purine and pyridine metabolism	(Zhang *et al.*, 2013)
Cu	28.2	human lung epithelial (A549)		cell extracts	HPLC-MS	oxidative stress	(Boyles *et al.*, 2016)
	25		male Wistar rats	blood serum, urine, and tissue extracts	^{1}H NMR	ketogenesis; fatty acid β-oxidation; glycolysis; lipidosis	(Lei *et al.*, 2008)

NP type	Size (nm)	Cell model	Animal model	Sample type	Analysis method	Perturbed metabolic pathways	Reference
ZnO	35, 250		male Sprague-Dawley rats	bronchoalveolar lavage fluid and lung tissues	^{1}H NMR	cellular oxidation; energy metabolism; DNA damage; membrane stability	(Lee *et al.*, 2016b)
	50		male rats	urine and kidney extracts	^{1}H NMR	membrane modification; energy metabolism; TCA cycle; oxidative stress	(Yan *et al.*, 2012)
MnO	10		Sprague-Dawley rats	blood plasma, urine, and tissue extracts	^{1}H NMR	energy, nucleotide, amino acid, and phospholipid metabolism	(Li *et al.*, 2013)
CeO_2	8, 58	human hepatoma (HepG2)		cell extracts	LC-MS/MS and GC-MS	glutathione depletion; oxidative stress	(Kitchin *et al.*, 2014)
TiO_2	18	human gingival fibroblasts (HGF)		cell extracts	CE-MS	amino acid metabolism; urea cycle; polyamine, *S*-adenosylmethionine, and glutathione synthesis	(Garcia-Contreras *et al.*, 2015)
	< 25		*Caenorhabditis elegans* soil nematode	extracts	GC-MS	TCA cycle; arachidonic acid and glyoxalate dicarboxylate metabolism	(Ratnasekhar *et al.*, 2015)
	25-142	human hepatoma (HepG2)		cell extracts	LC-MS/MS and GC-MS	glutathione depletion; oxidative stress	(Kitchin *et al.*, 2014)
	n. a.	mouse fibroblasts (L929)		cell extracts	GC-MS	carbohydrate, amino acid, and nucleotide metabolism	(Bo *et al.*, 2014)
	< 100	mouse fibroblasts (L929)		cell and culture media extracts	GC-MS	energy metabolism and oxidative stress	(Jin *et al.*, 2013)
	10-100	human keratinocytes (HaCaT)		cell extracts	GC–MS and LC–MS	energy metabolism; glutathione and polyamine synthesis; glucuronidation	(Tucci *et al.*, 2013)
	n. a.	mouse fibroblasts (L929)		cell extracts	GC-MS	TCA cycle; glycolysis; energy and purine metabolism	(Liu *et al.*, 2012b)
	5		*Eisenia fetida* earthworms	extracts	^{1}H NMR	oxidative stress	(Aslund *et al.*, 2012)

NP type	Size (nm)	Cell model	Animal model	Sample type	Analysis method	Perturbed metabolic pathways	Reference
	5		rats	blood serum	^{1}H NMR	TCA cycle; gluconeogenesis; energy, amino acid and lipid metabolism	(Tang *et al.*, 2011)
	< 50		male and female Wistar rats	blood serum and urine	^{1}H NMR	energy, amino acid and choline metabolism; gut flora disturbances	(Bu *et al.*, 2010)
SiO_2	30, 70, 300		male BALB/c mice	liver extracts	GC-MS	fatty acid oxidation; TCA cycle	(Lu *et al.*, 2015)
	15		male and female Wistar rats	blood plasma	GC–MS and LC–MS/MS	no changes	(Buesen *et al.*, 2014)
	7-14	human lung epithelial (A549)		medium supernatants	^{1}H NMR	glycolysis and amino acid catabolism	(Irfan *et al.*, 2014)
	20	human cervical adenocarcinoma (HeLa)		intact cells and medium supernatants	HRMAS and solution ^{1}H NMR	membrane modification; carbohydrate and protein catabolism; oxidative stress-response	(Feng *et al.*, 2013)
	15		male Sprague-Dawley rats	liver extracts	^{1}H NMR	glycolysis; TCA cycle; disruption of cellular membranes; amino acid metabolism	(Chen *et al.*, 2013)
	45	human fetal lung fibroblasts (MRC-5)		cell extracts	GC-MS and LC-MS	amino acid and phospholipid metabolism; TCA cycle; oxidative stress	(Huang *et al.*, 2012)
	10, 80		rats	blood serum	^{1}H NMR	TCA cycle; glycolysis	(Parveen *et al.*, 2012)
	30, 70, 300		male BALB/c mice	blood serum extracts and liver extracts	GC-MS	energy, amino acid, lipid, and nucleotide metabolism	(Lu *et al.*, 2011)
Fe_2O_3	13		Sprague-Dawley rats	blood plasma, urine, and tissue extracts	^{1}H NMR	energy, nucleotide, amino acid, and phospholipid metabolism	(Li *et al.*, 2014a)
	10		male Sprague-Dawley rats	tissues	HRMAS	energy, lipid, glucose, and amino acid metabolism	(Feng *et al.*, 2011b)

NP type	Size (nm)	Cell model	Animal model	Sample type	Analysis method	Perturbed metabolic pathways	Reference
	2.3-4	murine macrophages (RAW 264.7)		intact cells and medium supernatants	HRMAS and solution ^{1}H NMR	energy metabolism; TCA cycle	(Feng *et al.*, 2011a)
	10		male Sprague-Dawley rats	blood plasma and urine	^{1}H NMR	energy, lipid, glucose and amino acid metabolism	(Feng *et al.*, 2010)
Al_2O_3	64.17	human bronchial epithelial (HBE)		cell lysate	GC-MS	downregulation of acetyl-L-carnitine	(Li *et al.*, 2016)
	40		male and female mice	mouse cortex	GC-MS	glutamate pathways	(Zhang *et al.*, 2015b)
Carbon	8-30	human bronchial epithelial (BEAS-2B) and human hepatoma (HepG2)		intact cells	^{1}H NMR	catecholamine biosynthesis; TCA cycle; amino acid, glycerolipid, and glutathione metabolism	(Chatterjee *et al.*, 2016)
	20-30	human liver (C3A)		cell extracts	^{1}H NMR	cellular oxidation; amino acid metabolism; fatty acid synthesis	(Henderson *et al.*, 2016)
	fullerene		*Eisenia fetida* earthworms	lyophilised earthworms	^{1}H NMR	alterations in amino acids and sugars	(Lankadurai *et al.*, 2015)
	2-40	astrocytoma type III (NG97)		cell extracts	MALDI MS/MS	alterations in *N*-stearoyl-Alanine and *N*-oleyl-alanine metabolites	(Zanin *et al.*, 2014)
	0.8-1.2 nanotubes		male Wistar rats	blood plasma and liver extracts	^{1}H NMR	energy metabolism; lipid peroxidation; glycogenolysis and glycolysis; amino acid metabolism	(Lin *et al.*, 2013)
Graphene	1.02		zebrafish larvae	brain extracts	GC-MS	amino acid and fatty acid metabolism	(Ren *et al.*, 2016)
	n. a.	human hepatoma (HepG2)		cell extracts	LC-MS	amino acid, purine and glycophospholipid metabolism; urea cycle	(Jiang *et al.*, 2014)
Polymeric	< 100		male BALB/c mice	blood serum, urine, and tissue extracts	^{1}H NMR	energy metabolism; antioxidant defense; co-metabolism of gut microbiota and host	(Song *et al.*, 2015)
	50		male BALBc mice	bronchoalveolar lavage fluid	LC-MS	purine metabolism	(Dailey *et al.*, 2015)

1.4. Scope and aims of this thesis

There is compelling evidence that the interaction of nanomaterials with cell membranes or internal organelles may affect multiple pathways (e.g. oxidative stress regulation, inflammation, apoptosis, cell cycle), translating into molecular alterations at the gene/protein level (Klaper *et al.*, 2014) and ultimately leading to changes in cell metabolism. This thesis aimed at deepening current understanding of the impact of AgNPs on cell metabolism and function, using a NMR-based metabolomics approach applied to cultured cells. Three cell models have been selected for the study, namely: i) human epidermis keratinocytes (HaCaT cells), as skin is a major entry portal for AgNPs, ii) human liver hepatoma (HepG2) cells, given the preferential accumulation of AgNPs in the liver and the role of hepatic cells in detoxification mechanisms, and iii) murine blood macrophages (RAW 264.7), which actively participate in the uptake of nanoparticles from the bloodstream and in the modulation of inflammatory responses. Well-characterised, ultra-purified AgNPs have been used to enable meaningful relationships between nanoparticle properties and biological outcomes to be established.

The specific objectives of this work were:

- To comprehensively characterise the metabolic activity and intracellular metabolomes of the three cell types studied (keratinocytes, liver cells and macrophages).

- To describe the changes in the exo- and endometabolome of cultured cells upon exposure to AgNPs, Ag^+ and H_2O_2.

- To obtain mechanistic insights into the modulation of cellular metabolism by AgNPs, particularly at sub-toxic concentrations.

- To enlighten structure-activity relationships in respect to the influence of AgNPs size and surface coating.

- To distinguish between AgNPs-specific effects and the effects due to Ag^+ released from the oxidised nanoparticle surface.

- To identify metabolic effects related to oxidative stress.

- To contribute for the validation of cell metabolomics as a novel approach in the risk-benefit assessment of nanomaterials.

Chapter 2. Materials and methods

2.1. Silver nanoparticles: sources and characterisation

Most AgNPs used in this work were purchased from a specialised supplier and were of high purity to avoid unwanted interferences in biological tests. Silver nanoparticles synthesised in-house by project collaborators (Dr C. Freire and co-workers) were also used. The physicochemical properties of all AgNPs were carefully checked and monitored throughout storage time, by different techniques, as described below. Nanoparticle characterisation was performed using the equipment available at CICECO (Universidade de Aveiro), with the assistance of project partners (Dr A.L. Daniel-da-Silva and co-workers).

2.1.1. Sources of AgNPs

Sterile, purified and endotoxin-free AgNPs (Biopure AgNPs 1.0 mg/mL), having either a citrate surface layer, with diameters of 10, 30 or 60 nm, or a methoxy(polyethylene glycol)-thiol coating (mPEG-SH 5 kDa), with diameters of 10 and 30 nm, were purchased from nanoComposix Europe (Prague, Czech Republic). Moreover, nanoparticles coated with bovine serum albumin (BSA) were prepared based on a procedure previously described (Beer *et al.*, 2012). Briefly, 7 µL of a BSA solution (135 mg/mL) were added to 63 µL of a commercial colloidal solution of citrate-stabilised 30 nm AgNPs (Biopure 1.0 mg/mL) and vortexed for 1 h at room temperature, protected from light, before overnight storage at 4 ºC.

Biogenic AgNPs were prepared by project collaborators through the reduction of silver nitrate with an aqueous extract of *Eucalyptus globulus* Labill. bark, as described in their published work, with minor modifications (Santos *et al.*, 2014). In brief, autoclaved *E. globulus* extract was added to an $AgNO_3$ aqueous solution (1 mM), at a 1:3 volume ratio, and allowed to react in a sealed container for 72 hours. Then, the nanoparticle suspension was centrifuged, and the supernatant was replaced with ultra-pure water, and centrifuged again. The final nanoparticle suspension was stored at 4 ºC, protected from light.

2.1.2. Transmission Electron Microscopy (TEM)

TEM is a powerful technique used for nanoparticle characterisation, since it allows the measurement of particle and/or grain size, size distribution, morphology, and crystal

structure (Rao and Biswas, 2009). In a transmission electron microscope, a focused beam of electrons is transmitted at a high acceleration voltage through a thin sample; images are formed from electron scattering resulting from the interaction between the sample and the electron beam. The contrast of the sample in relation to the background gives information on the size and shape of the nanoparticles.

In this work, samples for TEM analysis were prepared by placing a drop of a diluted aliquot of AgNP colloidal solution on a copper support grid coated with an amorphous carbon film. The solvent was allowed to air dry at room temperature. Then, the morphology and size of AgNPs were assessed by TEM using a Hitachi H9000 NAR microscope (Hitachi High-Technologies Europe GmbH, Krefeld, Germany) operating at 300 kV.

2.1.3. UV-Visible (UV-Vis) Spectroscopy

UV-Vis spectroscopy enables a rapid and simple evaluation of AgNPs stability. The optical properties of AgNPs arise from oscillating electron clouds at the metal-solution interface in resonance with the incident electromagnetic radiation, termed surface plasmon resonance (SPR) (Liz-Marzán, 2006). The characteristic SPR absorbance peak (λ_{max}) of AgNPs is observed at about 400 nm (Braun *et al.*, 2013). However, this peak is strongly affected by particle size and aggregation state, leading to either a lower wavelength, for smaller particles, or to a band broadening accompanied by red shifting, for larger/agglomerated particles (Hassellov *et al.*, 2008; MacCuspie, 2011).

The optical spectra of AgNPs colloidal solutions were recorded using a Jasco V-560 UV-Vis spectrophotometer, over a range from 300 to 900 nm, with a band width of 0.5 nm. 1 mL solutions were prepared by adding AgNPs to either ultra-pure water or complete culture medium, to a final concentration of 10 µg/mL. Samples were incubated at 37 ºC, simulating cell culture conditions, for variable periods (0, 4, 24 or 48 h) before UV-Vis measurements.

2.1.4. Dynamic Light Scattering (DLS)

DLS is a commonly used technique for measuring the size of nanoparticles in solution. It is based on the ability of individual particles in solution to scatter light from a laser and on the fluctuating movements originating from the Brownian motion (Calzolai *et al.*, 2012). Considering that larger particles diffuse slower than smaller particles, and taking

into account liquid viscosity and temperature, particle size can be calculated from the Stokes-Einstein equation (Equation 2.1), where D_h is the hydrodynamic diameter, k is the Boltzmann's constant, T is the absolute temperature, η is the refractive index of the solvent, and D is the diffusion coefficient (Hassellov *et al.*, 2008):

$$D_h = \frac{kT}{3\pi\eta D}$$ **Equation 2.1.**

Another important parameter measured by DLS is the polydispersity index (PdI), which indicates the width of the particle size distribution. A PdI < 0.1 generally indicates monodispersity, while PdI values in the 0.1 – 0.4 range or > 0.4 reflect moderate or broad polydisperse size distributions, respectively (Nobbmann, 2014).

Here, the D_h and the PdI of the nanoparticles were measured by DLS, using a Zetasizer Nano ZS (Malvern Instruments, Malvern, UK). Samples were prepared by adding AgNPs to 1 mL of either ultra-pure water or complete culture medium, to a final concentration of 10 µg/mL. Prior to analysis, samples were incubated at 37 ºC, simulating cell culture conditions, for variable periods (0, 4, 24 or 48 h).

2.1.5. Zeta potential

The surface charge of nanoparticles in solution can be measured through zeta potential analysis. The zeta potential typically ranges from +100 mV to -100 mV and is defined as the electric potential formed at the boundary of the electrostatic double layer of particles in solution as measured by electrophoresis (Hassellov *et al.*, 2008). At values greater than +25 mV or less than -25 mV, the nanoparticle dispersion presents high stability due to electrostatic repulsion (nanoComposix, 2016b).

In this work, the zeta potential was assessed by electrophoretic mobility, using a Zetasizer Nano ZS (Malvern Instruments, Malvern, UK). Samples of 10 µg/mL AgNPs were prepared in ultra-pure water or complete culture medium, and incubated at 37 ºC, simulating cell culture conditions, for variable periods (0, 4, 24 or 48 h).

2.1.6. Inductively Coupled Plasma Optical Emission Spectrometry (ICP-OES)

In order to quantify the amount of free ionic silver in AgNPs colloidal suspensions and study the Ag^+ release behaviour in culture medium, we have used ICP-OES. Samples for ICP-OES were prepared by addition of 10 µL AgNPs (1.0 mg/mL) to 990 µL of either ultra-pure water or complete culture medium, incubated for variable periods (0, 4, 24 or 48 h), followed by centrifugation at 40000 x g for 120 min at 4 ºC (in accordance with the manufacturer's recommendations) to deposit the nanoparticles and separate the supernatant. Acid digestion of the supernatant was then performed by mixing 500 µL with 100 µL of acids ($HCl:HNO_3$ 2:1 v/v) and 400 µL of ultrapure water (HCl from Merck, Darmstadt, Germany, and HNO_3 from Panreac, Barcelona, Spain). The percentage dissolution of AgNPs to ionic silver was calculated as 100 x *F* x [Ag]/C_i, where *F* is the dilution factor, C_i the initial concentration of AgNPs and [Ag] the concentration of silver determined by ICP-OES. Silver quantification measurements were performed by ICP-OES at Laboratório Central de Análises (Universidade de Aveiro) by a specialised technician. An Activa M Radial spectrometer (Horiba Jobin Yvon, Kyoto, Japan), employing a charge coupled device (CCD) array detector, with a wavelength range of 166–847 nm and radial plasma view was used. Samples were introduced into the ICP plasma using an HF resistant sample introduction system including a Burgener nebuliser, a cyclonic spray chamber and a quartz torch with aluminium injector.

2.2. Cell culture and biological assays

2.2.1. Chemicals

Dulbecco's modified Eagle's medium (DMEM), foetal bovine serum (FBS), antibiotics, L-glutamine, sodium pyruvate, phosphate buffer saline (PBS, pH 7.4) and trypsin-ethylenedieminetetraacetic acid (trypsin-EDTA) were purchased from Life Technologies (Carlsbad, CA, USA). Silver nitrate ($AgNO_3$), hydrogen peroxide (H_2O_2), bovine serum albumin (BSA), sodium citrate, 3-(4,5-dimethylthiazol-2-yl)-2,5-diphenyltetrazolium bromide (MTT), dimethyl sulfoxide (DMSO), chloroform, methanol, sodium phosphate monobasic (NaH_2PO_4), sodium phosphate dibasic (Na_2HPO_4) and deuterium oxide containing 3-(trimethylsilyl)propionic-2,2,3,3-d_4 acid, sodium salt (D_2O/TSP, 99.9 atom % D, 0.75 wt. % TSP) were obtained from Sigma-Aldrich (St. Louis, MO, USA). Polyethylene glycol (PEG, Mw 5 kDa) was purchased from Laysan Bio ® (Arab,

AL, USA). D_2O (99.96%) and deuterated chloroform with 0.03% tetramethylsilane (TMS) were purchased from Euriso-top (Saint-Aubin, France).

2.2.2. Cell lines

Human epidermis keratinocytes (HaCaT) are a spontaneously immortalised epithelial cell line established from adult skin (Boukamp *et al.*, 1988). This cell line maintains full epidermal differentiation capacity, has an approximate doubling time of 24 hours and can be propagated for more than 140 passages. The HaCaT cells used in this work were obtained from Cell Lines Service (Eppelheim, Germany).

The human hepatoma cell line (HepG2) derives from a liver biopsy of a 15-year old Caucasian boy with a well-differentiated hepatocellular carcinoma (Aden et al., 1979). These cells have epithelial morphology comparable to liver parenchymal cells. HepG2 were obtained from European Collection of Authenticated Cell Cultures (ECACC) and supplied by Sigma Aldrich (St. Louis, MO, USA).

Murine RAW 264.7 macrophages are a blood macrophage cell line isolated from the ascites of a tumour induced in a male BAB/14 mouse by the intraperitoneal injection of Abelson leukaemia virus (Raschke et al., 1978). When placed in mice, these cells are tumorigenic. In culture, RAW 264.7 grow very fast, with a doubling time of 12 h (Bancos and Tyner, 2014). The RAW 264.7 cells used in this work were gently provided by Dr Philipp Seib, University of Strathclyde, Glasgow, UK.

2.2.3. Routine cell culture maintenance

All cells were grown in high glucose DMEM supplemented with 10% FBS, 2 mM L-glutamine, 100 U/mL penicillin, 100 µg/mL streptomycin and 250 µg/mL fungizone, in 75 cm^2-flasks, at 37 ºC in 5% CO_2 humidified atmosphere, until 80% confluency was reached. The medium of HepG2 cells additionally contained 1 mM sodium pyruvate, as this was recommended by the supplier and found to improve cell growth.

Cells were then washed with PBS (pH 7.4), and either trypsinized (HaCaT and HepG2 cells) or gently scraped (RAW 264.7 macrophages). For trypsinization, cells were incubated with 0.25% trypsin/EDTA at 37 ºC in 5% CO_2 humidified atmosphere, for 5 min; HaCaT cells were previously incubated with PBS/EDTA, at 37 ºC in 5% CO_2 humidified atmosphere, for 10 min. After cell dislodging, trypsin was neutralised by adding complete

DMEM (twice the volume of trypsin/EDTA); cells were counted and re-seeded in complete DMEM. Cells were subcultured every 3 to 4 days.

2.2.4. Cell viability assay

Cell viability was measured through a colorimetric assay using the yellow-coloured tetrazolium salt (MTT) that is reduced by mitochondrial dehydrogenases of metabolically active cells, forming purple formazan crystals (Mosmann, 1983). Formazan accumulates inside viable cells, and thus the percentage of living cells can be estimated from the sample's absorbance at 570 nm.

HaCaT cells

For the MTT assay, HaCaT cells were seeded in 96-well plates, at densities of 1.8 x 10^4/cm^2 or 1.5 x 10^4/cm^2, for 24 and 48 h response curves, respectively. Twenty four hours later the medium was replaced with fresh medium containing: AgNPs (concentration range 0.5-100 µg/mL), ionic silver (Ag^+), added as $AgNO_3$ (concentration range 0.5-2 µg/mL), H_2O_2 (concentration range 50-500 µM), sodium citrate (50-400 µM), mPEG(-SH) (6-200 µg/mL) or BSA (10-200 µg/mL). After additional 24 h or 48 h, 50 µL of MTT (1 mg/mL) in PBS were added to each well, and incubated for 4 h at 37 ºC, 5% CO_2 humidified atmosphere. MTT solution was then removed and 150 µL of DMSO were added to each well for formazan crystal solubilisation. The optical density of reduced MTT (formazan) was measured at 570 nm in a microtiter plate reader (Synergy HT Multi-Mode, BioTek, Winooski, VT, USA) and the cell metabolic activity (MA) was calculated from Equation 2.2, where Abs_{EXP} is the absorbance measured in exposed samples, Abs_{DMSO} is the absorbance measured in wells containing only DMSO, and Abs_{CT} is the absorbance measured for control cells (non-exposed). Three independent assays, with three technical replicates each, were performed.

$$MA = \frac{Abs_{EXP} - Abs_{DMSO}}{Abs_{CT} - Abs_{DMSO}} \times 100 \qquad \textbf{Equation 2.2.}$$

HepG2 cells

Cells were seeded at a density of 5.6 x 10^4, in 96-well plates, and after 24 h the medium was replaced with fresh medium containing: AgNPs (concentration range 1-25 µg/mL), ionic silver (Ag^+), added as $AgNO_3$ (concentration range 0.5-2 µg/mL), H_2O_2 (concentration range 1-15 mM), sodium citrate (15 and 20 µM), or *Eucalyptus globulus* Labill. (EG) bark extract (0.20 and 0.50 mg/mL). After 24 h, the MTT assay proceeded as described for HaCaT cells.

RAW 264.7 cells

Cells were seeded at a density of 2.5 x 10^4, in 96-well plates, and after 24 h the medium was replaced with fresh medium containing: AgNPs (concentration range 10-150 µg/mL), ionic silver (Ag^+), added as $AgNO_3$ (concentration range 1-7.5 µg/mL), H_2O_2 (concentration range 50-500 µM), or sodium citrate (20 and 300 µM). After 24 h, the MTT assay proceeded as described for HaCaT cells.

2.2.5. Reactive Oxygen Species (ROS) assay

Intracellular ROS generation was assessed by flow cytometry with the probe 2',7'-dichlorodihydrofluorescein diacetate ($DCFH_2$-DA, Sigma-Aldrich, St. Louis, MO, USA), according to the procedure previously described (Ferreira de Oliveira *et al.*, 2014). In brief, cells were seeded in 6-well plates (at 1.2 x $10^4/cm^2$, 5.6 x $10^4/cm^2$, and 2.5 x $10^4/cm^2$, for HaCaT, HepG2 and RAW 264.7 cells, respectively) and after 24 h, the culture medium was replaced with medium containing AgNPs or H_2O_2, as well as Ag^+ (from $AgNO_3$) in the case of HepG2 and RAW 264.7 cells, at concentrations corresponding to IC_{20} and IC_{50} values. Additionally, HepG2 and RAW 264.7 cells were exposed to EG extract and citrate, respectively, at the maximum concentrations present in the AgNPs exposure. Following exposure, cells were washed with PBS and incubated in the dark with serum-free DMEM containing 10 µM $DCFH_2$-DA, for 30 min, at 37 ºC. Then, after PBS washing and trypsinization (or scraping, in the case of RAW 264.7 macrophages), cells were collected for analysis in an Attune® Acoustic Focusing Cytometer (ThermoFisher Scientific, Waltham, MA). ROS formation was estimated from the mean fluorescence intensity (MFI) of DCF using the FlowJo software (Tree Star Inc., Ashland, OR, USA).

2.3. NMR metabolomics

2.3.1. Cell culture and exposure for metabolomics

HaCaT cells

HaCaT cells were seeded at a density of 1.5 x 10^4 cells/cm^2 onto 10 cm diameter Petri dishes and allowed to adhere for 24 h. Then, the medium was replaced by fresh complete medium containing: AgNPs at final concentrations of 10 µg/mL or 40 µg/mL, Ag^+ (added as $AgNO_3$) or H_2O_2, at the IC_{20} or IC_{50} concentrations (selected based on the cell viability results). Fresh medium without AgNPs was added to control cells. In addition, to account for possible effects of the coating substances, cells were also incubated with medium containing citrate, mPEG, mPEG-SH or BSA, at concentrations equivalent to those added when cells were exposed to coated AgNPs. At least three independent assays were performed.

HepG2 cells

Similarly, HepG2 cells were seeded at a density of 5.6 x 10^4/cm^2 onto 10 cm diameter Petri dishes and allowed to adhere for 24 h. Then, the medium was replaced by fresh complete medium containing: AgNPs, Ag^+ or H_2O_2, at the IC_5 or IC_{20} concentrations (selected based on the cell viability results). Fresh medium without AgNPs was added to control cells. Furthermore, cells were also incubated with medium containing citrate or EG bark extract, at concentrations equivalent to those added when cells were exposed to AgNPs. Five independent assays were performed.

RAW 264.7 cells

RAW 264.7 macrophages were seeded at a density of 2.5 x 10^4/cm^2 onto 10 cm diameter Petri dishes and allowed to grow for 24 h. Culture medium was then replaced by fresh complete medium containing: AgNPs, Ag^+ or H_2O_2, at the IC_5 or IC_{20} concentrations (selected based on the cell viability results). Fresh medium without AgNPs was added to control cells. Furthermore, cells were also incubated with medium containing citrate, at a concentration equivalent to that added when cells were exposed to the IC_{20} of AgNPs. Five independent assays were performed.

2.3.2. Sample collection

Cell culture supernatants

Medium aliquots were collected from each dish, centrifuged (1000 x g, 5 min) and the supernatant stored at -80 ºC until NMR analysis. Aliquots from medium without cells incubated in the same conditions as exposed cells, were also collected. At the time of analysis, 540 µL of thawed medium were mixed with 60 µL of D_2O containing 0.25% TSP-d_4 and 550 µL of each sample were transferred into 5 mm NMR tubes.

Cell extracts

To collect cell samples, the remaining medium was aspirated and each dish was washed 2-4 times with PBS. Then, intracellular metabolites were extracted using a dual phase extraction, with methanol:chloroform:water (1:1:0.7), as adapted from (Teng *et al.*, 2008). Briefly, 650 µL of cold methanol 80% was added, to stop metabolic activity, and the cells were scraped off the dish and vortexed for 2 min in microcentrifuge tubes containing 0.5 mm glass beads (150 mg), to aid cell breakage. Chloroform (260 µL) and chloroform + water (260 µL + 220 µL) were then added to each sample, each addition being followed by 2 min vortexing, and the samples were left to rest on ice for 10 min. After centrifuging at 2000 g for 15 min, and at 10000 g for 1 min, the upper aqueous phase (polar) and the lower organic phase (lipophilic) were carefully transferred into new vials, dried under vacuum and stored at -80 ºC.

At the time of NMR analysis, dried polar extracts were reconstituted in 600 µL of deuterated phosphate buffer (100 mM, pH 7.4) containing 0.1 mM TSP, and 550 µL of each sample were transferred into 5 mm NMR tubes.

Lipophilic extracts were reconstituted in deuterated chloroform containing 0.03% TMS. For NMR analysis, 550 µL of each sample were transferred into 5 mm NMR tubes.

2.3.3. Acquisition and processing of NMR spectra

^{1}H NMR spectra of all samples were acquired on a Bruker Avance DRX-500 spectrometer (Universidade de Aveiro, Rede Nacional de RMN, Portugal) operating at 500.13 MHz for ^{1}H observation, at 298 K, using 5 mm BBI or TXI Bruker probes. Standard 1D ^{1}H spectra with water suppression by presaturation during the relaxation delay (RD) and mixing time (t_m) (pulse program 'noesypr1d' from Bruker library, RD-90º-*t*-90º-t_m-90º-ACQ,

t being a short delay of 3 μs) were recorded for medium samples and polar extracts; for lipophilic extracts, 1D ^{1}H spectra were acquired using a standard Bruker proton pulse sequence ('zg') with a 90º pulse. Acquisition time (ACQ) for each FID was set to 2.34 s and the relaxation delay to 4 s. Spectral processing was performed using Topspin 3.2 (Bruker Biospin, Rheinstetten, Germany). Each FID was zero-filled to 64 k points and multiplied by an exponential line-broadening window function (LB 0.30/1.00 Hz, for medium and polar extracts/lipophilic extracts) prior to Fourier transformation. Spectra were manually phased and baseline corrected, and chemical shifts were referenced internally to TSP/TMS (medium and polar extracts/lipophilic extracts). Typical acquisition and processing parameters for these 1D experiments are provided in Table 2.1.

Table 2.1. Main parameters used for the acquisition and processing of 500 MHz 1D ^{1}H NMR spectra of culture media, polar extracts, and lipophilic extracts, of HaCaT, HepG2 and RAW 264.7 cells. [a]Bruker library

	Culture medium	**Polar extracts**	**Lipophilic extracts**
Acquisition parameters			
Pulse programme[a]	*noesypr1d*	*noesypr1d*	*zg*
FID data points, TD	32768	32768	32768
Number of scans	256	256	256
Spectral width (ppm)	20.6557	14.0019	14.0019
Relaxation delay, RD (s)	4	4	4
Mixing time, t_m (ms)	100	100	
Processing parameters			
Window function	Exponential	Exponential	Exponential
Spectrum data points, SI	65536	65536	65536
Line broadening, LB (Hz)	0.30	0.30	1.00

2D ^{1}H-^{1}H total correlation (TOCSY), ^{1}H-^{13}C heteronuclear single quantum correlation (HSQC) and *J*-resolved spectra were also registered for selected samples to assist spectral assignment. TOCSY spectra were recorded in phase-sensitive mode using time proportional phase incrementation (TPPI) and the MLEV 17 pulse sequence for the spin-lock (clmlevprtp pulse programme from Bruker library); phase sensitive (echo/antiecho) HSQC spectra were recorded with inverse detection and carbon decoupling (invietgpsi pulse programme from Bruker library); *J*-resolved spectra were acquired with F2 decoupling (jresgpprqf pulse programme from Bruker library). 2D spectral processing was also

performed using Topspin 3.2 (Bruker Biospin, Rheinstetten, Germany). The acquired FIDs were zero-filled to the spectrum data points (SI) shown in Table 2.2 and multiplied by a sine-bell-squared/sine-bell function (qsine/sine) prior to FT and phasing. *J*-resolved spectra were tilted (45º) to provide orthogonality of the chemical shift and coupling constant axes were subsequently symmetrised about the F1 axis. In all spectra, chemical shifts were calibrated internally to TSP/TMS (medium and polar extracts/lipophilic extracts). Typical acquisition and processing parameters for these 2D experiments are provided in Table 2.2.

Table 2.2. Main parameters used for the acquisition and processing of 500 MHz 2D NMR spectra of culture media, polar extracts, and lipophilic extracts, of HaCaT, HepG2 and RAW 264.7 cells. [a]Bruker library

	Culture medium/Polar extracts/Lipophilic extracts		
Acquisition parameters			
Experiments	^{1}H-^{1}H TOCSY	^{1}H-^{13}C HSQC	*J*-resolved
Pulse programme[a]	*clmlevprtp*	*invietgpsi*	*jresgpprqf*
FID data points [F1]	160	128	40
FID data points [F2]	2048	2048	8192
Number of scans	64	120	64
Spectral width [F1] (ppm)	16.0214	172.8503	0.0868
Spectral width [F2] (ppm)	16.0214	9.9974/9.5395/12.0161	12.6549
Relaxation delay, RD (s)	1.5	2	2
Mixing time, D9 (ms)	80		
Processing parameters			
Window function	qsine/qsine	qsine/qsine	sine
Spectrum data points [F1], SI	1024	256	128
Spectrum data points [F2], SI	4096	2048	16384
Line broadening [F1], LB (Hz)	0.30		0.30
Line broadening [F2], LB (Hz)			0.50

2.4. Multivariate and statistical analysis of NMR spectra

2.4.1. Data pre-treatment

Full resolution ^{1}H NMR spectra were converted to matrices of *n* observations (samples, in rows), and *m* variables (peak intensities, in columns), in Amix-Viewer 3.9.15 (Bruker BioSpin, Rheinstetten, Germany). Selected regions comprising solvent signals

(water in polar extracts and culture media, chloroform in lipophilic extracts), culture media traces in polar extracts, and other contaminants (ethanol, methanol), were excluded from data matrices. Spectra (rows in data matrices) were normalised by total spectral area to compensate for differences in the number of cells, and then aligned in MATLAB version 7.9.0 (The MathWorks, Inc., Natick, MA, USA), using recursive segment-wise peak alignment (Veselkov *et al.*, 2009) to minimise chemical shift variations. Data matrices were uploaded in SIMCA-P 11.5 (Umetrics, Umeå, Sweden), where variables were mean centred (subtraction by average value), and scaled to unit variance (UV, each column divided by its standard deviation).

2.4.2. Principal Component Analysis (PCA) and Partial Least Squares – Discriminant Analysis (PLS-DA)

PCA and PLS-DA were applied to mean centred and UV scaled data, in the SIMCA-P software, with a default seven-fold internal cross validation, from which Q^2 and R^2 values, respectively reflecting predictive capability and explained variance, were extracted. Results from PCA and PLS-DA were visualised in scores scatter plots. PLS-DA model robustness was further assessed by Monte Carlo cross validation (MCCV) with 500 iterations and permutation testing (class membership randomly assigned), in an in-house software developed by Dr António Barros. The distribution of Q^2 values and the receiver operating characteristic (ROC) maps, representing the true positive rate (TPR or sensitivity) as a function of the false positive rate (FPR or 1-specificity), were recovered from MCCV applied to both original and permuted models. PLS-DA models were considered valid when: in the ROC map, permuted classes fell along the line of no discrimination (TPR = FPR), and true models presented high sensitivity and specificity; in the Q^2 histogram, there was minimal overlap between classes, and median Q^2 was > 0.5 for true models.

The PLS-DA loadings plots were back-transformed by multiplying the loading weight *w* by the standard deviation of each variable, and coloured according to variable importance to the projection (VIP) using the R-statistical software (R Foundation for Statistical Computing, Vienna, Austria).

2.4.3. Spectral integration and univariate statistical analysis

Selected signals in the normalised 1D spectra were integrated using the Amix-Viewer software. In cases of significant overlap, spectral deconvolution was employed, using a variable Gaussian/Lorentzian curve fitting, with a default line width of 1 Hz.

For each metabolite, the percentage of variation and respective error were calculated, along with the effect size (ES), corrected for small sample numbers, and respective standard error, according to equations 1.1-1.5 (Chapter 1). Metabolites presenting variations with absolute ES larger than 0.8 (and with standard error < ES) were expressed in a heatmap coloured as a function of the percentage of variation, using the R-statistical software. Moreover, the statistical significance of the difference between the means of two groups (control and exposed) was assessed using the two-sample t-test or the non-parametric Wilcoxon rank sum test with continuity correction, and considering the False Discovery Rate (FDR)-corrected *p* values (confidence level 95%) (Benjamini and Hochberg, 1995).

2.4.4. Correlation analysis

In order to assign unknown resonances or to confirm the presence of specific metabolites, statistical total correlation spectroscopy (STOCSY) analysis was applied to spectral matrices containing samples where those resonances were found to vary. Selected signals (driver peaks) were correlated to the full spectral matrix, in the Matlab software, and the correlation coefficients were used to colour the median spectrum, resulting in a 1D STOCSY plot (Cloarec *et al.*, 2005).

Correlation analysis was also performed to seek biochemical relations among metabolite variations. To this end, matrices with metabolite integrals were imported to the Matlab software, where the Pearson correlation coefficients (r), and respective significance, were calculated. A threshold of $|r| > 0.75$, with $p < 0.005$, was applied. The obtained correlation values are mentioned throughout this report when relevant.

Chapter 3. Metabolite profiling of cultured cells: keratinocytes (HaCaT), hepatoma cells (HepG2) and macrophages (RAW 264.7)

3.1. Background and aims

This chapter describes the basal metabolic activity and composition of the three cell lines used in this work: human keratinocytes (HaCaT), human hepatoma cells (HepG2) and murine macrophages (RAW 264.7). High resolution ^{1}H NMR spectroscopy was used to obtain the spectral profiles of culture medium supernatants, as well as of polar and lipophilic cell extracts, providing detailed information on both the exometabolome and endometabolome of each cell type. This information is crucial to interpret the metabolic effects induced by silver nanoparticles, presented in subsequent chapters.

Metabolite identification was strongly supported by recording two-dimensional (2D) experiments, namely: i) ^{1}H-^{1}H TOCSY, which revealed intramolecular coupling networks (spin systems), ii) ^{1}H-^{13}C HSQC, useful to show ^{1}H-^{13}C connectivities and confirm the assignment of singlets or of highly overlapped multiplets, and iii) *J*-resolved spectra, characterised by reduced spectral complexity and clearer information on signal multiplicity. The statistical correlation between 1D spectra, using the STOCSY method (Cloarec *et al.*, 2005), was also used to probe molecular or biochemical correlations, further aiding spectral assignment. Additionally, the identity of some signals was confirmed by spiking the sample of interest with pure reference compounds and observing the increase in the corresponding resonances. The chemical shift, signal multiplicity and coupling pattern information retrieved from 1D and 2D spectra was then matched to the reference spectra available in different databases. The main databases consulted were Bruker BBIOREFCODE-2-0-0 database (Bruker Biospin, Rheinstetten, Germany), HMDB (Wishart *et al.*, 2013) and BioMagResBank (Ulrich *et al.*, 2008). Also, spectral assignment relied on existing literature reports for HepG2 cells (Bayet-Robert *et al.*, 2010; Ruiz-Aracama *et al.*, 2011; Li *et al.*, 2015c; Zheng *et al.*, 2015) and for RAW 264.7 macrophages (Santini *et al.*, 2004; Stuckey *et al.*, 2005; Strelko *et al.*, 2011), while, to our knowledge, the NMR metabolic profile of HaCaT cells was newly reported within the framework of this thesis (Carrola *et al.*, 2016a).

3.2. Metabolic activity of cells assessed by the NMR analysis of culture media

During *in vitro* incubation, cells take up nutrients from the culture medium and excrete metabolic products. Thus, the variations in the medium composition provide valuable information on cellular metabolic activity. Figure 3.1 shows the ^{1}H NMR spectra of acellular medium and of HaCaT cells conditioned medium, collected after 24 h incubation. Corresponding 2D spectra, used for spectral assignment, are shown in Figure 3.2.

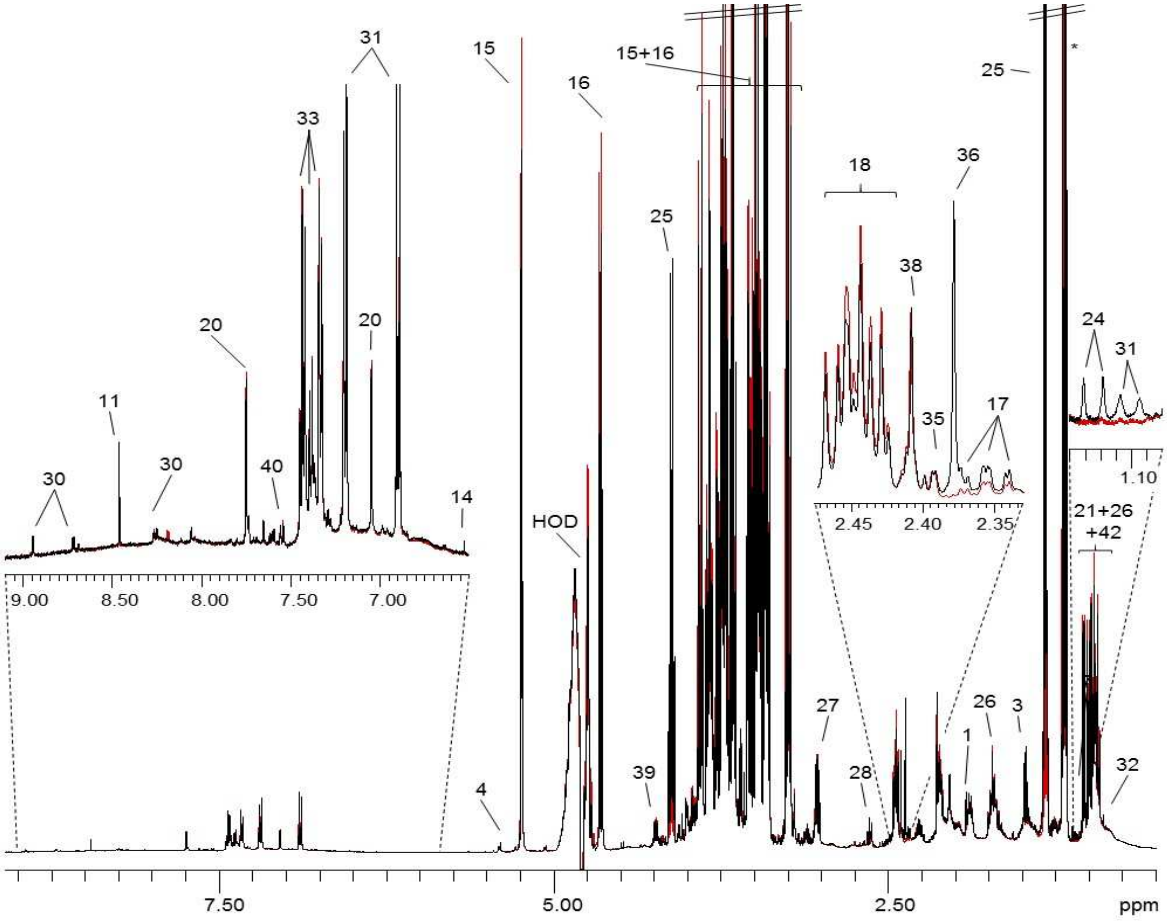

Figure 3.1. 500 MHz ^{1}H NMR spectra of culture media: comparison between acellular medium (red) and culture medium supernatant from HaCaT control cells (black), grown for 24 hours. Signals are numbered in accordance with Table 3.1. *ethanol.

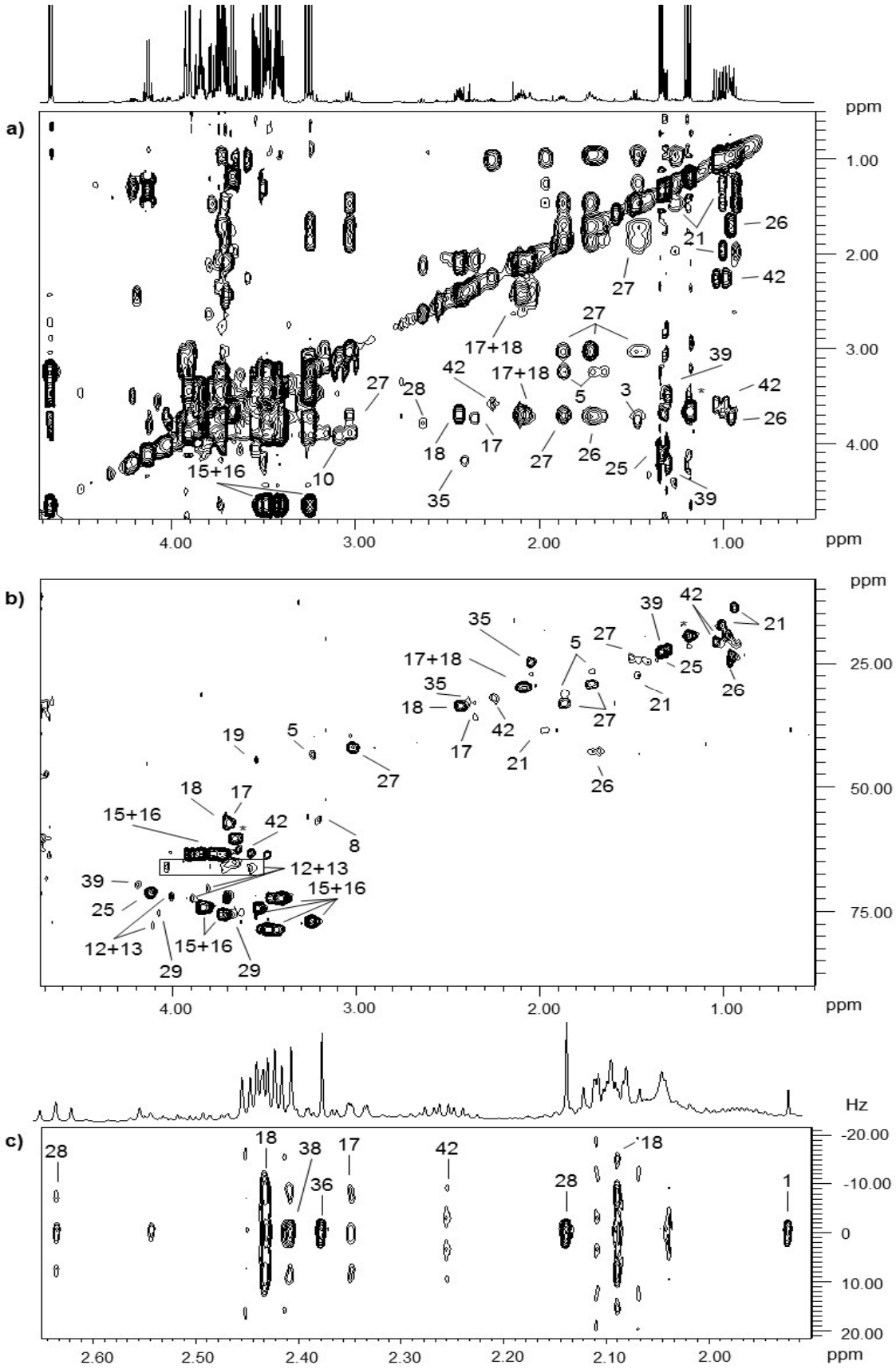

Figure 3.2. Expansions of a) ^{1}H-^{1}H TOCSY, b) ^{1}H-^{13}C HSQC, and c) *J*-resolved spectra of culture medium from HaCaT control cells. Signals are numbered in accordance with Table 3.1. *ethanol.

The same medium (DMEM with 10% FBS) was used for growing all cell types, although in the case of HepG2 cells, the medium was further supplemented with sodium pyruvate (1 mM), as this was specifically recommended by the cell line supplier and found to greatly enhance cell growth. The impact of pyruvate addition on the results will be addressed later on. All organic nutrients listed in the medium formulation (Table S3.1) were detected in the NMR spectrum, although some vitamins (e.g. pyridoxine, thiamine), present at concentrations below 20 µM, showed only very weak signals in the 1D spectrum, hindering unambiguous identification or any quantitative analysis. Some compounds arising from medium supplementation with 10% FBS, such as glutamate, organic acids, fructose and allantoin, were also unequivocally identified. Moreover, a few metabolites not present in complete acellular medium were identified, reflecting their excretion from cells. This was the case of 2-oxoisoleucine and *α*-ketovaline, resulting from the catabolism of branched chain amino acids, or of itaconate, detected only in the RAW 264.7 conditioned medium. The full list of metabolites detected in the NMR spectra of complete culture medium, used to grow the three cell lines, is shown in Table 3.1.

Table 3.1. Assignment of resonances in the NMR profile of culture media from HaCaT, HepG2, and RAW 264.7 cells. Multiplicity: s, singlet; d, doublet; t, triplet; m, multiplet; dd, doublet of doublets.

No.	Compound	δ ^{1}H in ppm (multiplicity, assignment)/ δ ^{13}C in ppm	Cell type		
			HaCaT	HepG2	RAW
1	Acetate	1.92 (s, *β*-CH_3)/26.0	✓	✓	✓
2	*N*-acetylaspartate	2.04 (s, CH_3)/24.7; 2.51 (dd, *β*-CH_2); 2.68 (dd, *β*'-CH_2); 4.40 (dd, *α*-CH)	✓	✓	✓
3	Alanine (Ala)	1.49 (d, *β*-CH_3)/18.9; 3.78 (q, *α*-CH)	✓	✓	✓
4	Allantoin	5.39 (s, CH)	✓	✓	✓
5	Arginine (Arg)	1.69 (m, *γ*-CH_2)/26.7; 1.92 (m, *β*-CH_2)/30.9; 3.24 (t, *δ*-CH_2)/43.2; 3.78 (*α*-CH)	✓	✓	✓
6	Aspartate (Asp)	2.66 (dd, *β*-CH); 2.81 (dd, *β*'-CH); 3.90 (dd, *α*-CH)	✓	✓	✓
7	Citrate	2.53 (d, *α*, *β*-CH_2); 2.70 (d, *α*', *β*'-CH_2)	✓	✓	✓
8	Choline	3.21 (s, $N(CH_3)_3$)/56.5; 3.53 (m, C**H_2**(NH)); 4.07 (m, C**H_2**(OH))	✓	✓	✓
9	Creatine	3.04 (s, CH_3); 3.93 (s, CH_2)	✓	✓	✓
10	Cysteine (Cys)	3.08 (m, *β*-CH_2); 3.91 (dd, *α*-CH)	✓	✓	✓
11	Formate	8.46 (s, CH)	✓	✓	✓

No.	Compound	δ ^{1}H in ppm (multiplicity, assignment)/ δ ^{13}C in ppm	Cell type		
			HaCaT	HepG2	RAW
12	*α*-Fructose	3.66 (m, C1H)/65.3; 3.64, 3.86 (m, C6H)/72.3; 3.99 (m, C4H)/71.8; 4.04 (dd, C5H)/65.9; 4.11 (m, C3H)/78.1	✓	✓	✓
13	*β*-Fructose	3.57 (m, C1H)/66.5; 3.64, 3.79 (m, C6H)/70.2; 3.82 (m, C5H)/82.9; 4.10 (dd, C4H); 4.11 (m, C3H)/76.7	✓	✓	✓
14	Fumarate	6.52 (s, CH)	✓	✓	✓
15	*α*-Glucose	3.40 (m, C4H)/72.3; 3.55 (dd, C2H)/74.0; 3.71 (m, C3H)/75.5; 3.83 (m, C6H)/63.2; 3.85 (m, C5H)/74.2; 5.24 (d, C1H)/94.8	✓	✓	✓
16	*β*-Glucose	3.26 (dd, C2H)/76.8; 3.41 (m, C4H)/72.3; 3.47 (m, C5H)/78.6; 3.49 (t, C3H)/78.4; 3.74 (m, C6H)/63.4; 3.90 (dd C6'H)/63.4; 4.66 (d, C1H)/98.6	✓	✓	✓
17	Glutamate (Glu)	2.06 (m, *β*-CH)/29.7; 2.13 (m, *β*'-CH)/29.7; 2.35 (m, *γ*-CH_2)/36.2; 3.73 (t, *α*-CH)/57.2	✓	✓	✓
18	Glutamine (Gln)	2.14 (m, *β*-CH_2)/29.6; 2.45 (m, *γ*-CH_2)/33.7; 3.68 (t, *α*-CH)/55.9	✓	✓	✓
19	Glycine (Gly)	3.57 (s, *α*-CH_2)/44.2	✓	✓	✓
20	Histidine (His)	3.22 (m, *β*-CH_2); 7.03 (s, C4H, ring); 7.74 (s, C2H, ring)	✓	✓	✓
21	Isoleucine (Ile)	0.94 (t, *δ*-CH_3)/13.8; 1.01 (d, *β*'-CH_3)/17.4; 1.26 (m, *γ*-CH_2)/27.2; 1.48 (m, *γ*'-CH_2)/27.2; 1.98 (m, *β*-CH)/38.7; 3.68 (d, *α*-CH)/62.0	✓	✓	✓
22	Itaconate	3.18 (m, *α*-CH_2); 5.38 (m, *β*-CH); 5.86 (m, *β*'-CH)			✓
23	Ketoleucine	0.93 (d, *δ*-CH_3); 2.09 (m, *γ*-CH); 2.65 (d, *β*-CH_2)	✓	✓	✓
24	*α*-Ketovaline	1.12 (d, *γ*-CH_3); 3.01 (dq, *β*-CH)	✓	✓	✓
25	Lactate	1.33 (d, *β*-CH_3)/22.8; 4.12 (q, *α*-CH)/71.3	✓	✓	✓
26	Leucine (Leu)	0.96 (d, *δ*-CH_3)/23.7; 0.97 (d, *δ*'-CH_3)/24.9; 1.70 (m, *γ*-CH)/27.0; 1.72 (m, *β*-CH_2)/42.4; 3.74 (t, *α*-CH)	✓	✓	✓
27	Lysine (Lys)	1.47 (m, *γ*-CH_2)/24.2; 1.73 (m, *δ*-CH_2)/29.2; 1.92 (m, *β*-CH_2)/32.9; 3.03 (t, *ε*-CH_2)/41.9; 3.76 (t, *α*-CH)	✓	✓	✓
28	Methionine (Met)	2.14 (s, *β*-CH_2); 2.16 (t, *β*-CH_2); 2.65 (t, *γ*-CH_2); 3.80 (t, *α*-CH)	✓	✓	✓

No.	Compound	δ ^{1}H in ppm (multiplicity, assignment)/ δ ^{13}C in ppm	Cell type		
			HaCaT	HepG2	RAW
29	*myo*-Inositol	3.29 (t, C5H)/77.1; 3.54 (C1H, C3H)/73.8; 3.63 (dd, C4H, C6H)/75.2; 4.07 (t, C2H)/74.9	✓	✓	✓
30	Niacinamide	7.60 (dd, N5, ring); 8.26 (dd, N4, ring); 8.72 (dd, N6, ring); 8.95 (s, N2, ring)	✓	✓	✓
31	2-Oxoisoleucine	0.89 (t, *δ*-CH_3); 1.10 (d, *β*'-CH_3); 1.45 (m, *γ*-CH_2); 1.70 (m, *γ*'-CH_2); 2.93 (m, *β*-CH)	✓	✓	✓
32	Pantothenate	0.90 (s, CH_3); 0.92 (s, CH_3); 2.42 (t, *α*-CH_2); 3.39 (d, CH_2); 3.43 (q, *β*-CH_2); 3.51 (d, CH_2); 3.98 (s, CH)	✓	✓	✓
33	Phenylalanine (Phe)	3.14 (m, *β*-CH); 3.27 (dd, *β*'-CH); 4.00 (m, *α*-CH); 7.33 (d, C2H, C6H, ring)/131.9; 7.39 (d, C4H, ring); 7.43 (t, C3H, C5H, ring)/131.7	✓	✓	✓
34	Proline (Pro)	2.01 (m, *γ*-CH_2); 2.07 (m, *β*-CH); 2.35 (m, *β*'-CH); 3.35 (dt, *δ*-CH); 3.42 (dt, *δ*'-CH); 4.13 (dd, *α*-CH)	✓	✓	✓
35	Pyroglutamate	2.04 (m, *β*-CH_2)/27.7; 2.41 (m, *γ*-CH_2)/32.2; 2.51 (m, *β*'-CH_2)/27.7; 4.17 (dd, *α*-CH)/61.0	✓	✓	✓
36	Pyruvate	2.38 (s, *β*-CH_3)	✓	✓	✓
37	Serine (Ser)	3.83 (dd, *α*-CH); 3.96 (m, *β*-CH_2)	✓	✓	✓
38	Succinate	2.41 (s, CH_2)/36.8	✓	✓	✓
39	Threonine (Thr)	1.34 (d, *γ*-CH_3)/22; 3.59 (d, *α*-CH)/63.1; 4.20 (m, *β*-CH)/69.0	✓	✓	✓
40	Tryptophan (Trp)	3.31 (dd, *β*-CH); 3.48 (dd, *β*'-CH); 4.05 (dd, *α*-CH); 7.21 (t, C5H, ring); 7.29 (t, C6H, ring); 7.31 (s, C2H, ring); 7.55 (d, C7H, ring); 7.74 (d, C4H,ring)	✓	✓	✓
41	Tyrosine (Tyr)	3.07 (m, *β*'-CH); 3.21 (m, *β*-CH); 3.96 (m, *α*-CH); 6.91 (d, C3H, C5H, ring)/118.6; 7.20 (d, C2H, C6H, ring)/133.6	✓	✓	✓
42	Valine (Val)	0.99 (d, *γ*-CH_3)/ 19.5; 1.05 (d, *γ*'-CH_3)/20.7; 2.26 (m, *β*-CH)/31.7; 3.62 (d, *α*-CH)/63.0	✓	✓	✓

The quantitative analysis of variations in medium metabolites upon cellular incubations was then carried out based on NMR signal integration. The results obtained for each cell type are shown graphically in Figure 3.3, where negative bars represent metabolites consumed by cells and positive bars represent metabolites excreted by cells.

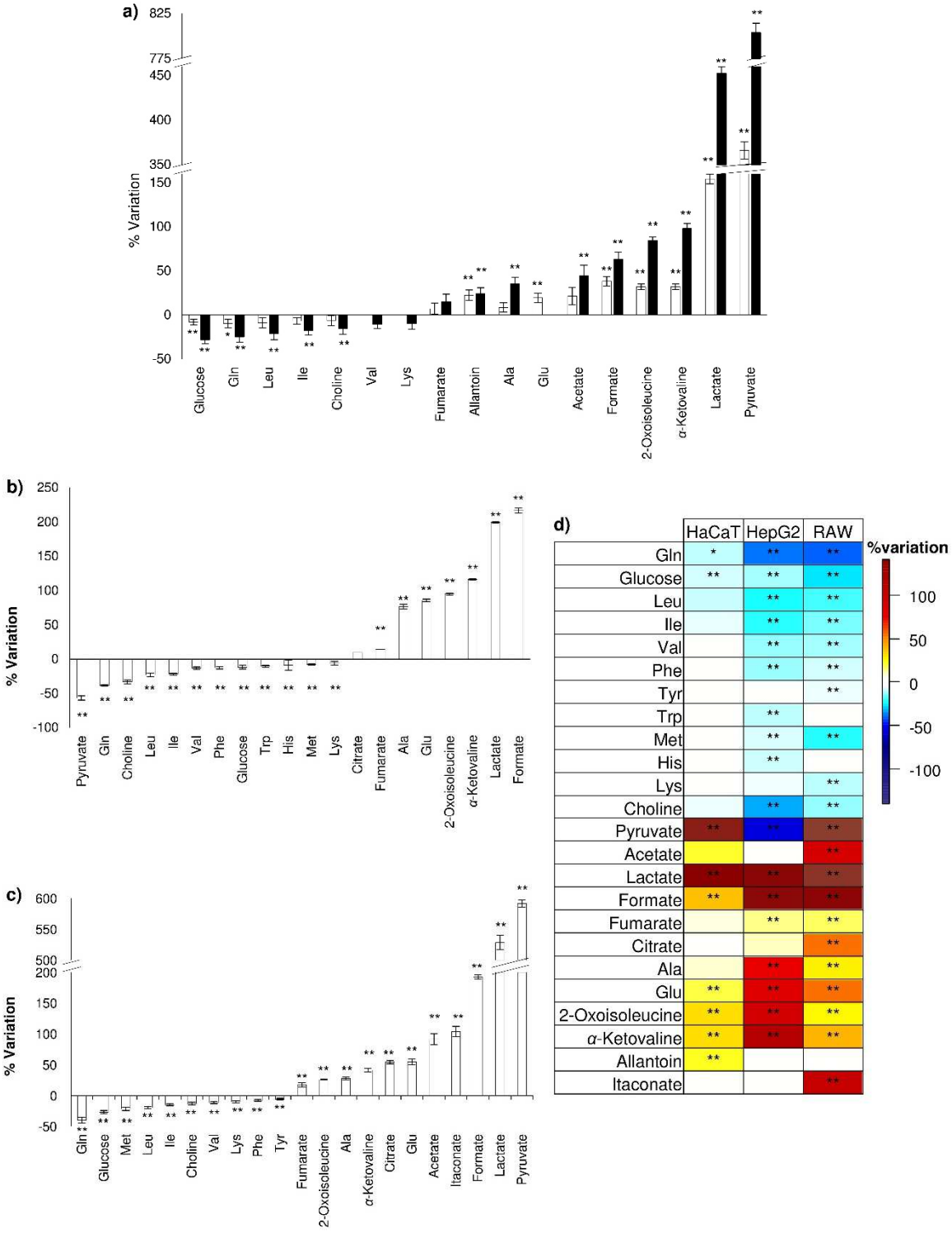

Figure 3.3. Variations in metabolites consumed (negative bars) and excreted (positive bars) by a) HaCaT, b) HepG2, and c) RAW 264.7 cells, as assessed through comparison of acellular culture media and culture medium supernatants from control cells, grown for 24 (white bars) or 48 hours (black bars); d) summary heatmap for the three cell types colour-coded as a function of %variation in 24 h cell medium relatively to acellular medium. *p-value < 0.05; ** FDR-corrected p-value < 0.05. Three-letter code used for amino acids.

HaCaT cells (Figure 3.3a) consumed mainly glucose, glutamine, leucine, isoleucine and choline and excreted several organic acids (mainly lactate and pyruvate, together with smaller amounts of formate, acetate and fumarate), ketoacids, alanine, glutamate and allantoin. As expected, the variations in relation to acellular medium were greater in the 48 h cell conditioned medium than in the 24 h medium. In the case of HepG2 cells (Figure 3.3b), a substantial difference was that pyruvate, used to supplement the culture medium, was consumed by cells. Several other substrates were also used, namely glutamine, glucose, choline and amino acids (including branched chain and aromatic amino acids). The main products released were organic acids (mainly lactate and formate), ketoacids, alanine and glutamate. As for the RAW 264.7 macrophages (Figure 3.3c), the most noticeable difference in metabolite balances was the excretion of itaconate, not seen for the other cell types.

To conduct a more thorough comparison of the metabolic activity of the three cell types, the magnitude of variations in the 24 h conditioned media in relation to the acellular media was expressed in a colour-coded table (Figure 3.3d). Taking the consumption of glucose as a measure of glycolytic activity, macrophages appeared to be the most glycolytic cell line. This is in agreement with early works showing that macrophages readily convert glucose to lactate at high rates, mainly in order to generate glycolytic intermediates for biosynthetic purposes (Newsholme *et al.*, 1987; Newsholme *et al.*, 1996). HepG2 cells, in turn, are also known for their dominant glycolytic metabolism (Miccheli *et al.*, 2006b; Loiseau *et al.*, 2009), consistent with the 'Warburg' phenotype of tumour cells (Mazurek, 2007). However, it should be noted that, in the present work, the HepG2 medium supplementation with pyruvate could have reduced the need for glucose uptake.

Glutamine was also consumed from the culture medium, especially by HepG2 and RAW 264.7 cells. High glutamine consumption by HepG2 cells is consistent with the decreased activity of glutamine synthetase and increased activity of glutaminase in hepatocellular carcinoma (Matsuno and Goto, 1992). Likewise, it has also been reported that glutamine is utilised at high rates by macrophages and other isolated immune cells (Newsholme *et al.*, 2003). The consumption of other amino acids was also clear, again with varying magnitudes for the different cell lines. For instance, HepG2 consumed more branched chain amino acids than the other cell types, while methionine was more avidly consumed by macrophages.

In regard to the excretion patterns of the three cell types, there were a few distinctive features. For instance, allantoin (a product of purine catabolism, namely of uric acid

oxidation) was detected only in the HaCaT conditioned medium. On the other hand, the HepG2 conditioned medium showed much higher levels of alanine and glutamate (likely reflecting the high glycolytic and glutaminolytic activity of these cells), as well as of ketoacids derived from branched chain amino acids catabolism. Finally, the macrophage conditioned medium showed distinctly high levels of acetate, citrate and itaconate, possibly in relation to the TCA cycle activity. Acetate may arise from citrate through the action of citrate lyase, while itaconate has been shown to be generated in macrophages by the decarboxylation of the citrate-derived metabolite cis-aconitate (Strelko *et al.*, 2011).

Overall, it should be noted that the metabolic activities of the three cell lines may reflect not only their different genetic backgrounds and enzymatic profiles, but also differences in cell confluence state, proliferation rate and cell cycle distribution, as these factors are all known to affect cellular metabolism (Miccheli *et al.*, 2006a; Miccheli *et al.*, 2006b; Valverde *et al.*, 2006). Importantly, the culture conditions were strictly maintained for all experiments performed with each cell line, to ensure that the biological responses to silver nanoparticles were not biased by variations in experimental conditions.

3.3. Intracellular polar metabolites

Typical ^{1}H NMR spectra of polar extracts from HaCaT, HepG2, and RAW 264.7 cells are shown in Figure 3.4 (a, b, and c, respectively). For each cell type, concentrated samples, prepared from at least 4 polar extracts, have been used to record 2D experiments, to aid spectral assignment. As an example, Figure 3.5 shows expansions of a) ^{1}H-^{1}H TOCSY, b) ^{1}H-^{13}C HSQC, and c) *J*-resolved spectra of a polar extract from HaCaT cells. Table 3.2 lists the compounds present in the polar extracts of each cell type, identified by matching 1D and 2D spectral data to reference spectra, as explained before. A total of 51 compounds have been identified.

In the low-frequency region (δ 0-3 ppm), the spectra of cellular polar extracts showed resonances from several amino acids (e.g. branched chain amino acids, threonine, alanine, glutamate, glutamine, methionine, aspartate), and organic acids (e.g. lactate, acetate, pyruvate, succinate). Moreover, the reduced form of the tripeptide glutathione (GSH) was also clearly detected in both 1D and 2D spectra, while the oxidised form (GSSG) could only be distinguished in 2D spectra.

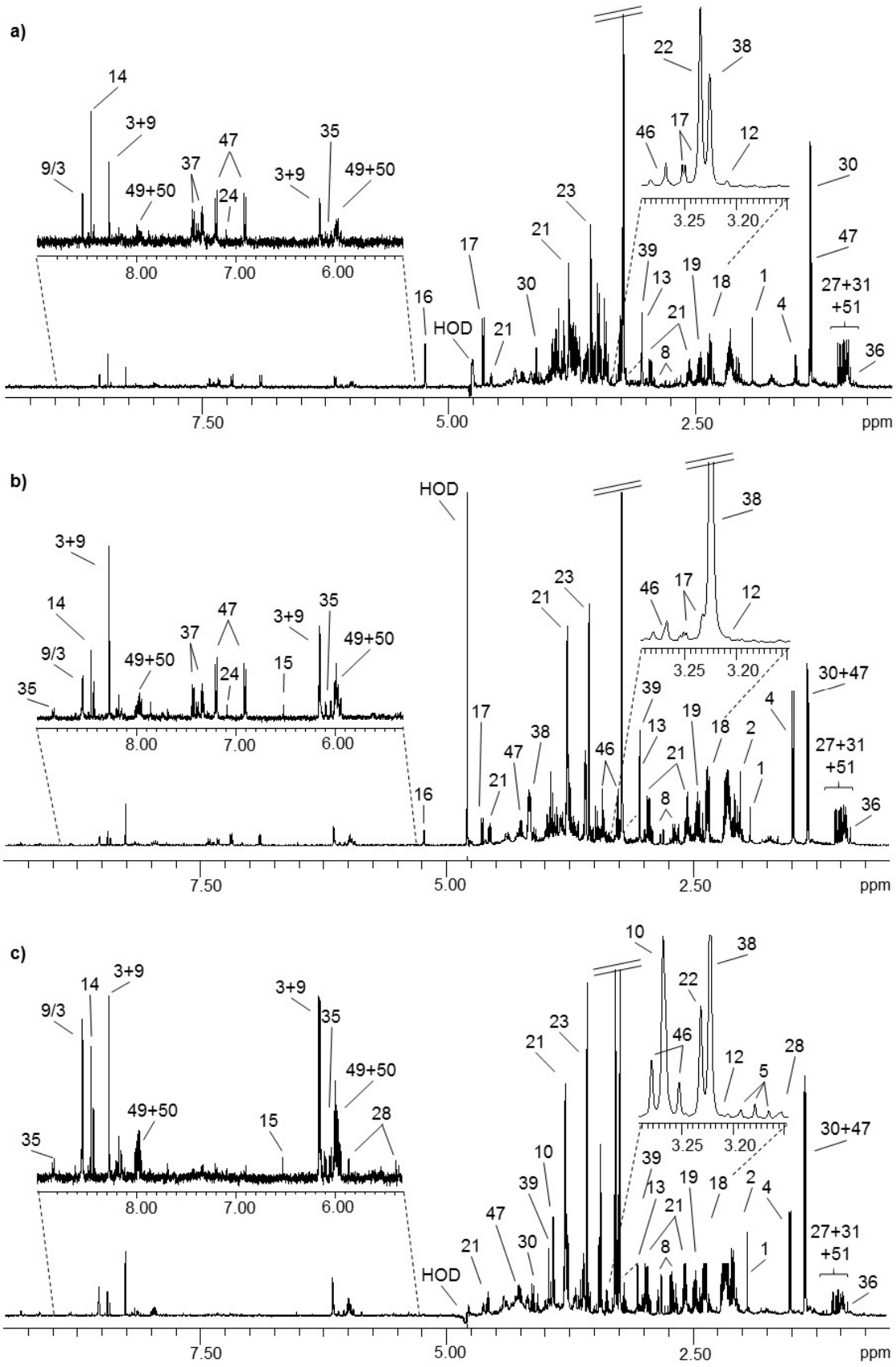

Figure 3.4. 500 MHz ^{1}H NMR spectra of polar extracts from a) HaCaT, b) HepG2, and c) RAW 264.7 control cells, grown for 24 hours. Signals are numbered in accordance with Table 3.2.

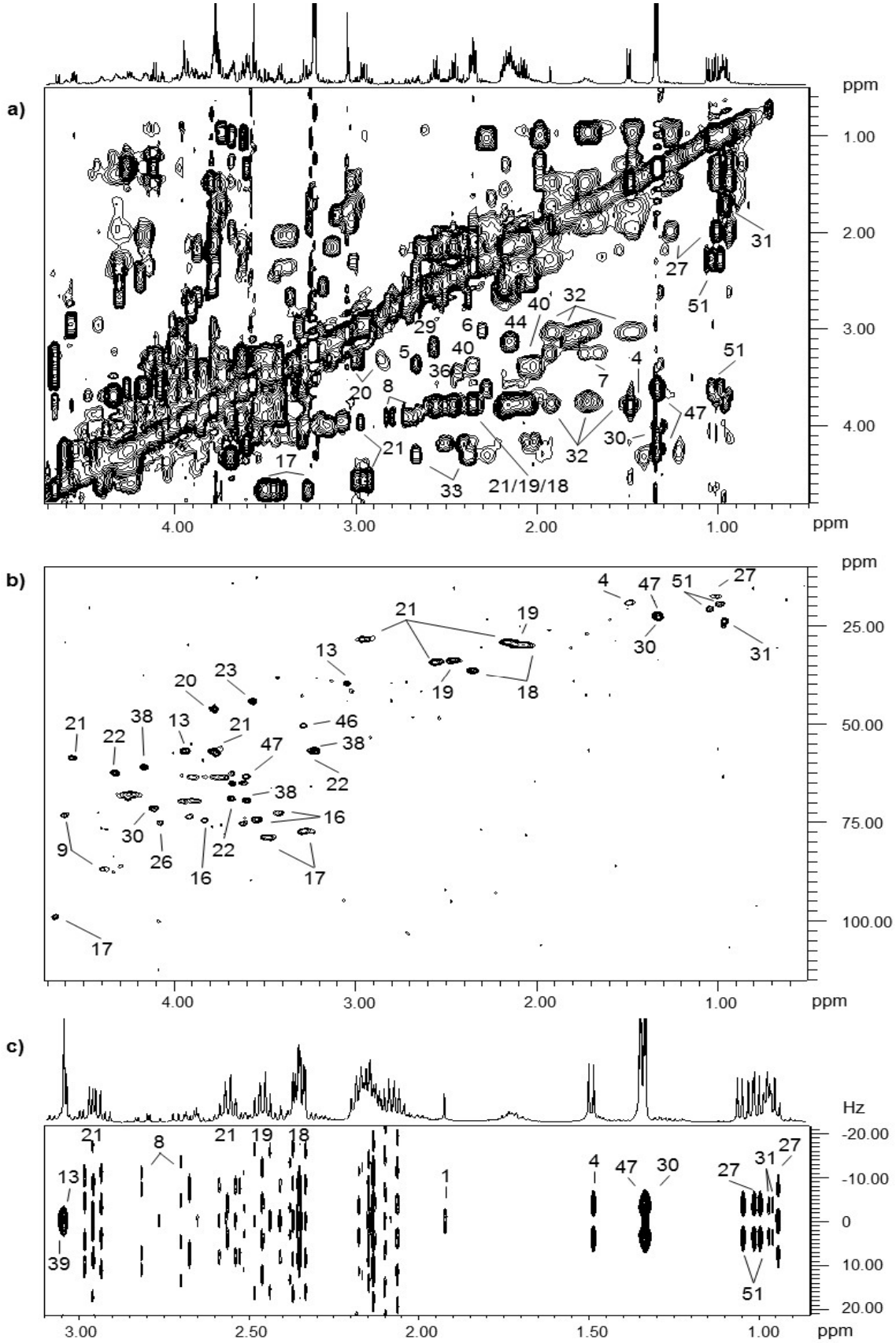

Figure 3.5. Expansions of a) ^{1}H-^{1}H TOCSY, b) ^{1}H-^{13}C HSQC, and c) *J*-resolved spectra of a polar extract from HaCaT control cells. Signals are numbered in accordance with Table 3.2.

Table 3.2. Assignment of resonances in the NMR profile of polar extracts from HaCaT, HepG2, and RAW 264.7 cells. Multiplicity: s, singlet; d, doublet; t, triplet; m, multiplet; dd, doublet of doublets.

No.	Compound	δ ^{1}H in ppm (multiplicity, assignment) / δ ^{13}C in ppm	Cell type		
			HaCaT	HepG2	RAW
1	Acetate	1.92 (s, *β*-CH_3)/26.0	✓	✓	✓
2	*N*-Acetylaspartate	2.02 (s, CH_3)/24.6; 2.50 (dd, *β*-CH_2); 2.70 (dd, *β*'-CH_2); 4.39 (dd, *α*-CH)		✓	
3	ADP	4.22 (m, C5'H, ribose); 4.38 (m, C4'H, ribose); 4.61 (m, C2'H, ribose); 6.15 (d, C1'H, ribose)/89.4; 8.28 (s, C8, ring); 8.54 (s, C2, ring)	✓	✓	✓
4	Alanine	1.49 (d, *β*-CH_3)/18.9; 3.78 (q, *α*-CH)	✓	✓	✓
5	*β*-Alanine	2.56 (t, *β*-CH_2); 3.18 (t, *α*-CH_2)	✓	✓	✓
6	*γ*-Aminobutyrate	1.89 (m, *β*-CH_2); 2.31 (t, *α*-CH_2); 3.00 (t, *γ*-CH_2)	✓		✓
7	Arginine	1.69 (m, *γ*-CH_2); 1.92 (m, *β*-CH_2); 3.24 (t, *δ*-CH_2); 3.78 (*α*-CH)	✓	✓	✓
8	Aspartate	2.69 (dd, *β*-CH); 2.82 (dd, *β*'-CH); 3.90 (dd, *α*-CH)	✓	✓	✓
9	ATP	4.22 (m, C5'H, ribose); 4.29 (m, C5''H, ribose); 4.41 (m, C4'H, ribose)/86.8; 4.62 (m, C2'H, ribose)/72.9; 6.15 (d, C1'H, ribose)/89.4; 8.28 (s, C2, ring); 8.55 (s, NH, ring)	✓	✓	✓
10	Betaine	3.27 (s, CH_3)/56.1; 3.90 (s, CH_2)/68.6			✓
11	Citrate	2.53 (d, *α*, *β*-CH_2); 2.67 (d, *α*', *β*'-CH_2)	✓	✓	✓
12	Choline	3.21 (s, $N(CH_3)_3$); 3.53 (m, C**H_2**(NH)); 4.07 (m, C**H_2**(OH))	✓	✓	✓
13	Creatine	3.04 (s, CH_3)/39.6; 3.93 (s, CH_2)/56.6	✓	✓	✓
14	Formate	8.46 (s, CH)	✓	✓	✓
15	Fumarate	6.52 (s, CH)	✓	✓	✓
16	*α*-Glucose	3.40 (m, C4H)/72.3; 3.55 (dd, C2H)/74.0; 3.71 (m, C3H)/75.5; 3.83 (m, C6H)/63.2; 3.85 (m, C5H)/74.2; 5.24 (d, C1H)/94.8	✓	✓	✓
17	*β*-Glucose	3.26 (dd, C2H)/76.8; 3.41 (m, C4H)/72.3; 3.47 (m, C5H)/78.6; 3.49 (t, C3H)/78.4; 3.74 (m, C6H)/63.4; 3.90 (dd C6'H)/63.4; 4.66 (d, C1H)/98.6	✓	✓	✓

No.	Compound	δ ^{1}H in ppm (multiplicity, assignment) / δ ^{13}C in ppm	Cell type		
			HaCaT	HepG2	RAW
18	Glutamate	2.06 (m, *β*-CH_2)/29.7; 2.13 (m, *β*'-CH_2)/29.7; 2.35 (m, *γ*-CH_2)/36.2; 3.75 (*α*-CH)/57.4	✓	✓	✓
19	Glutamine	2.14 (m, *β*-CH_2)/29.6; 2.45 (m, *γ*-CH_2)/33.7; 3.76 (*α*-CH)/57.2	✓	✓	✓
20	Glutathione, oxidised (GSSG)	2.16 (m, *β*-CH_2, Glu)/29.1; 2.53 (m, *γ*-CH_2, Glu)/34.2; 2.97 (m, *β*-CH_2, Cys)/41.4; 3.31 (m, *β*-CH_2, Cys')/41.4; 3.78 (*α*-CH, Gly)/46.1; 3.78 (*α*-CH, Glu)/56.8; 4.77 (m, *α*-CH, Cys)/55.2	✓	✓	✓
21	Glutathione, reduced (GSH)	2.17 (m, *β*-CH_2, Glu)/29.1; 2.56 (m, *γ*-CH_2, Glu)/34.2; 2.96 (m, *β*-CH_2, Cys)/28.4; 3.78 (*α*-CH, Gly)/46.1; 3.78 (*α*-CH, Glu)/56.8; 4.57 (m, *α*-CH, Cys)/58.5; 8.37 (NH, Gly); 8.56 (NH, Cys)	✓	✓	✓
22	Glycerophosphocholine	3.235 (s, $N(CH_3)_3$)/56.6; 3.68 (*β*'-CH_2(N))/68.6; 4.33 (m, *α*'-CH_2(P)/62.2	✓		✓
23	Glycine	3.57 (s, *α*-CH_2)/44.2	✓	✓	✓
24	Histidine	3.22 (m, *β*-CH_2); 7.11 (s, C4H, ring); 7.92 (s, C2H, ring)	✓	✓	✓
25	*β*-Hydroxybutyrate	1.20 (d, *γ*-CH_3); 2.30 (dd, CH_2); 2.42 (dd, CH_2); 4.16 (m, CH)	✓	✓	✓
26	*myo*-Inositol	3.29 (t, C5H)/77.1; 3.54 (C1H, C3H)/73.8; 3.63 (dd, C4H, C6H)/75.2; 4.07 (t, C2H)/74.9	✓	✓	✓
27	Isoleucine	0.94 (t, *δ*-CH_3)/13.8; 1.01 (d, *β*'-CH_3)/17.4; 1.26 (m, *γ*-CH_2)/27.2; 1.48 (m, *γ*'-CH_2)/27.2; 1.98 (m, *β*-CH)/38.7; 3.68 (d, *α*-CH)/62.0	✓	✓	✓
28	Itaconate	3.16 (m, *α*-CH_2)/44.9; 5.38 (m, CH_2)/124.8; 5.83 (m, CH_2')/124.8			✓
29	*α*-Ketoglutarate	2.44 (t, *β*-CH_2); 3.00 (t, *γ*-CH_2)	✓	✓	✓
30	Lactate	1.33 (d, *β*-CH_3)/22.8; 4.12 (q, *α*-CH)/71.3	✓	✓	✓
31	Leucine	0.96 (d, *δ*-CH_3)/23.7; 0.97 (d, *δ*'-CH_3)/24.9; 1.70 (m, *γ*-CH)/27.0; 1.72 (m, *β*-CH_2)/42.4; 3.74 (t, *α*-CH)	✓	✓	✓

No.	Compound	δ ^{1}H in ppm (multiplicity, assignment) / δ ^{13}C in ppm	Cell type		
			HaCaT	HepG2	RAW
32	Lysine	1.47 (m, *γ*-CH_2); 1.73 (m, *δ*-CH_2); 1.92 (m, *β*-CH_2); 3.03 (t, *ε*-CH_2); 3.76 (t, *α*-CH)	✓	✓	✓
33	Malate	2.38 (dd, *β*'-CH); 2.67 (dd, *β*-CH); 4.30 (dd, *α*-CH)	✓	✓	✓
34	Methionine	2.14 (s, *β*-CH_2); 2.16 (t, *β*-CH_2); 2.65 (t, *γ*-CH_2); 3.86 (t, *α*-CH)	✓	✓	✓
35	NAD^+	4.23 (m, A5'); 4.36 (m, A4'); 4.39 (m, A4'/N5'); 4.42 (dd, N3'); 4.50 (m, A3'); 4.54 (m, N2'); 6.04 (d, N1'); 6.10 (d, A1'); 8.18 (s, A2); 8.19 (N5); 8.43 (s, A8); 8.83 (d, N4); 9.14 (d, N6); 9.34 (s, N2)	✓	✓	✓
36	Pantothenate	0.90 (s, CH_3); 0.92 (s, CH_3); 2.42 (t, *α*-CH_2); 3.39 (d, CH_2); 3.43 (q, *β*-CH_2); 3.51 (d, CH_2); 3.98 (s, CH)	✓	✓	✓
37	Phenylalanine	3.14 (m, *β*-CH); 3.27 (dd, *β*'-CH); 4.00 (m, *α*-CH); 7.33 (d, C2H, C6H, ring)/131.9; 7.39 (d, C4H, ring); 7.43 (t, C3H, C5H, ring)/131.7	✓	✓	✓
38	Phosphocholine	3.226 (s, N(CH_3)$_3$)/56.6; 3.62 (m, N-CH_2)/69.3; 4.17 (m, PO_3-CH_2)/60.7	✓	✓	✓
39	Phosphocreatine	3.05 (s, CH_3); 3.95 (s, CH_2)/63.2	✓	✓	✓
40	Proline	2.01 (m, *γ*-CH_2); 2.07 (m, *β*-CH); 2.35 (m, *β*'-CH); 3.35 (dt, *δ*-CH); 3.42 (dt, *δ*'-CH); 4.13 (dd, *α*-CH)	✓	✓	✓
41	Pyroglutamate	2.04 (m, *β*-CH_2); 2.41 (m, *γ*-CH_2); 2.51 (m, *β*'-CH_2); 4.17 (dd, *α*-CH)	✓	✓	✓
42	Pyruvate	2.38 (s, *β*-CH_3)	✓	✓	✓
43	Serine	3.85 (dd, *α*-CH); 3.98 (m, *β*-CH_2)	✓	✓	✓
44	Spermidine	1.82 (m, *β*, *β*'-CH_2); 2.15 (m, *γ*, *γ*'-CH_2); 3.12 (m, *α*, *α*'-CH_2)	✓	✓	✓
45	Succinate	2.41 (s, CH_2)	✓	✓	✓
46	Taurine	3.26 (t, S-CH_2)/50.3; 3.43 (t, N-CH_2)/37.9	✓	✓	✓
47	Threonine	1.34 (d, *γ*-CH_3)/22; 3.59 (d, *α*-CH)/63.1; 4.26 (m, *β*-CH)/68.0	✓	✓	✓

No.	Compound	δ ^{1}H in ppm (multiplicity, assignment) / δ ^{13}C in ppm	Cell type		
			HaCaT	HepG2	RAW
48	Tyrosine	3.07 (m, *β*'-CH); 3.21 (m, *β*-CH); 3.96 (m, *α*-CH); 6.91 (d, C3H, C5H, ring)/118.6; 7.20 (d, C2H, C6H, ring)/133.6	✓	✓	✓
49	UDP	4.23 (m); 4.27 (m); 4.40 (t); 4.44 (t); 5.97 (s); 5.98 (d); 8.00 (d)	✓	✓	✓
50	UTP	5.97 (s); 5.99 (d);7.98 (d)	✓	✓	✓
51	Valine	0.99 (d, *γ*-CH_3)/19.5; 1.05 (d, *γ*'-CH_3)/20.7; 2.28 (m, *β*-CH)/31.7; 3.62 (d, *α*-CH)/63.0	✓	✓	✓

In the mid-frequency region (δ 3-5.5 ppm), additional intracellular metabolites detected included creatine, phosphocreatine, choline-containing compounds, taurine, *myo*-inositol, and glucose. In the high-frequency region (δ 5.5-10 ppm), the signals detected were assigned mainly to aromatic amino acids (tyrosine, phenylalanine), organic acids (fumarate and formate) and nucleotides (ADP, ATP, UDP, UTP and NAD^{+}). The assignment of nucleotides was confirmed through spiking with reference compounds.

Most metabolites were present in all cell types, although in varying relative amounts. Still, a few qualitative differences were noticed. Acetylated amino acids were found in HepG2 cells, but not in HaCaT or RAW 264.7 cells. In particular, *N*-acetylaspartate was clearly identified in the HepG2 *J*-resolved spectrum, through a singlet at 2.02 ppm and two doublets of doublets at 2.50 and 2.70 ppm, not present in the spectra of the other cell types. Furthermore, another *N*-acetylated amino acid, with a singlet at 2.01 ppm, was detected in HepG2 cells, but its unambiguous identification was not possible. On the other hand, glycerophosphocholine, clearly identified in keratinocytes and macrophages through the *N*--trimethyl singlet (3.23 ppm) and the scalar-coupled methylene protons (3.68 and 4.33 ppm), was not detectable in HepG2 cells. Furthermore, betaine and itaconate were found in RAW 264.7 macrophages, but not in the other cell types. The assignment to itaconate was confirmed through statistical correlation between 1D spectra (STOCSY), as shown in Figure 3.6.

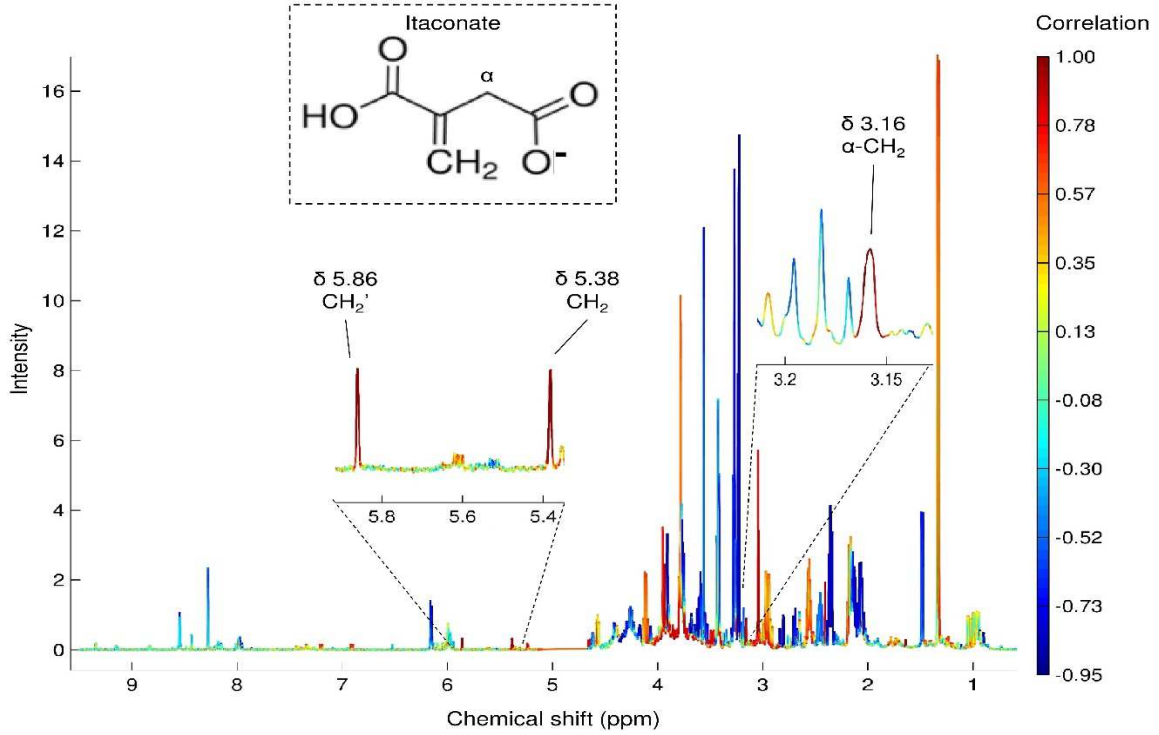

Figure 3.6. STOCSY confirming the assignment of itaconate in RAW 264.7 cells; driver peak 5.86 ppm.

3.4. Lipophilic metabolites

The NMR analysis of lipophilic extracts, obtained by dual phase extraction of cells, enabled the cellular lipid pool to be characterised. Figure 3.7 shows typical ^{1}H NMR spectra of lipophilic extracts from HaCaT, HepG2 and RAW 264.7 cells. Two-dimensional experiments (^{1}H-^{1}H TOCSY, ^{1}H-^{13}C HSQC, and *J*-resolved) have also been recorded for each cell type, as exemplified in Figure 3.8 for a HepG2 lipophilic extract. Spectral assignment relied primarily on matching the chemical shift information derived from 1D and 2D spectra to previous literature reports (Casu *et al.*, 1991; Adosraku *et al.*, 1994; Oostendorp *et al.*, 2006; Mannina *et al.*, 2008; Ruiz-Aracama *et al.*, 2011). Moreover, ^{1}H NMR spectra of a few standard lipids have been recorded in-house. The different lipid species identified and their corresponding NMR resonances are listed in Table 3.3.

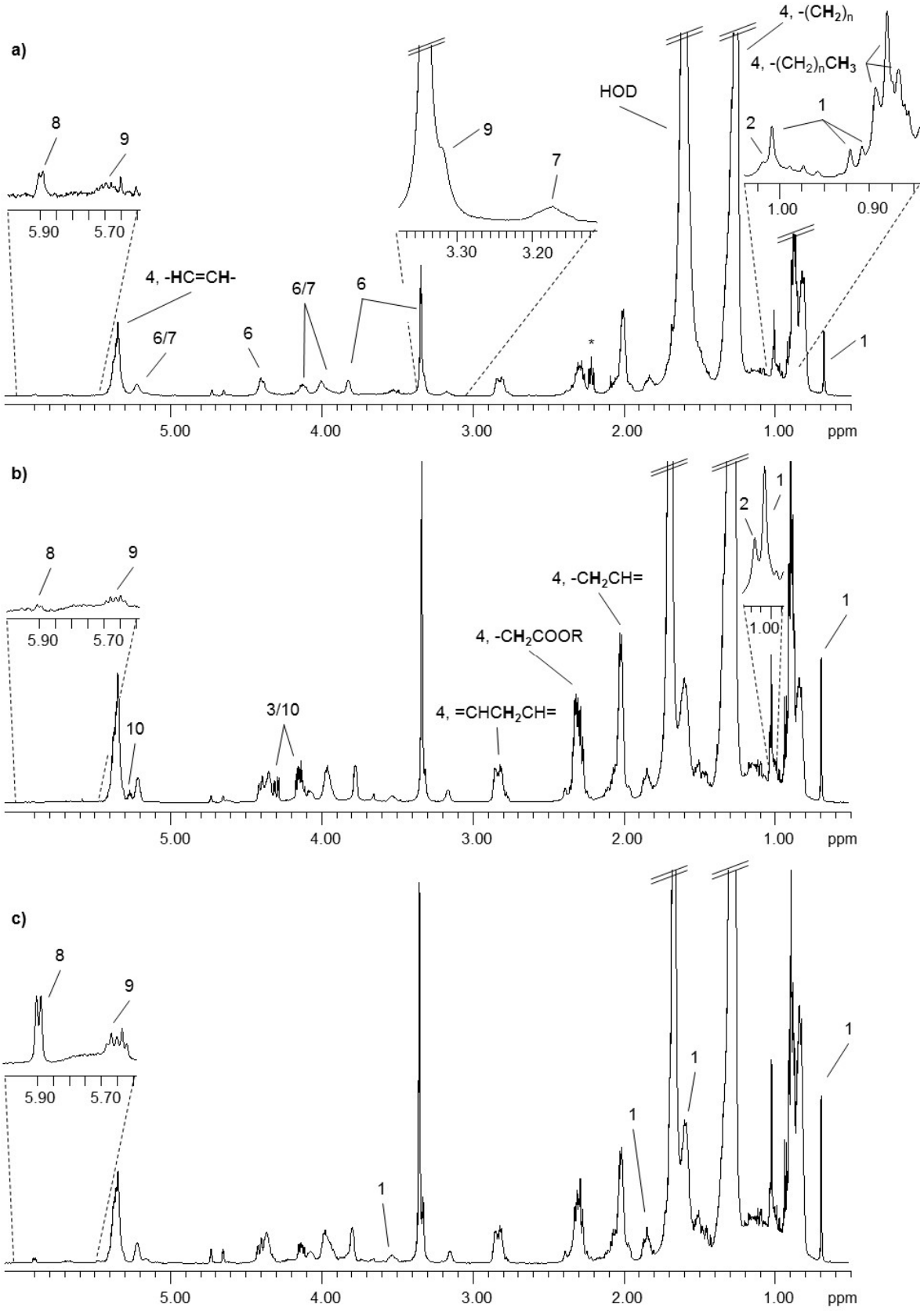

Figure 3.7. 500 MHz ^{1}H NMR spectra of lipophilic extracts from a) HaCaT, b) HepG2, and c) RAW 264.7 control cells, grown for 24 hours. Signals are numbered in accordance with Table 3.3.

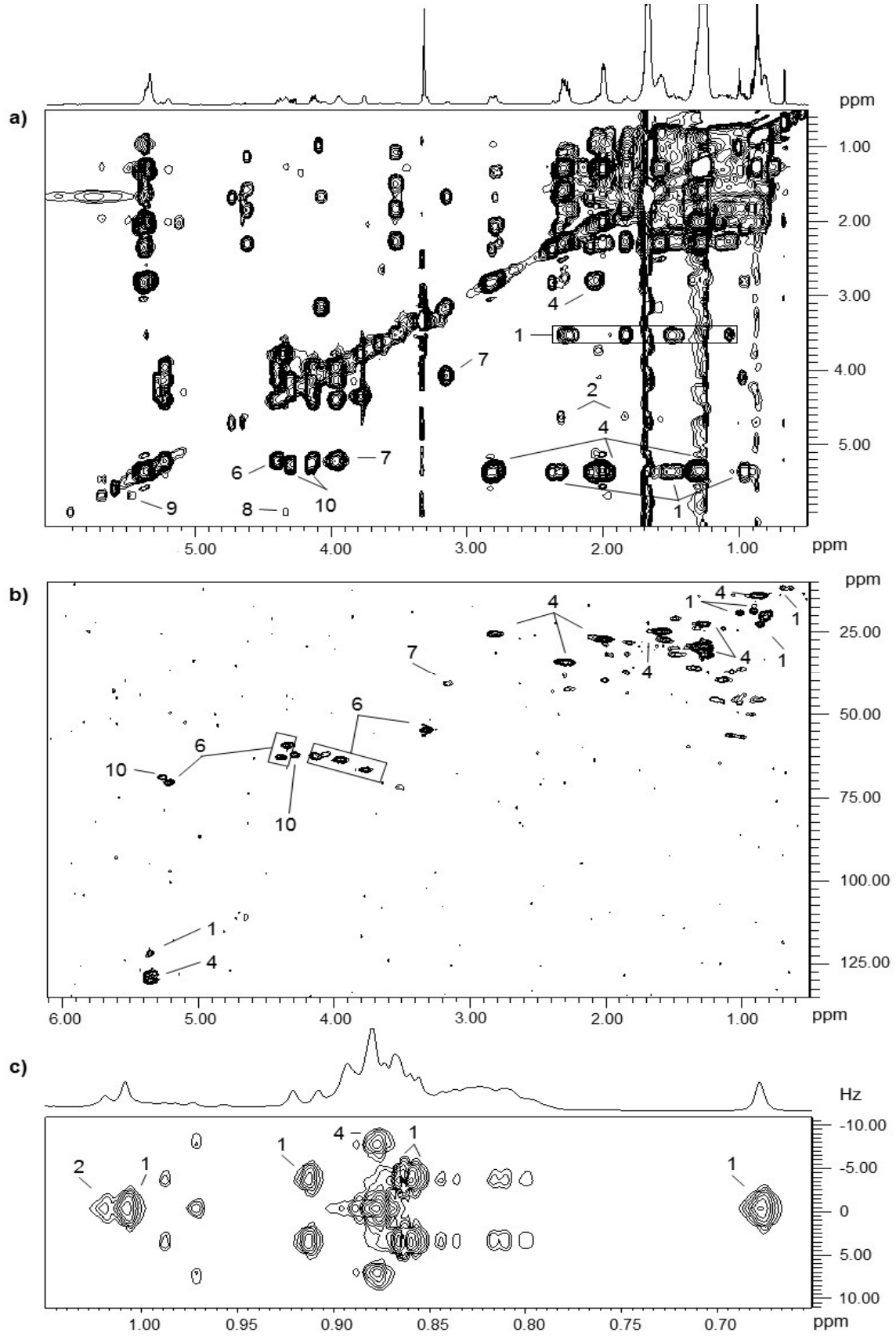

Figure 3.8. Expansions of a) ^{1}H-^{1}H TOCSY, b) ^{1}H-^{13}C HSQC, and c) *J*-resolved spectra of a lipophilic extract from HepG2 control cells. Signals are numbered in accordance with Table 3.3.

Table 3.3. Assignment of resonances in the NMR profile of lipophilic extracts from HaCaT, HepG2, and RAW 264.7 cells. Multiplicity: s, singlet; d, doublet; t, triplet; m, multiplet; dd, doublet of doublets.

No.	Compound	δ ^{1}H in ppm (multiplicity, assignment)/ δ ^{13}C in ppm	Cell type		
			HaCaT	HepG2	RAW
1	Cholesterol	0.68 (s, CH_3-18)/11.8; 0.86/0.87 (2xd, CH_3-26/ CH_3-27)/22.7; 0.91 (d, CH_3-21)/18.6; 1.01 (s, CH_3-19)/19.4; 1.05-1.19 (m, multiple protons)/39.7; 1.42-1.55 (m, multiple protons)/31.8; 1.78-1.88 (m, multiple protons); 2.00 (m, multiple protons); 2.26 (m, CH_2-4); 3.48-3.57 (m, CH-3)/71.8; 5.35 (m, CH-6)/122.02	✓	✓	✓
2	Cholesterol ester	1.02 (s, CH_3-19); 1.57 (m, multiple protons); 1.84 (m, CH_2-2); 2.31 (m, CH_2-4); 4.62 (m, CH-3)	✓	✓	✓
3	Diglycerides (DG)	3.71, 4.27 (glyceryl CH_2 *sn*1/*sn*3); 5.08 (glyceryl CH s*n*2)	✓	✓	✓
4	Fatty acyl chains (mainly in phospholipids)	0.88 (t, C**H$_3$**(CH_2)$_n$)/14.1; 1.25 (m, (C**H$_2$**)n)/22.8/29.6/31.8; 1.55-1.65 (m, -C**H$_2$**-CH_2CO)/24.8/27.0; 1.98-2.09 (m, -C**H$_2$**CH=)/27.0; 2.25-2.35 (m, -C**H$_2$**COOR)/34.1; 2.77-2.87 (m, =CHC**H$_2$**CH=)/25.6; 5.35 (m, -**H**C=C**H**-)/130.1	✓	✓	✓
5	Free fatty acids	0.97 (t, C**H$_3$**(CH_2)n); 1.63 (m, -C**H$_2$**-CH_2CO); 2.05 (m, -C**H$_2$**CH=); 2.35 (t, -C**H$_2$**COOH); 2.77 (t, =CHC**H$_2$**CH=)	✓	✓	✓
6	Phosphatidylcholine (PTC)	3.35 (s, N(CH_3)$_3$)/54.7; 3.82 (CH_2-N)/66.7; 3.99 (glyceryl CH_2 *sn*3)/63.5; 4.12, 4.38 (glyceryl CH_2 *sn*1)/62.8; 4.40 (CH_2-OP)/59.4; 5.22 (glyceryl CH *sn*2)/70.4	✓	✓	✓

No.	Compound	δ ^{1}H in ppm (multiplicity, assignment)/ δ ^{13}C in ppm	Cell type		
			HaCaT	HepG2	RAW
7	Phosphatidylethanol-amine (PTE, diacyl form)	3.18 (s, CH_2-N)/40.7; 3.55 (glyceryl CH_2 *sn*1)/71.6; 3.92 (glyceryl CH_2 *sn*3)/63.9; 4.12 (CH_2-OP)/62.7; 5.22 (glyceryl CH *sn*2)/70.4	✓	✓	✓
8	PTE plasmalogen (PTE, plasmenyl form)	1.27 ((CH_2)$_n$); 1.99 (-CH=CH-C**H$_2$**); 3.90 (glyceryl CH_2 *sn*3); 4.34 (glyceryl CH_2 *sn*1); 5.15 (glyceryl CH *sn*2); 5.91 (-C**H**=C**H**-)	✓	✓	✓
9	Sphingomyelin (SM)	3.34 (s, N(CH_3)$_3$); 5.45 (-C**H**=C**H**-); 5.70 (-C**H**=C**H**-)	✓	✓	✓
10	Triglycerides (TG)	4.12, 4.28 (glyceryl CH_2 *sn*1/*sn*3)/62.0; 5.27 (glyceryl CH s*n*2)/68.9		✓	

The main contributors to the lipophilic profile were the signals of cholesterol and phosphatidylcholine, two major components of cell membranes. Cholesterol was easily identified through its characteristic singlet at 0.68 ppm, arising from C18, and several other resonances (Table 3.3). Phosphatidylcholine was positively identified through the intense singlet at 3.35 ppm, arising from the N(CH_3)$_3$ headgroup, and a number of other signals, namely those from CH_2-N and CH_2-OP protons, glyceryl protons, and fatty acyl chains. The latter comprise methyl (CH_3), methylene (CH_2), olefinic (CH=CH) and allylic (CH_2-CH=) protons, which largely overlap within different fatty acids, producing broad, complex spectral signals.

Other membrane phospholipids, namely phosphatidylethanolamine and sphingomyelin, were also identified based on their typical chemical shifts (Table 3.3). Phosphatidylethanolamine comprised both the diacyl and plasmenyl forms, distinguishable through their glyceryl *sn*-2 proton resonances. Additionally, smaller amounts of neutral lipids, namely cholesterol esters, free fatty acids, diglycerides and triglycerides were also detected, especially in HepG2 cells. Indeed, the characteristic glyceryl *sn*-1 and *sn*-3 proton resonances of triglycerides (4.12 and 4.28 ppm) were not found in the spectra of HaCaT nor RAW 264.7 cells. Other differences between the three cell types in terms of their lipid composition could be highlighted through the consideration of signal ratios (Table 3.4).

HepG2 cells were characterised by a higher proportion of neutral lipids in relation to membrane phospholipids, likely reflecting the storage of lipid reserves in the form of cytosolic droplets typically seen in liver cells (Gao and Goodman, 2015). Moreover, HepG2 lipids showed, on average, higher chain lengths (greater $(CH_2)_n/CH_3$ ratio) and higher degree of unsaturation ($CH=CH/CH_3$ ratio), while HaCaT keratinocytes showed the highest relative amount of polyunsaturated fatty acids ($=CH-CH_2-CH=/CH=CH$ ratio).

Table 3.4. Lipid ratios in HaCaT, HepG2, and RAW 264.7 cells, as obtained by integration of NMR signals in the spectra of lipophilic extracts. Data is expressed as mean ± standard deviation, of at least 3 samples. PL, phospholipids; FA, fatty acyl; PUFA, polyunsaturated fatty acyl chains.

	Neutral lipids/PL	FA chain length $[(CH_2)_n/CH_3]$	FA unsaturation $[CH=CH/CH_3]$	PUFA $[=CH-CH_2-CH=/CH=CH]$
HaCaT	0.16±0.03	4.13±0.16	0.86±0.07	0.48±0.00
HepG2	0.27±0.04	4.80±0.32	1.08±0.08	0.32±0.01
RAW	0.12±0.01	4.70±0.53	0.79±0.08	0.33±0.01

Supplementary information to Chapter 3

Table S3.1. Dulbecco's Modified Eagle Medium (DMEM) formulation, from GIBCO®.

Components	Molecular Weight	Concentration (mg/L)	Concentration (mM)
Amino acids			
Glycine	75	30	0.4
L-Arginine hydrochloride	211	84	0.398
L-Cystine 2HCl	313	63	0.201
L-Histidine hydrochloride-H_2O	210	42	0.2
L-Isoleucine	131	105	0.802
L-Leucine	131	105	0.802
L-Lysine hydrochloride	183	146	0.798
L-Methionine	149	30	0.201
L-Phenylalanine	165	66	0.4
L-Serine	105	42	0.4
L-Threonine	119	95	0.798
L-Tryptophan	204	16	0.0784
L-Tyrosine disodium salt dihydrate	261	104	0.398
L-Valine	117	94	0.803
Vitamins			
Choline chloride	140	4	0.0286
D-Calcium pantothenate	477	4	0.00839
Folic Acid	441	4	0.00907
Niacinamide	122	4	0.0328
Pyridoxine hydrochloride	204	4	0.0196
Riboflavin	376	0.4	0.00106
Thiamine hydrochloride	337	4	0.0119
i-Inositol	180	7.2	0.04
Inorganic Salts			
Calcium Chloride ($CaCl_2$) (anhyd.)	111	200	1.8
Ferric Nitrate ($Fe(NO_3)_3 \cdot 9H_2O$)	404	0.1	0.000248
Magnesium Sulfate ($MgSO_4$) (anhyd.)	120	97.67	0.814
Potassium Chloride (KCl)	75	400	5.33
Sodium Bicarbonate ($NaHCO_3$)	84	3700	44.05

Components	**Molecular Weight**	**Concentration (mg/L)**	**Concentration (mM)**
Sodium Chloride (NaCl)	58	6400	110.34
Sodium Phosphate monobasic (NaH_2PO_4-H_2O)	138	125	0.906
Other Components			
D-Glucose (Dextrose)	180	4500	25
Phenol Red	376.4	15	0.0399

Chapter 4. Metabolomic analysis of human keratinocytes (HaCaT cells) exposed to silver nanoparticles of different sizes and coatings

4.1. Background and aims

In this chapter, the impact of silver nanoparticles (AgNPs) on the endo- and exometabolome of human epidermal keratinocytes (HaCaT cell line) is addressed. AgNPs present in skin care and wound healing products are able to penetrate across the skin barrier and translocate into the epidermis, especially if the skin barrier is damaged (for example, due to inflammation) (Vogt *et al.*, 2014). HaCaT cells have several morphological and functional features of normal epidermal keratinocytes, thus being a relevant *in vitro* model for studying the biological effects of AgNPs. Indeed, previous studies have used HaCaT cells to test the cytotoxic effects of AgNPs. The results, were, however, highly variable with respect to cellular uptake, cytotoxicity and genotoxicity. For instance, Lu and co-workers found that 30 nm citrate-stabilised silver nanospheres and PVP-coated nanoprisms could enter HaCaT cells and accumulate in the nucleus, but were not cytotoxic and did not appear to affect DNA integrity up to 100 µg/mL and 48 h exposure (Lu *et al.*, 2010). In contrast, other studies have shown that PVP-coated AgNPs with metallic core diameters of 25 nm (Zanette *et al.*, 2011) or 70 nm (Vogt *et al.*, 2014), resuspended Ag nanopowder (< 100 nm) (Mukherjee *et al.*, 2012) and 50 nm citrate-stabilised AgNPs (Comfort *et al.*, 2014) were cytotoxic to HaCaT keratinocytes (IC_{50} near or below 50 µg/mL). The different properties of the tested AgNPs, as well as the different incubation times and endpoints assessed, are likely to account for these discrepancies. As mentioned in section 1.1 of the Introduction, the physicochemical properties of AgNPs (size, shape, surface chemistry and charge) are known to impact their biological outcomes. Thus, in this work, a panel of six well-characterised AgNPs, varying in size and coating, has been selected to systematically study the structure-activity relationships of metabolic changes induced in HaCaT cells. The nanoparticles tested included citrate-stabilised AgNPs with diameters of 10, 30 and 60 nm (here designated as Cit10, Cit30 and Cit60, respectively), AgNPs coated with polyethylene glycol (PEG), sized 10 and 30 nm (PEG10 and PEG30), and AgNPs coated with bovine serum albumin (BSA), sized 30 nm (BSA30). The choice of the coating agents was based on their low inherent toxicity and on their relevance in the context of AgNPs behaviour in a biological environment. Citrate is one of the most commonly used reductants, stabilising AgNPs by electrostatic repulsion, and yielding negatively charged

particles (Tolaymat *et al.*, 2010). PEG, a polymer of ethylene oxide, stabilises the AgNPs and minimises their agglomeration by steric hindrance (Luo *et al.*, 2005); PEG is known for its ability to prevent protein adsorption and promote extended circulation, being frequently used in the pharmaceutical industry (Xu *et al.*, 2007). BSA has also been previously shown to provide great colloidal stability to AgNPs dispersions (MacCuspie, 2011); it is a protein with large homology to the human serum albumin, encountered by the AgNPs as soon as they enter the bloodstream, having less stringent biosafety requirements than the human protein. In addition to the AgNPs mentioned above, silver ions (Ag^+ from $AgNO_3$) and hydrogen peroxide (H_2O_2) were also added to HaCaT cells and their metabolic effects evaluated, with a view to better understand the role of ionic silver and oxidative stress in AgNPs toxicity.

4.2. Physicochemical properties of the AgNPs tested

The main properties of aqueous colloidal solutions of the AgNPs used in this work are summarised in Table 4.1. Transmission electron microscopy (TEM) (Figure S4.1) showed that AgNPs were approximately spherical in shape, with mean diameters agreeing with those indicated by the manufacturer. The wavelength of the maximum absorbance peak in the UV-Vis spectra also matched the expected values, increasing with particle size. Regarding the DLS measurement of hydrodynamic diameters (D_h), with the exception of Cit10 and PEG10, all aqueous colloidal solutions of nanoparticles showed PdI values below 0.3, indicating reasonably monodisperse distributions. Therefore, the Z-average size, obtained from the light scattering intensity distribution, was considered for comparison of particle sizes. In the case of 10 nm nanoparticles, accurate DLS measurements were hindered by the reduced light scattering typical of small particles, and the values presented in Table 4.1 correspond to rough estimates of average sizes. The D_h of citrate-coated nanoparticles was slightly above the diameter of the inorganic core, whereas this difference was greater for PEG and BSA coatings, as expected based on the larger size of these molecules compared to citrate. As to the zeta potential, citrate-stabilised particles carried a strongly negative surface charge (ζ -29 to -43 mV) while the surface of the PEG- and BSA-stabilised nanoparticles was less negative (ζ -12 to -18 mV, Table 4.1). Ionic silver was quantified in these colloidal solutions by ICP-OES and found to be below 4% for all nanoparticles, except in the case of PEG10, which showed a high amount of free Ag^+ (19%), likely because this suspension had been stored for over 6 months at the time of the ICP measurement. Note, however, that the PEG10 AgNPs used in biological and metabolomics

assays had been stored for much shorter time (< 1 month) and should not have such high amounts of free ionic silver.

Table 4.1. Physicochemical properties of the AgNPs used in this work, dispersed in ultrapure distilled water. Cit10, Cit30 and Cit60 stand for citrate-coated AgNPs with nominal diameters of 10, 30 and 60 nm, respectively; PEG10 and PEG30 are AgNPs coated with polyethylene glycol, sized 10 and 30 nm, respectively; BSA30 designates 30 nm AgNPs coated with bovine serum albumin.

AgNP	D (nm)[a]	D (nm)[b]	D_h (nm)[c]	PdI[c]	ζ (mV)[d]	λ_{max}[e] (nm)	%Ag^+[f]
Cit10	9.3±1.8	11.0±2.4	25.1±3.6	0.42-0.52	-34.5±3.3	386	0.93±0.02
Cit30	32.7±4.8	29.1±3.9	43.3±0.5	0.25-0.26	-42.7±2. 7	408	3.32±0.04
Cit60	59.6±5.8	59.0±6.9	63.4±0.4	0.13-0.14	-29.2±3. 9	427	0.16±0.01
PEG10	9.8±2.0	7.8±3.7	40.6±3.9	0.26-0.37	-14.3±1.0	396	19.14±0.70
PEG30	31.8±3.2	26.8±5.3	62.1±0.5	0.15-0.16	-12.1±0. 5	411	0.63±0.01
BSA30	n.a.	26.3±4.4	75.6±0.7	0.15-0.21	-18.4±0.7	40 9	1.92±0.01

[a]Diameter indicated by the manufacturer; [b]Diameter measured by TEM; [c]Hydrodynamic diameter and polydispersity index (PdI) measured by DLS; [d]Zeta potential assessed by electrophoretic mobility; [e]Wavelength of maximum absorbance peak in the UV-Vis spectrum; [f]Percentage of ionic silver in the AgNPs suspension (10 µg/mL). Standard deviations calculated for D_h, ζ and %Ag^+ correspond to 3 replicate measurements. n.a. Not available (NPs coated with BSA in-house).

The behaviour of AgNPs in cell culture medium (DMEM with 10% FBS) was assessed by monitoring D_h and ionic silver release over time (Figure 4.1a and 4.1b, respectively). The Cit10 nanoparticles, for which DLS measurements were inherently less accurate, showed a sudden increase in D_h to ~150 nm, as soon as they were placed in the culture medium, and the PdI values were greater than 0.3, indicating large dispersion in particle size. Together with the significant broadening of the respective UV-Vis absorption spectra (not shown), these observations suggest the formation of variable-sized agglomerates, induced by the high ionic strength of the culture medium. The more reactive surface and the less effective protection of small nanoparticles by FBS proteins (Shannahan *et al.*, 2013) may have accounted for this effect. The D_h of Cit30 and Cit60 nanoparticles progressively increased with incubation time (up to 94 and 119 nm, respectively), likely due to the displacement of citrate and the formation of a protein corona, as shown by others (Bolea *et al.*, 2014; Hansen and Thunemann, 2015). Agglomeration did not seem significant for these particles, based on the rather monodisperse D_h peaks (PdI < 0.3) and the small red shift (by 10-20 nm) in the UV-Vis absorbance maxima, which could be due to changes in the local dielectric constant surrounding the nanoparticles as a result of protein binding (Zook *et al.*, 2011). Regarding PEG-coated nanoparticles, while PEG10 appeared to form

variable-sized agglomerates, the D_h of PEG30 did not vary much upon incubation in culture medium, showing that PEG provided high colloidal stability to these particles. BSA30 AgNPs showed moderate variations in D_h, which increased to 103 nm at 48 h, suggesting that additional coating with FBS proteins could have occurred.

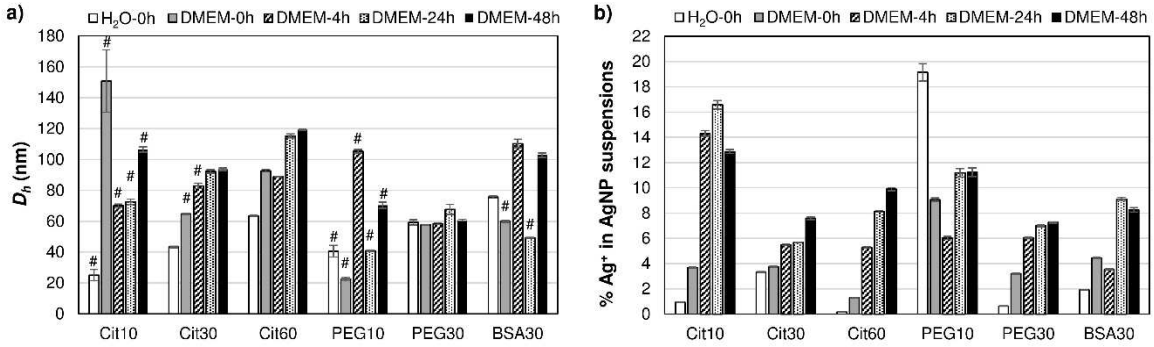

Figure 4.1. a) Hydrodynamic diameter (D_h) of different AgNPs in ultrapure water and in culture medium (DMEM + 10% FBS) at 0, 4, 24 and 48 h incubations. # PdI > 0.3 or poor quality of results (as reported by the DLS instrument); b) Amount (%) of ionic silver (Ag^+) in suspensions of different AgNPs in water and in culture medium (0, 4, 24 and 48 h incubations).

Regarding ionic silver release (Figure 4.1b), the highest rate of dissolution was observed for Cit10, in agreement with the premise that smaller metal nanoparticles show enhanced ion release due to increased specific surface area and curvature (Butler *et al.*, 2015). Thus, the formation of agglomerates of Cit10, suggested to occur based on the DLS data, was less determinant to the dissolution than the primary size, consistently with the observations of others (Zhang *et al.*, 2011; Gliga *et al.*, 2014). In the case of PEG10, there was a decrease in the amount of free ionic silver as soon as the suspension was added to culture medium; this could possibly be due to the formation of insoluble silver salts with medium ions (e.g. AgCl) which remained in the centrifugation pellet and were not quantified. Then, during incubation in culture medium, there was an additional release of Ag^+ up to 11%. As for the other nanoparticles, there was a progressive Ag^+ release over time, reaching maximum values of 7-10%. Notably, the Ag^+ release profiles of Cit30, PEG30 and BSA30 AgNPs were similar, showing that coating had little influence on nanoparticle dissolution.

4.3. Viability of HaCaT cells exposed to AgNPs, Ag^+ and H_2O_2

The dose-response curves of HaCaT cells exposed to each AgNP type for 24 h, as obtained by the MTT assay, are depicted in Figure 4.2. Equivalent results for the 48 h

exposures are presented in Figure S4.2. All nanoparticles caused dose-dependent decreases in cell viability, except for the 24 h exposure to PEG30 which did not affect cell viability in a significant way up to the maximum concentration tested (100 µg/mL). Among the citrate-coated AgNPs, Cit30 were the most cytotoxic, with IC_{50} values around 40 µg/mL, at both 24 and 48 h.

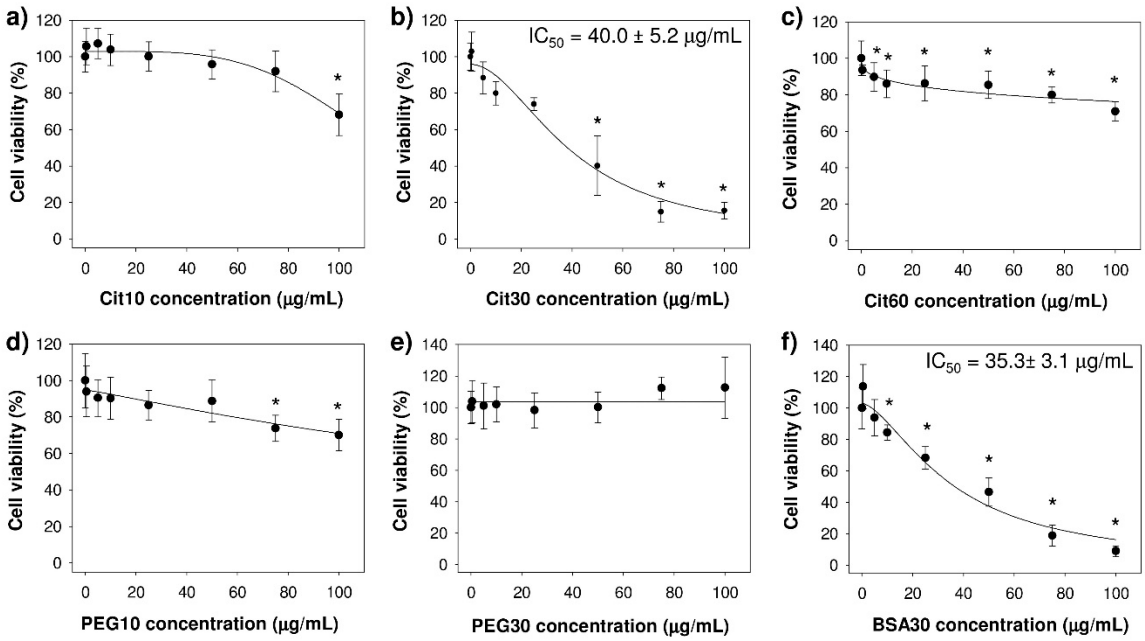

Figure 4.2. Viability (%) of HaCaT cells, measured by the MTT assay, after 24 h of exposure to AgNPs: a) Cit10, b) Cit30, c) Cit60, d) PEG10, e) PEG30 and f) BSA30. Data was acquired by project partners Verónica Bastos and Tiago Pedrosa (CESAM, UA), and is expressed as mean ± standard deviation of three independent assays with three replicates each (n 9). Calculated IC_{50} value shown only when it fell within the concentration range tested. Statistically significant ($p < 0.05$) differences relatively to controls are indicated by *.

The lower cytotoxicity of Cit10 compared to the other citrate-coated nanoparticles contradicted previous reports which noted an inverse correlation between nanoparticle size and toxicity (Liu *et al.*, 2010; Park *et al.*, 2011). However, in the present work, the above mentioned agglomeration of Cit10 in culture medium could have limited the cellular uptake of these nanoparticles and, consequently, their damaging effects. The cells exposed to PEG-coated AgNPs decreased their viability down to 60 % (for 48 h exposure to 100 µg/mL PEG10), with an apparent inverse correlation between size and toxicity. As for BSA30, their IC_{50} concentration was 35 µg/mL at 24 h and 25 µg/mL at 48 h. However, this larger cytotoxicity of BSA30 could be partially related with the toxicity of the coating protein in itself. As shown in Figure S4.3, neither citrate nor PEG decreased cell viability at the

maximum concentrations possibly present when citrate- or PEG-coated AgNPs were administered to cells (up to 21 µg/mL citrate or 8 µg/mL PEG). On the other hand, BSA caused a statistically significant decrease in cell viability down to ~80% at the highest concentration tested (200 µg/mL), which is the BSA concentration present in ~15 µg/mL of BSA30. Furthermore, it should be recalled that the specific surface chemistry and charge may influence the extent of nanoparticle uptake and interaction with cell membranes, and thus nanoparticle toxicity (Caballero-Diaz *et al.*, 2013; Chunyan and Valiyaveettil, 2013; Kaur and Tikoo, 2013). As to the ionic silver released extracellularly, it may have contributed to toxicity but did not have a determinant effect on cell viability, in agreement with the findings of others (Caballero-Diaz *et al.*, 2013; Gliga *et al.*, 2014).

The effect of Ag^+, administered as $AgNO_3$, on cell viability is expressed in the dose-response curve shown in Figure 4.3a. Exposure to 1.0-1.5 µg/mL Ag^+ for 24 h caused a steep decrease in cell viability (IC_{50} 1.26 ± 0.02 µg/mL), agreeing with previous results reported for HaCaT cells (Zanette *et al.*, 2011) and other cell types (Kim *et al.*, 2009b; Liu *et al.*, 2010). This much higher toxicity of Ag^+ compared to the same concentration of silver given as AgNPs has also been reported by others (Beer *et al.*, 2012; Cronholm *et al.*, 2013; Caballero-Diaz *et al.*, 2013; Butler *et al.*, 2015). It has been argued that, while AgNPs enter cells by endocytosis releasing Ag^+ intracellularly (Cronholm *et al.*, 2013; Gliga *et al.*, 2014), Ag^+ from $AgNO_3$ is not as readily taken up by cells and induces toxicity via extracellular mechanisms causing cell membrane damage (Cronholm *et al.*, 2013).

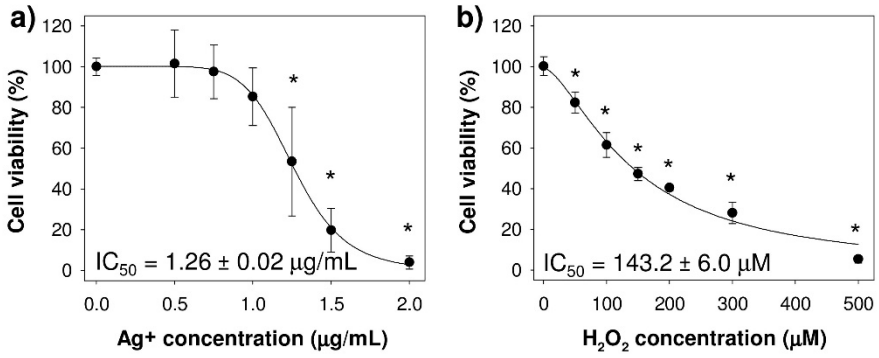

Figure 4.3. Viability (%) of HaCaT cells, measured by the MTT assay, after 24 h of exposure to: a) Ag^+, and b) H_2O_2. Data was acquired by project partners Verónica Bastos and Tiago Pedrosa (CESAM, UA), and is expressed as mean ± standard deviation of three independent assays with three replicates each (n 9). Statistically significant ($p < 0.05$) differences relatively to controls are indicated by *.

The cytotoxicity of H_2O_2 was also assessed; the dose-response curve for 24 h exposure is shown in Figure 4.3b. H_2O_2 is a nonradical ROS which is usually generated from any source of oxidative stress and can easily transform into more reactive oxygen radicals, leading to the propagation of cellular oxidative damage. Upon exposure to increasing concentrations of H_2O_2, cells progressively showed decreasing viability, down to less than 20% at 500 μM, the IC_{50} value being calculated as 143 ± 6 μM. An approximate result was obtained by Ramanauskienė and colleagues that calculated the IC_{50} value of H_2O_2 in HaCaT cells as 183.7 ± 20.4 μM (Ramanauskienė *et al.*, 2015).

4.4. Generation of reactive oxygen species (ROS)

Intracellular ROS generation was measured in HaCaT cells exposed to either Cit30 AgNPs or H_2O_2, at IC_{20} and IC_{50} concentrations (Figure 4.4). ROS levels showed a dose-dependent increase with exposure to both chemicals. In particular, Cit30 induced a significant 1.4 fold increase in ROS at 24 h exposure, which was not sustained at 48 h, for which the ROS levels, although still slightly elevated, approached those of controls. Exposure to H_2O_2 for 24 h caused an increase in ROS generation similar to that observed for AgNPs, which was further enhanced at 48 h.

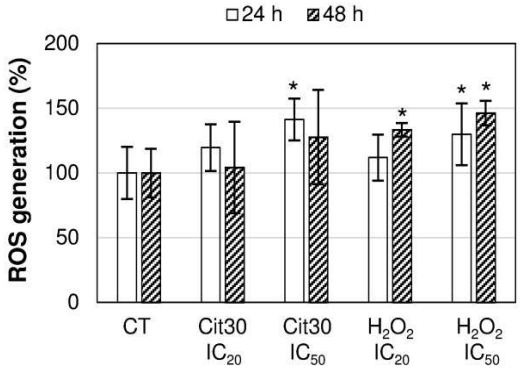

Figure 4.4. Intracellular generation of reactive oxygen species (ROS), at 24 and 48 h exposure to Cit30 AgNPs or H_2O_2. The data are expressed as mean ± standard deviation of three independent assays with three replicates each (n 9). Statistically significant ($p < 0.05$) differences relatively to controls are indicated by *.

4.5. Metabolic variations induced by AgNPs in HaCaT cells

In order to assess the impact of AgNPs on cell metabolism, HaCaT cells were exposed to the six nanoparticle types described above (Table 4.1), at two concentration levels, and their metabolic profiles compared to those of control cells. The dose-response

behaviour of Cit30 (Figure 4.2b) was taken as reference to select the two concentrations used for all nanoparticles: a lower value of 10 μg/mL, corresponding to a small reduction in cell viability (~15-20%), and a higher value of 40 μg/mL, which was the estimated IC_{50} concentration at 24 h. Cell viability data for the other nanoparticles at these concentrations, calculated from the dose-response curves shown above, is summarised in Table S4.1. Three sets of spectra – culture medium supernatants, polar cell extracts, and lipophilic cell extracts – were then subjected to multivariate analysis and spectral integration, to reveal the metabolic changes induced by each type of AgNPs.

Analysis of the culture medium enabled the assessment of the metabolic activity of cells. The main cell-mediated extracellular changes upon exposure to AgNPs are summarised in Figure 4.5a. Glucose consumption and lactate excretion, reflective of glycolytic activity, were not greatly different between control and exposed cells. On the other hand, the excretion of pyruvate generally decreased (although less markedly for Cit60), while that of citrate increased in a few cases. Furthermore, HaCaT cells exposed to AgNPs generally intensified the consumption of glutamine and significantly increased the excretion of glutamate. Other metabolites with altered extracellular levels included formate, acetate and allantoin (Figure 4.5a and Supplementary Table S4.2).

Additionally, it has been verified whether the quantitative variations in the culture medium could be due to direct interactions with AgNPs or Ag^+, since compounds like some amino acids have been reported to form complexes with both silver forms (Blaske *et al.*, 2013; Shi *et al.*, 2014). However, no significant differences in the spectra of acellular media with or without AgNPs/Ag^+ were found, apart from an increase in citrate in the medium incubated with citrate-coated AgNPs. Still, this increase had lower magnitude than upon cellular incubation, thus indicating that at least part of the citrate released in the presence of AgNPs arose from cell metabolism rather than from the nanoparticles surface.

The polar cell extracts, which contained tens of small hydrophilic metabolites (as described in Chapter 3), showed marked changes in their composition upon exposure to all nanoparticle types. Indeed, the PCA scores scatter plots (Figure 4.6, left) showed reasonable separation between control and exposed samples, and PLS-DA discriminated these two groups with high predictive power ($Q^2 \geq 0.7$), producing scores plots with a clear separation along LV1 (Figure 4.6, centre). The robustness of such discrimination was

confirmed through Monte Carlo cross validation (MCCV) and permutation testing (results shown in Figure S4.4).

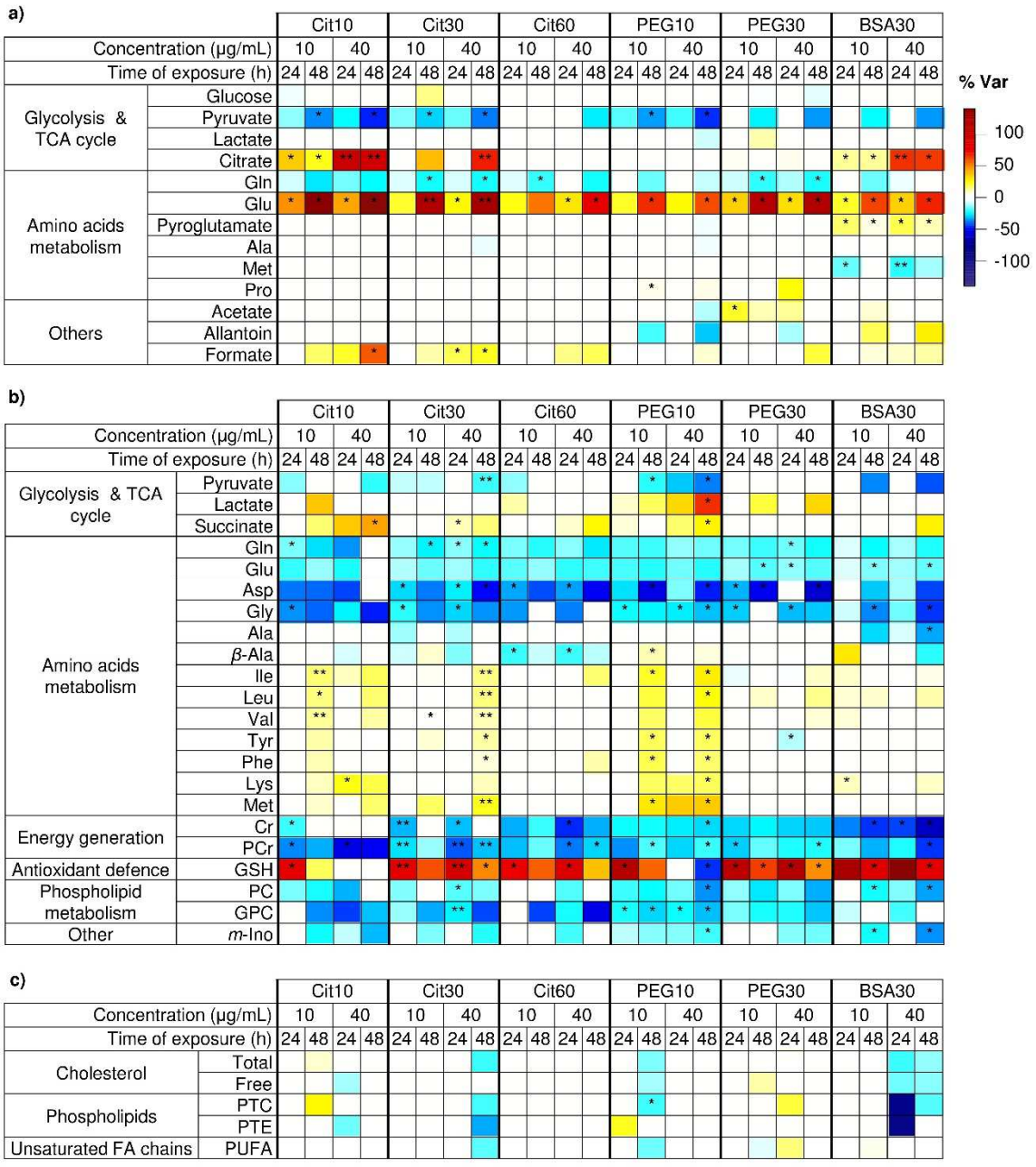

Figure 4.5. Heatmap of the main metabolite variations in a) culture media, b) polar extracts, and c) lipophilic extracts, from HaCaT cells exposed to different AgNP types (at 10 and 40 µg/mL), coloured according to % variation in relation to controls. * Uncorrected *p*-value < 0.05; ** FDR-corrected *p*-value < 0.05. Three letter code used for amino acids; Cr, creatine; PCr, phosphocreatine; GSH, reduced glutathione; PC, phosphocholine; GPC, glycerophosphocholine; *m*-Ino, *myo*-inositol; PTC, phosphatidylcholine; PTE, phosphatidylethanolamine; FA, fatty acyl; PUFA, polyunsaturated fatty acyl chains.

Inspection of PLS-DA loadings (Figure 4.6, right), which qualitatively show the leading metabolites responsible for sample discrimination, provided immediate assessment of the main similarities and differences between the metabolic effects produced by the six nanoparticle types. For instance, GSH showed intensely coloured negative loadings for the models pertaining to 30 and 60 nm AgNPs (suggesting increased levels in exposed cells), while it was not highlighted as an important variation in cells exposed to 10 nm AgNPs. Lactate, on the other hand, appeared to be increased mainly in cells exposed to 10 nm nanoparticles. Furthermore, several metabolites apparently decreased in exposed cells (positive loadings), such as (phospho)creatine and choline compounds, showed different relative importance among the various nanoparticles.

The magnitude and significance of differences in individual metabolites, at each nanoparticle concentration and exposure time (compared to controls) were then assessed through spectral integration to enable a more detailed analysis of metabolic variations. The results were summarised in a heatmap colour-coded as a function of % variation in relation to controls (Figure 4.5b and Supplementary Table S4.3). Only the metabolites with an absolute effect size greater than 0.8, accepted as representative of a large effect (Berben *et al.*, 2012), were included. The intracellular levels of pyruvate, lactate and succinate, involved in glycolysis and the tricarboxylic acid (TCA) cycle, were affected upon exposure to most AgNPs: pyruvate decreased (except in cells exposed to PEG30, where it did not vary); lactate increased, especially in cells exposed to PEG10 (showing no variation with exposure to Cit30 or BSA30); and succinate increased, except in PEG30-exposed cells (no change). Several amino acids varied significantly upon exposure to AgNPs: glutamine, glutamate and aspartate were generally decreased, except in cells exposed for 48 h to the high concentration of Cit10 (no change); glycine was also consistently decreased while alanine decreased to a lesser extent (only with Cit30 and BSA30); *β*-alanine had a variable behaviour; lysine, methionine, aromatic and branched chain amino acids generally increased, although less markedly in cells exposed to some nanoparticles (Cit60, PEG30 and BSA30). Furthermore, the energy-related amino acid derivatives creatine and phosphocreatine decreased consistently in most exposed cells; only Cit10 were seen to cause a less marked decrease in creatine. Another prominent variation regarded the levels of GSH: this antioxidant molecule was generally increased, except in cells exposed to the high dose of the 10 nm nanoparticles, where it showed no variation (with Cit10) or a decrease (with PEG10). Choline-containing compounds were another family of metabolites affected by AgNP exposure, with phosphocholine and glycerophosphocholine generally

decreasing upon exposure to all nanoparticle types. Finally, decreasing trends in *myo*-inositol were also observed for all nanoparticles.

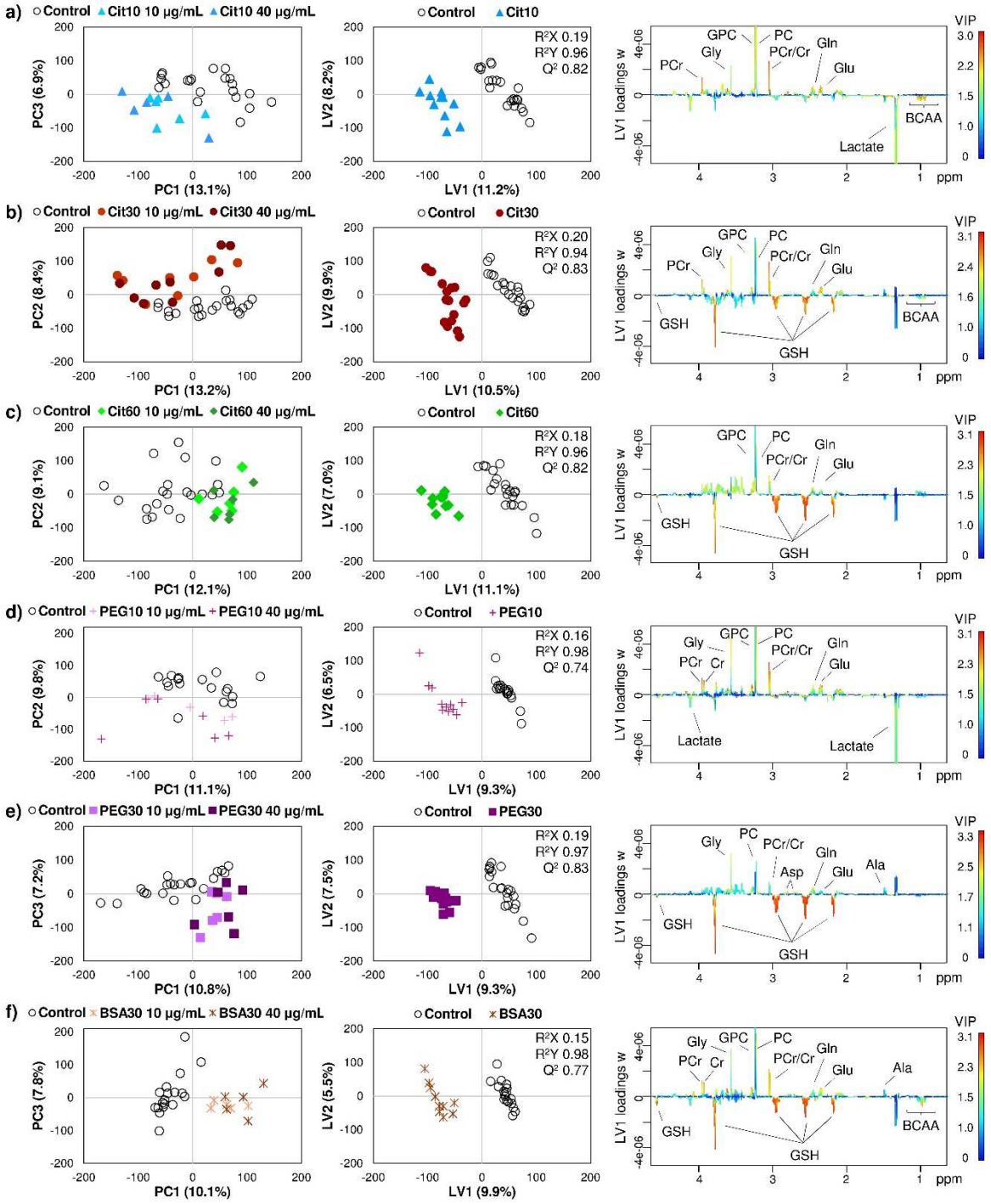

Figure 4.6. Multivariate analysis of ^{1}H NMR spectra from polar extracts of HaCaT control cells and cells exposed to different AgNP types, namely a) Cit10, b) Cit30, c) Cit60, d) PEG10, e) PEG30 and f) BSA30 AgNPs: PCA and PLS-DA scores scatter plots (left and centre, respectively) and LV1 loadings *w* (right), coloured as a function of variable importance to the projection (VIP). BCAA, branched chain amino acids; for other metabolite codes, *vide* legend of Figure 4.5.

The analysis of lipophilic cell extracts, composed mainly of membrane lipids (section 3.4 of Chapter 3), revealed a few, moderate changes upon exposure to AgNPs. Indeed, multivariate methods hardly distinguished control from exposed cells based on their lipid profile, resulting in poorly validated PLS-DA models (Figures S4.5 and S4.6). Accordingly, most lipid signals assessed through spectral integration (cholesterol, fatty acyl chains and phospholipids) showed slight variations (Figure 4.5c and Supplementary Table S4.4). The most noticeable changes were the decreases in phosphatidylcholine and in phosphatidylethanolamine caused by BSA30 AgNPs.

4.6. Metabolic variations induced by the coating substances alone

In parallel with the assessment of AgNPs effects, the coating substances alone (citrate, PEG(-SH) and BSA) were also evaluated for their ability to affect the cellular metabolome, at concentrations approximately matching those estimated to be present in coated AgNPs suspensions added to cells. The results revealed that the HaCaT profile was not greatly affected by the presence of the coating substances alone. The high concentration of citrate caused small (< 10%) decreases in intracellular glutamate and pyruvate and no changes in the medium composition (besides the expected increase in citrate levels). PEG(-SH) did not cause any significant intracellular changes and the only variations seen in the medium were decreases in the aromatic amino acids phenylalanine and tryptophan, possibly reflecting the direct interaction between the free polymer and these compounds. BSA induced a less than 10% decrease in intracellular glycerophosphocholine and no variation in the medium. It should also be noted that although statistically significant ($p < 0.05$), the intracellular variations just mentioned were clearly less marked than those observed for the same metabolites in the presence of AgNPs (all above 10%).

4.7. Metabolic variations induced by Ag^+ in HaCaT cells

The metabolic effects of extracellular Ag^+, administered as $AgNO_3$, at IC_{20} and IC_{50} concentrations, to match the viability of cells resulting from exposure to Cit30 AgNPs, were assessed. The extracellular metabolome of cells exposed to Ag^+ presented a few differences in comparison to control cells (Figure 4.7a and Supplementary Table S4.5). Cells exposed to Ag^+ excreted less lactate in relation to controls and appeared to consume citrate from the medium (whereas citrate was released by cells exposed to AgNPs).

Glutamine consumption and glutamate excretion were increased, although to a lesser extent than seen for AgNPs. Another difference was seen for extracellular allantoin, which showed opposite variations upon exposure to the IC_{20} and IC_{50} concentrations of Ag^+.

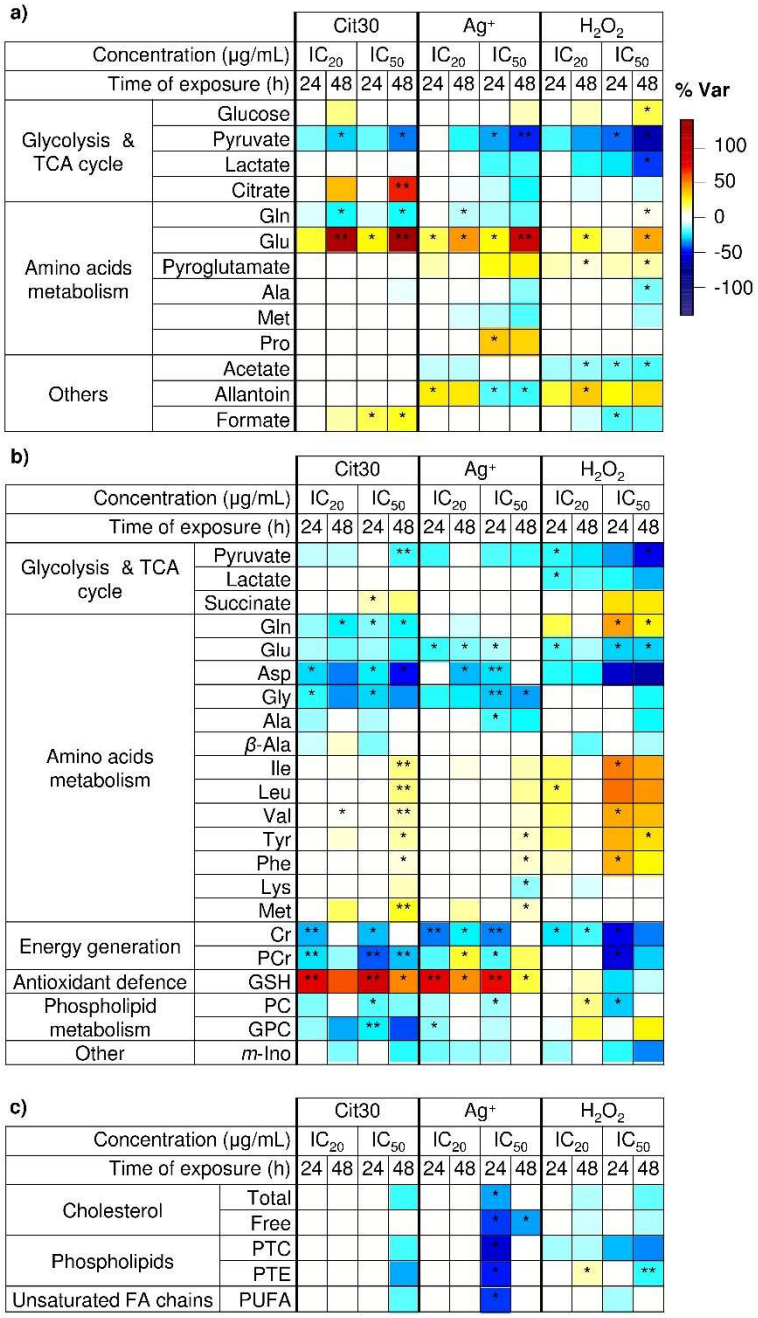

Figure 4.7. Heatmap of the main metabolite variations in a) culture media, b) polar extracts, and c) lipophilic extracts, from HaCaT cells exposed to Cit30, Ag^+, and H_2O_2, at the IC_{20} and IC_{50}, coloured according to % variation in relation to controls. * Uncorrected *p*-value < 0.05; ** FDR-corrected *p*-value < 0.05. Three letter code used for amino acids; Cr, creatine; PCr, phosphocreatine; GSH, reduced glutathione; PC, phosphocholine; GPC, glycerophosphocholine; *m*-Ino, *myo*-inositol; PTC, phosphatidylcholine; PTE, phosphatidylethanolamine; FA, fatty acyl; PUFA, polyunsaturated fatty acyl chains.

Regarding the polar intracellular profiles, HaCaT cells exposed to Ag^+ showed several differences relatively to control cells, allowing for the two sample classes to be clearly discriminated through multivariate analysis. The respective PLS-DA scores and loadings are shown in Figure 4.8. The main discriminant features (higher VIP) were in fact common to some of those identified for the nanoparticles: GSH (increased in cells exposed to Ag^+), glycine, creatine and phosphocholine (decreased in cells exposed to Ag^+). A more thorough comparison between Ag^+ and Cit30 AgNPs was then performed based on signal integrals, as summarised in the heatmap shown in Figure 4.7b (numerical values in Supplementary Table S4.6). The intracellular metabolic signature of Ag^+ was remarkably similar to that of AgNPs; still, a few differences were noted. Succinate, which increased in cells exposed to the high concentration of Cit30, did not vary with Ag^+. In regard to amino acids, the main differences were in glutamine (lesser intracellular decrease upon exposure to Ag^+) and lysine (decreased levels in Ag^+-exposed cells). Moreover, while phosphocreatine consistently decreased with AgNPs exposure, incubation with Ag^+ caused a decrease in this metabolite only at 24 h, increasing thereafter at 48 h.

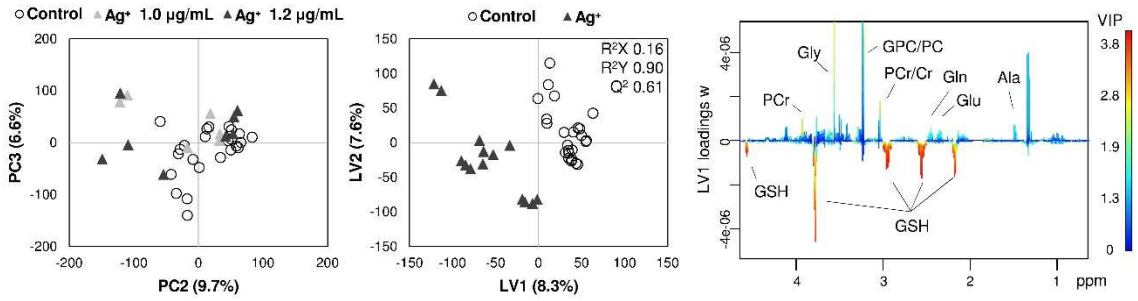

Figure 4.8. Multivariate analysis of ^{1}H NMR spectra from polar extracts of HaCaT control cells and cells exposed to Ag^+: PCA and PLS-DA scores scatter plots (left and centre, respectively) and LV1 loadings *w* (right), coloured as a function of variable importance to the projection (VIP). PLS-DA was validated by Monte-Carlo cross validation (MCCV), resulting in true models with median Q^2 0.65 and classification rate 93.4%; permuted models resulted in median Q^2 -0.15 and classification rate 54.8%. For metabolite codes, *vide* legend of Figure 4.7.

Analysis of the lipophilic fractions revealed that only the higher Ag^+ concentration induced marked changes in the levels of lipids (Figure 4.7c and Supplementary Table S4.7). In particular, cholesterol, phosphatidylcholine, phosphatidylethanolamine and polyunsaturated fatty acyl chains were significantly decreased in cells exposed to the IC_{50} concentration of Ag^+ for 24 h.

4.8. Metabolic variations induced by H_2O_2 in HaCaT cells

The changes in the exometabolome of H_2O_2-exposed cells are summarised in Figure 4.7a and Supplementary Table S4.5 (columns on the right). There was a trend for decreased glucose consumption and lactate excretion, already suggested for Ag^+, but much clearer with H_2O_2, especially at the 48 h exposure to the IC_{50} concentration. The excretion of pyruvate was also decreased, in a concentration and time-dependent way, similarly to the effect induced by AgNPs/Ag^+. A major difference regarded the use of glutamine by cells exposed to H_2O_2: the extracellular levels of this amino acid either remained unchanged (at the IC_{20}) or increased (at the IC_{50}), indicating that, unlike AgNPs or Ag^+, H_2O_2 did not induce higher glutamine consumption. On the other hand, glutamate excretion did increase, but at a lesser magnitude than for AgNPs or Ag^+. Additionally, H_2O_2 caused cells to excrete less acetate and formate, and to release allantoin.

Analysis of polar extracts from cells exposed to H_2O_2 allowed several intracellular metabolic effects to be highlighted and compared to those of AgNPs and Ag^+. The discrimination of H_2O_2-exposed cells from controls was not as robust as for AgNPs or Ag^+, as it was apparent from the corresponding PLS-DA scores plot (Figure 4.9, left) and the lower Q^2 value (0.35). This was mainly due to the lesser impact of the low H_2O_2 concentration, since, when only high concentration samples were included in the PLS-DA model (not shown), the respective Q^2 improved to 0.7. The loadings explaining sample discrimination due to H_2O_2 exposure (Figure 4.9, right) highlighted as main variations: increases in branched chain amino acids, glutamine and methionine, together with decreases in lactate, glutamate, aspartate, creatine and *myo*-inositol. These and other variations were confirmed through spectral integration (results summarised in Figure 4.7b and Supplementary Table S4.6).

Comparing the effects of H_2O_2 and AgNPs/Ag^+, a clear difference was seen for intracellular lactate, which decreased upon exposure to H_2O_2, contrarily to the observation made for some AgNPs. Other striking differences regarded glutamine, increased in H_2O_2-exposed cells, and GSH, which was unaltered or slightly elevated in cells exposed to the IC_{20} concentration of H_2O_2, but decreased in cells exposed to the IC_{50} concentration, especially at 24 h. Furthermore, phosphocholine and glycerophosphocholine also showed distinct variations with H_2O_2, by increasing their levels at 48h.

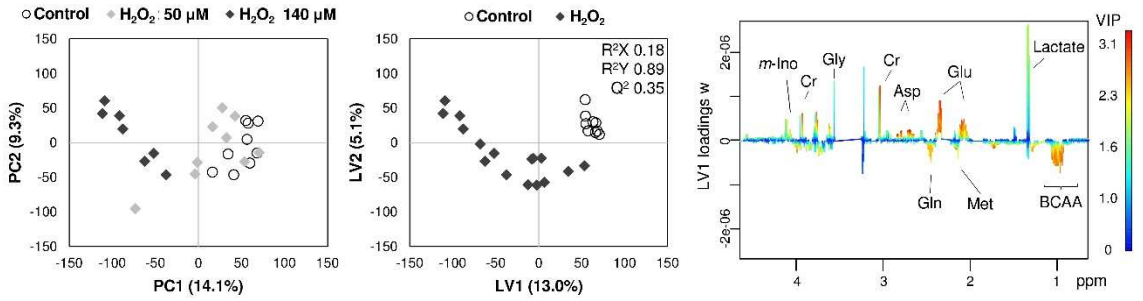

Figure 4.9. Multivariate analysis of ^{1}H NMR spectra from polar extracts of HaCaT control cells and cells exposed to H_2O_2: PCA and PLS-DA scores scatter plots (left and centre, respectively) and LV1 loadings *w* (right), coloured as a function of variable importance to the projection (VIP). For metabolite codes, *vide* legend of Figure 4.7.

Regarding the lipophilic fractions, H_2O_2 induced significant changes only in phosphatidylethanolamine, which increased upon exposure to the IC_{20} concentration and decreased when cells were exposed to the IC_{50} concentration (Figure 4.7c and Supplementary Table S4.7).

4.9. Discussion of metabolic variations in HaCaT cells

The integrated analysis of the changes presented in the above sections allowed the impact of AgNPs on major cellular metabolic pathways to be proposed and the influence of nanoparticles properties on those changes to be discussed. Figure 4.10 shows a schematic diagram of the putative effects on glycolysis and the TCA cycle. Glucose consumption and lactate excretion were not greatly affected in exposed cells, implying no major impact on glycolytic activity. Still, intracellular lactate was increased in a few cases, especially in cells exposed to the PEG-coated 10 nm nanoparticles, suggesting that lactic acid fermentation (converting glycolytic pyruvate into lactate) could be enhanced in these cells. Indeed, pyruvate levels (intracellular and extracellular) were decreased, similarly to the observation made by others in HaCaT cells exposed to TiO_2 nanoparticles (Tucci *et al.*, 2013). Furthermore, increases in citrate excretion and intracellular succinate may be indicative of an altered TCA cycle activity, whereas the strong intracellular decreases in some amino acids, namely glutamine, glutamate, aspartate and glycine, could mean that they were being used up by exposed cells to replenish TCA cycle intermediates. The increased use of glutamine was also corroborated by its increased consumption from the culture medium. When entering cells, glutamine is converted to glutamate, which can in turn be excreted as an effective way to get rid of cytosolic hydrogen (Mazurek, 2007); excretion of glutamate

was indeed observed after AgNP exposure. Furthermore, glutamate can feed the TCA cycle by conversion into α-ketoglutarate or aspartate (which in turn transforms into oxaloacetate). Hence, our results suggest that exposed cells generally increased glutaminolysis and other amino acid catabolic routes to help sustain the TCA cycle. As for other changes in amino acids metabolism, the increased intracellular levels of lysine, methionine, branched chain and aromatic amino acids (especially prominent in cells exposed to Cit10, Cit30 and PEG10) could be indicative of protein degradation. In fact, mobilisation of branched chain and/or aromatic amino acids from protein has also been suggested to be involved in the response of different cell types to gold nanorods (Zhang *et al.*, 2013) or silica nanoparticles (Feng *et al.*, 2013).

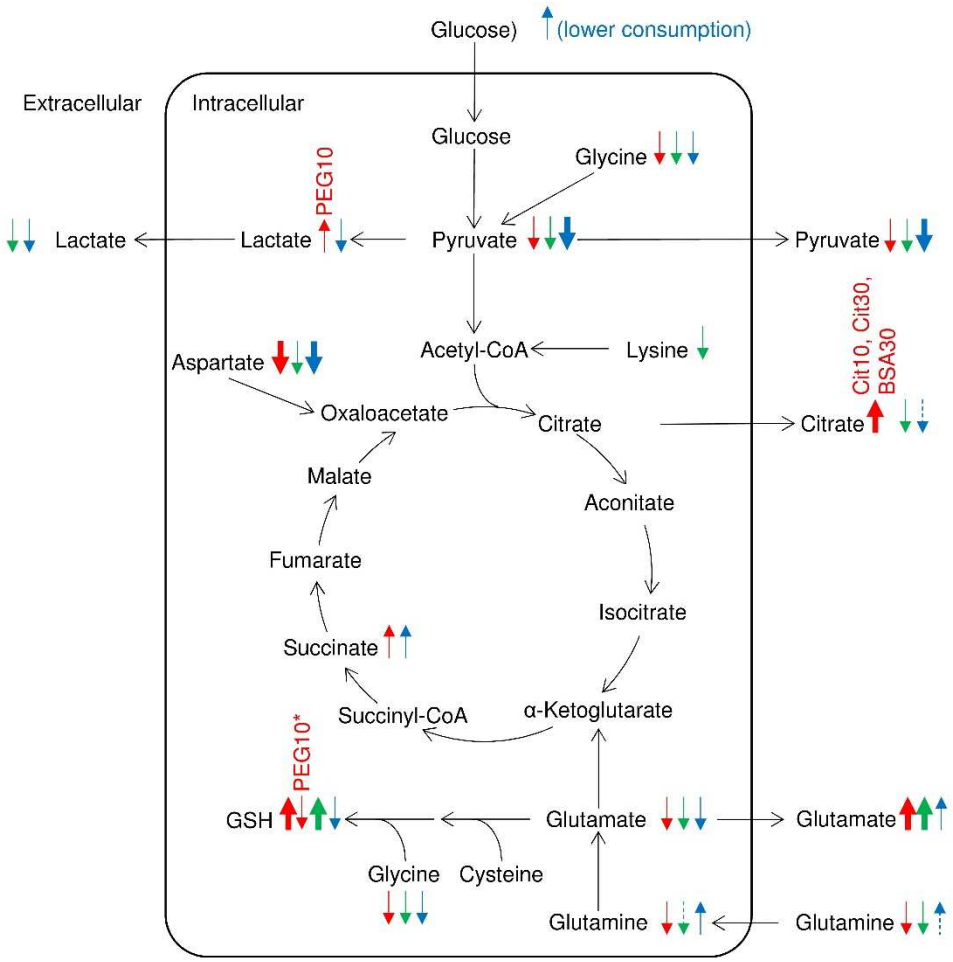

Figure 4.10. Schematic diagram of the putative effects of AgNPs (red arrows), Ag^{+} (green arrows), and H_2O_2 (blue arrows), on glycolysis and the TCA cycle of HaCaT cells. Dashed arrows indicate |% variation| < 10%; thick arrows indicate |% variation| > 50%; *40 μg/mL, at 48 h.

The intracellular levels of creatine and phosphocreatine were generally decreased in exposed cells (with Cit10 producing a lesser impact on creatine levels). These

metabolites are part of the so-called PCr/Cr-shuttle or circuit (Figure 4.11), which is used for temporal and spatial energy buffering (Schlattner *et al.*, 2006). Phosphocreatine is a reusable high energy phosphate reservoir, which can be broken down by the enzyme creatine kinase (CK) into creatine and inorganic phosphate, the latter being used to form ATP. As the phosphocreatine system is known to be particularly important in situations of high metabolic demand, when the rate of ATP use exceeds its generation by other metabolic pathways (Wallimann *et al.*, 1992), the observed decreases suggest that this system is activated upon exposure to AgNPs, possibly to cope with impaired energy production through the TCA cycle and oxidative phosphorylation.

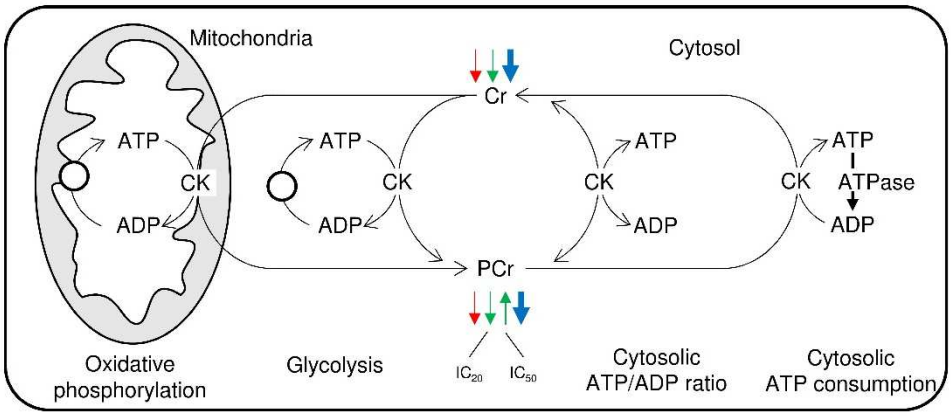

Figure 4.11. Schematic diagram of the creatine (Cr)/phosphocreatine (PCr) system and its association with ATP-producing processes (oxidative phosphorylation or glycolysis) and ATP-consuming processes (maintenance of ATP/ADP ratios). Arrows indicate effects caused by Cit30 (red arrows), Ag^{+} (green arrows), and H_2O_2 (blue arrows). CK: creatine kinase. Adapted from (Schlattner *et al.*, 2006).

Another noticeable change in the endometabolome of HaCaT cells regarded the levels of reduced glutathione (GSH). Four of the nanoparticles tested (sized 30 or 60 nm) induced higher GSH levels; as for the 10 nm nanoparticles, GSH was increased only upon exposure to the low concentration (10 µg/mL), showing no variation upon exposure to 40 µg/mL of Cit10, and decreased levels in cells exposed for 48 h to 40 µg/mL of PEG10. GSH is a sulfhydryl-containing tripeptide (γ-Glu-Cys-Gly) with a key role in the cell's defence system against oxidative stress, either by directly binding and reducing ROS or by serving as a cofactor for some antioxidant enzymes. Induction of oxidative stress, through excessive ROS accumulation, is regarded as a main mechanism by which AgNPs exert toxicity and cause different types of cellular injury, such as membrane lipid peroxidation, DNA damage and apoptosis (Kim and Ryu, 2013). Thus, the ability of cells to preserve the

GSH-mediated defence is critical for cellular redox homeostasis, GSH levels being an indication of such ability. Several studies have reported AgNPs exposure to cause GSH depletion in different cell types, including keratinocytes, and have interpreted this observation as arising from inhibition of GSH synthesising enzymes or increased conversion to the oxidised form (GSSG) (Kim and Ryu, 2013; Mukherjee *et al.*, 2012). On the other hand, GSH was shown to increase upon exposure of fibroblasts, liver and renal epithelial cells to AgNPs, suggesting the triggering of a protective mechanism for coping with nanoparticle-mediated oxidative stress (Arora *et al.*, 2009; Kang *et al.*, 2012). Accordingly, Kang *et al.* have demonstrated that exposure of human renal cells to AgNPs increased the expression of GSH synthesising enzymes and raised GSH levels, likely in relation to activation of Nrf2 transcription factor signalling, since in Nrf2 knockdown cells GSH levels did not increase, resulting in DNA damage and growth arrest (Kang *et al.*, 2012). Thus, the increase in GSH observed here upon exposure to most AgNPs could reflect the upregulation of GSH synthesis (also supported by decreases in precursor amino acids) to avoid oxidative damage. Another possibility is that GSH is being more intensely recycled from GSSG, using the reducing power of NADPH. As the major source of NADPH in animal cells is the pentose phosphate pathway (PPP) (Fujii *et al.*, 2011), assessment of fluxes through this pathway could be important to verify this hypothesis. In our group, this has been attempted by using the stable isotope tracer [2-^{13}C]glucose and quantifying the lactate isotopomers which result from glucose metabolism through glycolysis ([2-^{13}C]lactate) or the PPP ([3-^{13}C] and [1,3-^{13}C]lactate). The results (not shown) suggested that the contribution of PPP for total glucose expenditure was indeed significantly increased by approximately 25% in HaCaT cells exposed to Cit30 AgNPs at the IC_{20} concentration. Therefore, either if the increased GSH pool arises from upregulated *de novo* synthesis, intensified recycling, or both, it reflects the strong antioxidant capacity characterising skin keratinocytes (Mukherjee *et al.*, 2012; D'Errico *et al.*, 2007). On the other hand, the different GSH variations induced by Cit10 and PEG10 could mean that GSH was not as much synthesised/recycled or that it was more extensively used to neutralise ROS, leading to an overall depletion. Measurement of ROS levels upon exposure to the different types of nanoparticles, together with the assessment of enzymes involved in GSH synthesis and recycling, would be needed to test these hypotheses.

Other alterations in AgNPs-exposed cells comprised decreased levels of phosphocholine, glycerophosphocholine and *myo*-inositol. A similar variation in choline-containing compounds has also been reported in macrophages exposed to iron oxide nanoparticles and may be reflective of cell membrane modification and/or proliferation

arrest, as these metabolites are important constituents of membrane lipids (Feng *et al.*, 2010). The decrease in *myo*-inositol may also be related to phospholipid (namely phosphoinositides) turnover and/or reflect the role of this metabolite in osmoregulation and detoxification pathways, as suggested in several studies addressing the metabolic response of cultured cells to low molecular weight drugs (Knijn *et al.*, 2005; Triba *et al.*, 2010; Lamego *et al.*, 2014).

Taken together, metabolomics results have shown that HaCaT cells adapt their metabolism to cope with the presence of AgNPs, even at concentrations inducing minimal changes in cell viability. Hence, metabolic reprogramming seemed to be independent of AgNPs direct cytotoxic effects, corroborating previous findings (Chen *et al.*, 2014). Several metabolic variations were commonly seen across all the tested AgNPs; however, a few changes were more prominent or even exclusive for some of the nanoparticles, suggesting that their different size and coating (and respective aggregation and dissolution behaviours) influenced the cells metabolic responses. In particular, the 10 nm AgNPs showed the most distinct behaviour in terms of variations related to glycolysis and GSH metabolism.

The similarity of metabolic signatures found for Cit30 AgNPs and Ag^+ (Figure 4.7) indicates that ionic silver plays a major role in AgNPs toxicity. Still, a few differences could be noted; mainly, Ag^+ appeared to cause a lesser impact on the TCA cycle (citrate excretion and intracellular succinate not increased) and glutaminolysis (less expressive medium glutamine consumption and intracellular use); on the other hand, catabolic routes involving the use of extracellular citrate and intracellular lysine could be activated upon exposure to Ag^+. Another distinct variation regarded phosphocreatine levels, which increased in cells exposed to Ag^+ for 48 h, suggesting some recovery in energy metabolism, not seen with AgNPs. Additionally, Ag^+ elicited much stronger changes in cellular lipids, causing prominent decreases in cholesterol and membrane phospholipids.

Hydrogen peroxide is a nonradical ROS which is usually generated from any source of oxidative stress and can easily transform into more reactive oxygen radicals, leading to the propagation of cellular oxidative damage. In agreement with other studies (Alia *et al.*, 2005; Liu *et al.*, 2012a; Jiang *et al.*, 2014), there was an increase in intracellular ROS levels upon exposure to H_2O_2 (Figure 4.4). Interestingly, the magnitude of this increase was very similar to that driven by Cit30 AgNPs at concentrations inducing an equivalent decrease in cell viability, thus confirming the important role of ROS-mediated effects in AgNPs toxicity.

Nevertheless, when taking a closer look at metabolite variations, several differences were detected in the way H_2O_2 affected cell metabolism, compared to AgNPs (Figures 4.7). For instance, H_2O_2 appeared to inhibit glycolysis, based on lower glucose consumption and lactate production and excretion. This is consistent with other studies reporting reduced glycolytic flux in mammalian cells challenged with H_2O_2 (Brand *et al.*, 1999; Colussi *et al.*, 2000; Kuehne *et al.*, 2015). Another major difference regarded the variation of glutamine; with H_2O_2, cells did not appear to intensify glutaminolysis (as they did when exposed to AgNPs/Ag^+). Thus, the upregulation of this pathway is likely a ROS-independent effect. As for the variation in GSH, the effect of H_2O_2 was similar to that of PEG10 (but not the other nanoparticles): there was a decrease in GSH levels at the higher concentration of exposure, suggesting that GSH synthesis/recycling did not compensate its use. Finally, the cellular response to H_2O_2 also differed from AgNPs in the variation of choline-containing compounds (phosphocholine and glycerophosphocholine). As these metabolites are constituents of membrane phospholipids, it is possible that their decreased levels may be indicative of reduced cell proliferation and lower membrane turnover, whereas their increase, observed in cells exposed to H_2O_2 for 48 h, may reflect membrane degradation. A similar finding of increased choline levels was reported for mesenchymal stem cells exposed to H_2O_2 (Kim *et al.*, 2011b). Exposure to H_2O_2 further caused a more marked increase in the intracellular levels of branched chain and aromatic amino acids, suggesting more extensive protein degradation. Other effects, common to AgNPs, included the decreases in *myo*-inositol, creatine and phoshocreatine, agreeing with literature reports on the cellular responses to H_2O_2 (Brand *et al.*, 1999; Straadt *et al.*, 2010).

Overall, we can conclude that although the metabolic signatures of AgNPs, Ag^+ and H_2O_2 in HaCaT cells have several features in common, there are some important differences in the way these stimuli affect glucose and amino acid metabolism, oxidative balance and cell membranes.

Supplementary information to Chapter 4

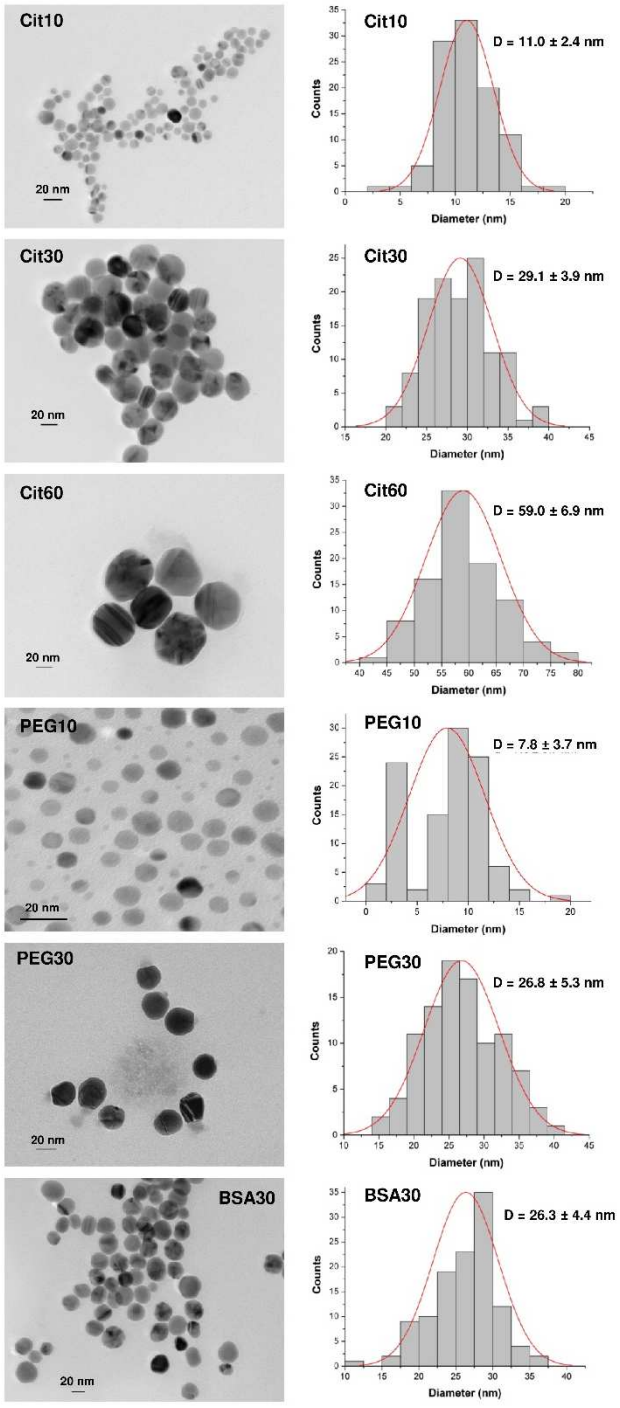

Figure S4.1. TEM images (left) and particle size histograms (right) of the AgNPs used in this work. Data acquired at CICECO (UA) by Dr A. L. Daniel-da-Silva and co-workers.

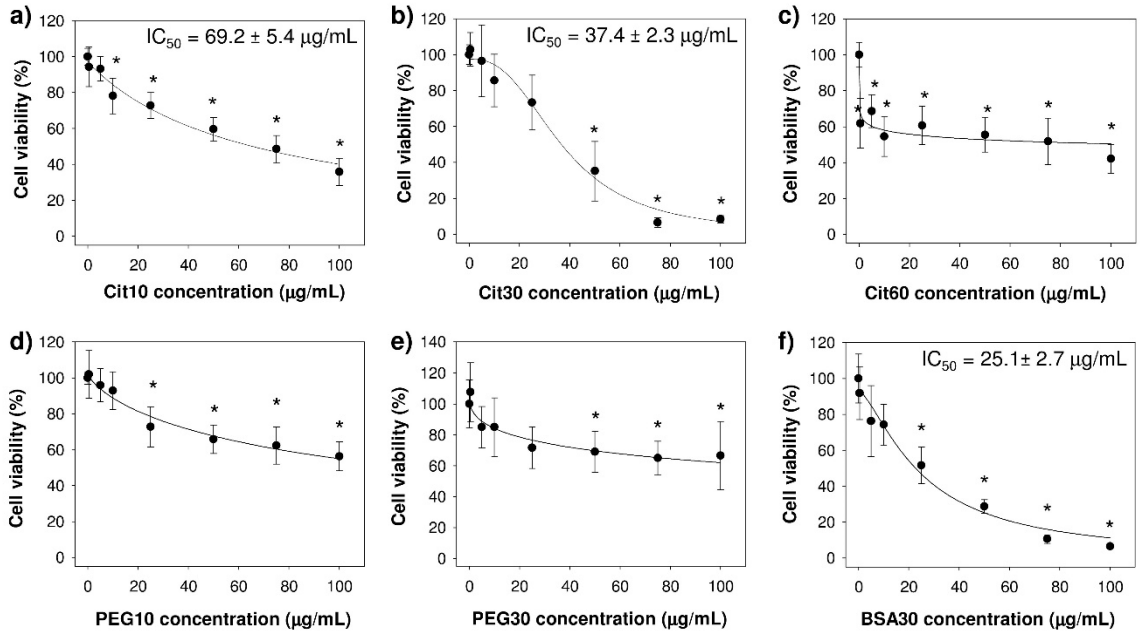

Figure S4.2. Viability (%) of HaCaT cells, measured by the MTT assay, after 48 h of exposure to AgNPs: a) Cit10, b) Cit30, c) Cit60, d) PEG10, e) PEG30 and f) BSA30. Data was acquired by project partners Verónica Bastos and Tiago Pedrosa (CESAM, UA), and is expressed as mean ± standard deviation of three independent assays with three replicates each (n 9). Calculated IC_{50} value shown only when it fell within the concentration range tested. Statistically significant ($p < 0.05$) differences relatively to controls are indicated by *.

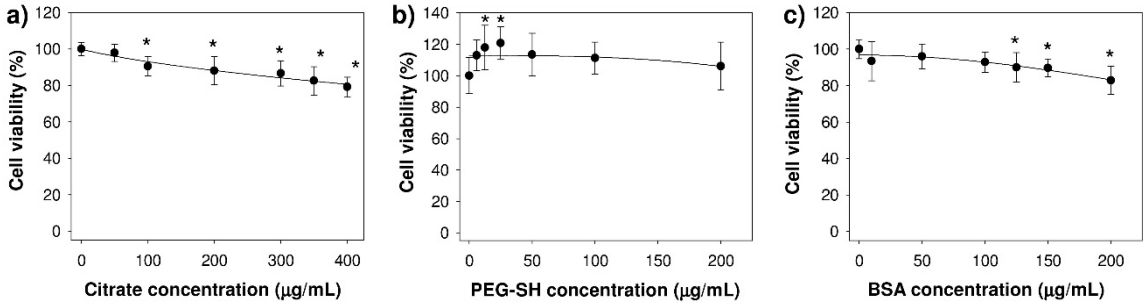

Figure S4.3. Viability (%) of HaCaT cells, measured by MTT assay, after 24 h of exposure to: a) citrate, b) PEG-SH and c) BSA. Data was acquired by project partners Verónica Bastos and Tiago Pedrosa (CESAM, UA), and is expressed as mean ± standard deviation of three independent assays with three replicates each (n 9). Statistically significant ($p < 0.05$) differences relatively to controls are indicated by *.

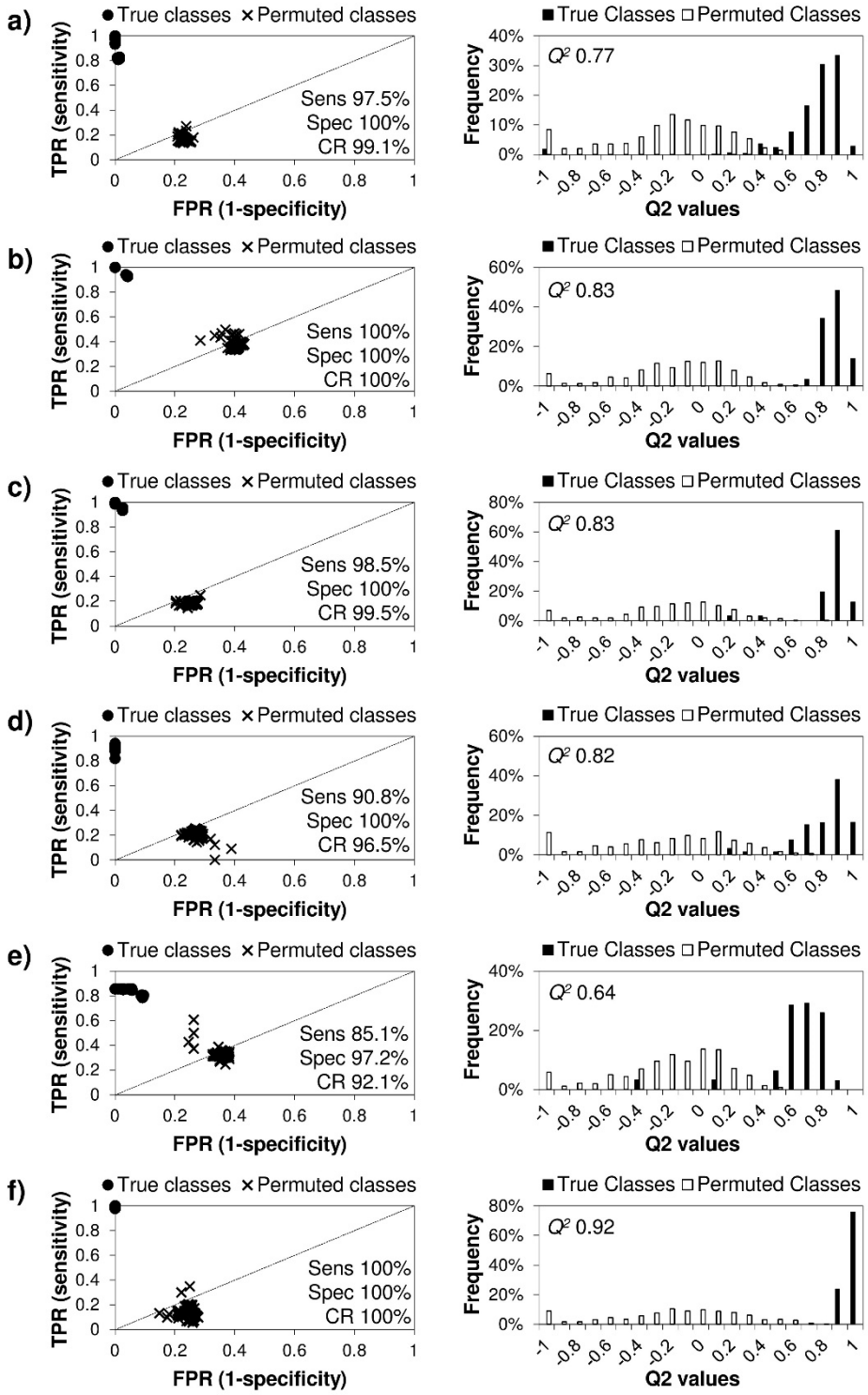

Figure S4.4. ROC space (left) and Q^2 histogram (right) obtained by MCCV and permutation testing of the PLS-DA models obtained for polar extracts' data from controls cells and cells exposed to: a) Cit10, b) Cit30, c) Cit60, d) PEG10, e) PEG30 and f) BSA30 AgNPs. TPR: true positive rate; FPR: false positive rate; Sens: sensitivity; Spec: specificity; CR: classification rate.

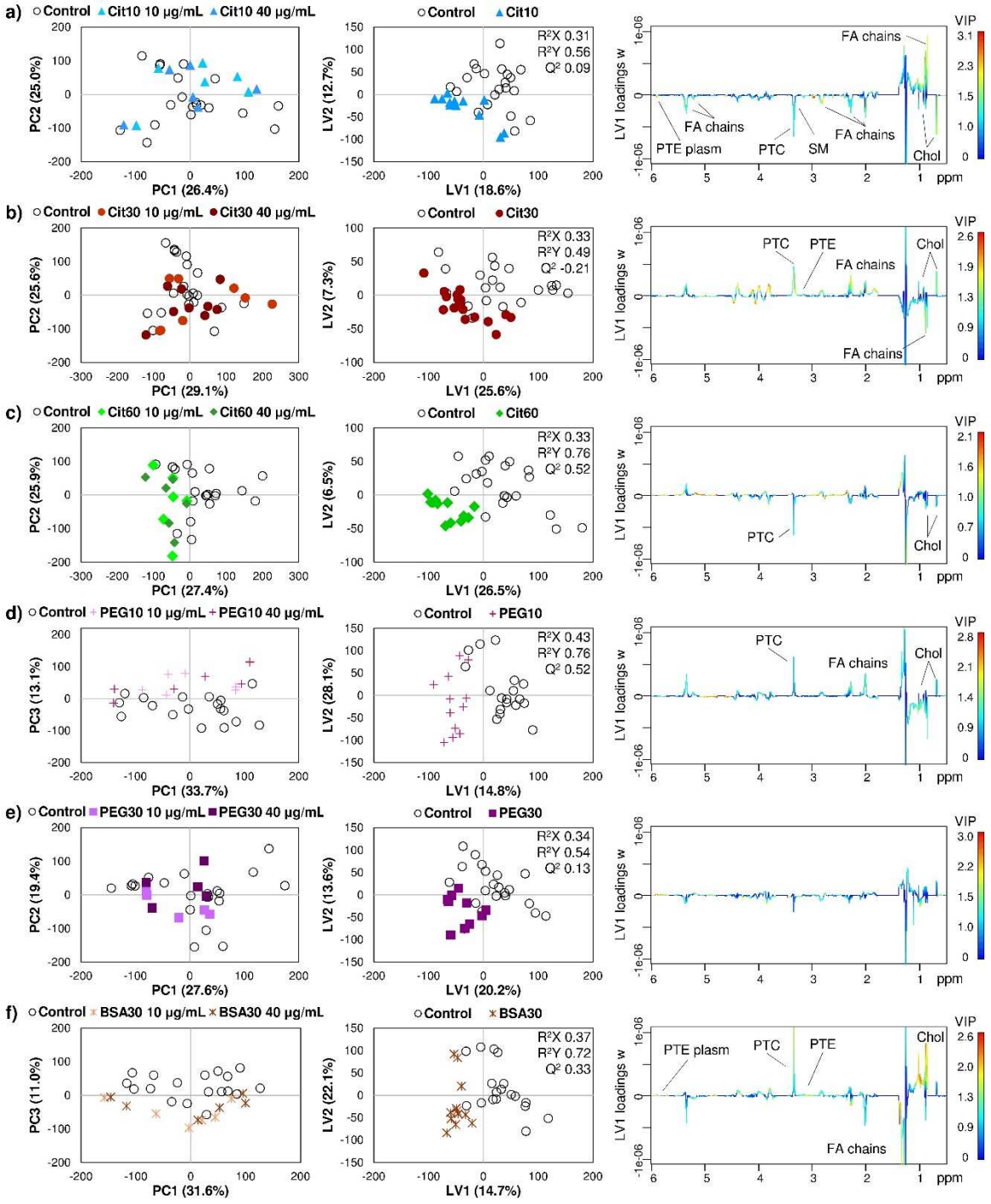

Figure S4.5. Multivariate analysis of ^{1}H NMR spectra from lipophilic extracts of control cells and cells exposed to different AgNP types, namely a) Cit10, b) Cit30, c) Cit60, d) PEG10, e) PEG30 and f) BSA30 AgNPs: PCA and PLS-DA scores scatter plots (left and centre, respectively) and LV1 loadings *w* (right), coloured as a function of variable importance to the projection (VIP).

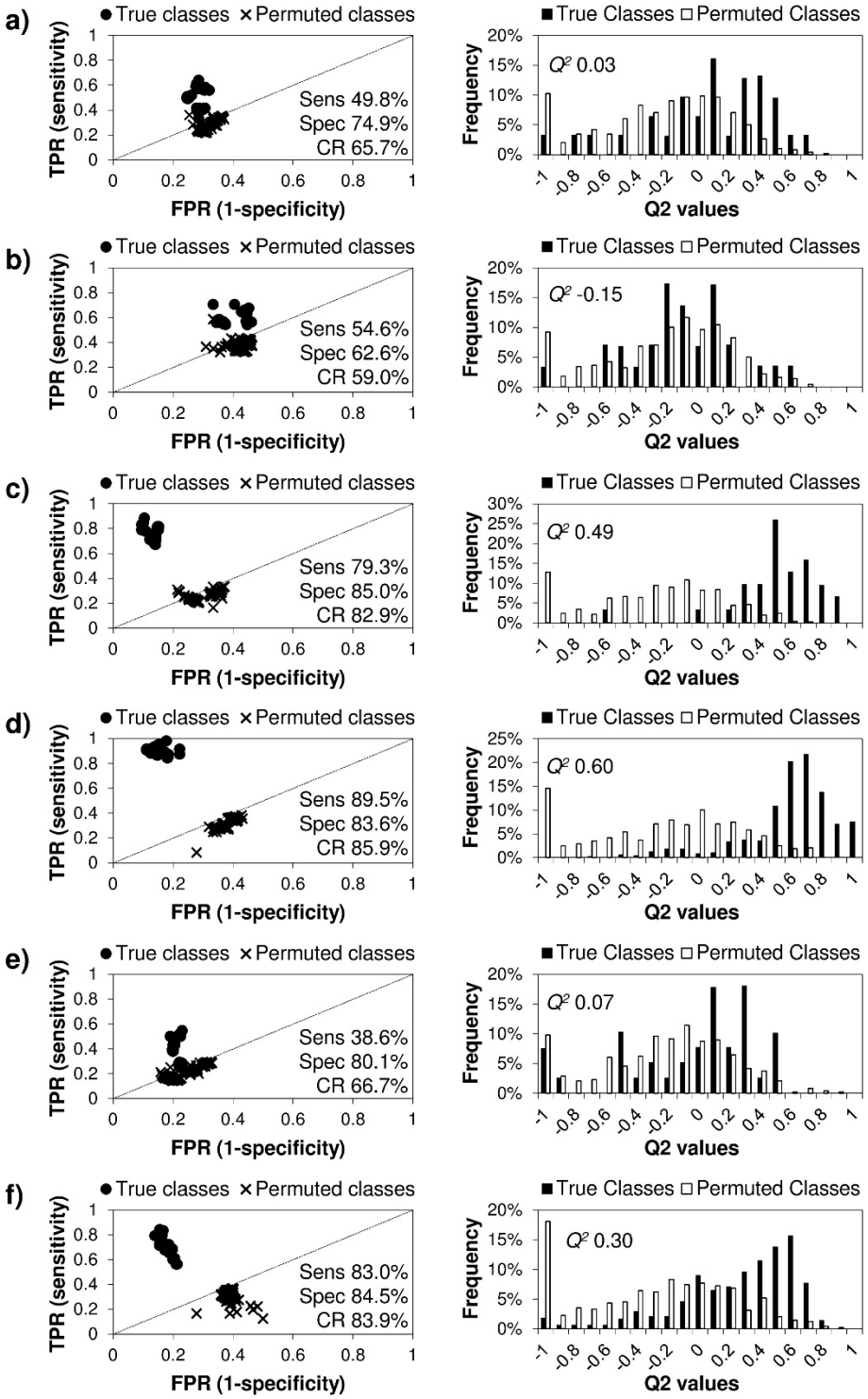

Figure S4.6. ROC space (left) and Q^2 histogram (right) obtained by MCCV and permutation testing of the PLS-DA models obtained for lipophilic extracts' data from controls cells and cells exposed to: a) Cit10, b) Cit30, c) Cit60, d) PEG10, e) PEG30 and f) BSA30 AgNPs. TPR: true positive rate; FPR: false positive rate; Sens: sensitivity; Spec: specificity; CR: classification rate.

Table S4.1. Viability (%) of HaCaT cells, after 24 or 48 h of exposure to 10 and 40 µg/mL of Cit10, Cit30, Cit60, PEG10, PEG30, and BSA30 AgNPs, estimated based on curve fitting of data measured by the MTT assay, by project partners Verónica Bastos and Tiago Pedrosa (CESAM, UA).

Concentration	10 µg/mL		40 µg/mL	
Time	24 h	48 h	24 h	48 h
Cit10	102.9%	84.4%	101.7%	61.3%
Cit30	89.7%	94.5%	48.0%	44.6%
Cit60	88.1%	58.1%	81.8%	53.5%
PEG10	91.6%	88.9%	83.7%	71.5%
PEG30	103.5%	84.2%	103.5%	72.0%
BSA30	90.9%	73.3%	46.6%	32.3%

Table S4.2. Main metabolite variations in culture media of HaCaT cells exposed to 10 and 40 µg/mL of Cit10, Cit30, Cit60, PEG10, PEG30, and BSA30 AgNPs, for 24 or 48 h, in relation to culture medium of control cells, expressed as % variation (%var) and respective error (±), effect size (ES), *p*-value (*p*), and FDR-adjusted (FDR) *p*-value. The variations with |ES| < 0.8 (or standard error > |ES|, or mean error > |% variation|) were considered null. Conc., concentration. PyroGlu, pyroglutamate: for other metabolite codes, *vide* legend of Figure 4.5.

		Cit10				Cit30				Cit60				PEG10				PEG30				BSA30			
Conc. (µg/mL)		10		40		10		40		10		40		10		40		10		40		10		40	
Time (h)		24	48	24	48	24	48	24	48	24	48	24	48	24	48	24	48	24	48	24	48	24	48	24	48
Glucose	%var	-5.97	0	0	0	0	14.26	0	0	0	0	0	0	0	0	0	0	-2.20	-5.15	-3.07	-6.96	0	0	0	0
	±	3.84					10.26											1.62	4.28	1.10	4.46				
	ES	-1.05	0	0	0	0	0.85	0	0	0	0	0	0	0	0	0	0	-1.22	-0.81	-2.49	-1.06	0	0	0	0
	p	0.2003					0.2999											0.3994	0.2869	0.2117	0.1856				
	FDR	0.9669					0.8341											0.7917	0.7505	0.4549	0.5172				
Pyruvate	%var	-13.64	-35.96	-24.64	-46.93	0	-28.89	0	-37.57	0	0	0	-26.13	-18.01	-34.28	-19.76	-45.24	0	-25.59	0	-34.85	0	-24.62	0	-34.73
	±	10.48	11.41	10.77	11.23		11.48		9.96				16.57	8.56	3.56	9.11	2.33		22.53		21.00		20.13		20.16
	ES	-0.91	-2.51	-1.71	-3.57	0	-1.92	0	-3.04	0	0	0	-1.18	-1.70	-7.21	-1.70	-14.31	0	-0.85	0	-1.31	0	-0.91	0	-1.36
	p	0.2359	0.0340	0.0597	0.0279		0.0462		0.0340				0.1506	0.1615	0.0013	0.1327	0.0167		0.2631		0.1252		0.2459		0.1273
	FDR	0.9669	0.4059	0.6644	0.1393		0.3694		0.2549				0.9934	0.9652	0.0508	0.9680	0.2222		0.7505		0.4552		0.5464		0.3624
Lactate	%var	0	0	0	0	0	0	0	0	0	0	0	0	0	0	0	-8.59	0	11.06	0	0	0	0	0	0
	±																4.37		8.16						
	ES	0	0	0	0	0	0	0	0	0	0	0	0	0	0	0	-1.17	0	0.84	0	0	0	0	0	0
	p																0.2505		0.2711						
	FDR																0.5378		0.7505						
Citrate	%var	35.77	22.97	100.41	94.98	0	39.35	47.40	69.67	0	0	0	0	0	0	0	0	5.50	3.15	5.92	0	12.99	13.00	65.92	64.39
	±	6.89	6.40	5.72	3.77		14.63	15.29	2.06									2.78	2.19	2.69		2.54	1.92	2.38	2.67
	ES	2.88	2.10	7.63	11.16	0	1.47	1.41	16.37	0	0	0	0	0	0	0	0	1.02	0.93	1.11	0	3.13	4.15	13.62	11.90
	p	0.0120	0.0345	0.0003	0.0001		0.1492	0.0789	4.6e-5									0.1772	0.2337	0.1636		0.0186	0.0063	4.1e-5	0.0013
	FDR	0.2392	0.4059	0.0123	0.0048		0.6514	0.7888	0.0018									0.7369	0.7505	0.4362		0.1060	0.1268	0.0016	0.0364
Gln	%var	-8.31	-26.89	-15.51	-24.93	-5.63	-23.59	-5.04	-23.30	-7.24	-20.88	0	-23.58	0	-16.42	0	-9.44	-8.78	-21.10	-10.98	-22.94	0	-16.36	-6.11	0
	±	6.19	13.62	13.40	12.88	3.22	5.18	3.65	4.70	4.98	6.95		9.58		7.15		6.14	6.86	3.77	5.07	5.93		12.28	4.89	
	ES	-0.92	-1.49	-0.82	-1.44	-1.01	-3.37	-0.84	-3.66	-0.99	-2.19	0	-1.82	0	-1.74	0	-0.92	-0.98	-4.09	-1.49	-2.86	0	-0.95	-0.84	0
	p	0.2336	0.0891	0.3142	0.0939	0.1476	0.0149	0.2186	0.0265	0.2196	0.0440		0.0505		0.1228		0.2883	0.3428	0.0187	0.1326	0.0133		0.2228	0.2727	
	FDR	0.9669	0.5093	0.7672	0.3509	0.9291	0.1989	0.8184	0.2549	0.9666	0.7501		0.4037		0.6942		0.5378	0.7917	0.2015	0.3790	0.1779		0.5464	0.5156	
Glu	%var	48.62	149.06	43.70	193.42	23.04	120.04	29.60	127.62	23.73	53.75	29.67	77.96	21.97	67.11	25.47	61.21	34.82	116.01	31.59	118.39	21.63	62.72	34.70	68.48
	±	6.51	15.79	3.92	10.00	6.38	4.59	4.96	3.87	8.56	21.45	7.24	18.22	8.81	6.42	8.52	4.97	2.14	12.54	2.19	11.37	5.09	6.30	6.22	6.98
	ES	3.92	3.53	5.98	6.42	2.07	10.67	3.06	13.16	1.62	1.29	2.33	2.01	1.42	4.36	1.68	5.38	7.50	3.82	6.78	4.27	2.51	4.95	3.11	4.77
	p	0.0063	0.0061	0.0042	0.0027	0.0234	0.0002	0.0045	0.0009	0.0694	0.1310	0.0244	0.0418	0.1326	0.0050	0.1001	0.0150	0.0029	0.0091	0.0033	0.0150	0.0460	0.0063	0.0335	0.0087
	FDR	0.2392	0.2455	0.0842	0.0539	0.9291	0.0066	0.0909	0.0172	0.9252	0.9489	0.4876	0.4037	0.9652	0.1002	0.9680	0.2222	0.1146	0.1812	0.1301	0.1779	0.1842	0.1268	0.1339	0.0868
PyroGlu	%var	0	0	0	0	0	0	0	0	0	0	0	0	0	-2.48	0	-5.64	0	0	0	0	16.56	6.70	18.68	10.35
	±														1.70		2.20					3.74	2.20	3.33	2.60
	ES	0	0	0	0	0	0	0	0	0	0	0	0	0	-1.15	0	-1.50	0	0	0	0	2.67	1.93	3.35	2.48
	p														0.3239		0.1192					0.0150	0.0424	0.0077	0.0244
	FDR														0.9951		0.5333					0.1060	0.4236	0.0557	0.1629

		Cit10				Cit30				Cit60				PEG10				PEG30				BSA30			
Conc. (µg/mL)		10		40		10		40		10		40		10		40		10		40		10		40	
Time (h)		24	48	24	48	24	48	24	48	24	48	24	48	24	48	24	48	24	48	24	48	24	48	24	48
Ala	%var	0	0	0	0	-5.46	0	-4.27	-6.40	0	0	0	0	0	0	0	-5.91	0	0	0	0	0	0	0	0
	±					2.81		2.94	4.47								2.63								
	ES	0	0	0	0	-1.09	0	-0.83	-0.97	0	0	0	0	0	0	0	-1.32	0	0	0	0	0	0	0	0
	p					0.1347		0.2163	0.2143								0.1648								
	FDR					0.9291		0.8184	0.6195								0.5333								
Met	%var	0	0	0	0	0	0	0	0	0	0	0	0	0	0	0	-1.44	0	0	0	0	-16.77	0	-21.53	-11.76
	±																0.61					2.86		1.85	6.15
	ES	0	0	0	0	0	0	0	0	0	0	0	0	0	0	0	-1.37	0	0	0	0	-4.18	0	-8.54	-1.33
	p																0.1866					0.0053		0.0006	0.1334
	FDR																0.5333					0.1060		0.0114	0.3624
Pro	%var	0	0	0	0	0	0	0	0	0	0	0	0	0	6.37	0	6.42	0	-4.09	24.93	0	0	2.80	0	0
	±														1.66		3.13		3.39	14.06			1.88		
	ES	0	0	0	0	0	0	0	0	0	0	0	0	0	2.42	0	1.13	0	-0.80	0.83	0	0	0.96	0	0
	p	0	0	0	0	0	0	0	0	0	0	0	0	0	0.0498		0.2405		0.2879	0.2474			0.2154		
	FDR														0.4953		0.5378		0.7505	0.4629			0.5464		
Acetate	%var	0	0	0	0	0	0	0	0	0	0	0	0	0	0	0	-10.52	21.80	10.53	13.25	0	0	8.31	0	0
	±	0	0	0	0	0	0	0	0	0	0	0	0	0			6.35	3.40	4.11	3.55			4.60		
	ES														0	0	-1.00	3.04	1.59	1.84	0	0	1.13	0	0
	p																0.2743	0.0268	0.0754	0.0658			0.1974		
	FDR																0.5378	0.5366	0.4308	0.3790			0.5464		
Formate	%var	0	16.81	21.72	58.77	6.65	11.24	20.58	22.44	0	0	14.21	18.14	0	0	0	8.38	0	0	0	20.20	0	7.45	8.89	11.86
	±		11.42	7.72	8.04	4.53	6.23	3.50	4.13			9.17	13.14				5.01				8.06		4.61	6.41	5.15
	ES	0	0.89	1.66	3.69	0.96	1.12	3.46	3.19	0	0	0.95	0.83	0	0	0	0.92	0	0	0	1.49	0	1.02	0.87	1.42
	p		0.2465	0.0664	0.0066	0.2344	0.1628	0.0039	0.0382			0.2224	0.2889				0.3543				0.0852		0.1981	0.2550	0.1071
	FDR		0.9011	0.6644	0.0879	0.9291	0.6514	0.0909	0.2549			0.9891	0.9934				0.5668				0.3407		0.5464	0.5156	0.3570
Allantoin	%var	0	0	0	0	0	0	0	0	0	0	0	0	0	-19.40	0	-30.00	0	0	-11.50	0	0	18.27	0	27.84
	±														16.54		19.30			7.36			9.22		9.30
	ES	0	0	0	0	0	0	0	0	0	0	0	0	0	-1.12	0	-1.04	0	0	-1.15	0	0	1.19	0	1.72
	p														0.3930		0.2393			0.2494			0.1799		0.0926
	FDR														0.9951		0.5378			0.4629			0.5464		0.3366

Table S4.3. Main metabolite variations in polar extracts of HaCaT cells exposed to 10 and 40 µg/mL of Cit10, Cit30, Cit60, PEG10, PEG30, and BSA30 AgNPs, for 24 or 48 h, in relation to controls, expressed as % variation (%var) and respective error (±), effect size (ES), *p*-value (*p*), and FDR-adjusted (FDR) *p*-value. The variations with |ES| < 0.8 (or standard error > |ES|, or mean error > |% variation|) were considered null. Conc., concentration. For metabolite codes, *vide* legend of Figure 4.5.

		Cit10				Cit30				Cit60				PEG10				PEG30				BSA30			
Conc. (µg/mL)		10		40		10		40		10		40		10		40		10		40		10		40	
Time (h)		24	48	24	48	24	48	24	48	24	48	24	48	24	48	24	48	24	48	24	48	24	48	24	48
Pyruvate	%var	-14.04	0	0	-21.34	-9.54	-9.66	0	-20.02	-13.53	0	0	0	0	-21.57	-29.81	-37.27	0	0	0	0	0	-36.53	0	-41.73
	±	8.45			16.23	6.00	4.52		3.14	10.23					4.57	7.57	8.55						22.62		21.65
	ES	-1.13	0	0	-0.96	-0.92	-1.53	0	-4.62	-0.93	0	0	0	0	-3.73	-3.74	-3.50	0	0	0	0	0	-1.58	0	-2.22
	p	0.1769			0.2343	0.1309	0.1549		0.0061	0.2329					0.0485	0.0809	0.0218						0.2203		0.2243
	FDR	0.5526			0.7029	0.3846	0.3932		0.0405	0.6987					0.1571	0.4888	0.0560						0.6234		0.4935
Lactate	%var	0	36.88	0	0	0	0	0	0	11.50	0	0	0	8.73	17.56	32.79	66.63	0	20.01	0	33.32	0	0	19.03	0
	±		18.81							7.08				8.68	15.81	11.19	11.95		15.34		20.55			8.16	
	ES	0	1.08	0	0	0	0	0	0	1.00	0	0	0	0.85	0.84	1.52	2.73	0	0.96	0	0.83	0	0	1.22	0
	p		0.1746							0.1998				0.5141	0.4583	0.0984	0.0335		0.4271		0.2741			0.2054	
	FDR		0.4265							0.6592				0.8984	0.5401	0.4888	0.0583		0.8010		0.5624			0.6721	
Succinate	%var	0	15.79	36.33	44.25	0	0	10.24	15.34	0	0	8.78	25.77	7.82	0	16.40	26.61	0	0	0	0	0	0	0	27.22
	±		10.06	8.58	10.95			4.03	9.84			2.78	14.22	5.64		4.09	6.18								12.71
	ES	0	0.95	2.05	2.16	0	0	1.25	0.95	0	0	1.98	1.24	0.85	0	3.07	2.48	0	0	0	0	0	0	0	1.10
	p		0.2224	0.1664	0.0315			0.0439	0.2213			0.0546	0.3130	0.2931		0.1464	0.0319								0.1646
	FDR		0.4265	0.6500	0.5968			0.1530	0.3652			0.2572	0.6899	0.8453		0.5127	0.0583								0.4177
Gln	%var	-15.39	-27.44	-35.58	0	-13.08	-25.65	-13.94	-24.46	-15.37	-21.94	-14.00	-26.71	-18.27	-20.09	-13.31	-16.07	-15.61	-20.03	-15.97	-23.50	-7.61	-24.63	-11.52	-22.52
	±	2.32	12.89	18.64		5.59	8.00	5.82	6.20	7.03	15.65	7.42	17.92	10.51	12.92	9.86	12.83	5.68	8.54	4.20	13.27	5.36	10.11	3.23	10.26
	ES	-3.79	-1.61	-1.33	0	-1.63	-2.25	-1.63	-2.94	-1.55	-1.35	-1.33	-1.30	-1.40	-1.14	-1.09	-0.89	-1.95	-1.95	-2.70	-1.20	-0.84	-2.02	-2.16	-1.75
	p	0.0162	0.0752	0.2588		0.0562	0.0450	0.0464	0.0286	0.0769	0.3289	0.1127	0.2439	0.2076	0.2234	0.3092	0.2488	0.0587	0.1407	0.0159	0.1313	0.3789	0.1131	0.1645	0.1257
	FDR	0.1356	0.3389	0.6857		0.2152	0.3702	0.1530	0.0857	0.3217	0.7814	0.3720	0.6899	0.8453	0.3352	0.6001	0.3306	0.3227	0.5732	0.1752	0.4751	0.6393	0.4051	0.6721	0.4148
Glu	%var	-20.67	-12.96	-23.12	0	-10.88	-16.39	-12.08	-21.08	-18.03	-13.17	-21.33	-19.91	-19.17	-21.78	-15.83	-22.05	-11.72	-18.31	-13.62	-18.19	-7.30	-14.81	-12.11	-16.98
	±	6.72	10.78	4.74		6.76	12.65	7.06	11.02	7.48	11.31	6.94	12.74	5.62	4.47	7.27	8.44	5.08	4.35	2.98	3.36	3.44	2.82	3.94	2.54
	ES	-1.81	-0.84	-3.15	0	-1.10	-0.83	-1.14	-1.40	-1.73	-1.10	-2.25	-1.38	-2.99	-4.30	-1.50	-1.92	-1.60	-3.13	-3.21	-5.37	-1.26	-3.02	-1.87	-3.93
	p	0.0701	0.3037	0.1066		0.1487	0.2611	0.1212	0.1354	0.0780	0.4182	0.0666	0.2698	0.1053	0.0821	0.1037	0.0917	0.1102	0.0320	0.0110	0.1019	0.2056	0.0223	0.0922	0.0119
	FDR	0.3751	0.4773	0.6500		0.3846	0.5386	0.3333	0.2642	0.3217	0.7814	0.2748	0.6899	0.7626	0.1935	0.4888	0.1441	0.4058	0.3516	0.1752	0.4460	0.6393	0.2310	0.6721	0.0842
Asp	%var	-38.18	-39.61	-43.18	0	-28.04	-37.87	-25.79	-49.62	-33.16	-42.29	-34.03	-50.97	-27.49	-54.72	-14.72	-47.33	-32.01	-52.19	0	-59.82	0	-29.98	-11.97	-43.22
	±	14.94	32.65	16.35		9.88	15.03	8.91	12.42	7.77	30.12	10.18	33.42	12.33	14.15	10.12	15.35	9.56	8.49		7.71		13.57	7.76	15.23
	ES	-1.71	-0.99	-1.93	0	-2.24	-1.95	-2.50	-3.47	-3.34	-1.49	-2.63	-1.67	-1.37	-2.67	-0.82	-2.64	-2.61	-5.63	0	-8.47	0	-1.89	-0.94	-2.66
	p	0.0796	0.2327	0.1828		0.0244	0.0797	0.0399	0.0128	0.0287	0.2609	0.0161	0.2018	0.1156	0.0226	0.2506	0.0253	0.0326	0.0046		0.0081		0.1228	0.2425	0.0646
	FDR	0.3751	0.4265	0.6500		0.2013	0.3702	0.1530	0.0543	0.2567	0.7814	0.1410	0.6899	0.7626	0.1487	0.6001	0.0560	0.3227	0.1502		0.2685		0.4051	0.6721	0.2368
Gly	%var	-35.38	-39.67	-25.53	-47.47	-21.77	-35.45	-28.29	-35.26	-34.71	0	-37.31	0.00	-23.79	-25.21	-26.21	-30.77	-29.36	0	-31.23	-29.93	-8.64	-36.54	-16.25	-44.81
	±	9.98	25.24	18.02	25.89	8.05	12.44	8.33	12.46	23.39		23.86	42.80	3.41	11.45	5.51	6.46	11.21		9.98	25.96	6.29	7.37	5.78	5.96
	ES	-2.61	-1.28	-0.93	-1.57	-2.15	-1.76	-2.86	-2.24	-1.17	0	-1.26	-0.86	-4.27	-1.84	-2.93	-3.68	-2.01	0	-2.42	-1.15	-0.82	-3.37	-1.75	-5.59
	p	0.0205	0.1739	0.3236	0.1344	0.0406	0.0636	0.0196	0.0726	0.1836		0.1621	0.4106	0.0103	0.1725	0.0268	0.0080	0.0456		0.0489	0.3646	0.2922	0.0154	0.1249	0.0034
	FDR	0.1356	0.4265	0.6857	0.5968	0.2152	0.3702	0.1077	0.1711	0.6592		0.4459	0.6899	0.1325	0.2845	0.3018	0.0560	0.3227		0.2380	0.6186	0.6393	0.2310	0.6721	0.0555

		Cit10				Cit30				Cit60				PEG10				PEG30				BSA30			
Conc. (µg/mL)		10		40		10		40		10		40		10		40		10		40		10		40	
Time (h)		24	48	24	48	24	48	24	48	24	48	24	48	24	48	24	48	24	48	24	48	24	48	24	48
	%var	0	0	0	0	-12.44	0	-10.90	0	0	0	0	0	0	0	0	0	0	0	0	0	0	-28.27	-7.69	-33.23
	±					7.87		7.41															13.96	4.00	10.73
Ala	ES	0	0	0	0	-1.09	0	-1.05	0	0	0	0	0	0	0	0	0	0	0	0	0	0	-1.28	-1.14	-2.06
	p					0.1515		0.1909															0.1216	0.2260	0.0440
	FDR					0.3846		0.4534															0.4051	0.6721	0.1815
	%var	0	0	-7.95	0	-8.59	8.48	-14.57	0	-20.53	-9.01	-20.05	-10.45	0	10.81	0	7.28	0	0	0	0	29.43	0	0	-21.47
	±			3.70		6.16	4.35	7.42		4.21	3.87	2.11	3.20		2.32		3.57					5.40			6.99
β-Ala	ES	0	0	-1.28	0	-0.95	0.98	-1.25	0	-3.55	-1.48	-6.88	-2.30	0	2.39	0	1.29	0	0	0	0	2.72	0	0	-3.05
	p			0.1822		0.2065	0.1902	0.0702		0.0271	0.0922	0.0028	0.0595		0.0314		0.1244					0.1317			0.1634
	FDR			0.6500		0.4867	0.4184	0.2106		0.2567	0.7814	0.0865	0.6899		0.1487		0.1784					0.6393			0.4177
	%var	0	15.87	9.69	17.85	0	5.70	0	14.44	0	0	0	16.03	0	21.89	0	27.80	-6.39	0	-5.05	9.09	8.92	0	0	6.60
	±		0.81	3.91	7.01		2.05		1.99				12.14		5.29		5.61	2.97		2.26	5.60	3.80			5.17
Ile	ES	0	11.80	1.35	1.53	0	1.69	0	4.41	0	0	0	0.80	0	2.06	0	2.84	-1.45	0	-1.50	1.07	1.28	0	0	0.92
	p		0.0003	0.1445	0.1418		0.0799		0.0025				0.3409		0.0406		0.0162	0.0958		0.0865	0.2653	0.2147			0.3757
	FDR		0.0092	0.6500	0.5968		0.3702		0.0322				0.6899		0.1487		0.0560	0.4058		0.2595	0.5624	0.6393			0.5928
	%var	0	14.87	0	16.05	0	4.48	0	15.08	0	0	0	0	0	19.95	0	24.42	0	8.99	0	13.70	8.24	8.71	0	11.10
	±		2.15		6.74		1.27		1.44						5.45		5.85		6.89		6.20	3.27	5.37		5.65
Leu	ES	0	4.21	0	1.44	0	1.85	0	6.35	0	0	0	0	0	1.84	0	2.43	0	0.82	0	1.43	1.38	1.36	0	1.46
	p		0.0032		0.1447		0.0555		0.0008						0.0524		0.0254		0.3264		0.1840	0.1580	0.3635		0.2697
	FDR		0.0388		0.5968		0.3702		0.0272						0.1571		0.0560		0.7694		0.5060	0.6393	0.7324		0.5236
	%var	0	12.96	0	11.78	0	5.04	0	10.61	0	0	0	0	0	17.06	0	20.14	0	0	-4.97	7.87	7.94	0	-1.60	0
	±		1.77		7.69		1.46		1.55						5.41		5.63			1.43	6.39	4.26		1.09	
Val	ES	0	4.48	0	0.94	0	2.05	0	4.24	0	0	0	0	0	1.52	0	2.12	0	0	-2.33	0.83	1.02	0	-0.85	0
	p		0.0035		0.2769		0.0455		0.0029						0.0975		0.0581			0.0600	0.3691	0.3163		0.2845	
	FDR		0.0388		0.7614		0.3702		0.0322						0.2092		0.0959			0.2380	0.6186	0.6393		0.6831	
	%var	0	11.60	0	0	0	8.15	0	11.68	0	0	0	0	0	17.64	0	17.43	0	0	-10.62	0	0	0	0	0
	±		4.62				2.15		2.40						2.79		4.41			3.25					
Tyr	ES	0	1.55	0	0	0	2.40	0	3.00	0	0	0	0	0	3.04	0	2.38	0	0	-2.25	0	0	0	0	0
	p		0.0822				0.0507		0.0132						0.0274		0.0239			0.0328					
	FDR		0.3389				0.3702		0.0543						0.1487		0.0560			0.2380					
	%var	0	10.62	0	0	0	3.07	0	7.52	0	0	0	11.19	0	18.51	0	16.15	0	0	-4.24	0	0	0	0	0
	±		3.68				2.19		1.75				8.59		2.75		2.95			2.70					
Phe	ES	0	1.79	0	0	0	1.09	0	2.71	0	0	0	0.84	0	3.94	0	3.30	0	0	-1.05	0	0	0	0	0
	p		0.0758				0.3537		0.0255				0.3438		0.0116		0.0076			0.1953					
	FDR		0.3389				0.6143		0.0857				0.6899		0.1487		0.0560			0.4717					
	%var	0	9.71	23.64	19.31	0	0	0	10.17	0	0	0	0	0	17.47	16.81	17.54	0	0	0	0	9.75	0	0	9.28
	±		5.36	3.64	9.75				5.76						7.02	7.32	4.27					0.65			4.36
Lys	ES	0	1.13	3.32	1.18	0	0	0	1.10	0	0	0	0	0	1.88	1.27	2.47	0	0	0	0	8.19	0	0	1.25
	p		0.2194	0.0312	0.2106				0.1851						0.2177	0.1323	0.0272					0.0376			0.1448
	FDR		0.4265	0.5146	0.7029				0.3214						0.3352	0.5127	0.0560					0.6393			0.4177

		Cit10				Cit30				Cit60				PEG10				PEG30				BSA30			
Conc. (µg/mL)		10			40	10			40	10			40	10			40	10			40	10			40
Time (h)		24	48	24	48	24	48	24	48	24	48	24	48	24	48	24	48	24	48	24	48	24	48	24	48
Met	%var	16.23	8.81	22.59	16.20	16.11	17.17	29.69	22.69	0	0	0	23.60	0	28.99	35.45	35.84	0	0	0	11.13	29.57	15.70	21.26	17.90
	±	8.17	5.76	8.54	7.20	8.75	5.65	7.44	2.63				10.61		6.59	18.08	5.05				3.11	9.41	6.57	10.36	6.73
	ES	1.22	0.96	1.36	1.36	0.91	2.16	1.90	5.07	0	0	0	1.21	0	2.44	1.21	3.93	0	0	0	2.81	1.56	1.90	1.06	1.97
	p	0.2008	0.2235	0.1419	0.1299	0.1323	0.1458	0.0109	0.0049				0.1550		0.0335	0.2822	0.0105				0.1584	0.1150	0.2645	0.2137	0.2160
	FDR	0.5526	0.4265	0.6500	0.5968	0.3846	0.3932	0.0897	0.0403				0.6899		0.1487	0.6001	0.0560				0.4751	0.6393	0.6234	0.6721	0.4935
Cr	%var	-20.01	0	0	0	-31.70	0	-31.02	0	-32.70	-20.41	-46.11	-32.37	-23.81	-23.74	-26.06	-28.04	-28.30	-25.23	-28.91	-29.97	-37.02	-45.15	-43.38	-62.34
	±	4.08				8.09		11.47		14.96	12.71	14.20	14.97	19.74	8.47	18.85	7.16	10.72	17.19	10.12	17.18	6.55	15.36	4.70	15.48
	ES	-3.35	0	0	0	-2.43	0	-1.61	0	-1.71	-1.28	-2.76	-1.77	-1.02	-2.03	-1.27	-2.98	-2.01	-1.42	-2.18	-1.85	-3.96	-2.67	-6.74	-4.83
	p	0.0121				0.0017		0.0153		0.0593	0.2132	0.0171	0.0978	0.3143	0.0722	0.2944	0.0131	0.0517	0.3012	0.0547	0.2703	0.0766	0.0446	0.0328	0.0433
	FDR	0.1356				0.0268		0.1007		0.3217	0.7814	0.1410	0.6899	0.8453	0.1935	0.6001	0.0560	0.3227	0.7694	0.2380	0.5624	0.6393	0.2452	0.6721	0.1815
PCr	%var	-36.61	-32.34	-54.67	-51.65	-27.25	-12.61	-41.19	-30.69	-31.04	-16.60	-37.63	-28.63	-35.77	-18.74	-28.75	-20.37	-29.37	-17.07	-22.74	-22.40	-15.16	-32.15	-22.41	-44.86
	±	6.19	23.43	6.65	27.09	5.83	5.58	5.42	5.99	11.52	6.91	13.52	8.32	14.45	4.78	13.83	5.10	10.65	6.26	11.03	5.66	11.55	12.94	12.19	10.81
	ES	-4.20	-1.08	-6.46	-1.68	-2.61	-1.37	-4.72	-3.96	-2.08	-1.59	-2.24	-2.40	-2.75	-2.25	-2.16	-2.91	-2.11	-1.88	-1.52	-3.05	-0.81	-1.70	-1.18	-3.35
	p	0.0060	0.2224	0.0200	0.0971	0.0024	0.0979	0.0001	0.0077	0.0594	0.0766	0.0319	0.0255	0.1866	0.0382	0.2259	0.0267	0.0410	0.0614	0.0844	0.0357	0.3613	0.0594	0.2444	0.0109
	FDR	0.1356	0.4265	0.5146	0.5968	0.0268	0.3702	0.0042	0.0423	0.3217	0.7814	0.1754	0.6899	0.8453	0.1487	0.6001	0.0560	0.3227	0.4050	0.2595	0.3808	0.6393	0.2801	0.6721	0.0842
GSH	%var	79.49	17.73	0	0	79.91	60.20	92.85	50.18	75.33	57.71	86.78	37.94	114.76	56.56	0	-45.28	109.83	63.71	118.17	49.33	124.62	84.23	168.32	80.51
	±	8.10	12.92			8.02	25.46	8.90	11.41	3.05	13.85	4.81	18.28	5.88	9.23		9.89	12.23	6.99	11.54	8.74	13.17	3.49	11.18	10.41
	ES	3.45	0.82	0	0	4.21	1.58	3.81	2.30	11.73	1.81	8.22	0.95	6.98	4.44	0	-3.87	3.79	3.41	4.20	2.25	3.33	13.45	4.67	2.78
	p	0.0187	0.2928			0.0010	0.2776	0.0003	0.0265	0.0017	0.0535	0.0052	0.1938	0.0016	0.1245		0.0264	0.0103	0.0207	0.0072	0.0472	0.0978	0.0280	0.0680	0.0224
	FDR	0.1356	0.4773			0.0268	0.5389	0.0042	0.0857	0.0568	0.7814	0.0865	0.6899	0.0524	0.2417		0.0560	0.3227	0.3421	0.1752	0.3808	0.6393	0.2310	0.6721	0.1234
PC	%var	-15.02	-23.25	-32.25	0	-14.66	0.00	-18.06	-14.90	0	0	-18.39	0	-20.11	-24.26	-15.79	-35.37	-13.38	-26.94	-14.71	-32.63	0	-23.50	-14.60	-33.61
	±	4.12	12.12	18.96		6.23		6.89	8.99			11.13		10.38	9.32	9.51	10.59	5.90	9.38	4.79	10.57		3.74	9.35	4.22
	ES	-3.21	-1.42	-1.16	0	-1.70	0.00	-1.81	-1.17	0	0	-1.19	0	-1.68	-1.86	-1.52	-2.65	-1.59	-2.50	-2.17	-2.61	0	-4.51	-0.96	-6.04
	p	0.1129	0.1285	0.2731		0.0576		0.0293	0.1644			0.1431		0.2050	0.0792	0.2895	0.0161	0.1107	0.0970	0.0503	0.0577		0.0066	0.3200	0.0024
	FDR	0.4193	0.4265	0.6857		0.2152		0.1380	0.3013			0.4294		0.8453	0.1935	0.6001	0.0560	0.4058	0.5336	0.2380	0.3808		0.2173	0.7040	0.0555
GPC	%var	0	-35.97	-44.15	-30.75	-12.91	-33.03	-25.32	-42.81	0	-43.52	-23.26	-54.69	-23.16	-28.48	-24.16	-30.88	-15.22	-23.02	-22.49	-30.21	-9.39	0	-19.69	0
	±		15.66	33.36	18.19	5.76	21.38	6.43	20.39		38.77	12.25	42.82	3.17	3.97	2.82	5.47	10.42	11.66	11.89	13.59	4.61		4.90	
	ES	0	-1.83	-0.97	-1.30	-1.44	-1.03	-2.71	-1.74	0	-1.35	-1.40	-1.67	-5.78	-4.98	-7.73	-4.36	-1.03	-1.63	-1.39	-1.79	-1.22	0	-2.55	0
	p		0.0568	0.2962	0.1166	0.0502	0.1732	0.0029	0.0987		0.3692	0.0982	0.3035	0.0120	0.0049	0.0274	0.0041	0.1893	0.1633	0.1009	0.0961	0.2784		0.1361	
	FDR		0.3389	0.6857	0.5968	0.2152	0.4083	0.0315	0.2172		0.7814	0.3601	0.6899	0.1325	0.1487	0.3018	0.0560	0.6246	0.5732	0.2776	0.4460	0.6393		0.6721	
m-Ino	%var	0	-23.97	-9.49	-31.56	0	-14.83	0	-21.96	0	0	-19.52	0	-9.99	-14.11	-14.16	-19.78	0	0	-14.41	-15.86	0	-23.68	0	-35.57
	±		13.97	6.44	14.05		6.28		6.92			16.95		6.07	3.82	6.51	1.65			12.39	14.11		7.42		8.16
	ES	0	-1.27	-0.88	-1.74	0	-1.30	0	-2.33	0	0	-0.83	0	-1.30	-3.02	-1.69	-8.71	0	0	-0.82	-0.97	0	-2.27	0	-3.36
	p		0.1532	0.3390	0.0937		0.1234		0.0522			0.2789		0.2562	0.1014	0.1554	0.0049			0.3074	0.3868		0.0363		0.0128
	FDR		0.4265	0.6857	0.5968		0.3702		0.1437			0.6575		0.8453	0.2092	0.5127	0.0560			0.6762	0.6186		0.2399		0.0842

Table S4.4. Main metabolite variations in lipophilic extracts of HaCaT cells exposed to 10 and 40 µg/mL of Cit10, Cit30, Cit60, PEG10, PEG30, and BSA30 AgNPs, for 24 or 48 h, in relation to controls, expressed as % variation (%var) and respective error (±), effect size (ES), *p*-value (*p*), and FDR-adjusted (FDR) *p*-value. The variations with |ES| < 0.8 (or standard error > |ES|, or mean error > |% variation|) were considered null. Conc., concentration. For metabolite codes, *vide* legend of Figure 4.5.

		Cit10				Cit30				Cit60				PEG10				PEG30				BSA30			
Conc. (µg/mL)		10		40		10		40		10		40		10		40		10		40		10		40	
Time (h)		24	48	24	48	24	48	24	48	24	48	24	48	24	48	24	48	24	48	24	48	24	48	24	48
Total cholesterol	%var	0	8.52	0	8.29	0	0	0	-20.04	0	0	0	0	0	-14.84	0	0	0	0	0	0	0	0	-20.27	-13.17
	±		4.98		7.82				18.76						6.80									15.35	8.60
	ES	0	1.07	0	0.00	0	0	0	-0.98	0	0	0	0	0	-1.54	0	0	0	0	0	0	0	0	-0.91	-1.16
	p		0.2070		0.4038				0.4042						0.0779									0.2323	0.2448
	FDR		0.6984		0.9405				0.6246						0.4361									0.6713	0.9913
Free cholesterol	%var	0	0.00	-11.69	0	0	0	0	0	0	0	0	0	0	-11.82	0	0	0	11.51	0	0	0	0	-16.18	-14.08
	±		4.26	9.06											7.14				5.47					10.79	11.34
	ES	0	0.71	-0.90	0	0	0	0	0	0	0	0	0	0	-1.15	0	0	0	1.14	0	0	0	0	-0.86	-1.05
	p		0.3527	0.2427											0.2079				0.1997					0.2369	0.3537
	FDR		0.6984	0.7597											0.5892				0.7408					0.6713	0.9913
PTC	%var	0	25.57	0.00	0	0	0	0	-19.68	0	0	0	0	0	-19.76	0	0	0	0	20.30	0	0	0	-76.88	-18.28
	±		16.02	19.51					15.14						3.73					13.23				53.02	7.27
	ES	0	0.92	-0.72	0	0	0	0	-1.00	0	0	0	0	0	-3.84	0	0	0	0	0.91	0	0	0	-1.58	-1.75
	p		0.2755	0.3387					0.2714						0.0052					0.2401				0.0744	0.0731
	FDR		0.6984	0.7597					0.6246						0.0884					0.7934				0.6321	0.6212
PTE	%var	0	0	-16.21	0	0	0	0	-33.00	0	0	0	0	22.73	0	0	0	0	0	0	0	0	0	-82.61	0
	±			10.72					25.16					12.71										81.44	
	ES	0	0	-1.07	0	0	0	0	-1.17	0	0	0	0	0.82	0	0	0	0	0	0	0	0	0	-1.54	0
	p			0.1813					0.2572					0.2484										0.2280	
	FDR			0.7597					0.6246					0.7094										0.6713	
PUFA chains	%var	0	0	0	0	0	0	0	-17.82	0	0	0	0	0	-16.24	0	0	0	-6.99	15.33	0	0	5.91	0	0
	±								14.29						7.25				2.76	7.42			3.51		
	ES	0	0	0	0	0	0	0	-1.03	0	0	0	0	0	-1.59	0	0	0	-1.50	1.25	0	0	0.92	0	0
	p								0.3229						0.1026				0.1544	0.1327			0.2045		
	FDR								0.6246						0.4361				0.7408	0.7934			0.9769		

Table S4.5. Main metabolite variations in the culture media of HaCaT cells exposed to IC_{20} and IC_{50} of Cit30 AgNPs, Ag^+, and H_2O_2, for 24 or 48 h, in relation to culture medium of control cells, expressed as % variation (%var) and respective error (±), effect size (ES), *p*-value (*p*), and FDR-adjusted (FDR) *p*-value. The variations with |ES| < 0.8 (or standard error > |ES|, or mean error > |% variation|) were considered null. PyroGlu, pyroglutamate, for other metabolite codes, *vide* legend of Figure 4.7.

		Cit30				Ag^+				H_2O_2			
		IC_{20}		IC_{50}		IC_{20}		IC_{50}		IC_{20}		IC_{50}	
Time (h)		24	48	24	48	24	48	24	48	24	48	24	48
Glucose	%var	0	14.26	0	0	0	0	3.58	10.02	0	9.91	3.97	18.84
	±		10.26					1.49	6.54		5.83	1.64	4.49
	ES	0	0.85	0	0	0	0	1.25	0.95	0	1.06	1.41	2.54
	p		0.2999					0.0449	0.2196		0.1952	0.0975	0.0434
	FDR		0.8341					0.0945	0.3819		0.4879	0.3486	0.1609
Pyruvate	%var	0	-28.89	0	-37.57	0	-22.43	-33.52	-46.62	-18.97	-34.29	-39.64	-66.89
	±		11.48		9.96		12.39	14.63	14.54	14.50	19.04	11.39	12.97
	ES	0	-1.92	0	-3.04	0	-1.33	-1.40	-2.70	-0.94	-1.42	-2.32	-4.02
	p		0.0462		0.0340		0.1115	0.0295	0.0074	0.2243	0.1111	0.0279	0.0061
	FDR		0.3694		0.2549		0.3637	0.0715	0.0492	0.7436	0.4324	0.2323	0.0701
Lactate	%var	0	0	0	0	0	0	-19.49	-19.19	0	-22.49	-26.31	-44.23
	±							9.97	15.91		15.28	9.37	11.94
	ES	0	0	0	0	0	0	-1.14	-0.89	0	-1.08	-1.81	-2.85
	p							0.0669	0.2450		0.1895	0.0521	0.0274
	FDR							0.1216	0.4083		0.4879	0.2323	0.1368
Citrate	%var	0	39.35	47.40	69.67	0	-5.36	-9.25	-24.39	-2.10	-7.38	-3.53	-8.36
	±		14.63	15.29	2.06		2.83	4.50	10.10	1.13	2.97	1.52	2.76
	ES	0	1.47	1.41	16.37	0	-1.27	-1.00	-2.09	-1.23	-1.68	-1.53	-1.61
	p		0.1492	0.0789	4.6e-5		0.1743	0.0846	0.0914	0.1587	0.0938	0.1178	0.0870
	FDR		0.6514	0.7888	0.0018		0.4101	0.1254	0.2031	0.7052	0.4324	0.3486	0.2176
Gln	%var	-5.63	-23.59	-5.04	-23.30	-4.44	-9.96	-11.41	-16.64	0	0	0	5.96
	±	3.22	5.18	3.65	4.70	1.21	1.70	8.00	8.53				0.72
	ES	-1.01	-3.37	-0.84	-3.66	-2.44	-4.03	-0.97	-1.38	0	0	0	4.20
	p	0.1476	0.0149	0.2186	0.0265	0.0253	0.0091	0.2019	0.0889				0.0114
	FDR	0.9291	0.1989	0.8184	0.2549	0.2370	0.1142	0.2884	0.2031				0.0914
Glu	%var	23.04	120.04	29.60	127.62	18.61	47.26	24.90	95.87	5.33	21.41	7.67	43.67
	±	6.38	4.59	4.96	3.87	2.77	4.06	5.62	5.08	2.26	5.30	2.37	5.13
	ES	2.07	10.67	3.06	13.16	4.02	6.16	2.39	8.64	1.50	2.38	2.36	4.40
	p	0.0234	0.0002	0.0045	0.0009	0.0128	0.0034	0.0064	0.0015	0.1025	0.0235	0.1220	0.0061
	FDR	0.9291	0.0066	0.0909	0.0172	0.2370	0.1142	0.0562	0.0195	0.6967	0.3042	0.3486	0.0701
PyroGlu	%var	0	0	0	0	10.96	5.15	23.94	27.25	10.56	7.56	10.42	11.64
	±					3.05	2.21	8.98	9.53	4.41	2.19	5.98	1.93
	ES	0	0	0	0	2.22	1.48	1.16	1.48	1.49	2.17	1.47	4.27
	p					0.0640	0.1141	0.0525	0.0568	0.1433	0.0496	0.3366	0.0480
	FDR					0.3325	0.3637	0.1000	0.1607	0.7052	0.3395	0.5853	0.1609
Ala	%var	-5.46	0	-4.27	-6.40	-2.11	0	-3.94	-13.80	0	0	-3.87	-14.79
	±	2.81		2.94	4.47	1.72		1.98	6.70			1.78	4.44
	ES	-1.09	0	-0.83	-0.97	-0.81	0	-1.10	-1.40	0	0	-1.33	-2.23
	p	0.1347		0.2163	0.2143	0.2869		0.0786	0.0778			0.1158	0.0456
	FDR	0.9291		0.8184	0.6195	0.6751		0.1254	0.1946			0.3486	0.1609
Met	%var	0	0	0	0	0	-7.99	-10.80	-18.56	0	-3.54	0	-11.66
	±						4.87	5.33	9.21		2.83		4.20
	ES	0	0	0	0	0	-1.12	-1.00	-1.72	0	-0.83	0	-2.50
	p						0.2225	0.0824	0.1498		0.3146		0.1950
	FDR						0.4684	0.1254	0.2723		0.5389		0.3545
Pro	%var	0	0	0	0	0	0	36.68	33.88	0	0	0	0
	±							7.22	10.37				
	ES	0	0	0	0	0	0	2.20	1.53	0	0	0	0
	p							0.0029	0.0581				
	FDR							0.0393	0.1607				
Acetate	%var	0	0	0	0	-9.64	-9.85	0	0	-11.93	-12.64	-16.01	-18.99
	±					3.57	3.16			4.26	3.99	2.01	4.29
	ES	0	0	0	0	-1.85	-2.14	0	0	-1.94	-2.21	-4.80	-2.94
	p					0.0634	0.0741			0.0652	0.0304	0.0038	0.0195
	FDR					0.3325	0.3295			0.6967	0.3042	0.1533	0.1303

		Cit30				Ag^+				H_2O_2			
		IC_{20}		IC_{50}		IC_{20}		IC_{50}		IC_{20}		IC_{50}	
Time (h)		24	48	24	48	24	48	24	48	24	48	24	48
Formate	%var	6.65	11.24	20.58	22.44	0	0	0	0	0	-8.29	-18.74	-16.96
	±	4.53	6.23	3.50	4.13						6.93	5.53	9.54
	ES	0.96	1.12	3.46	3.19	0	0	0	0	0	-0.82	-2.14	-1.43
	p	0.2344	0.1628	0.0039	0.0382						0.2843	0.0352	0.2333
	FDR	0.9291	0.6514	0.0909	0.2549						0.5389	0.2323	0.4058
Allantoin	%var	0	0	0	0	27.78	29.33	-17.69	-20.47	20.58	35.78	24.78	31.50
	±					5.72	7.33	6.96	6.99	7.34	2.57	12.24	7.56
	ES	0	0	0	0	2.79	2.28	-1.31	-2.33	1.66	7.71	1.59	3.16
	p					0.0296	0.0641	0.0343	0.0463	0.1045	0.0005	0.3037	0.1509
	FDR					0.2370	0.3207	0.0762	0.1607	0.6967	0.0185	0.5853	0.3018

Table S4.6. Main metabolite variations in polar extracts of HaCaT cells exposed to IC_{20} and IC_{50} of Cit30 AgNPs, Ag^+, and H_2O_2, for 24 or 48 h, in relation to controls, expressed as % variation (%var) and respective error (±), effect size (ES), *p*-value (*p*), and FDR-adjusted (FDR) *p*-value. The variations with |ES| < 0.8 (or standard error > |ES|, or mean error > |% variation|) were considered null. For metabolite codes, *vide* legend of Figure 4.7.

		Cit30				Ag^+				H_2O_2			
		IC_{20}		IC_{50}		IC_{20}		IC_{50}		IC_{20}		IC_{50}	
Time (h)		24	48	24	48	24	48	24	48	24	48	24	48
Pyruvate	%var	-9.54	-9.66	0	-20.02	-20.12	0	-18.41	-20.92	-21.41	-26.84	-34.66	-53.07
	±	6.00	4.52		3.14	6.80		10.22	10.52	7.39	11.02	13.66	6.65
	ES	-0.92	-1.53	0	-4.62	-2.15	0	-1.04	-1.58	-2.12	-1.84	-2.18	-5.22
	p	0.1309	0.1549		0.0061	0.0506		0.0878	0.1076	0.0398	0.0572	0.1282	0.0093
	FDR	0.3846	0.3932		0.0405	0.2681		0.3219	0.3227	0.2795	0.3514	0.2350	0.1537
Lactate	%var	0	0	0	0	0	0	0	0	-20.20	-17.52	-22.18	-31.99
	±									5.35	15.15	11.99	13.59
	ES	0	0	0	0	0	0	0	0	-2.75	-0.83	-1.64	-1.41
	p									0.0140	0.2836	0.2507	0.1027
	FDR									0.2795	0.5856	0.4136	0.2407
Succinate	%var	0	0	10.24	15.34	0	0	0	0	0	0	30.94	28.83
	±			4.03	9.84							23.96	24.41
	ES	0	0	1.25	0.95	0	0	0	0	0	0	0.84	0.89
	p			0.0439	0.2213							0.3908	0.4654
	FDR			0.1530	0.3652							0.5373	0.5296
Gln	%var	-13.08	-25.65	-13.94	-24.46	0	-8.35	0	0	18.86	0	45.30	26.48
	±	5.59	8.00	5.82	6.20		4.11			6.24		7.19	2.72
	ES	-1.63	-2.25	-1.63	-2.94	0	-1.39	0	0	1.80	0	3.67	4.71
	p	0.0562	0.0450	0.0464	0.0286		0.1013			0.0508		0.0329	0.0064
	FDR	0.2152	0.3702	0.1530	0.0857		0.4179			0.2795		0.1207	0.1537
Glu	%var	-10.88	-16.39	-12.08	-21.08	-20.45	-14.73	-10.85	0	-18.76	-11.11	-28.90	-28.83
	±	6.76	12.65	7.06	11.02	5.17	3.47	3.99		5.70	8.22	4.39	5.25
	ES	-1.10	-0.83	-1.14	-1.40	-2.88	-2.99	-1.42	0	-2.37	-0.93	-3.83	-4.46
	p	0.1487	0.2611	0.1212	0.1354	0.0160	0.0105	0.0243		0.0227	0.2682	0.0171	0.0344
	FDR	0.3846	0.5386	0.3333	0.2642	0.1411	0.1145	0.1393		0.2795	0.5856	0.0978	0.2407
Asp	%var	-28.04	-37.87	-25.79	-49.62	0	-31.56	-27.48	0	-22.12	-24.65	-60.23	-67.96
	±	9.88	15.03	8.91	12.42		5.90	5.24		14.71	13.90	41.86	22.78
	ES	-2.24	-1.95	-2.50	-3.47	0	-4.15	-3.40	0	-1.10	-1.32	-1.65	-3.40
	p	0.0244	0.0797	0.0399	0.0128		0.0100	0.0007		0.2056	0.1492	0.3012	0.1249
	FDR	0.2013	0.3702	0.1530	0.0543		0.1145	0.0110		0.4730	0.5470	0.4518	0.2407
Gly	%var	-21.77	-35.45	-28.29	-35.26	-21.85	-25.93	-30.18	-33.61	0	0	0	-23.22
	±	8.05	12.44	8.33	12.46	6.79	8.11	8.45	8.22				12.10
	ES	-2.15	-1.76	-2.86	-2.24	-2.36	-2.40	-2.02	-3.60	0	0	0	-1.40
	p	0.0406	0.0636	0.0196	0.0726	0.0624	0.0606	0.0048	0.0174				0.1532
	FDR	0.2152	0.3702	0.1077	0.1711	0.2681	0.3333	0.0393	0.2181				0.2407
Ala	%var	-12.44	0	-10.90	0	0	0	-19.52	-24.50	0	0	13.72	-24.56
	±	7.87		7.41				8.43	12.96			4.81	10.50
	ES	-1.09	0	-1.05	0	0	0	-1.39	-1.44	0	0	1.41	-1.54
	p	0.1515		0.1909				0.0375	0.0899			0.1040	0.0817
	FDR	0.3846		0.4534				0.1619	0.3077			0.2244	0.2407
β-Ala	%var	-8.59	8.48	-14.57	0	8.86	0	0	0	0	-17.05	19.49	-11.46
	±	6.16	4.35	7.42		3.21					10.10	4.99	6.66
	ES	-0.95	0.98	-1.25	0	1.73	0	0	0	0	-1.21	2.88	-0.94
	p	0.2065	0.1902	0.0702		0.0640					0.1396	0.1238	0.2013
	FDR	0.4867	0.4184	0.2106		0.2681					0.5470	0.2350	0.3019
Ile	%var	0	5.70	0	14.44	6.95	6.67	0	10.71	17.06	0	52.11	43.41
	±		2.05		1.99	2.36	3.20		2.66	4.86		3.01	9.02
	ES	0	1.69	0	4.41	1.86	1.32	0	2.84	2.11	0	11.95	3.63
	p		0.0799		0.0025	0.0731	0.1643		0.0529	0.0765		0.0303	0.1497
	FDR		0.3702		0.0322	0.2681	0.6026		0.2181	0.3156		0.1207	0.2407
Leu	%var	0	4.48	0	15.08	5.30	0	0	13.09	18.78	0	54.68	47.90
	±		1.27		1.44	3.66			4.05	4.34		4.79	9.53
	ES	0	1.85	0	6.35	0.92	0	0	2.30	2.58	0	8.04	3.75
	p		0.0555		0.0008	0.2741			0.0932	0.0479		0.0573	0.1479
	FDR		0.3702		0.0272	0.7320			0.3077	0.2795		0.1718	0.2407

		Cit30				Ag^+				H_2O_2			
		IC_{20}		IC_{50}		IC_{20}		IC_{50}		IC_{20}		IC_{50}	
Time (h)		24	48	24	48	24	48	24	48	24	48	24	48
	%var	0	5.04	0	10.61	0	0	0	7.73	17.89	0	43.41	39.34
	±		1.46		1.55				3.21	5.49		1.82	6.98
Val	ES	0	2.05	0	4.24	0	0	0	1.73	1.95	0	16.65	4.32
	p		0.0455		0.0029				0.1354	0.0933		0.0178	0.1272
	FDR		0.3702		0.0322				0.3575	0.3422		0.0978	0.2407
	%var	0	8.15	0	11.68	0	0	0	8.88	17.89	0	41.64	31.07
	±		2.15		2.40				2.47	6.25		8.12	4.37
Tyr	ES	0	2.40	0	3.00	0	0	0	2.44	1.72	0	3.31	4.62
	p		0.0507		0.0132				0.0472	0.0616		0.0776	0.0373
	FDR		0.3702		0.0543				0.2181	0.2904		0.2135	0.2407
	%var	0	3.07	0	7.52	0	0	0	8.48	9.74	-7.69	40.70	25.52
	±		2.19		1.75				2.28	5.88	1.65	2.53	6.38
Phe	ES	0	1.09	0	2.71	0	0	0	2.21	1.03	-3.17	7.48	3.08
	p		0.3537		0.0255				0.0170	0.2151	0.0386	0.0018	0.1519
	FDR		0.6143		0.0857				0.2181	0.4730	0.3514	0.0535	0.2407
	%var	0	0	0	10.17	0	0	0	-13.36	0	-7.68	0	0
	±				5.76				4.49		6.09		
Lys	ES	0	0	0	1.10	0	0	0	-1.78	0	-0.86	0	0
	p				0.1851				0.0415		0.2865		
	FDR				0.3214				0.2181		0.5856		
	%var	16.11	17.17	29.69	22.69	0	11.81	0	8.85	0	0	0	12.20
	±	8.75	5.65	7.44	2.63		8.93		3.18				5.40
Met	ES	0.91	2.16	1.90	5.07	0	0.82	0	1.67	0	0	0	1.32
	p	0.1323	0.1458	0.0109	0.0049		0.3018		0.0481				0.1251
	FDR	0.3846	0.3932	0.0897	0.0403		0.6860		0.2181				0.2407
	%var	-31.70	0	-31.02	0	-37.73	-25.32	-36.69	0	-26.71	-19.65	-53.60	-37.43
	±	8.09		11.47		5.10	4.29	7.55		8.50	6.19	5.46	7.44
Cr	ES	-2.43	0	-1.61	0	-5.95	-4.42	-2.75	0	-2.37	-2.30	-8.19	-4.50
	p	0.0017		0.0153		0.0008	0.0025	0.0012		0.0441	0.0364	0.0032	0.0537
	FDR	0.0268		0.1007		0.0138	0.0831	0.0130		0.2795	0.3514	0.0535	0.2407
	%var	-27.25	-12.61	-41.19	-30.69	-18.27	20.79	-19.00	17.68	0	0	-55.60	-29.17
	±	5.83	5.58	5.42	5.99	15.99	4.76	7.84	7.34			18.03	18.83
PCr	ES	-2.61	-1.37	-4.72	-3.96	-0.82	2.59	-1.57	1.65	0	0	-2.22	-1.52
	p	0.0024	0.0979	0.0001	0.0077	0.2884	0.0213	0.0393	0.1517			0.0310	0.3182
	FDR	0.0268	0.3702	0.0042	0.0423	0.7320	0.1403	0.1619	0.3575			0.1207	0.3889
	%var	79.91	60.20	92.85	50.18	78.19	49.41	73.52	20.10	0	9.95	-27.35	-9.33
	±	8.02	25.46	8.90	11.41	3.40	5.73	5.09	6.42		3.45	7.05	6.00
GSH	ES	4.21	1.58	3.81	2.30	10.79	4.52	5.45	1.64	0	1.79	-3.55	-1.31
	p	0.0010	0.2776	0.0003	0.0265	0.0007	0.0139	1.7e-5	0.0404		0.0639	0.1088	0.3149
	FDR	0.0268	0.5389	0.0042	0.0857	0.0138	0.1145	0.0006	0.2181		0.3514	0.2244	0.3889
	%var	-14.66	0	-18.06	-14.90	-11.78	0	-12.10	0	0	14.49	-29.30	0
	±	6.23		6.89	8.99	4.97		4.49			2.53	5.49	
PC	ES	-1.70	0	-1.81	-1.17	-1.64	0	-1.40	0	0	3.49	-3.74	0
	p	0.0576		0.0293	0.1644	0.0669		0.0253			0.0075	0.0113	
	FDR	0.2152		0.1380	0.3013	0.2681		0.1393			0.2490	0.0978	
	%var	-12.91	-33.03	-25.32	-42.81	-13.58	0	-10.01	0	-5.57	21.08	0	25.86
	±	5.76	21.38	6.43	20.39	3.06		5.99		2.78	4.87		2.70
GPC	ES	-1.44	-1.03	-2.71	-1.74	-3.11	0	-1.06	0	-1.35	2.56	0	7.60
	p	0.0502	0.1732	0.0029	0.0987	0.0171		0.1348		0.1461	0.0584		0.0676
	FDR	0.2152	0.4083	0.0315	0.2172	0.1411		0.3799		0.4018	0.3514		0.2407
	%var	0	-14.83	0	-21.96	-16.25	-12.89	-11.91	0	-12.76	0	-21.70	-36.77
	±		6.28		6.92	10.28	8.08	7.53		7.30		9.75	13.95
m-Ino	ES	0	-1.30	0	-2.33	-1.12	-1.11	-0.95	0	-1.22	0	-1.52	-2.13
	p		0.1234		0.0522	0.1609	0.1920	0.1403		0.1740		0.1016	0.0912
	FDR		0.3702		0.1437	0.4827	0.6336	0.3799		0.4417		0.2244	0.2407

Table S4.7. Main metabolite variations in lipophilic extracts of HaCaT cells exposed to IC_{20} and IC_{50} of Cit30 AgNPs, Ag^+, and H_2O_2, for 24 or 48 h, in relation to controls, expressed as % variation (%var) and respective error (±), effect size (ES), *p*-value (*p*), and FDR-adjusted (FDR) *p*-value. The variations with |ES| < 0.8 (or standard error > |ES|, or mean error > |% variation|,) were considered null. For metabolite codes, *vide* legend of Figure 4.7.

		Cit30				Ag^+				H_2O_2			
		IC_{20}		IC_{50}		IC_{20}		IC_{50}		IC_{20}		IC_{50}	
Time (h)		24	48	24	48	24	48	24	48	24	48	24	48
Total cholesterol	%var	0	0	0	-20.04	0	-4.58	-33.45	0	0	-10.65	0	-16.79
	±				18.76		3.64	15.05			4.88		3.56
	ES	0	0	0	-0.98	0	-0.84	-1.42	0	0	-1.51	0	-4.00
	p				0.4042		0.3038	0.0338			0.1308		0.0804
	FDR				0.6246		0.8449	0.0912			0.5402		0.3689
Free cholesterol	%var	0	0	0	0	0	-2.99	-44.37	-33.59	0	-8.59	4.80	-11.15
	±						2.38	22.23	15.32		2.77	1.64	1.99
	ES	0	0	0	0	0	-0.83	-1.37	-1.58	0	-2.12	1.55	-4.84
	p						0.3201	0.0491	0.0335		0.0741	0.0766	0.0802
	FDR						0.8449	0.0928	0.1901		0.5402	0.2606	0.3689
PTC	%var	0	0	0	-19.68	0	0	-58.95	0	-11.90	-11.00	-31.34	-36.57
	±				15.14			28.21		9.42	9.10	13.51	10.36
	ES	0	0	0	-1.00	0	0	-1.58	0	-0.88	-0.84	-1.87	-3.43
	p				0.2714			0.0245		0.2507	0.3124	0.1270	0.1223
	FDR				0.6246			0.0912		0.7393	0.5402	0.2699	0.3689
PTE	%var	0	0	0	-33.00	0	-2.81	-47.51	0	0	10.64	0	-21.27
	±				25.16		1.57	19.03			1.94		1.65
	ES	0	0	0	-1.17	0	-1.18	-1.74	0	0	3.40	0	-7.48
	p				0.2572		0.1805	0.0123			0.0065		0.0025
	FDR				0.6246		0.8449	0.0912			0.1102		0.0426
PUFA chains	%var	0	0	0	-17.82	0	0	-44.51	0	0	2.81	-11.75	0
	±				14.29			20.96			1.51	4.85	
	ES	0	0	0	-1.03	0	0	-1.53	0	0	1.20	-1.66	0
	p				0.3229			0.0209			0.1576	0.1050	
	FDR				0.6246			0.0912			0.5402	0.2699	

Chapter 5. Metabolomic analysis of human hepatoma cells (HepG2) exposed to citrate-coated and biogenic silver nanoparticles

5.1. Background and aims

This chapter describes the cytotoxic and metabolic effects of two types of silver nanoparticles (AgNPs) with diameters of 30 nm – citrate-coated (Cit30) and biogenic (phytosynthesised) AgNPs (GS30) – towards human liver cells. Liver is a major site of AgNPs accumulation following intravenous injection (Dziendzikowska *et al.*, 2012; Xue *et al.*, 2012). Moreover, whether exposure occurs through ingestion, inhalation or dermal contact, AgNPs may enter the central blood circulation and translocate to several organs, including the liver (Oberdorster *et al.*, 2005; Johnston *et al.*, 2010). As a major detoxification organ and the body's metabolic hub, liver largely contributes to regulate metabolite levels in the blood and to supply energy to other peripheral organs (Rui, 2014). Thus, assessing the impact of AgNPs on the metabolism of liver cells is relevant to understand the toxicity and biological effects of these nanoparticles. Constituting about 80% of all liver cells, hepatocytes have been the focus of many toxicity studies (Wiśniewski *et al.*, 2016). In particular, the human hepatocellular carcinoma HepG2 cell line has been often used as an *in vitro* model, since it is well characterised, easy to culture, and has a stable phenotype. Moreover, it maintains the antioxidant defences and several liver-specific metabolic functions normally present in hepatocytes (Alia *et al.*, 2005; Maier *et al.*, 2010). Previous studies have demonstrated the toxicity of AgNPs towards HepG2 cells based on the assessment of abnormal cell morphologies (Kawata *et al.*, 2009), decreased mitochondrial function (Avalos *et al.*, 2014; Xue *et al.*, 2016), membrane leakage of lactate dehydrogenase (Avalos *et al.*, 2014; Vrček *et al.*, 2016), disturbance of the redox balance (Avalos *et al.*, 2014; Vrček *et al.*, 2016), multiple altered genes (Kawata *et al.*, 2009; Sahu *et al.*, 2015), induction of micronucleus (Kawata *et al.*, 2009; Prasad *et al.*, 2013; Sahu *et al.*, 2016), apoptosis (Jain *et al.*, 2009; Xue *et al.*, 2016), and alterations in cell cycle dynamics (Bastos *et al.*, 2016). However, biological effects at low, sub-toxic concentrations (more physiologically relevant) have been poorly documented.

The green synthesis of metal nanoparticles using plant extracts has been growing as an alternative approach to the well-established chemical reduction methods (Iravani, 2011; Santos *et al.*, 2014). Besides mediating silver reduction, the plant components may

potentially stabilise the nanoparticles and reduce their toxicity, thus favouring biomedical applications (Iravani, 2011). In addition, by taking advantage of the synergism between AgNPs toxicity and the bioactivity of natural compounds, plant-derived biogenic AgNPs have shown interesting anticancer activity towards different cell lines, including liver cells (Guo *et al.*, 2015; Krishnasamy *et al.*, 2015). On the other hand, little is known about the mechanisms underlying the biological effects of biogenic AgNPs or the specific role of the biocapping agents. In this work, we have compared the impact on viability and metabolism of HepG2 cells exposed to citrate-coated AgNPs or to biogenic AgNPs. The latter were prepared by our collaborators through the reduction of silver nitrate with an aqueous extract of *Eucalyptus globulus* Labill. (EG) bark (Santos *et al.*, 2014); this extract was composed mainly of polyphenolic compounds and sugars which were shown to play dominant roles in the metal-ion reduction and the NPs stabilisation, respectively (Santos et al., 2014). Cellular responses to coating agents (citrate and EG extract), ionic silver and hydrogen peroxide were also assessed.

5.2. Physicochemical properties of the AgNPs tested

In order to facilitate the comparison between the two types of AgNPs studied, the characterisation of Cit30 AgNPs, already shown in Chapter 4, is repeated in this section and presented along with the results obtained for the biogenic AgNPs (GS30). TEM showed that both nanoparticles presented an approximately spherical morphology, with average core diameters of 29.1±3.9 nm and 32.9±4.0 nm for Cit30 and GS30, respectively (Supplementary Figure S5.1). DLS measurements of AgNPs aqueous colloidal solutions (Table 5.1) indicated a higher hydrodynamic diameter for GS30 (76.1±3.3 nm, compared to 43.3±0.5 nm for Cit30), which is consistent with the coating of the silver core by phenolic compounds and other biomolecules present in the bark extract used for synthesising GS30 AgNPs (Santos *et al.*, 2014). The negative zeta-potential value for these nanoparticles further indicates the presence of negatively charged capping compounds. In terms of soluble ionic silver (Ag^+), the aqueous colloidal suspensions of Cit30 and GS30 were found to contain 3.32±0.04% and 1.68±0.01% Ag^+, respectively.

When placed in complete culture medium (DMEM containing 10% FBS), Cit30 progressively increased their D_h to about 94 nm at 48 h likely due to the formation of a protein corona, as already explained in Chapter 4. On the other hand, the D_h of GS30 increased immediately after dispersion in culture medium to over 100 nm and remained approximately constant up to 48 h incubation (Figure 5.1a). As suggested by others for

carbohydrate-coated AgNPs (Kennedy *et al.*, 2014), this increase in hydrodynamic size may also relate to the adsorption of proteins at the nanoparticle surface.

Table 5.1. Physicochemical properties of the citrate-coated AgNPs (Cit30) and the biogenic AgNPs obtained by green synthesis (GS30), dispersed in ultrapure distilled water.

AgNP	D (nm)[a]	D (nm)[b]	D_h (nm)[c]	PdI[c]	ζ (mV)[d]	λ_{max}[e] (nm)	%Ag^+[f]
Cit30	32.7±4.8	29.1±3.9	43.3±0.5	0.25-0.26	-42.7±2. 7	408	3.32±0.04
GS30	n.a.	32.9±4.0	76.1±3.3	0.20-0.22	-37.1±8.1	434	1.68±0.01

[a]Diameter indicated by the manufacturer; [b]Diameter measured by TEM; [c]Hydrodynamic diameter and polydispersity index (PdI) measured by DLS; [d]Zeta potential assessed by electrophoretic mobility; [e]Wavelength of maximum absorbance peak in the UV-Vis spectrum; [f]Percentage of ionic silver in the AgNPs suspension. Standard deviations calculated for D_h, ζ and %Ag^+ correspond to 3 replicate measurements. n.a. not available (NPs synthesised in-house).

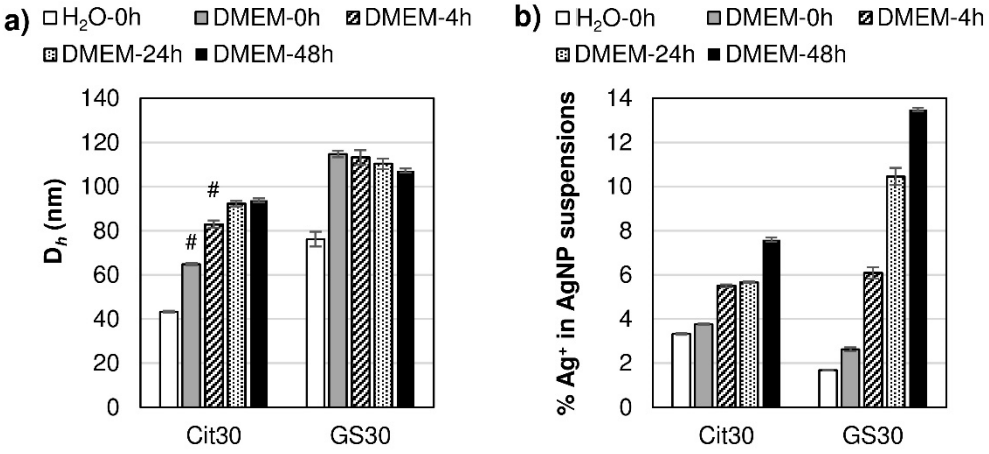

Figure 5.1. a) Hydrodynamic diameter (D_h) of Cit30 and GS30 AgNPs in water and in culture medium (DMEM + 10% FBS), at 0, 4, 24 and 48 h incubations. # PdI > 0.3 or poor quality of results (as reported by the DLS instrument); b) Amount (%) of ionic silver (Ag^+) in suspensions of Cit30 and GS30 AgNPs in water and in culture medium (0, 4, 24 and 48 h incubations).

Concerning the Ag^+ release behaviour in culture medium, GS30 appeared to suffer more extensive dissolution upon incubation for 48 h than Cit30 (Figure 5.1b); indeed, the amount of silver in 48 h medium supernatants was about 8 and 14% of total silver for Cit30 and GS30, respectively. This result underscores that, in spite of the reducing environment provided by the phenolic and sugar compounds present in the EG extract, the biocapping layer did not prevent AgNPs oxidation and dissolution. If, on one hand, this could have implications in toxicity, on the other, it may be viewed as a positive asset in regard to the therapeutic application of these particles.

5.3. Viability of HepG2 cells exposed to AgNPs, Ag^+ and H_2O_2

The dose-response curves of HepG2 cells exposed for 24 h to Cit30 or GS30 AgNPs, obtained through the MTT assay, are shown in Figure 5.2a and 5.2b, respectively. Both nanoparticles decreased the viability of HepG2 cells in a dose-dependent way, inducing a significant decrease in cell viability at a concentration of 10 µg/mL or higher. The IC_{50} values calculated from these curves were 18.9 µg/mL and 26.0 µg/mL for Cit30 and GS30, respectively, indicating that GS30 were slightly less cytotoxic to HepG2 cells than Cit30. Previous studies have reported varying IC_{50} values for HepG2 cells exposed to AgNPs, ranging from as low as 5 µg/mL (Mishra *et al.*, 2016) to over 200 µg/mL (Jain *et al.*, 2009). The different properties of the AgNPs evaluated, together with the different cytotoxicity assays used, certainly contributed for these discrepancies. In particular, the size of AgNPs was shown by others to be determinant to their toxicity towards HepG2 cells. For instance, citrate-coated AgNPs of 20 and 50 nm in diameter caused a 50 % decrease in the viability of HepG2 cells at approximately 5 and 50 µg/mL, respectively (Sahu *et al.*, 2015; Sahu *et al.*, 2016). Moreover, the IC_{50} concentrations of PVP-coated AgNPs of 5, 20 and 50 nm in diameter were reported to be 0.6, 25 and 34 µg/mL, respectively (Liu *et al.*, 2010) showing relatively good agreement with our results.

Compared to AgNPs, Ag^+ administered to cells as $AgNO_3$ was much more cytotoxic, with a concentration as low as 0.75 µg/mL inducing a significant decrease in cell viability (Figure 5.2c). The calculated IC_{50} value of 1.19 µg/mL matches the value of 1.11 µg/mL reported in the literature for the same cell line using the MTT assay (Liu *et al.*, 2010). This much larger toxicity of Ag^+ compared to AgNPs agrees with other studies of HepG2 cells (Liu *et al.*, 2010; Vrček *et al.*, 2016; Sahu *et al.*, 2016) and, as argued for HaCaT cells in Chapter 4, it may relate to the different ways by which AgNPs and free extracellular Ag^+ interact with cells. It has been shown that AgNPs are readily internalised by HepG2 cells (Jain *et al.*, 2009; Liu *et al.*, 2010; Mishra *et al.*, 2016) and release Ag^+ intracellularly (Yu *et al.*, 2013b), while Ag^+ in the form of $AgNO_3$ has a lower rate of cellular uptake (Prasad *et al.*, 2013), acting mainly through membrane damage.

The effect of exposure of HepG2 cells to H_2O_2 is illustrated in Figure 5.2d. Cell viability decreased with increasing H_2O_2 concentrations and the calculated IC_{50} was 3.08 mM. This much larger value compared to the IC_{50} found for HaCaT cells (143 µM, Chapter

4) could mean that HepG2 cells are less sensitive to this stressor. However, another good explanation relates to the supplementation of the medium used to culture HepG2 cells with sodium pyruvate (1 mM). Pyruvate is known to be an excellent ROS scavenger, which neutralises H_2O_2 in a reaction that produces acetate, carbon dioxide and water (Kelts *et al.*, 2015). Thus, it is likely that the decrease in cell viability upon H_2O_2 exposure would be much stronger if pyruvate had not been added to the culture medium. Indeed, in a study where pyruvate was not used to supplement the culture medium, a much lower IC_{50} of 500 µM has been reported for the 24 h exposure of HepG2 cells to H_2O_2, as assessed by the MTT assay (Chen *et al.*, 2011).

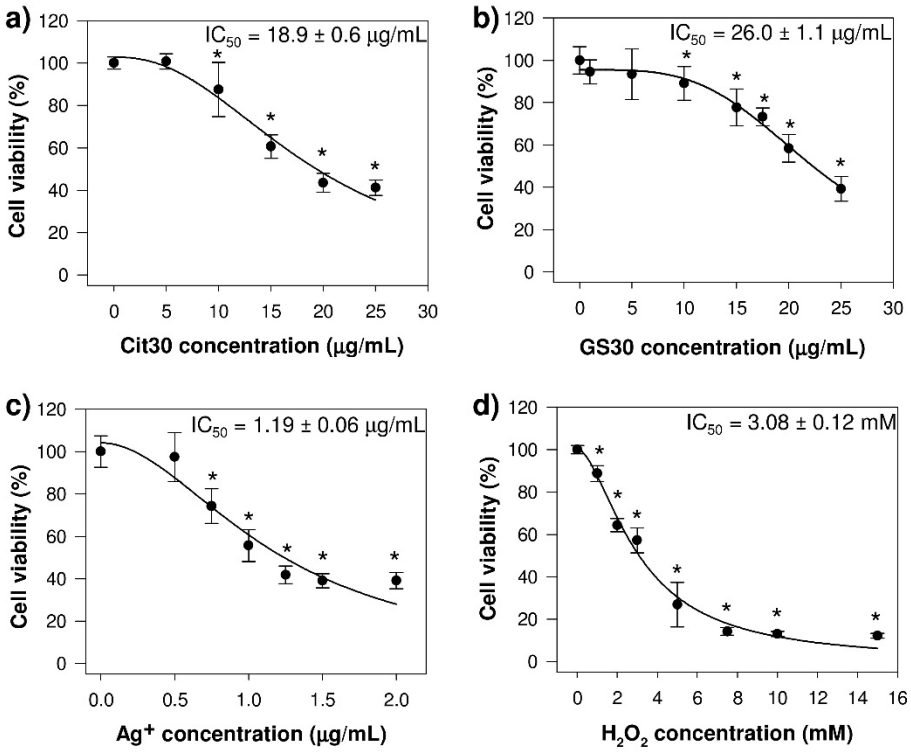

Figure 5.2. Viability (%) of HepG2 cells, measured by MTT assay, after 24 h of exposure to: a) Cit30, b) GS30, c) Ag^+ and d) H_2O_2. Data expressed as mean ± standard deviation of three independent assays with three replicates each (n 9). Statistically significant ($p < 0.05$) differences relatively to controls are indicated by *.

Based on the dose response curves presented above, two concentration levels were selected for the metabolomics study of each AgNP type, as well as of Ag^+ and H_2O_2; these were the concentrations that caused minimal (5%) and small (20%) decreases in cell

viability (Table 5.2). The choice of exposing cells to non-toxic or sub-toxic concentrations of each tested substance was based on the hypothesis that cell metabolism would sensitively respond even in the absence of major toxicity, as it was indeed observed for HaCaT cells (Chapter 4).

Table 5.2. Concentrations of Cit30 AgNPs, GS30 AgNPs, Ag^+ (from $AgNO_3$) and H_2O_2 selected for the metabolomic analysis of HepG2 cells.

	Cit30	GS30	Ag^+	H_2O_2
IC_5	6.4 µg/mL	5.4 µg/mL	0.35 µg/mL	0.58 mM
IC_{20}	11.0 µg/mL	14.0 µg/mL	0.64 µg/mL	1.38 mM

Assuming that citrate and the phenolic/sugar compounds used to stabilise the nanoparticles could also influence the cellular responses, the cell viability and metabolomic effects were also determined upon exposure of HepG2 cells to citrate or the EG extract. The concentrations used for these exposures were calculated to reflect the maximum amounts present when IC_5 and IC_{20} concentrations of AgNPs were administered to cells. As shown in Figure 5.3, neither citrate nor the EG extract affected cell viability at the concentrations tested. The impact on the cellular metabolic profiles will be presented in the next section.

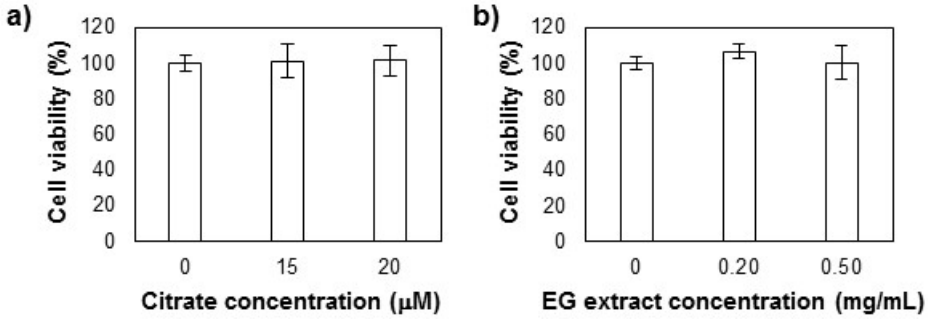

Figure 5.3. Viability (%) of HepG2 cells, measured by MTT assay, after 24 h of exposure to: a) citrate and b) the *Eucalyptus globulus* Labill. (EG) bark extract used in the green synthesis of GS30 AgNPs. Data expressed as mean ± standard deviation of three independent assays with three replicates each (n 9).

5.4. Generation of reactive oxygen species

In addition to cell viability, intracellular ROS generation was measured in HepG2 cells exposed to Cit30 or GS30 AgNPs at IC_{20} concentrations, as well as in cells exposed to the EG extract at the maximum concentration possibly present upon incubation with GS30. The results are presented in Figure 5.4. Intracellular ROS levels did not appear to vary upon exposure to IC_{20} concentrations of either Cit30 or GS30. On the other hand, the EG extract caused a significant increase in ROS production. It has been reported that certain polyphenolic and other food derived antioxidants added to cell culture medium undergo redox cycling and induce extracellular formation of H_2O_2 (Halliwell, 2008; Babich *et al.*, 2009; Long *et al.*, 2010). Thus, it is possible that the polyphenol-rich EG extract used in this work also led to increased H_2O_2 levels in the culture medium, which in turn resulted in higher intracellular ROS production.

ROS generation upon exposure to Ag^+ (from $AgNO_3$) and to H_2O_2, at IC_{20} and IC_{50} concentrations, was also assessed (Figure 5.4). Exposure to Ag^+ did not significantly alter ROS levels, although there was a trend for increase at the IC_{50} concentration. In the literature, intracellular ROS have been shown to increase in HepG2 cells exposed to Ag^+ (at the IC_{50}), especially for shorter incubation times (2-3 h) (Liu *et al.*, 2010; Vrček *et al.*, 2016). In regard to H_2O_2, the IC_{50} concentration caused a significant increase in intracellular ROS generation, in agreement with other studies (Alia *et al.*, 2005; Chen *et al.*, 2011; Jiang *et al.*, 2014).

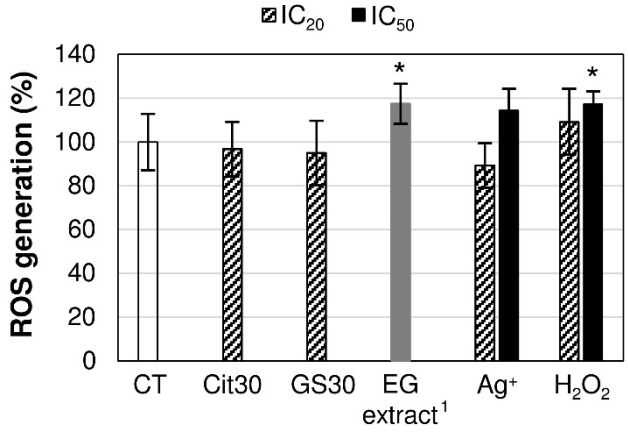

Figure 5.4. Intracellular generation of reactive oxygen species (ROS), at 24 h exposure to Cit30, GS30, EG extract, Ag^+ or H_2O_2. [1] In the case of EG extract, the concentration used matched the maximum amount estimated to be present when GS30 AgNPs were administered to cells at the IC_{20}. Data is expressed as mean ± standard deviation of three independent assays with three replicates each (n 9). Statistically significant ($p < 0.05$) differences relatively to controls are indicated by *.

5.5. Metabolic variations induced by AgNPs in HepG2 cells

As explained above, the metabolic effects of citrate-stabilised (Cit30) and biogenic AgNPs (GS30) on HepG2 cells were evaluated upon 24 h exposures to the IC_5 and IC_{20} concentrations of these nanoparticles. NMR profiling of culture medium supernatants was performed to assess the metabolic activity of control and nanoparticle exposed cells (in terms of substrate consumption and metabolite excretion), while analysis of cell extracts (polar and lipophilic) was conducted to assess the variations in the cellular metabolic composition.

The metabolic variations in culture medium supernatants of AgNPs-exposed cells relatively to control cells are summarised in Figure 5.5a and Supplementary Table S5.1. Most changes were concentration-dependent, with the low IC_5 concentration generally inducing fewer changes in the medium composition. Another general observation is that the extracellular metabolic signatures of the two AgNP types compared were relatively similar. Both nanoparticles induced a higher consumption of pyruvate (as indicated by decreased levels compared to the medium of control cells), although in the case of GS30 this decrease was only relevant at the IC_{20} concentration. Moreover, the excretion of lactate and of the TCA cycle intermediates citrate and fumarate increased. In this respect, it should be noted that while in the case of exposure to Cit30, the increased citrate levels in the medium could be partially due to citrate release from the nanoparticles surface, this should not be the case for GS30 as no citrate was expected in the bioacapping layer; thus, some citrate excretion must have originated from the cells altered metabolic activity. Nanoparticle exposure also induced alterations in the extracellular levels of several amino acids. Changes common to the two nanoparticle types comprised increased excretion of glutamate and decreased consumption of the amino acids phenylalanine, leucine and isoleucine. This variation in branched chain amino acids was in turn highly correlated to decreased release of their catabolic products 2-oxoisoleucine and *α*-ketovaline ($|r| > 0.9$, $p < 0.001$). Interestingly, GS30, but not Cit30, caused a higher consumption of glutamine at the IC_5 concentration (as compared to non-exposed control cells). Furthermore, both AgNPs induced decreased formate excretion and choline consumption, this latter change being clearly more marked upon exposure to GS30. Finally, the medium of GS30-exposed cells, but not of Cit30-exposed cells, showed significantly higher acetate levels than the medium of control cells.

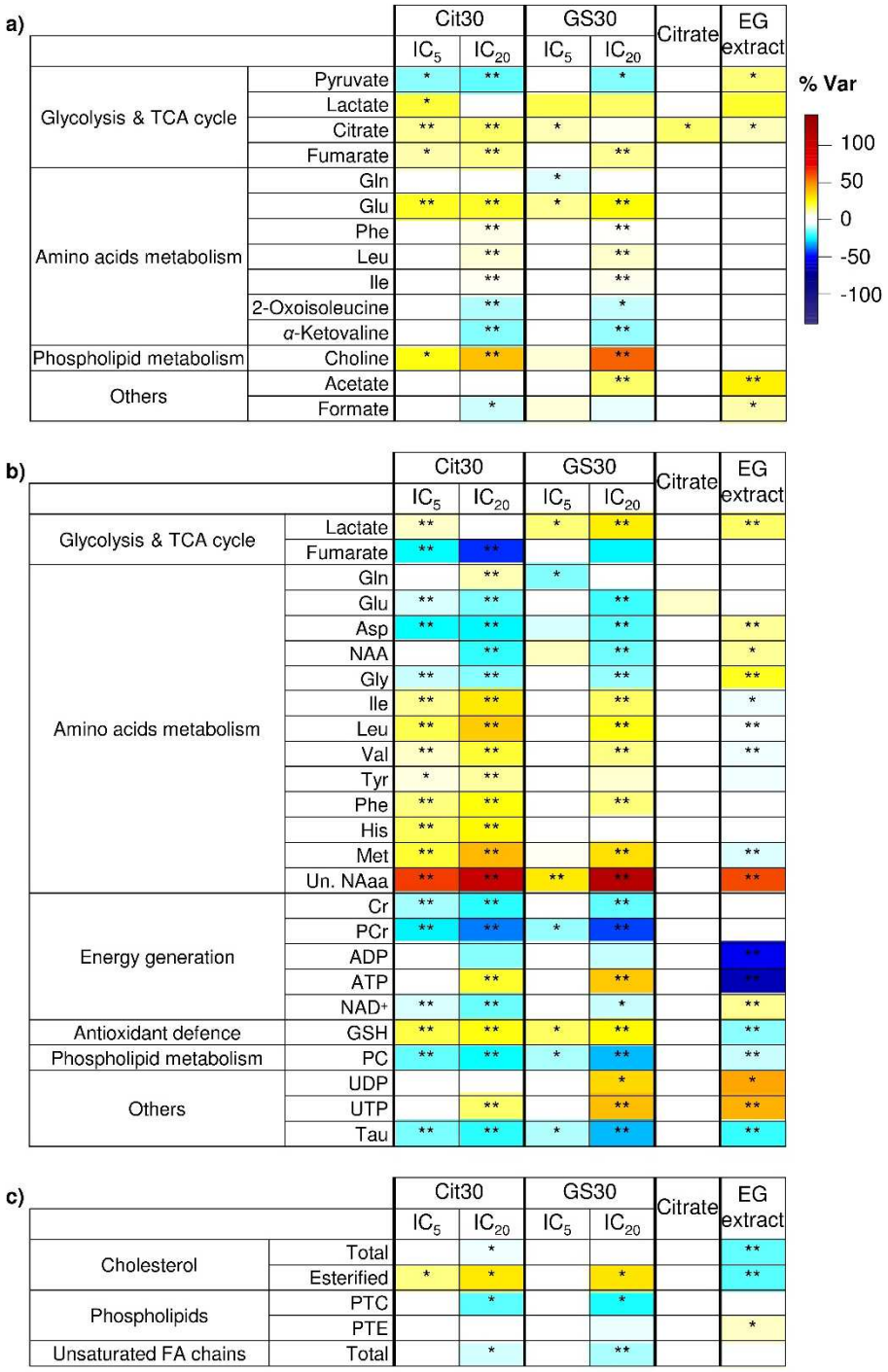

Figure 5.5. Heatmap of the main metabolite variations in a) culture media, b) polar extracts, and c) lipophilic extracts, from HepG2 cells exposed to Cit30 and GS30 AgNPs, both at the IC_5 and IC_{20} concentrations, and to citrate and EG extract (at concentrations that reflected the maximum amounts present when IC_{20} concentrations of AgNPs were administered to cells), coloured according to % variation in relation to controls, from maximum decrease (dark blue) to maximum increase (dark red). * Uncorrected *p*-value < 0.05; ** FDR-corrected *p*-value < 0.05. Three letter code used for amino acids; NAA, *N*-acetylaspartate; Un. NAaa, unidentified *N*-acetylated amino acid; Cr, creatine; PCr, phosphocreatine; ADP/ATP, adenosine di/triphosphate; NAD^+, nicotinamide adenine dinucleotide; GSH, reduced glutathione; PC, phosphocholine; UDP/UTP, uridine di/triphosphate; PTC, phosphatidylcholine; PTE, phosphatidylethanolamine; FA, fatty acyl.

Cell incubations with citrate (stabiliser of Cit30) and the *Eucalyptus globulus* (EG) extract used to prepare the GS30 AgNPs were also performed to assess the possible influence of these capping substances on the metabolic responses. As shown in Figure 5.5a (5^{th} column), addition of citrate to the cell culture did not produce changes in the medium composition other than the expected increase in citrate. On the other hand, the incubation of cells with the EG extract induced a few significant changes in the exometabolome (Figure 5.5a, 6^{th} column). These included decreased pyruvate consumption and increased formate release, as compared to control cells, variations which were actually in the opposite sense to those induced by GS30 AgNPs. Additionally, the medium of cells incubated with the EG extract showed increased levels of lactate (although not statistically significant), citrate and acetate. As mentioned before, acetate may be formed from the reaction between pyruvate (present in the medium) and H_2O_2. Thus, the higher acetate levels in the medium of cells exposed to the EG extract corroborates the generation of extracellular H_2O_2 suggested to arise from redox reactions involving the EG extract compounds. A similar effect may be postulated to explain the increase in extracellular acetate caused by GS30 AgNPs.

Analysis of the intracellular metabolic composition of HepG2 cells exposed to AgNPs allowed the impact of nanoparticle exposure on cell metabolism to be further investigated. The scores scatter plot resulting from applying principal component analysis (PCA) to the ^{1}H NMR spectra of polar extracts readily showed the separation between control and AgNPs-exposed cells along the first principal component (PC1) (Figure 5.6). Moreover, exposed samples showed grouping trends according to AgNP type and concentration, with cells exposed to the higher concentration (IC_{20}) being more distant from controls than those exposed to the lower concentration (IC_5). In order to assess the effects of each AgNP type in detail, multivariate analysis was applied separately to Cit30 and GS30-exposed samples. The results are presented in Figure 5.7. For both types of AgNPs, the PCA scores scatter plots maintained a clear dose-dependent separation between control and exposed samples (Figures 5.7a and 5.7d). Additionally, partial least squares discriminant analysis (PLS-DA, Figures 5.7b and 5.7e) allowed the two sample classes (control and exposed) to be discriminated with high robustness (Q^2 0.8 and 0.7 for Cit30 and GS30 models, respectively), as confirmed through Monte Carlo cross validation and permutation testing (Supplementary Figure S5.2). The corresponding loadings (Figures 5.7c and 5.7f) showed that many of the metabolic features responsible for class discrimination were common to

the two nanoparticle types, although with varying importance (different VIP colouring of loadings).

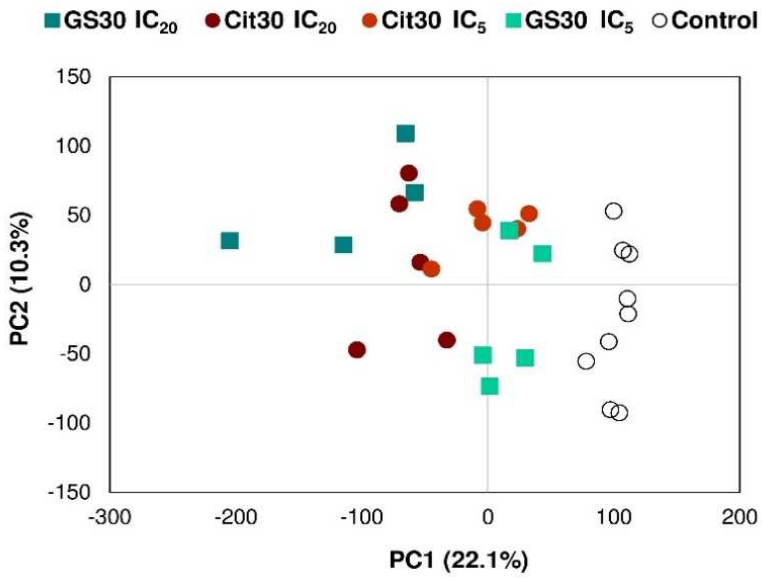

Figure 5.6. Scores scatter plot obtained by PCA of ^{1}H NMR spectra from polar extracts of HepG2 control cells and cells exposed to Cit30 and GS30 AgNPs at respective IC_5 and IC_{20} concentrations.

Spectral integration of individual metabolite signals further allowed the magnitude of those changes to be studied in detail. The more relevant variations (absolute effect size > 0.8) were expressed as the percentage variation in relation to controls and are presented in Figure 5.5b and Supplementary Table S5.2.

The variation of most intracellular polar metabolites was clearly dependent on the nanoparticle concentration, showing higher magnitude at the higher concentration of exposure. Additionally, while Cit30 significantly altered the levels of several metabolites already at the IC_5 concentration, the impact of an equivalent concentration of GS30 on the metabolic profile was smaller (19 vs. 9 metabolites with relevant variations); at the IC_{20} concentration, however, the overall impact of the two nanoparticle types was qualitatively similar (23 metabolite levels consistently affected upon exposure to either Cit30 or GS30). On the other hand, in quantitative terms, there are some differences to point out, as described in the next paragraphs.

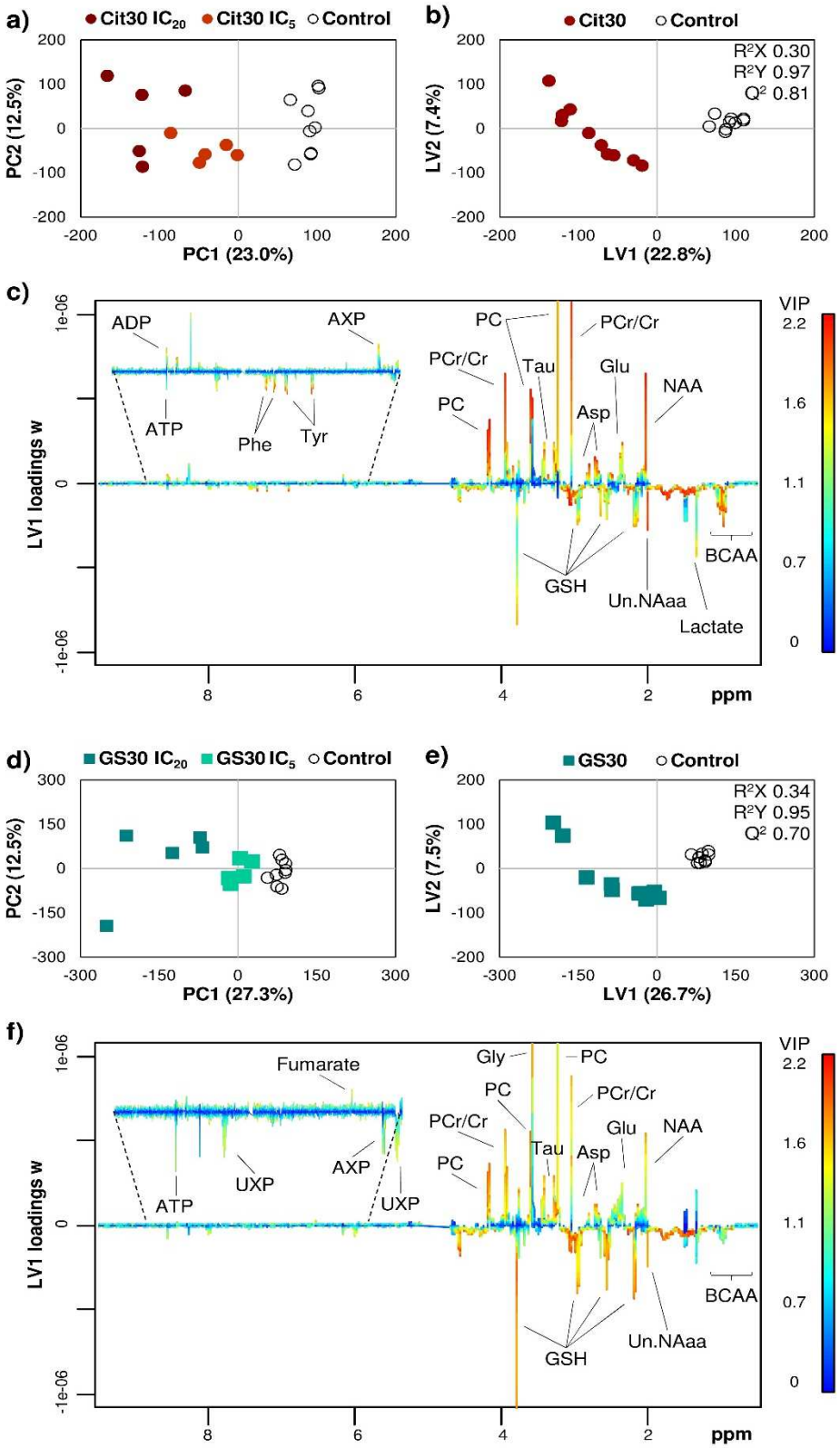

Figure 5.7. Multivariate analysis of ^{1}H NMR spectra from polar extracts of HepG2 control cells and cells exposed to a-c) Cit30, and d-f) GS30 AgNPs: a, d) PCA; b, e) PLS-DA scores scatter plots; and c, f) LV1 loadings *w*, coloured as a function of variable importance to the projection (VIP). BCAA, branched chain amino acids; AXP, ADP+ATP; UXP, UDP+UTP; for other metabolite codes, *vide* legend of Figure 5.5.

The increase in intracellular lactate was especially prominent in cells exposed to GS30 (15-28%), while Cit30 caused a smaller increase (9%) in lactate levels, seen only at the IC_5 concentration. On the other hand, fumarate was more markedly decreased upon exposure to Cit30 (-46% vs. -25% for GS30). In regard to amino acids, the two nanoparticle types induced distinct variations in the levels of intracellular glutamine: cells exposed to the IC_{20} concentration of Cit30 contained significantly higher glutamine levels (10% more in relation to controls) while exposure to GS30 caused a significant decrease (-14%) in glutamine at the IC_5 concentration (and no change at the IC_{20}). As for other amino acids, both nanoparticle types induced significant decreases in glutamate, aspartate, *N*-acetylaspartate and glycine and significant increases in isoleucine, leucine, valine, phenylalanine, methionine and an unassigned *N*-acetylated amino acid; these changes were generally more prominent upon exposure to Cit30 (Figure 5.5b and Supplementary Table S5.2). Moreover, the Cit30 particles additionally caused significant increases in tyrosine and histidine, not seen upon exposure to GS30 AgNPs.

Nanoparticle exposure also affected the levels of several metabolites known to be involved in energy generation and transfer processes, namely creatine, phosphocreatine, ADP and NAD^+ (decreased in relation to control cells), along with ATP and UTP (increased compared to control cells). Also of notice was the specific increase in UDP and the relatively larger increases in ATP and UTP upon exposure to GS30 (near 40% increases vs. 17-21% increases with Cit30). The intracellular levels of reduced glutathione (GSH) increased 17-19% upon exposure to the IC_5 of either Cit30 or GS30, and 23-25% in cells exposed to the IC_{20} of each nanoparticle type; thus, this variation showed little dependency on either the concentration or type of AgNPs. Finally, upon exposure to AgNPs, the endometabolome of HepG2 cells showed significantly decreased levels of phosphocholine (-24 and -32% in Cit30 and GS30-exposed cells, respectively) and of taurine (-22 and -31% in Cit30 and GS30-exposed cells, respectively).

The intracellular metabolic changes induced by citrate and the EG extract used to prepare/stabilise the AgNPs were also assessed. As seen in Figure 5.5b (5^{th} column), citrate (20 μM) did not induce any significant changes in the endometabolome of HepG2 cells. On the other hand, the EG extract (at 0.5 mg/mL) caused relevant changes in several metabolites (Figure 5.5b, 6^{th} column). Among these, some were common to the effects observed in cells exposed to either Cit30 or GS30, namely the increases in lactate, an *N*-acetylated amino acid and UTP, together with the decreases in phosphocholine and taurine.

Hence, it may be postulated that these variations reflected common cellular responses to certain exogenous stimuli rather than nanoparticle-specific effects. Additionally, the increase in UDP, seen only in cells exposed to GS30 or the EG extract (not to Cit30) could possibly reflect the specific interaction of plant extract compounds with the cells. On the other hand, a number of alterations seen upon exposure to AgNPs were not observed in cells exposed to the EG extract; for instance, fumarate, glutamine, glutamate, creatine and phosphocreatine levels were unaffected in those cells, and the variation of several other metabolites was in the opposite direction between cells exposed to AgNPs and the EG extract. To cite a few examples, cells exposed to the EG extract showed increased levels of aspartate, glycine and NAD^+, compared to control cells, and decreased levels of ATP and GSH. This latter change is consistent with the induction of oxidative stress, also suggested by the significantly increased intracellular ROS generation observed upon exposure to the EG extract (Figure 5.4).

Analysis of lipophilic extracts further revealed a few changes in the intracellular lipid composition (Figure 5.5c and Supplementary Table S5.3), most of which were common to cells exposed to Cit30 and GS30. These included increased levels of esterified cholesterol and decreased levels of unsaturated fatty acyl chains and phosphatidylcholine. Additionally, cells exposed to Cit30 presented significantly lower levels of total cholesterol, while cells exposed to GS30 showed a non-significant decrease in phosphatidylethanolamine. Exposure to citrate alone did not alter the lipid profile, whereas the EG extract caused decreases in total and esterified cholesterol and a slight but significant increase in phosphatidylethanolamine, again exhibiting a mode of action different from the nanoparticles.

5.6. Metabolic variations induced by Ag^+ in HepG2 cells

Following a similar strategy to that presented above for the AgNPs, the impact of Ag^+ (from $AgNO_3$) on cell metabolism has been evaluated by NMR analysis of culture medium supernatants, as well as of polar and lipophilic extracts. Sub-toxic concentrations of Ag^+ (IC_5 and IC_{20}) were selected to produce an impact on cell viability similar to that of AgNPs.

The changes in the culture medium arising from cell exposure to Ag^+ are summarised in Figure 5.8a (and in Supplementary Table S5.4), where the results for Cit30 are also included to aid comparative analysis. Similarly to AgNPs, Ag^+ enhanced the consumption of pyruvate, downregulated the consumption of branched chain amino acids and choline, and increased the excretion of lactate, fumarate and glutamate. Unlike for AgNPs, citrate levels were not altered, whereas non-significant decreases in alanine and acetate and a significant increase in allantoin were noted.

The polar extract profiles of Ag^+-treated cells also showed evident differences from control cells, as readily seen through multivariate analysis. Indeed, the PCA scores scatter plot (Figure 5.9a) showed a clear dose-dependent separation between control and exposed samples, further evidenced by PLS-DA (Figure 5.9b, and Supplementary Figure S5.3). The joint analysis of the corresponding loadings (Figure 5.9c) and individual metabolite integrals allowed the most relevant variations to be highlighted and compared to those induced by the AgNPs.

As it can be seen in Figure 5.8b (with support from Supplementary Table S5.5), the intracellular metabolic signature of Ag^+ in HepG2 cells was remarkably similar to that of Cit30 AgNPs. Still, a few differences could be noted. These included larger increases of branched chain and aromatic amino acids, histidine, methionine and threonine, especially at the IC_{20} concentration, along with a less expressive non-significant decrease in NAD^+ and smaller increases in GSH (less than 10%, as compared to ~20% induced by Cit30). Additionally, UTP levels were not increased upon exposure to Ag^+ while pantothenate registered a non-significant increase, not seen with AgNPs.

In what concerns the lipid profile, the most marked effects were the increase in cholesterol esters and the decrease in phosphatidylcholine (Figure 5.8c and Supplementary Table S5.6), similarly to the observations made for AgNPs. However, Ag^+ seemed to produce lesser effects on total cholesterol and unsaturated fatty acyl chains.

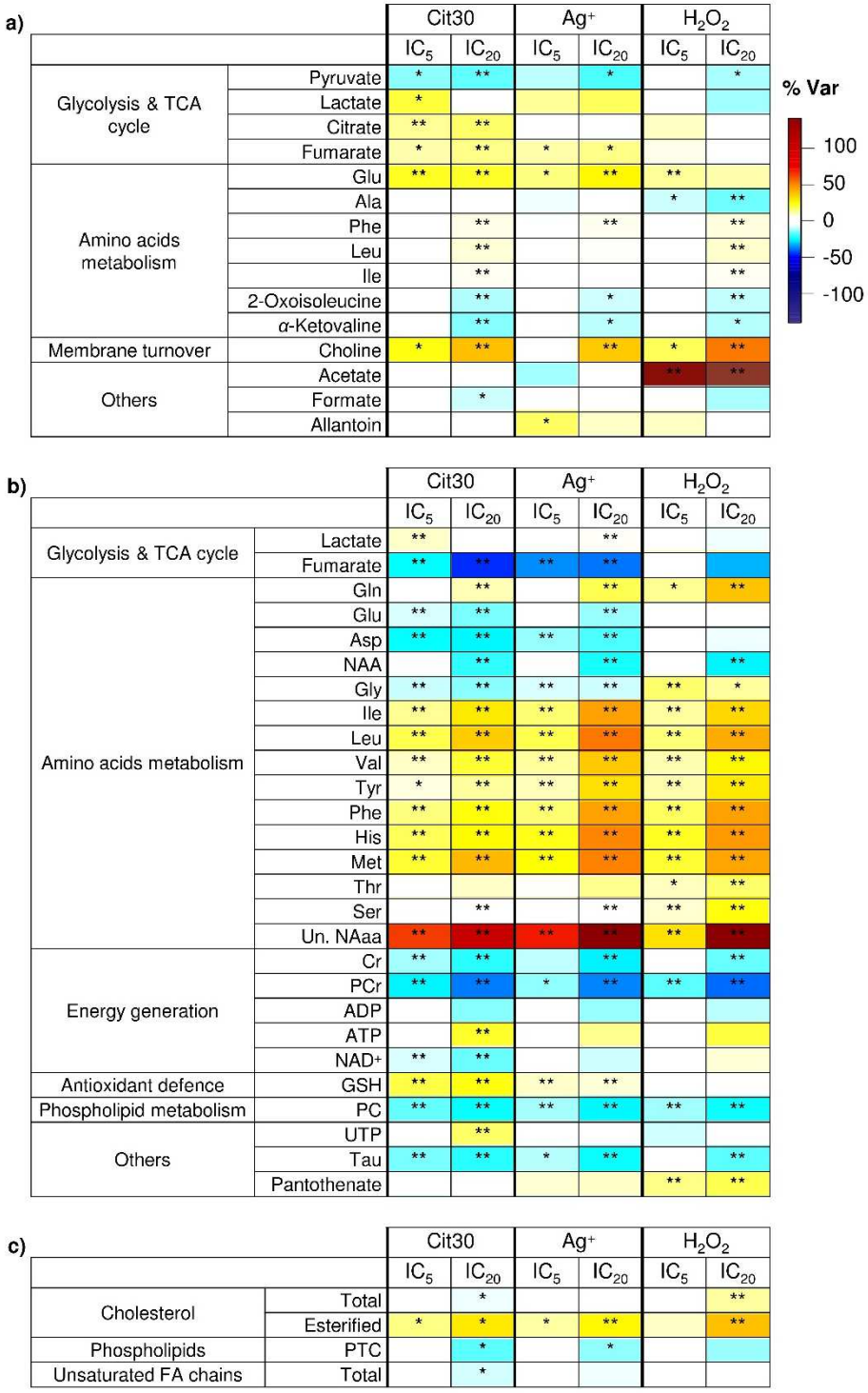

Figure 5.8. Heatmap of the main metabolite variations in a) culture media, b) polar extracts, and c) lipophilic extracts, from HepG2 cells exposed to Cit30, Ag^+, and H_2O_2, at the IC_5 and IC_{20}, coloured according to % variation in relation to controls, from maximum decrease (dark blue) to maximum increase (dark red). * Uncorrected *p*-value < 0.05; ** FDR-corrected *p*-value < 0.05. Three letter code used for amino acids; NAA, *N*-acetylaspartate; Un. NAaa, unidentified *N*-acetylated amino acid; Cr, creatine; PCr, phosphocreatine; ADP/ATP, adenosine di/triphosphate; NAD^+, nicotinamide adenine dinucleotide; GSH, reduced glutathione; PC, phosphocholine; UTP, uridine triphosphate; PTC, phosphatidylcholine; FA, fatty acyl.

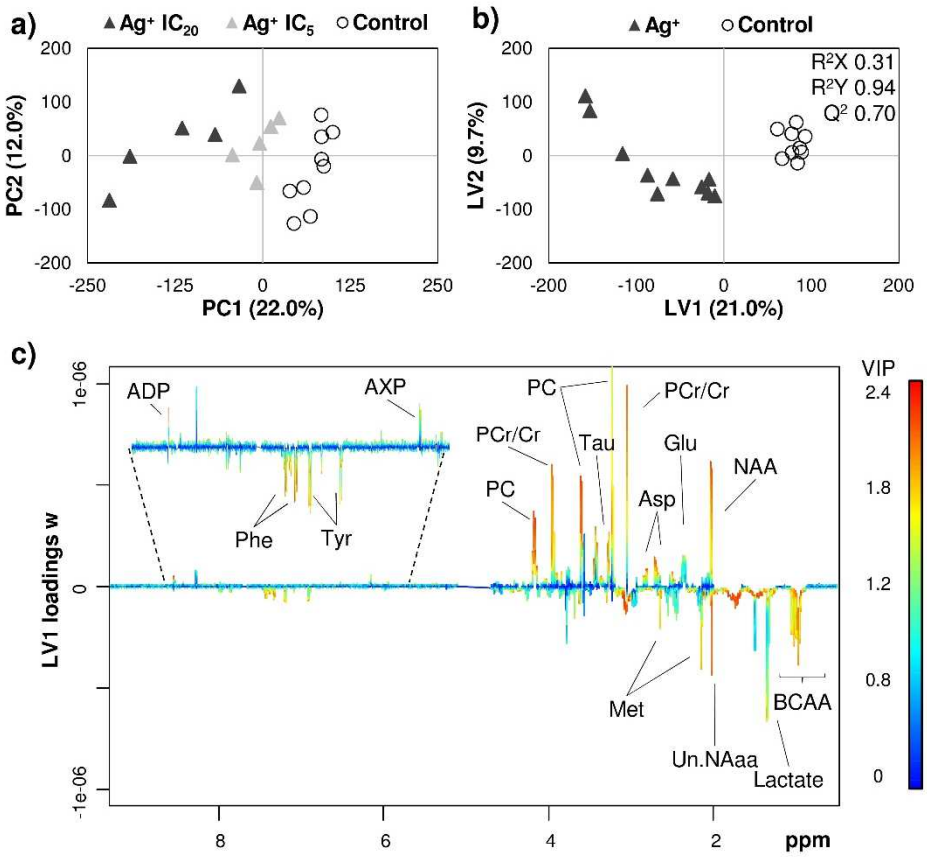

Figure 5.9. Multivariate analysis of ^{1}H NMR spectra from polar extracts of control and Ag^{+}-exposed HepG2 cells: a) PCA, b) PLS-DA scores scatter plots, and c) LV1 loadings *w*, coloured as a function of variable importance to the projection (VIP). BCAA, branched chain amino acids; AXP, ADP+ATP; for other metabolite codes, *vide* legend of Figure 5.8.

5.7. Metabolic variations induced by H_2O_2 in HepG2 cells

The metabolic impact resulting from exposure of HepG2 cells to IC_5 and IC_{20} concentrations of H_2O_2 was also investigated. Analysis of culture medium supernatants showed that, similarly to AgNPs/Ag^{+}, H_2O_2 downregulated the consumption of branched chain amino acids and choline, and increased the excretion of glutamate (Figure 5.8a and Supplementary Table S5.4). However, H_2O_2 did not stimulate the release of citrate nor fumarate to significant extent, while the excretion of lactate and alanine were decreased in H_2O_2-exposed cells relatively to control cells. Another marked variation in the extracellular medium of H_2O_2-treated cells was the increase in acetate levels, which was highly correlated with the pyruvate decrease (r -0.89, $p < 0.005$). This corroborates the known reaction of pyruvate with H_2O_2 whereby acetate is produced. Thus, it is possible that decreased pyruvate levels in the medium of H_2O_2-exposed cells mainly reflected H_2O_2 neutralisation rather than the increased consumption by cells suggested to take place upon exposure to AgNPs/Ag^{+}.

The changes on the intracellular metabolic composition of H_2O_2-exposed cells were revealed based on multivariate analysis and integration of spectral signals from polar extracts. The PCA separation between controls and H_2O_2-exposed cells (Figure 5.10a) was not as clear for the low concentration (IC_5) samples, thus rendering a less robust discrimination by PLS-DA (Figure 5.10b, and Supplementary Figure S5.4). Still, a number of relevant effects in polar metabolites could be identified (Figures 5.8b and 5.8c, and Supplementary Table S5.5). Many of these effects were common to those induced by AgNPs/Ag^+, namely the increased intracellular levels of several amino acids and of ATP (although non-significantly in the latter case), along with significantly reduced levels of *N*-acetylaspartate, creatine, phosphocreatine, phosphocholine and taurine. On the other hand, the intracellular composition of HepG2 cells was differently affected by H_2O_2 in the following aspects: lactate showed a non-significant decrease (while it increased in AgNPs/Ag^+-exposed cells); fumarate showed a lower, non-significant decrease; glutamate and aspartate (seen to decrease upon exposure to AgNPs/Ag^+) did not vary significantly; glycine and serine increased; NAD^+, UTP or GSH levels remained largely unaffected; pantothenate showed a significant increase not seen in AgNPs/Ag^+-treated cells.

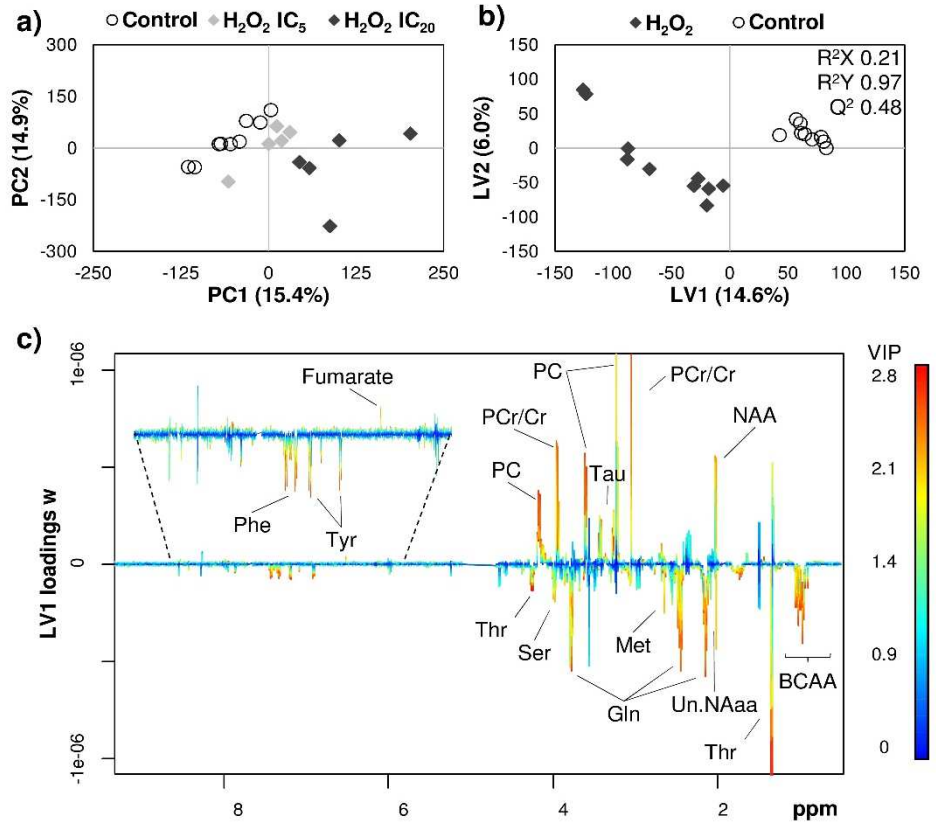

Figure 5.10. Multivariate analysis of ^{1}H NMR spectra from polar extracts of control and H_2O_2-exposed HepG2 cells: a) PCA, b) PLS-DA scores scatter plots, and c) LV1 loadings *w*, coloured as a function of variable importance to the projection (VIP). BCAA, branched chain amino acids; for other metabolite codes, *vide* legend of Figure 5.8.

As for the lipid composition (Figure 5.8c and Supplementary Table S5.6), H_2O_2-exposed cells showed increased levels of both total and esterified cholesterol and a non-significant decrease in phosphatidylcholine.

5.8. Discussion of metabolic variations in HepG2 cells

Exposure of HepG2 cells to silver nanoparticles with a metallic core diameter of 30 nm and coated with either citrate or a plant-derived phenolic/sugar layer, at sub-toxic concentrations, was found to induce profound changes in the cellular metabolome, reflecting metabolic adaptations within different pathways.

Based on the integrated analysis of the metabolite changes described above (Figure 5.5), Cit30 and GS30 AgNPs may be proposed to significantly affect HepG2 cells energy production processes, as summarised schematically in Figure 5.11. A first interesting observation is that cells increased their intracellular ATP production in the presence of AgNPs. The opposite effect, i.e. ATP depletion, has been implicated in the cytotoxicity of AgNPs (Zhang *et al.*, 2014b), as well as of other nanoparticles (Dong *et al.*, 2009; Bhattacharjee *et al.*, 2013; Yu *et al.*, 2013a). In particular, a low ATP yield in human fibroblasts and glioblastoma cells exposed to AgNPs has been associated to mitochondrial dysfunction caused by structural damage induced by nanoparticle deposition and/or the induction of oxidative stress (AshaRani *et al.*, 2009). Furthermore, it has been demonstrated that AgNPs can directly inhibit the activity of liver mitochondrial ATPase, thus reducing ATP synthesis (Chichova *et al.*, 2014), and that AgNPs can impair oxidative phosphorylation in liver mitochondria (Costa *et al.*, 2010; Teodoro *et al.*, 2011). Thus, the fact that, in the present work, AgNPs did not reduce ATP levels can be interpreted as an indicator of low cytotoxicity, in consonance with the small decreases (5-20%) in MTT-assessed cell viability.

Our results are also in contrast with those reported by Chen and co-workers whereby HepG2 cells (and other cell types) exposed to non-cytotoxic concentrations of AgNPs (up to 8 µg/mL) decreased intracellular ATP (Chen *et al.*, 2014). In that work, the ATP depletion was related to a shift in energy metabolism from oxidative phosphorylation and fatty acid oxidation to glycolysis, based on increased intracellular pyruvate, lactate, triglyceride and cholesterol levels. Contrastingly, our data suggest an intensification of pyruvate use, down to the TCA cycle and oxidative phosphorylation, as supported by increased pyruvate consumption from the culture medium and decreased intracellular levels of several TCA

cycle anaplerotic substrates (glycine, *N*-acetylaspartate, aspartate and glutamate) (Figure 5.11).

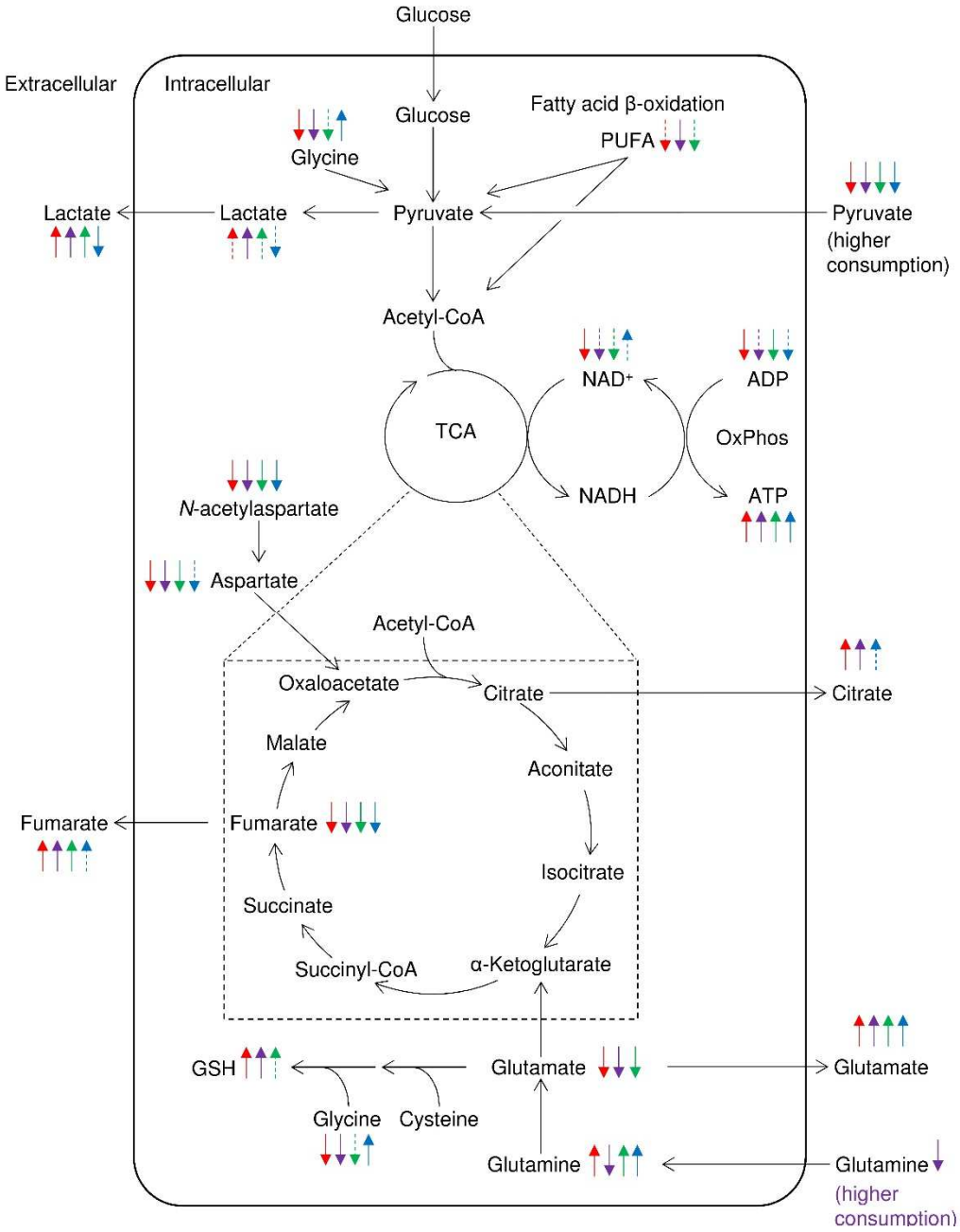

Figure 5.11. Schematic diagram of the putative effects of Cit30 (red arrows), GS30 (purple arrows), Ag^+ (green arrows), and H_2O_2 (blue arrows), on glycolysis and the TCA cycle. Dashed arrows indicate |% variation| < 10%.

Additionally, the decrease in unsaturated fatty acyl chains, possibly reflecting their oxidation for energy production, together with decreased intracellular fumarate and increased release of citrate and fumarate, further support the enhanced activity of the TCA

cycle. Altogether, our results suggest a metabolic response of HepG2 cells to AgNPs distinct from that reported by (Chen *et al.*, 2014). It may be hypothesised that the different physicochemical properties of the AgNPs used account for this discrepancy; the cited authors used PVP-coated AgNPs with a core diameter of 25 nm and a 76 nm hydrodynamic diameter in water, sizes which are actually comparable to those of the AgNPs used in this work (Table 5.1). Another possible explanation could relate to the supplementation of the culture medium used in this work with sodium pyruvate, according to the specific recommendations for culturing HepG2 cells (*vide* experimental section). Sheline and co-authors reported that adding pyruvate to the medium of neuronal cells attenuated the toxic effects induced by zinc ions, namely by mitigating ATP loss and cell death (Sheline *et al.*, 2000). This effect was attributed to the ability of pyruvate to serve as an energy substrate and to regenerate NAD^+ through conversion into lactate. Indeed, we have also seen increased production of lactate accompanying intensified pyruvate metabolism. Importantly, in the specific case of hepatocytes, the medium supplementation with pyruvate should better match the *in vivo* situation, as the liver is largely responsible for pyruvate recycling (produced from lactate by other organs) and gluconeogenesis.

Another literature report has shown that HepG2 cells exposed to 5 nm AgNPs for a short period (1-6 hours) at concentrations inducing 10-40% decreases in cell viability displayed decreased glucose consumption and lactate release (Lee *et al.*, 2016a); this effect was found to be size-dependent as it was not observed for 100 nm AgNPs. Also, the authors have shown that this alteration in glucose metabolism was tightly dependent on ROS production. Specifically, the downregulation of lactate release was accompanied by a progressive increase in ROS generation right from 1 h of exposure, while normal lactate release was restored in the presence of a ROS scavenger. Excessive ROS production has often been highlighted as a main mechanism through which AgNPs exert cytotoxicity; in HepG2 and other liver cells, exposure to AgNPs at cytotoxic concentrations was reported to induce increased intracellular ROS, along with decreased levels of reduced glutathione (GSH), postulated to reflect persistent oxidative stress (Piao *et al.*, 2011; Vrček *et al.*, 2016; Avalos *et al.*, 2014). Interestingly, in the present work, intracellular ROS did not increase under the exposure conditions tested (IC_{20}, 24h – Figure 5.4), while intracellular GSH was significantly increased in AgNPs-treated cells. These results agree with earlier works where HepG2 cells (Jain *et al.*, 2009) or primary mouse liver cells (Arora *et al.*, 2009) increased GSH levels (~1.1 fold), along with superoxide dismutase activity, upon exposure to AgNPs at ½ IC_{50} (corresponding to ~10 % decrease in cell viability).

Our results further showed significantly decreased levels of creatine and phosphocreatine, possibly reflecting reprogramming of energy storage and transmission. A similar observation has been made for HepG2 cells exposed to graphene nanosheets (Jiao *et al.*, 2014).

Additionally, AgNPs-treated cells showed significant increases in branched chain amino acids, aromatic amino acids, histidine and methionine, which were especially pronounced with Cit30. Increases in those amino acids (and some others) have been previously identified as part of the metabolic signature of drug-induced autophagy in tumour cells (Lin *et al.*, 2016). Autophagy is a catabolic process by which unnecessary or dysfunctional cellular components are sequestered into double-membrane vesicles (autophagosomes) and targeted for lysosomal degradation (Jiang and Mizushima, 2014). Recently, a variety of nanoparticles have been shown to induce autophagy, leading either to increased cell death or, paradoxically, to promotion of cell survival (Zabirnyk *et al.*, 2007). PVP-coated silver nanoparticles were shown to induce a size-dependent autophagic response in HepG2 cells, even at relatively low or non-cytotoxic doses. Furthermore, AgNPs-induced autophagy was shown to play a cytoprotective role at sub-toxic concentrations in HepG2 (Mishra *et al.*, 2016) and HeLa cells (Lin *et al.*, 2014). Thus, we may hypothesise that the observed increase in several amino acids could relate to an autophagic response, thus providing additional substrates for energy production and aiding cell survival.

Phospholipid metabolism also seemed to be affected upon exposure to both nanoparticle types, as suggested by decreased choline consumption from the medium along with decreased levels of phosphocholine and phosphatidylcholine. Phosphatidylcholines are major components of cellular membranes, synthesised mainly through the CDP-choline pathway, which is part of the Kennedy pathway (Chang and Carman, 2008). The CDP-choline pathway begins with the uptake of exogenous choline into the cell and proceeds with the phosphorylation of choline to form phosphocholine (Figure 5.12a). In AgNPs-treated cells, we found a significant negative correlation between choline uptake and phosphatidylcholine (Figure 5.12b), suggesting the downregulation of phospholipid synthesis. This effect was especially pronounced in GS30-treated cells, where significant correlations were found between several compounds of the CDP-choline pathway (Figure 5.12b). Also, in GS30-treated cells, the intermediates of this pathway additionally showed a strong correlation with the increase in UTP, possibly reflecting its role as a CTP precursor (Figure 5.12a). Furthermore, cholesterol esters increased in exposed cells, which could reflect a form of biologically inert storage (detoxification) of fatty acids.

a)

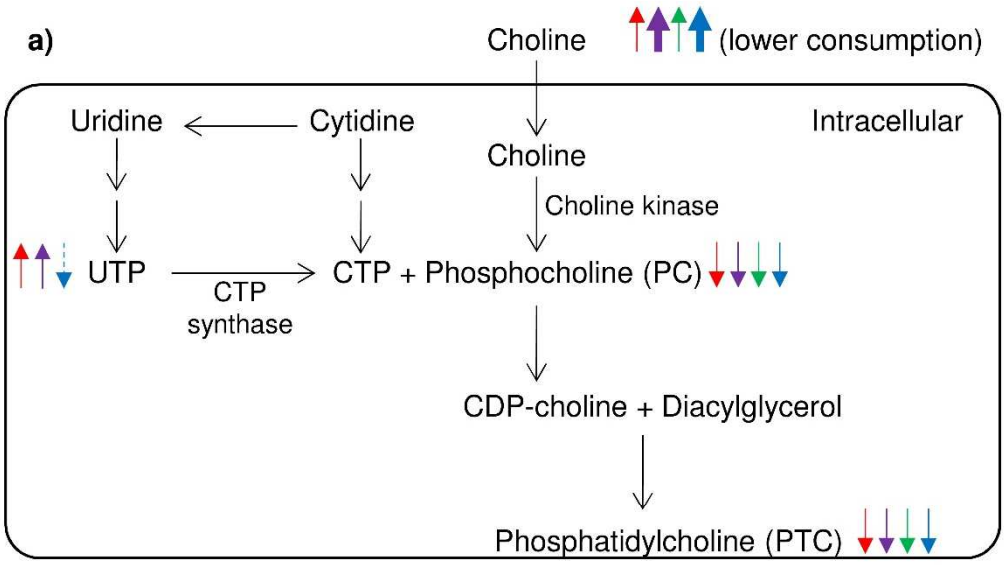

b)

	Choline (ext)	PC	PTC	UTP
Choline (ext)	1	-0.78 * -0.98 **	-0.96 ** -0.93 **	|r| < 0.75 0.95 **
PC	-0.78 * -0.98 **	1	0.82 * 0.86	|r| < 0.75 -0.96 **
PTC	-0.96 ** -0.93 **	0.82 * 0.86	1	|r| < 0.75 -0.95 **
UTP	|r| < 0.75 0.95 **	|r| < 0.75 -0.96 **	|r| < 0.75 -0.95 **	1

Figure 5.12. a) Schematic diagram of phosphatidylcholine biosynthesis via the CDP-choline pathway. Arrows indicate effects caused by Cit30 (red arrows), GS30 (purple arrows), Ag^+ (green arrows), and H_2O_2 (blue arrows); dashed arrows indicate |% variation| < 10%; thick arrows indicate |% variation| > 50%. b) Pearson correlation coefficients (*r*) between metabolites involved in phosphatidylcholine biosynthesis, found to vary after HepG2 exposure to Cit30 (red) or GS30 (purple) AgNPs. ext, extracellular; * $p < 0.05$; ** *p*-value < 0.005.

Although the putative AgNP-induced biochemical events described above were largely common to both nanoparticle types, the different extent of some variations suggests that Cit30 had a greater impact on the TCA cycle and protein degradation, whereas GS30 induced a stronger downregulation of phospholipid synthesis. Moreover, HepG2 cells appeared to use glutamine differently depending on exposure to Cit30 or GS30; while this amino acid increased in Cit30-treated cells (eventually reflecting the autophagic response seen for other amino acids), GS30 induced a higher glutamine consumption from the medium and decreased intracellular glutamine levels, suggesting higher glutaminolytic activity. Interestingly, the metabolic effects of the EG extract used to prepare and stabilise the GS30 were strikingly different from those of the nanoparticles themselves. For instance,

ATP and GSH decreased, most amino acids varied to a lesser extent and in opposite sense, creatine and phosphocreatine remained unaltered, and so did the levels of unsaturated fatty acyl chains and phosphatidylcholine, while cholesterol esters decreased. This could reflect not only the modified chemical nature of the compounds coating the GS30 AgNPs (and eventually released into the medium) compared to those present in the EG extract, but also the expectedly different uptake and interaction of nanoparticles and soluble organic compounds with cells.

Based on the high similarity between the AgNPs metabolic signature and the effects induced by Ag^+, described in section 5.6, it may be argued that the release of Ag^+ from AgNPs largely explains the interaction of nanoparticles with cells at the biochemical level. However, differences like the higher increase in several amino acids (possibly reflecting protein degradation), the less pronounced increases in ATP or GSH in Ag^+-exposed cells, together with the increase in the oxidative stress marker allantoin (product of uric acid oxidation) suggest that cells are less able to cope with the amount of ionic silver administered at once than with the gradual intracellular release from AgNPs. Indeed, this is consistent with the much larger cytotoxicity of Ag^+ compared to AgNPs (IC_{50} 1.19 and 18.9 µg/mL, respectively).

The H_2O_2 metabolic signature revealed a similar impact to AgNPs/Ag^+ in regard to putative autophagy-related protein degradation and phospholipid metabolism. On the other hand, some ROS-specific effects may be proposed. For instance, unlike AgNPs/Ag^+, H_2O_2 reduced lactate intra- and extracellular levels, as well as alanine excretion, suggesting downregulation of fermentative glycolysis, in agreement with other studies (Brand *et al.*, 1999; Colussi *et al.*, 2000; Kuehne *et al.*, 2015). On the other hand, H_2O_2 had a lesser impact on TCA cycle intermediates and anaplerotic substrates, and did not alter GSH levels. In liver cells, the enzyme catalase is an especially effective system to detoxify H_2O_2, therefore, similarly to the observations of others (Alia *et al.*, 2005), it is possible that little GSH was dedicated to H_2O_2 reduction under the exposure conditions tested. In addition, H_2O_2 induced a significant increase in pantothenate (vitamin B5), not seen upon exposure to AgNPs/Ag^+. This metabolite is a precursor of coenzyme A (CoA), which has a crucial role in the synthesis and oxidation of fatty acids, the biosynthesis of cholesterol, and pyruvate oxidation through the TCA cycle (Leonardi *et al.*, 2005; Snyder *et al.*, 2015). As mammals do not synthesise pantothenate *de novo*, its intracellular increase should reflect increased

consumption from the medium (not confirmed due to spectral overlap) and/or reduced intracellular use in the processes mentioned above.

Overall, the metabolic signature of AgNPs/Ag^+ in HepG2 cells suggests that, under the conditions tested, these cells were able to activate metabolism-mediated protective mechanisms. Notably, a protective response has also been found *in vivo* in the liver of mice intravenously injected with PEG-coated AgNPs (core diameter of 30 nm) (paper submitted by our group). Specifically, the liver of treated mice displayed upregulated synthesis of glycogen, lipolysis, fatty acid oxidation and production of antioxidative molecules (including GSH). Thus, our results demonstrate that *in vitro* metabolomics shows good potential in aiding to explain and predict the *in vivo* outcomes of nanoparticle exposure.

Supplementary information to Chapter 5

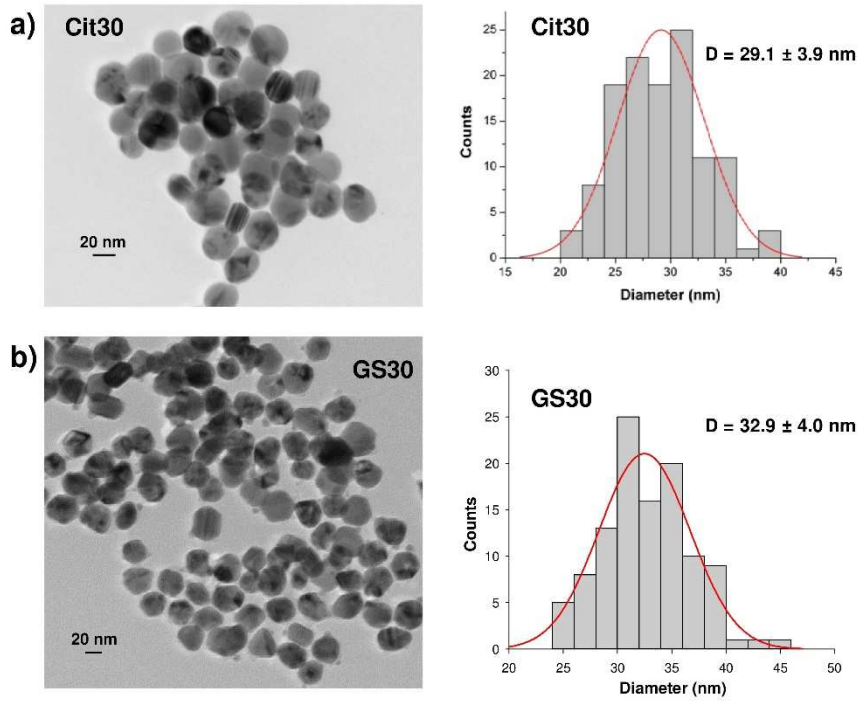

Figure S5.1. TEM images (left) and particle size histograms (right) of a) Cit30 and b) GS30 AgNPs. Data acquired at CICECO (UA) by Dr A. L. Daniel-da-Silva (Cit30) and Dr R. Pinto (GS30).

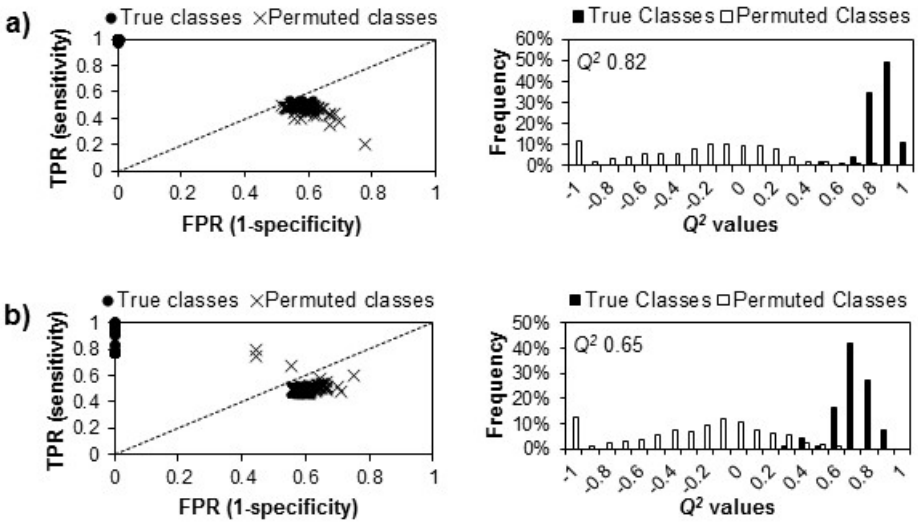

Figure S5.2. ROC space (left) and Q^2 histogram (right) obtained by MCCV and permutation testing of the PLS-DA models of polar extracts, corresponding to exposure to: a) Cit30 (sensitivity 98.3%, specificity 100%, classification rate 99.1%), and b) GS30 (sensitivity 77.0%, specificity 100%, classification rate 87.9%). TPR: true positive rate; FPR: false positive rate.

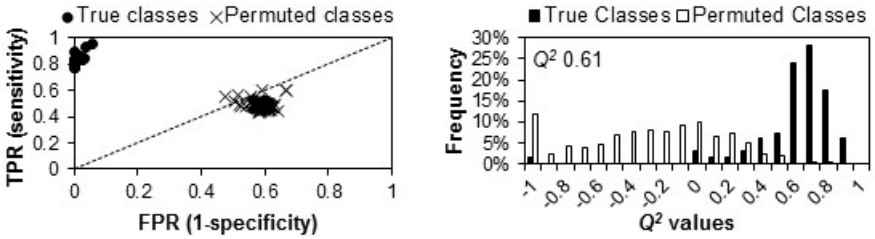

Figure S5.3. ROC space (left) and Q^2 histogram (right) obtained by MCCV and permutation testing of the PLS-DA models of polar extracts, corresponding to Ag^+ exposure (sensitivity 84.1%, specificity 97.8%, classification rate 90.6%). TPR: true positive rate; FPR: false positive rate.

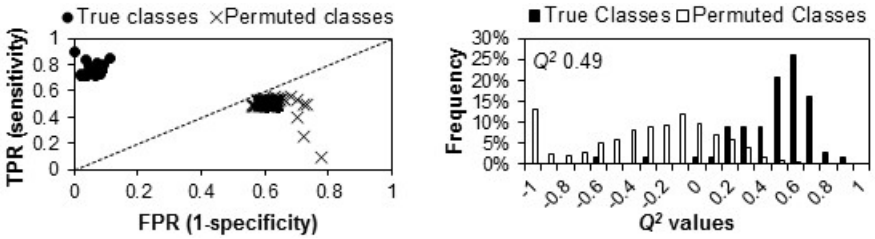

Figure S5.4. ROC space (left) and Q^2 histogram (right) obtained by MCCV and permutation testing of the PLS-DA models of polar extracts, corresponding to H_2O_2 exposure (sensitivity 74.5%, specificity 92.4%, classification rate 83.0%). TPR: true positive rate; FPR: false positive rate.

Table S5.1. Main metabolite variations in culture medium of HepG2 cells exposed to Cit30 and GS30 AgNPs at respective IC_5 and IC_{20} concentrations, and to citrate and EG extract (at the maximum amounts present when IC_{20} concentrations of AgNPs were administered to cells), in relation to culture medium of control cells, expressed as % variation (%var) and respective error (±), effect size (ES), *p*-value (*p*), and FDR-adjusted *p*-value (FDR). The variations with |ES| < 0.8 (or standard error > |ES|, or mean error > |% variation|) were considered null.

		Cit30		GS30		Citrate	EG extract
		IC_5	IC_{20}	IC_5	IC_{20}		
Pyruvate	%var	-13.81	-17.27	0	-14.32	0	15.30
	±	5.21	4.75		5.29		4.56
	ES	-1.66	-2.38	0	-1.66	0	1.74
	p	0.0239	0.0054		0.0227		0.0187
	FDR	0.1122	0.0207		0.0576		0.1187
Lactate	%var	20.23	0	18.75	16.62	0	21.24
	±	6.43		7.01	8.01		7.62
	ES	1.66	0	1.31	1.02	0	1.34
	p	0.0259		0.0584	0.1172		0.0553
	FDR	0.1122		0.4437	0.1856		0.1910
Citrate	%var	13.19	16.54	10.33	5.80	16.36	9.99
	±	1.17	0.98	3.52	3.53	3.09	3.45
	ES	5.79	8.71	1.64	0.95	2.52	1.63
	p	3.93E-05	1.65E-06	0.0285	0.1572	0.0017	0.0302
	FDR	0.0007	0.0001	0.4437	0.2297	0.0652	0.1273
Fumarate	%var	11.19	13.95	4.65	13.43	0	0
	±	2.72	3.78	3.52	3.34		
	ES	2.61	2.01	0.81	2.36	0	0
	p	0.0285	0.0113	0.2556	0.0144		
	FDR	0.1122	0.0308	0.8274	0.0395		
Glutamine	%var	-3.93	0	-7.41	0	0	0
	±	2.57		2.71			
	ES	-0.89	0	-1.52	0	0	0
	p	0.1628		0.0402			
	FDR	0.3701		0.4437			
Glutamate	%var	22.17	21.72	13.38	24.59	0	0
	±	1.63	2.01	2.59	3.19		
	ES	7.23	5.49	2.59	3.62	0	0
	p	9.11E-06	3.02E-05	0.0049	0.0015		
	FDR	0.0003	0.0006	0.1857	0.0125		
Phenylalanine	%var	3.50	6.56	0	5.19	0	0
	±	0.88	0.69		1.02		
	ES	2.13	5.11	0	2.93	0	0
	p	0.0092	0.0001		0.0019		
	FDR	0.0639	0.0008		0.0125		
Leucine	%var	2.36	7.83	0	8.76	0	0
	±	1.16	1.13		1.30		
	ES	1.11	3.67	0	3.41	0	0
	p	0.0913	0.0005		0.0023		
	FDR	0.2676	0.0036		0.0125		
Isoleucine	%var	1.60	5.70	0	6.08	0	0
	±	0.80	0.81		0.91		
	ES	1.11	3.79	0	3.54	0	0
	p	0.0916	0.0004		0.0008		
	FDR	0.2676	0.0036		0.0125		
2-Oxoisoleucine	%var	0	-10.95	0	-9.41	0	0
	±		3.06		3.02		
	ES	0	-2.12	0	-1.76	0	0
	p		0.0081		0.0244		
	FDR		0.0266		0.0579		
α-Ketovaline	%var	-4.46	-14.33	4.26	-12.99	0	0
	±	2.93	3.44	2.64	3.01		
	ES	-0.89	-2.54	0.84	-2.47	0	0
	p	0.1636	0.0032	0.1845	0.0081		
	FDR	0.3701	0.0146	0.8274	0.0281		

		Cit30		GS30		Citrate	EG extract
		IC_5	IC_{20}	IC_5	IC_{20}		
Choline	%var	23.53	38.47	8.02	57.15	0	0
	±	5.07	4.45	3.86	3.81		
	ES	2.23	3.88	1.14	6.31	0	0
	p	0.0082	0.0006	0.0872	2.13E-05		
	FDR	0.0639	0.0036	0.4733	0.0008		
Acetate	%var	0	0	0	16.65	0	27.19
	±				4.01		2.71
	ES	0	0	0	2.20	0	5.71
	p				0.0068		0.0012
	FDR				0.0281		0.0237
Formate	%var	0	-8.72	7.45	-6.52	0	11.31
	±		2.96	3.34	4.20		3.15
	ES	0	-1.67	1.22	-0.90	0	1.94
	p		0.0264	0.0701	0.1550		0.0118
	FDR		0.0627	0.4437	0.2297		0.0900

Table S5.2. Main metabolite variations in polar extracts of HepG2 cells exposed to Cit30 and GS30 AgNPs at respective IC_5 and IC_{20} concentrations, and to citrate and EG extract (at the maximum amounts present when IC_{20} concentrations of AgNPs were administered to cells), in relation to controls, expressed as % variation (%var) and respective error (±), effect size (ES), *p*-value (*p*), and FDR-adjusted *p*-value (FDR). The variations with |ES| < 0.8 (or standard error > |ES|, or mean error > |% variation|) were considered null.

		Cit30		GS30		Citrate	EG Extract
		IC_5	IC_{20}	IC_5	IC_{20}		
Lactate	%var	8.84	0	15.28	28.15	0	16.74
	±	1.72		3.72	2.90		4.33
	ES	2.81	0	2.14	4.91	0	1.95
	p	0.0014		0.0073	0.0001		0.0119
	FDR	0.0056		0.0642	0.0006		0.0374
Fumarate	%var	-24.86	-45.63	0	-25.34	0	0
	±	9.14	9.63		20.04		
	ES	-1.77	-3.51	0	-0.83	0	0
	p	0.0167	0.0008		0.1869		
	FDR	0.0324	0.0023		0.2337		
Glutamine	%var	0	10.48	-14.51	-4.12	0	0
	±		2.51	2.79	2.18		
	ES	0	2.27	-3.02	-1.04	0	0
	p		0.0071	0.0029	0.1100		
	FDR		0.0138	0.0515	0.1481		
Glutamate	%var	-7.64	-15.43	0	-20.15	9.03	0
	±	1.70	1.86		3.73	5.53	
	ES	-2.67	-5.15	0	-3.44	0.83	0
	p	0.0030	4.29E-05		0.0006	0.1533	
	FDR	0.0089	0.0002		0.0028	0.9712	
Aspartate	%var	-24.53	-25.13	-7.95	-18.31	0	13.05
	±	3.14	4.33	4.22	5.98		3.72
	ES	-5.09	-3.80	-1.19	-1.93	0	1.98
	p	2.03E-05	0.0004	0.0944	0.0119		0.0164
	FDR	0.0002	0.0013	0.3004	0.0261		0.0410
N-acetylaspartate	%var	0	-21.15	9.83	-16.02	0	13.06
	±		6.68	5.60	5.70		4.49
	ES	0	-2.02	0.91	-1.71	0	1.52
	p		0.0089	0.1493	0.0203		0.0321
	FDR		0.0152	0.4020	0.0419		0.0512
Glycine	%var	-8.88	-14.04	-2.45	-13.07	0	22.70
	±	2.24	2.51	1.37	3.10		2.50
	ES	-2.37	-3.43	-0.98	-2.41	0	4.26
	p	0.0094	0.0022	0.1255	0.0089		0.0009
	FDR	0.0205	0.0051	0.3661	0.0208		0.0055
Isoleucine	%var	13.33	28.82	-4.10	17.05	0	-6.11
	±	2.61	2.31	1.25	2.47		2.11
	ES	2.74	6.23	-1.89	3.36	0	-1.61
	p	0.0017	1.66E-05	0.0130	0.0021		0.0301
	FDR	0.0061	0.0001	0.0757	0.0065		0.0512
Leucine	%var	18.93	35.56	-1.69	23.92	0	-5.13
	±	2.05	2.25	1.11	2.89		1.64
	ES	4.81	7.68	-0.84	3.86	0	-1.72
	p	3.04E-05	2.06E-06	0.1769	0.0015		0.0247
	FDR	0.0003	2.12E-05	0.4423	0.0060		0.0455
Valine	%var	9.23	20.68	-4.24	14.31	0	-5.89
	±	2.41	2.14	1.65	2.99		1.63
	ES	2.09	5.01	-1.45	2.36	0	-2.07
	p	0.0069	0.0001	0.0393	0.0089		0.0095
	FDR	0.0187	0.0002	0.1529	0.0208		0.0334
Tyrosine	%var	7.17	12.40	0	8.54	0	-5.80
	±	2.61	2.71		3.97		3.23
	ES	1.52	2.46	0	1.08	0	-0.98
	p	0.0292	0.0026		0.1069		0.1335
	FDR	0.0511	0.0058		0.1481		0.1947
Phenylalanine	%var	14.76	24.15	0	15.47	0	0
	±	2.84	3.63		4.68		
	ES	2.77	3.39	0	1.65	0	0
	p	0.0014	0.0009		0.0260		
	FDR	0.0056	0.0025		0.0479		

		Cit30		GS30		Citrate	EG Extract
		IC_5	IC_{20}	IC_5	IC_{20}		
Histidine	%var	17.73	25.32	0	0	0	0
	±	3.29	5.65				
	ES	2.83	2.27	0	0	0	0
	p	0.0011	0.0087				
	FDR	0.0056	0.0152				
Methionine	%var	20.83	40.13	5.63	31.51	0	-7.52
	±	3.96	1.37	2.27	4.68		2.14
	ES	2.72	13.96	1.29	3.02	0	-1.97
	p	0.0075	1.53E-07	0.0643	0.0042		0.0149
	FDR	0.0187	5.36E-06	0.2251	0.0113		0.0402
Unidentified *N*-acetylated amino acid	%var	64.10	101.84	28.87	116.49	0	61.65
	±	2.84	3.82	2.61	3.40		7.28
	ES	9.78	10.09	5.96	11.44	0	3.36
	p	1.98E-07	1.14E-06	0.0002	9.51E-07		0.0020
	FDR	6.93E-06	2.00E-05	0.0071	3.33E-05		0.0088
Creatine	%var	-11.73	-21.72	0	-17.18	0	0
	±	3.51	4.07		3.20		
	ES	-2.03	-3.42	0	-3.75	0	0
	p	0.0205	0.0010		0.0023		
	FDR	0.0377	0.0025		0.0067		
Phosphocreatine	%var	-25.58	-37.39	-13.01	-43.62	0	0
	±	5.02	5.22	5.16	6.16		
	ES	-3.34	-5.03	-1.62	-5.61	0	0
	p	0.0007	4.95E-05	0.0317	0.0001		
	FDR	0.0041	0.0002	0.1421	0.0006		
ADP	%var	0	-14.10	0	-9.44	0	-52.82
	±		9.61		6.50		4.46
	ES	0	-0.90	0	-0.85	0	-11.14
	p		0.1679		0.1754		0.0002
	FDR		0.2176		0.2273		0.0018
ATP	%var	0	21.43	0	36.74	0	-64.69
	±		6.68		9.72		9.10
	ES	0	1.66	0	1.72	0	-6.98
	p		0.0222		0.0218		0.0001
	FDR		0.0324		0.0424		0.0013
NAD^+	%var	-7.78	-16.51	0	-9.22	0	13.38
	±	1.83	2.38		3.92		2.58
	ES	-2.53	-4.32	0	-1.38	0	2.83
	p	0.0030	0.0003		0.0456		0.0020
	FDR	0.0089	0.0011		0.0733		0.0088
UDP	%var	0	0	0	32.97	0	44.13
	±				10.68		12.95
	ES	0	0	0	1.51	0	1.52
	p				0.0349		0.0322
	FDR				0.0611		0.0512
UTP	%var	0	16.85	0	38.77	0	41.30
	±		4.89		4.02		3.14
	ES	0	1.81	0	4.46	0	6.29
	p		0.0133		0.0001		1.59E-05
	FDR		0.0202		0.0009		0.0003
GSH	%var	19.45	23.47	17.21	25.65	0	-13.75
	±	3.19	2.67	4.36	3.46		3.74
	ES	3.17	4.49	2.03	3.78	0	-2.41
	p	0.0005	0.0001	0.0095	0.0003		0.0068
	FDR	0.0038	0.0004	0.0666	0.0020		0.0264
Phosphocholine	%var	-17.05	-24.35	-11.36	-31.52	0	-9.08
	±	1.68	2.29	2.06	2.79		2.88
	ES	-6.33	-6.93	-3.85	-8.29	0	-1.92
	p	1.48E-05	2.42E-06	0.0049	8.41E-06		0.0128
	FDR	0.0002	2.12E-05	0.0571	0.0001		0.0374
Taurine	%var	-15.46	-21.58	-10.99	-31.43	-4.71	-20.65
	±	4.64	6.05	4.00	5.89	2.99	3.36
	ES	-2.06	-2.28	-1.58	-3.45	-0.86	-3.80
	p	0.0106	0.0091	0.0325	0.0018	0.1387	0.0005
	FDR	0.0218	0.0152	0.1421	0.0063	0.9712	0.0038

Table S5.3. Main metabolite variations in lipophilic extracts of HepG2 cells exposed to Cit30 and GS30 AgNPs at respective IC_5 and IC_{20} concentrations, and to citrate and EG extract (at the maximum amounts present when IC_{20} concentrations of AgNPs were administered to cells), in relation to controls, expressed as % variation (%var) and respective error (±), effect size (ES), *p*-value (*p*), and FDR-adjusted *p*-value (FDR). The variations with |ES| < 0.8 (or standard error > |ES|, or mean error > |% variation|) were considered null.

		Cit30		GS30		Citrate	EG extract
		IC_5	IC_{20}	IC_5	IC_{20}		
Total cholesterol	%var	0	-6.20	0	-4.27	0	-17.25
	±		2.34		2.53		1.37
	ES	0	-1.56	0	-1.06	0	-8.47
	p		0.0297		0.1589		7.78E-06
	FDR		0.0837		0.2393		0.0002
Cholesterol ester	%var	14.64	29.12	0	30.19	0	-18.08
	±	4.87	5.45		6.49		4.82
	ES	1.60	2.66	0	2.48	0	-2.35
	p	0.0326	0.0051		0.0180		0.0046
	FDR	0.4566	0.0837		0.0503		0.0214
PTC	%var	0	-17.84	0	-22.84	0	0
	±		6.54		6.94		
	ES	0	-1.71	0	-2.28	0	0
	p		0.0207		0.0119		
	FDR		0.0837		0.0503		
PTE	%var	0	0	0	-6.25	0	9.28
	±				3.37		2.88
	ES	0	0	0	-1.18	0	1.73
	p				0.1140		0.0193
	FDR				0.1996		0.0599
Total unsaturated fatty acyl chains	%var	0	-8.35	0	-11.65	0	4.71
	±		2.61		2.25		1.67
	ES	0	-1.91	0	-3.39	0	1.57
	p		0.0129		0.0028		0.0289
	FDR		0.0837		0.0265		0.0809

Table S5.4. Main metabolite variations in culture medium of HepG2 cells exposed to Cit30 AgNPs, Ag^+, and H_2O_2 at respective IC_5 and IC_{20} concentrations, in relation to culture medium of control cells, expressed as % variation (%var) and respective error (±), effect size (ES), *p*-value (*p*), and FDR-adjusted *p*-value (FDR). The variations with |ES| < 0.8 (or standard error > |ES|, or mean error > |% variation|) were considered null.

		Cit30		Ag^+		H_2O_2	
		IC_5	IC_{20}	IC_5	IC_{20}	IC_5	IC_{20}
Pyruvate	%var	-13.81	-17.27	-10.04	-18.80	0	-11.43
	±	5.21	4.75	5.63	5.84		4.85
	ES	-1.66	-2.38	-1.16	-2.18	0	-1.44
	p	0.0239	0.0054	0.1144	0.0140		0.0403
	FDR	0.1122	0.0207	0.3848	0.0686		0.1095
Lactate	%var	20.23	0	12.88	17.57	0	-12.10
	±	6.43		7.90	8.59		6.67
	ES	1.66	0	0.94	1.16	0	-1.07
	p	0.0259		0.1808	0.1180		0.1013
	FDR	0.1122		0.4404	0.2989		0.2238
Citrate	%var	13.19	16.54	0	0	9.54	0
	±	1.17	0.98			4.69	
	ES	5.79	8.71	0	0	1.08	0
	p	3.93E-05	1.65E-06			0.0975	
	FDR	0.0007	0.0001			0.2850	
Fumarate	%var	11.19	13.95	11.48	14.25	6.38	0
	±	2.72	3.78	3.42	3.39	3.48	
	ES	2.61	2.01	1.95	2.41	1.12	0
	p	0.0285	0.0113	0.0210	0.0087	0.1382	
	FDR	0.1122	0.0308	0.2660	0.0662	0.3100	
Glutamate	%var	22.17	21.72	14.76	26.44	12.77	11.32
	±	1.63	2.01	2.52	2.81	2.08	4.13
	ES	7.23	5.49	3.36	5.12	3.13	1.37
	p	9.11E-06	3.02E-05	0.0032	0.0009	0.0016	0.0562
	FDR	0.0003	0.0006	0.1205	0.0164	0.0262	0.1424
Alanine	%var	0	0	-6.13	0	-8.77	-15.95
	±			3.62		3.58	3.30
	ES	0	0	-1.07	0	-1.44	-3.01
	p			0.1316		0.0396	0.0012
	FDR			0.3848		0.1503	0.0092
Phenylalanine	%var	3.50	6.56	2.60	6.07	3.66	7.40
	±	0.88	0.69	1.05	0.55	0.95	1.27
	ES	2.13	5.11	1.51	6.58	2.29	3.16
	p	0.0092	0.0001	0.0730	4.31E-05	0.0091	0.0009
	FDR	0.0639	0.0008	0.3848	0.0016	0.0577	0.0087
Leucine	%var	2.36	7.83	0	5.29	0	8.75
	±	1.16	1.13		1.99		1.58
	ES	1.11	3.67	0	1.60	0	2.80
	p	0.0913	0.0005		0.0684		0.0053
	FDR	0.2676	0.0036		0.2150		0.0272
Isoleucine	%var	1.60	5.70	0	2.92	0	5.71
	±	0.80	0.81		1.76		1.11
	ES	1.11	3.79	0	1.01	0	2.68
	p	0.0916	0.0004		0.1904		0.0040
	FDR	0.2676	0.0036		0.3881		0.0251
2-Oxoisoleucine	%var	0	-10.95	-3.50	-8.62	0	-9.59
	±		3.06	2.46	2.48		2.57
	ES	0	-2.12	-0.89	-2.24	0	-2.12
	p		0.0081	0.2009	0.0120		0.0115
	FDR		0.0266	0.4491	0.0686		0.0437
α-Ketoleucine	%var	-4.46	-14.33	0.00	-9.96	0	-10.61
	±	2.93	3.44	3.19	3.00		3.62
	ES	-0.89	-2.54	-0.70	-2.15	0	-1.64
	p	0.1636	0.0032	0.3034	0.0144		0.0336
	FDR	0.3701	0.0146	0.5182	0.0686		0.0983
Choline	%var	23.53	38.47	0	36.07	17.99	52.73
	±	5.07	4.45		4.82	4.40	2.86
	ES	2.23	3.88	0	3.90	2.07	8.32
	p	0.0082	0.0006		0.0031	0.0089	2.11E-06
	FDR	0.0639	0.0036		0.0291	0.0577	0.0001

		Cit30		Ag^+		H_2O_2	
		IC_5	IC_{20}	IC_5	IC_{20}	IC_5	IC_{20}
Acetate	%var	0	0	-12.24	0	232.53	465.93
	±			6.10		9.55	8.14
	ES	0	0	-1.31	0	5.60	8.41
	p			0.1082		0.0004	0.0001
	FDR			0.3848		0.0140	0.0015
Formate	%var	0	-8.72	3.88	-4.35	0	-11.53
	±		2.96	2.40	3.40		5.30
	ES	0	-1.67	0.98	-0.81	0	-1.27
	p		0.0264	0.1854	0.2679		0.0623
	FDR		0.0627	0.4404	0.4731		0.1479
Allantoin	%var	0	0	17.32	9.21	9.51	0
	±			5.33	5.84	5.24	
	ES	0	0	1.84	0.93	0.93	0
	p			0.0384	0.1940	0.1469	
	FDR			0.3651	0.3881	0.3100	

Table S5.5. Main metabolite variations in polar extracts of HepG2 cells exposed to Cit30 AgNPs, Ag^+, and H_2O_2 at respective IC_5 and IC_{20} concentrations, in relation to controls, expressed as % variation (%var) and respective error (±), effect size (ES), *p*-value (*p*), and FDR-adjusted *p*-value (FDR). The variations with |ES| < 0.8 (or standard error > |ES|, or mean error > |% variation|) were considered null.

		Cit30		Ag^+		H_2O_2	
		IC_5	IC_{20}	IC_5	IC_{20}	IC_5	IC_{20}
Lactate	%var	8.84	0	-3.67	5.35	0	-5.99
	±	1.72		1.95	1.99		2.71
	ES	2.81	0	-1.09	1.50	0	-1.45
	p	0.0014		0.0923	0.0306		0.0750
	FDR	0.0056		0.1424	0.0465		0.1193
Fumarate	%var	-24.86	-45.63	-36.04	-38.25	0	-31.87
	±	9.14	9.63	8.64	13.42		17.52
	ES	-1.77	-3.51	-2.91	-2.01	0	-1.28
	p	0.0167	0.0008	0.0032	0.0087		0.0628
	FDR	0.0324	0.0023	0.0124	0.0161		0.1046
Glutamine	%var	0	10.48	0	18.45	13.39	37.60
	±		2.51		2.74	3.91	2.80
	ES	0	2.27	0	3.52	1.68	5.90
	p		0.0071		0.0011	0.0307	0.0002
	FDR		0.0138		0.0029	0.0767	0.0008
Glutamate	%var	-7.64	-15.43	0	-12.88	0	0
	±	1.70	1.86		1.78		
	ES	-2.67	-5.15	0	-4.42	0	0
	p	0.0030	4.29E-05		0.0002		
	FDR	0.0089	0.0002		0.0007		
Aspartate	%var	-24.53	-25.13	-12.89	-18.93	0	-6.20
	±	3.14	4.33	4.16	4.04		4.08
	ES	-5.09	-3.80	-1.89	-2.96	0	-0.96
	p	2.03E-05	0.0004	0.0150	0.0015		0.1664
	FDR	0.0002	0.0013	0.0404	0.0038		0.2240
N-acetylaspartate	%var	0	-21.15	0	-23.09	0	-25.66
	±		6.68		5.70		4.96
	ES	0	-2.02	0	-2.62	0	-3.45
	p		0.0089		0.0070		0.0005
	FDR		0.0152		0.0136		0.0016
Glycine	%var	-8.88	-14.04	-7.82	-8.73	16.18	12.44
	±	2.24	2.51	1.42	1.92	0.95	3.81
	ES	-2.37	-3.43	-3.27	-2.71	8.73	1.61
	p	0.0094	0.0022	0.0010	0.0045	2.44E-06	0.0362
	FDR	0.0205	0.0051	0.0087	0.0093	0.0001	0.0703
Isoleucine	%var	13.33	28.82	15.77	45.33	12.42	33.04
	±	2.61	2.31	3.24	3.43	1.67	2.04
	ES	2.74	6.23	2.58	6.16	3.78	7.33
	p	0.0017	1.66E-05	0.0021	1.67E-05	0.0007	0.0001
	FDR	0.0061	0.0001	0.0105	0.0001	0.0039	0.0005
Leucine	%var	18.93	35.56	18.89	53.07	15.23	42.80
	±	2.05	2.25	3.26	3.04	1.59	1.70
	ES	4.81	7.68	3.02	7.88	4.72	10.83
	p	3.04E-05	2.06E-06	0.0021	1.77E-05	0.0004	1.40E-05
	FDR	0.0003	2.12E-05	0.0105	0.0001	0.0030	0.0003
Valine	%var	9.23	20.68	12.29	36.36	10.87	25.90
	±	2.41	2.14	2.85	2.95	1.36	2.03
	ES	2.09	5.01	2.32	5.95	4.21	5.98
	p	0.0069	0.0001	0.0038	1.54E-05	0.0002	0.0001
	FDR	0.0187	0.0002	0.0134	0.0001	0.0024	0.0006
Tyrosine	%var	7.17	12.40	10.23	31.27	11.36	29.06
	±	2.61	2.71	2.71	3.61	2.58	2.10
	ES	1.52	2.46	2.05	4.28	2.19	6.33
	p	0.0292	0.0026	0.0071	0.0003	0.0124	0.0002
	FDR	0.0511	0.0058	0.0226	0.0011	0.0333	0.0007
Phenylalanine	%var	14.76	24.15	15.78	44.98	17.52	45.42
	±	2.84	3.63	4.02	3.20	2.88	3.13
	ES	2.77	3.39	2.08	6.56	3.19	6.44
	p	0.0014	0.0009	0.0113	1.79E-05	0.0009	1.73E-05
	FDR	0.0056	0.0025	0.0329	0.0001	0.0039	0.0003

		Cit30		Ag^+		H_2O_2	
		IC_5	IC_{20}	IC_5	IC_{20}	IC_5	IC_{20}
Histidine	%var	17.73	25.32	22.90	50.73	21.97	46.56
	±	3.29	5.65	4.34	5.42	4.93	5.19
	ES	2.83	2.27	2.70	4.26	2.29	3.99
	p	0.0011	0.0087	0.0024	0.0005	0.0054	0.0003
	FDR	0.0056	0.0152	0.0105	0.0017	0.0189	0.0008
Methionine	%var	20.83	40.13	24.58	51.44	20.61	44.28
	±	3.96	1.37	2.81	4.60	2.10	2.71
	ES	2.72	13.96	4.44	5.08	4.70	6.95
	p	0.0075	1.53E-07	0.0008	0.0007	0.0004	0.0001
	FDR	0.0187	5.36E-06	0.0087	0.0021	0.0030	0.0006
Serine	%var	4.03	9.15	5.20	13.52	9.80	16.40
	±	1.85	2.57	2.65	2.90	1.46	1.54
	ES	1.22	1.95	1.09	2.49	3.93	5.83
	p	0.0788	0.0097	0.0935	0.0034	0.0009	3.94E-05
	FDR	0.1254	0.0155	0.1424	0.0074	0.0039	0.0005
Threonine	%var	0	0	-3.38	0	8.47	23.59
	±			2.22		3.25	4.46
	ES	0	0	-0.89	0	1.41	2.54
	p			0.1633		0.0427	0.0046
	FDR			0.2381		0.0996	0.0095
Unidentified *N*-acetylated amino acid	%var	64.10	101.84	70.36	157.03	31.02	153.84
	±	2.84	3.82	7.04	4.13	3.18	12.08
	ES	9.78	10.09	4.22	12.15	4.88	3.62
	p	1.98E-07	1.14E-06	0.0009	2.07E-06	0.0001	0.0021
	FDR	6.93E-06	2.00E-05	0.0087	3.62E-05	0.0013	0.0057
Creatine	%var	-11.73	-21.72	-9.71	-25.93	-4.64	-16.80
	±	3.51	4.07	4.60	4.06	2.74	3.16
	ES	-2.03	-3.42	-1.27	-4.20	-1.15	-3.72
	p	0.0205	0.0010	0.0577	0.0005	0.1637	0.0026
	FDR	0.0377	0.0025	0.0961	0.0017	0.3015	0.0066
Phosphocreatine	%var	-25.58	-37.39	-13.58	-36.75	-17.80	-39.23
	±	5.02	5.22	5.15	4.44	4.55	5.86
	ES	-3.34	-5.03	-1.62	-5.80	-2.73	-5.17
	p	0.0007	4.95E-05	0.0284	8.92E-06	0.0077	0.0001
	FDR	0.0041	0.0002	0.0523	0.0001	0.0247	0.0006
ADP	%var	0	-14.10	0	-12.68	0	-9.90
	±		9.61		6.85		4.72
	ES	0	-0.90	0	-1.13	0	-1.30
	p		0.1679		0.0865		0.0620
	FDR		0.2176		0.1081		0.1046
ATP	%var	0	21.43	0	13.79	0	19.82
	±		6.68		7.49		9.75
	ES	0	1.66	0	0.98	0	1.01
	p		0.0222		0.1301		0.1176
	FDR		0.0324		0.1570		0.1715
NAD^+	%var	-7.78	-16.51	-3.54	-8.68	4.42	7.85
	±	1.83	2.38	1.33	3.51	2.71	3.19
	ES	-2.53	-4.32	-1.55	-1.48	0.93	1.33
	p	0.0030	0.0003	0.0271	0.0515	0.1560	0.0518
	FDR	0.0089	0.0011	0.0523	0.0693	0.3015	0.0954
UTP	%var	0	16.85	0	0	-8.46	0
	±		4.89			5.28	
	ES	0	1.81	0	0	-0.94	0
	p		0.0133			0.1394	
	FDR		0.0202			0.2870	
GSH	%var	19.45	23.47	9.00	8.03	0	0
	±	3.19	2.67	2.53	2.44		
	ES	3.17	4.49	1.95	1.80	0	0
	p	0.0005	0.0001	0.0182	0.0291		
	FDR	0.0038	0.0004	0.0454	0.0462		
Phosphocholine	%var	-17.05	-24.35	-11.85	-25.24	-12.12	-23.80
	±	1.68	2.29	2.20	2.00	2.16	2.32
	ES	-6.33	-6.93	-3.27	-8.27	-3.85	-7.58
	p	1.48E-05	2.42E-06	0.0005	5.84E-07	0.0029	0.0002
	FDR	0.0002	2.12E-05	0.0087	2.04E-05	0.0112	0.0007
Taurine	%var	-15.46	-21.58	-10.57	-24.07	0	-17.82
	±	4.64	6.05	4.01	5.23		3.83
	ES	-2.06	-2.28	-1.59	-2.99	0	-2.80
	p	0.0106	0.0091	0.0279	0.0020		0.0031
	FDR	0.0218	0.0152	0.0523	0.0048		0.0072

		Cit30		Ag^+		H_2O_2	
		IC_5	IC_{20}	IC_5	IC_{20}	IC_5	IC_{20}
Pantothenate	%var	0	0	8.15	9.05	14.17	18.58
	±			3.28	3.72	3.45	3.99
	ES	0	0	1.36	1.33	2.32	2.45
	p			0.0525	0.0614	0.0090	0.0040
	FDR			0.0919	0.0796	0.0264	0.0086

Table S5.6. Main metabolite variations in lipophilic extracts of HepG2 cells exposed to Cit30 AgNPs, Ag^+, and H_2O_2 at respective IC_5 and IC_{20} concentrations, in relation to controls, expressed as % variation (%var) and respective error (±), effect size (ES), *p*-value (*p*), and FDR-adjusted *p*-value (FDR). The variations with |ES| < 0.8 (or standard error > |ES|, or mean error > |% variation|) were considered null.

		Cit30		Ag^+		H_2O_2	
		IC_5	IC_{20}	IC_5	IC_{20}	IC_5	IC_{20}
Total cholesterol	%var	0	-6.20	0	0	3.31	12.41
	±		2.34			1.60	1.57
	ES	0	-1.56	0	0	1.16	4.18
	p		0.0297			0.0819	1.75E-04
	FDR		0.0837			0.8730	0.0026
Cholesterol ester	%var	14.64	29.12	12.05	26.33	9.15	38.18
	±	4.87	5.45	3.83	3.68	4.74	4.02
	ES	1.60	2.66	1.70	3.61	1.02	4.35
	p	0.0326	0.0051	0.0210	0.0004	0.1143	1.87E-04
	FDR	0.4566	0.0837	0.2947	0.0125	0.8730	0.0026
PTC	%var	0	-17.84	0	-13.44	0	-12.49
	±		6.54		5.36		5.79
	ES	0	-1.71	0	-1.54	0	-1.34
	p		0.0207		0.0283		0.0537
	FDR		0.0837		0.1134		0.1252
Total unsaturated fatty acyl chains	%var	0	-8.35	0	-5.89	0	0
	±		2.61		2.68		
	ES	0	-1.91	0	-1.29	0	0
	p		0.0129		0.0600		
	FDR		0.0837		0.1681		

Chapter 6. Metabolomic analysis of murine macrophages (RAW 264.7 cells) exposed to citrate-coated silver nanoparticles

6.1. Background and aims

In this Chapter, the cytotoxic and metabolic responses of blood-derived cells, namely murine RAW 264.7 macrophages, to citrate-coated silver nanoparticles with an average diameter of 30 nm (Cit30) are presented and discussed. Macrophages are important phagocytic cells of the immune system which, among other functions, strongly determine the biological responses to foreign particles, including nanoparticles administered intravenously for therapeutic purposes or those entering the bloodstream after exposure via other routes (Aude-Garcia *et al.*, 2016). Thus, knowledge on the interaction between macrophages and nanoparticles is important not only for toxicity assessments but also for the design of more effective nanomedicines. The murine cell line RAW 264.7 has emerged as a good *in vitro* model for assessing macrophages responses to various stimuli, since it retains representative characteristics of different macrophage types (Bordbar *et al.*, 2012). Thus, a number of reports comprising the effects of AgNPs in RAW 264.7 cells have been published. These studies have assessed the cytotoxic potential of AgNPs towards RAW 264.7 macrophages, for instance by looking at cell membrane damage (Park *et al.*, 2011; Suresh *et al.*, 2012), uptake and intracellular localisation of the nanoparticles (Orlowski *et al.*, 2013; Haase *et al.*, 2014), alterations in cellular morphology (Kaur and Tikoo, 2013), induction of oxidative stress/ROS generation (Park *et al.*, 2010; Nishanth *et al.*, 2011; Kaur and Tikoo, 2013; Munusamy *et al.*, 2015; Paul *et al.*, 2015), metallothionein expression (Park *et al.*, 2010; Zhang *et al.*, 2015a) and inflammatory response (Park *et al.*, 2010; Nishanth *et al.*, 2011; Park *et al.*, 2011; Kaur and Tikoo, 2013; Haase *et al.*, 2011; Aldossari *et al.*, 2015; Giovanni *et al.*, 2015; Paul *et al.*, 2015). The influence of size, surface coating, and dissolution rate of AgNPs in the viability of RAW 264.7 cells has also been addressed (Pratsinis *et al.*, 2013; Wang *et al.*, 2014).

Recent findings have established metabolic reprogramming as a key element of macrophages' functional behaviour, rather than being simply involved in energy generation and biosynthesis (El Kasmi and Stenmark, 2015; Mills and O'Neill, 2016). In particular, the activation of macrophages with different environmental signals, namely lipopolysaccharide (LPS) and interferon-γ (IFN-γ) (resulting in classically activated or M1 macrophages), or interleukins IL-4, IL-10 and IL-13 (resulting in alternatively activated or M2 macrophages), has been shown to be associated with marked alterations in cellular metabolism

(Rodriguez-Prados *et al.*, 2010; Biswas and Mantovani, 2012; Lamour *et al.*, 2012; Jha *et al.*, 2015). To our knowledge, however, the metabolic responses of macrophages to nanoparticles are poorly characterised. In this work, we use NMR metabolomics to assess the impact of AgNPs on macrophage metabolism, with a view to better describe the nanoparticle-induced activation profile, and to identify potential markers of macrophage response, as well as possible targets for modulation of macrophage metabolism.

6.2. Physicochemical properties of the AgNPs tested

The silver nanoparticles used for incubations with RAW 264.7 macrophages were stabilised in citrate and had a metallic core diameter of 30 nm (Cit30). Other physicochemical properties of these particles, as well as their aggregation and dissolution behaviour in culture medium, have already been described (Chapter 4, Table 4.1 and Figure 4.1) and, thus, are not repeated here.

6.3. Viability of RAW 264.7 cells exposed to AgNPs, Ag^+ and H_2O_2

The dose-response curve of RAW 264.7 cells exposed for 24 h to Cit30, obtained through the MTT assay, is shown in Figure 6.1a. At 40 µg/mL and above, cell viability was significantly reduced. The IC_{50} value calculated from this curve was 55.9 µg/mL, suggesting that these cells have a higher tolerance to AgNPs than HaCaT or HepG2 cells (results shown in Chapters 4 and 5, respectively). A similar result was obtained by Wang *et al.*, who observed a 40% decrease in cell viability after 24 h of exposure to 50 µg/mL of citrate-coated AgNPs, with diameters of 20 or 100 nm (Wang *et al.*, 2014). Higher cytotoxicity towards RAW 264.7 cells was found for smaller (< 10 nm) AgNPs (IC_{50} value between 0.1-4.9 µg/mL, depending on the coating) (Suresh *et al.*, 2012), 20 nm AgNPs supported on nanostructured SiO_2 (20 µg/mL reduced cell viability in 50%) (Pratsinis *et al.*, 2013), 33 nm AgNPs modified with tannic acid (IC_{50} value of 4.07 µg/mL) (Orlowski *et al.*, 2013), and 35 nm PVP-coated AgNPs (10 µg/mL reduced cell viability in 30%) (Giovanni *et al.*, 2015). On the other hand, there were also reports showing higher resistance of RAW 264.7 cells to AgNPs, with high viability (> 80%) being observed after exposure to concentrations above 50 µg/mL (Kaur and Tikoo, 2013; Munusamy *et al.*, 2015; Zhang *et al.*, 2015a).

Ag^+, administered as $AgNO_3$, was more cytotoxic to RAW 264.7 cells than Cit30 AgNPs, resulting in very low cell viability (< 5%) above 3.5 µg/mL (Figure 6.1b). The

calculated IC_{50} value was 2.94 µg/mL. This value represents a higher cytotoxicity of Ag^+ towards RAW 264.7 macrophages than that determined by Park and co-workers (Park *et al.*, 2011). In their work, a dose of 6.7 µg/mL Ag^+ was found to inhibit only 20% of cellular activity. On the contrary, in a study where exposure to Ag^+ was performed for 4 and 12 h, the IC_{50} value was 0.75 µg/mL (Suresh *et al.*, 2012). Haase and colleagues also tested the influence of Ag^+ in this cell line using a concentration of ~1 µg/mL (10 µM), which did not reduce cell viability (Haase *et al.*, 2014), thus agreeing with our results.

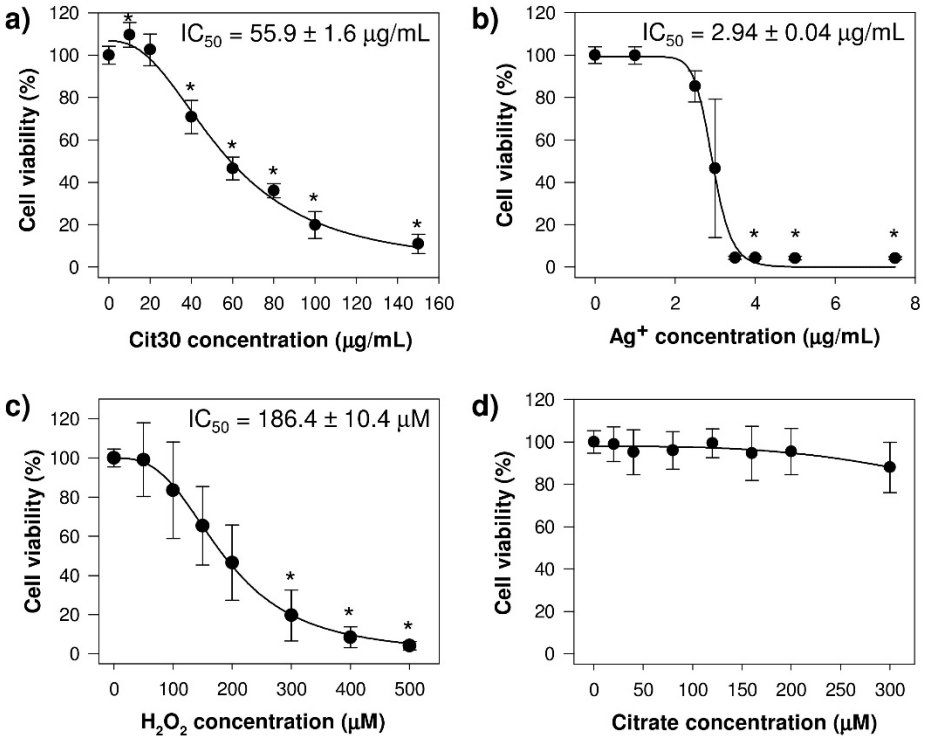

Figure 6.1. Viability (%) of RAW 264.7 cells, measured by MTT assay, after 24 h of exposure to: a) Cit30, b) Ag^+, c) H_2O_2 and d) citrate. Data expressed as mean ± standard deviation of three independent assays with three replicates each (n 9). Statistically significant ($p < 0.05$) differences relatively to controls are indicated by *.

Figure 6.1c shows the dose-response curve of the 24 h-exposure of RAW 264.7 macrophages to H_2O_2. Cell viability decreased with increasing H_2O_2 concentrations, although the difference to controls was not statistically significant below 300 µM. The IC_{50} value was calculated as 186 µM. Among the few literature studies assessing the cytotoxic effect of H_2O_2 towards RAW 264.7 cells, using the MTT assay, some authors reported a decrease to 50-60% viable cells with only 100 µM of H_2O_2 (Oh *et al.*, 2006; Jung *et al.*, 2014), while others indicated higher values such as 400 µM of H_2O_2 (Chow *et al.*, 2005). In

another report where RAW 264.7 cells were exposed to 500 μM of H_2O_2, for up to 24 h, cell viability was found to be lower at 12 h (about 59%), than at 24 h (around 70%) (Wen *et al.*, 2013).

The effect of citrate on cell viability was also evaluated and the resulting dose-response curve is presented in Figure 6.2d. There was no significant change in cell viability up to 300 μM. Thus, at the estimated maximum concentration present when cells were exposed to the IC_{20} concentration of AgNPs (69 μM of citrate), cells fully maintained their viability.

Based on the dose response curves presented above, the IC_5 and IC_{20} concentrations of each substance (Cit30 AgNPs, Ag^+ and H_2O_2) have been estimated and selected for further metabolomics studies (Table 6.1).

Table 6.1. Concentrations of Cit30 AgNPs, Ag^+ (from $AgNO_3$) and H_2O_2, selected for the metabolomic analysis of RAW 264.7 cells.

	Cit30	Ag^+	H_2O_2
IC_5	23.2 μg/mL	2.29 μg/mL	67.5 μM
IC_{20}	35.3 μg/mL	2.62 μg/mL	115.7 μM

6.4. Generation of reactive oxygen species

Intracellular ROS generation was measured in RAW 264.7 cells exposed for 24 h to Cit30, Ag^+, or H_2O_2, at IC_{20} concentrations, as well as in cells exposed to citrate at the maximum concentration possibly present upon incubation with Cit30 AgNPs (Figure 6.2). ROS levels showed a significant decrease with exposure to Cit30. A similar result has been reported in RAW 264.7 cells exposed to 100 μg/mL of AgNPs synthesised through chemical reduction with sodium borohydride (Kaur and Tikoo, 2013). However, an increase in ROS levels after exposure to AgNPs has been more commonly reported (Nishanth *et al.*, 2011; Park *et al.*, 2011; Orlowski *et al.*, 2014).

Upon exposure to Ag^+, H_2O_2 or citrate, ROS generation increased, although not significantly in the case of Ag^+. ROS levels have been previously reported to increase in human macrophages (THP-1 cells) exposed to Ag^+ in the 0.66 to 1.35 μg/mL concentration range (Foldbjerg *et al.*, 2009). This same study also measured ROS generation induced by PVP-coated AgNPs (30-50 nm), reporting an increase, followed by a decrease. The authors

suggested that the decrease in ROS levels could be due to the loss of dichlorofluorescein from dying cells. Regarding H_2O_2, the IC_{20} concentration caused a significant increase in intracellular ROS levels, in agreement with a previous report (Chow *et al.*, 2005).

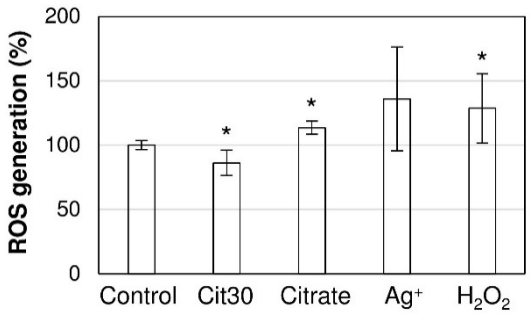

Figure 6.2. Intracellular generation of reactive oxygen species (ROS) in RAW 264.7 cells, after 24 h exposure to the IC_{20} concentration of Cit30, Ag^+ or H_2O_2, and to 69 µM of citrate (maximum concentration present in the AgNPs exposure). Data is expressed as mean ± standard deviation of three independent assays with two replicates each (n 6). Statistically significant ($p < 0.05$) differences relatively to controls are indicated by *.

6.5. Metabolic variations induced by AgNPs in RAW 264.7 macrophages

The effects of Cit30 AgNPs on the metabolic profile of RAW 264.7 cells were assessed after 24 h exposure to the IC_5 and IC_{20} concentrations. Analysis of culture medium supernatants from control and exposed cells allowed differences in extracellular metabolite balances to be evaluated. Furthermore, changes in intracellular metabolites were measured in polar and lipophilic cell extracts.

The metabolic variations in culture medium supernatants of RAW 264.7 cells exposed to AgNPs relatively to control cells are summarised in Figure 6.3a and in Supplementary Table S6.1. Only a few changes in substrate consumption and metabolite excretion were noted. Glucose appeared to be more consumed from the culture medium when cells were exposed to the IC_5 concentration, although this variation was not statistically significant. At the IC_{20} exposure, no alterations were found in substrate consumption. Regarding metabolite excretion, pyruvate levels were decreased after AgNPs-exposure, indicating that this metabolite was less excreted in exposed cells than in control cells. Increased excretion of citrate and of glutamate were observed with both concentrations. A non-significant increase in lactate levels was also observed in media from cells exposed to the IC_5 concentration of AgNPs.

When citrate was added to cells, to assess the influence of its presence as a stabiliser for AgNPs, there were no changes in the extracellular metabolome, except of course for the expected increase in citrate levels (Figure 6.3a, 3rd column).

Multivariate analysis of polar extracts indicated a strong impact of AgNPs on the intracellular composition of RAW 264.7 cells (Figure 6.4). A very clear separation between control and exposed cells was observed in the PCA scores scatter plot, along the first principal component (Figure 6.4a). This plot also showed that the concentration of AgNPs had little influence in class separation, since IC_5 and IC_{20} samples largely overlapped. In addition, control and exposed samples were discriminated with high robustness (Q^2 0.9) by PLS-DA (scores plot in Figure 6.4b), as confirmed through Monte Carlo Cross Validation and permutation testing (Supplementary Figure S6.1).

The corresponding PLS-DA loadings (Figure 6.4c) showed many metabolic features responsible for class discrimination, including glucose, GSH, choline-containing compounds, several amino acids and ADP/ATP. Subsequently, these changes were thoroughly evaluated through spectral integration of individual signals and relevant variations (absolute effect size > 0.8) were represented as the percentage variation in relation to controls (Figure 6.3b and Supplementary Table S6.2).

AgNPs caused marked alterations in 26 intracellular polar metabolites of RAW 264.7 macrophages. Except for lactate levels, which were slightly more affected by the IC_5 concentration, the highest exposure concentration generally caused changes of larger magnitude. Some metabolites, however, had variations of similar magnitude (< 3% difference) at the IC_5 and IC_{20} exposures (glutamate, aspartate, threonine, ATP, GSH, and pantothenate). Very high increases in the levels of glucose, itaconate, succinate, creatine and phosphocreatine were observed. Specifically, glucose levels were increased by 250% at the IC_5, and by 396% at the IC_{20}. Itaconate and creatine also had their levels increased by more than 200% upon exposure to AgNPs. Increases above 50% were observed for phosphocreatine, succinate and tyrosine (only at the IC_{20}). Relevant increases below 10% were also noted for lactate, serine, GSH, choline, isoleucine, and valine.

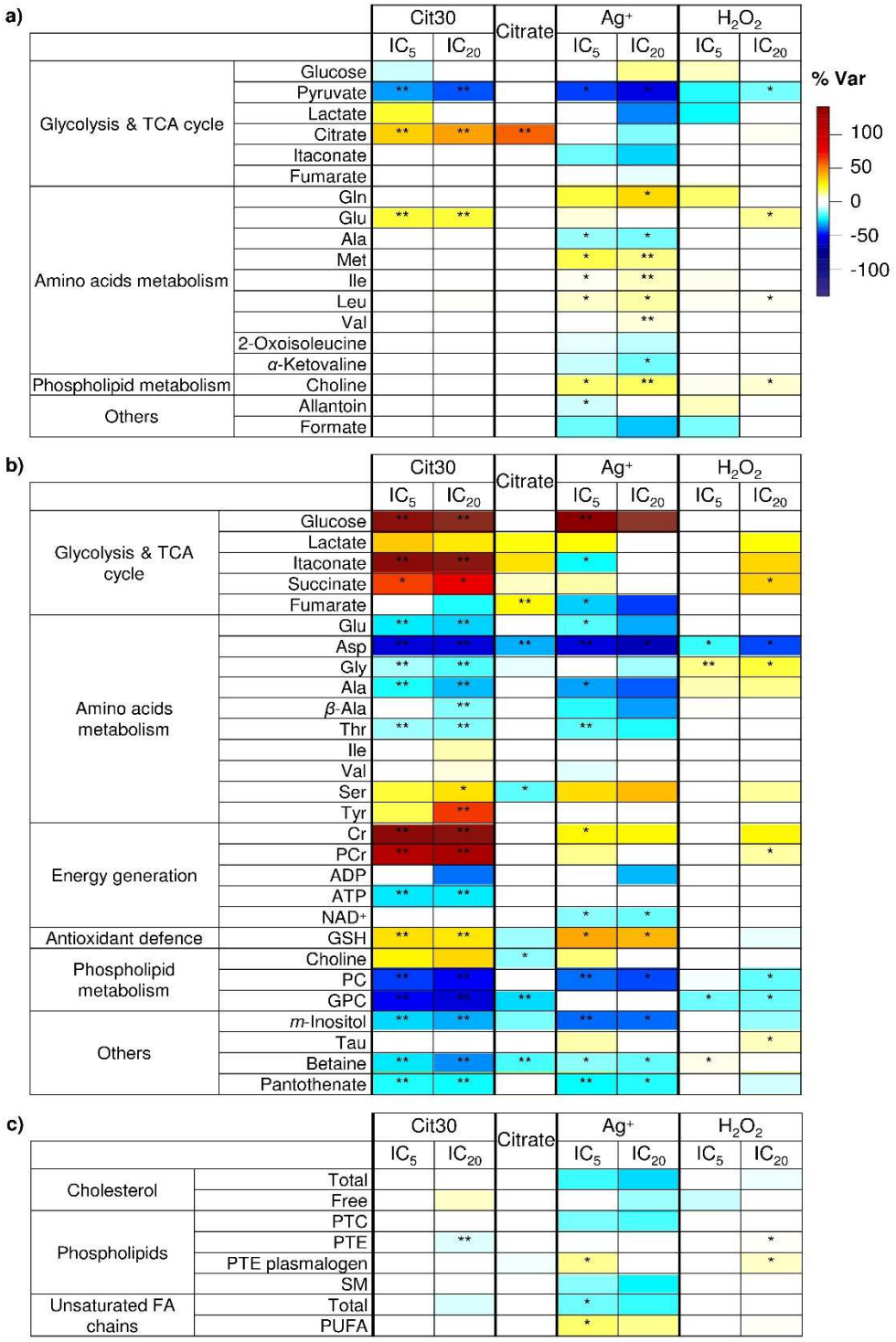

Figure 6.3. Heatmap of the main variations in a) culture media, b) polar extracts, and c) lipophilic extracts, from RAW 264.7 cells exposed to Cit30, Ag^+ and H_2O_2, at IC_5 and IC_{20} concentrations, coloured according to % variation in relation to controls; metabolic changes resulting from exposure to citrate (69 µM) also shown. * Uncorrected *p*-value < 0.05; ** FDR-corrected *p*-value < 0.05. Three letter code used for amino acids; Cr, creatine; PCr, phosphocreatine; ADP/ATP, adenosine di/triphosphate; NAD^+, nicotinamide adenine dinucleotide; GSH, reduced glutathione; PC, phosphocholine; GPC, glycerophosphocholine; PTC, phosphatidylcholine; PTE, phosphatidylethanolamine; SM, sphingomyelin; FA, fatty acyl; PUFA, polyunsaturated fatty acyl chains.

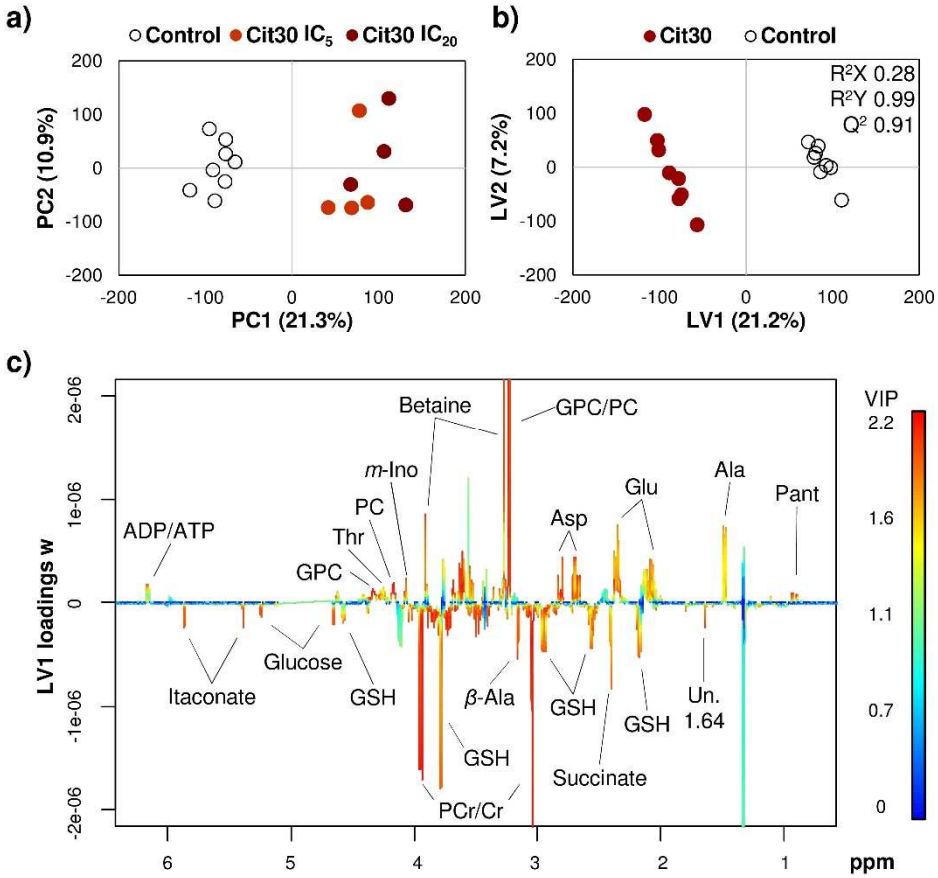

Figure 6.4. Multivariate analysis of ^{1}H NMR spectra from polar extracts of control and Cit30-exposed RAW 264.7 cells: a) PCA, b) PLS-DA scores scatter plots, and c) LV1 loadings *w*, coloured as a function of variable importance to the projection (VIP). Pant, pantothenate; Un. 1.64, unidentified metabolite at 1.64 ppm; for other metabolite codes, *vide* legend of Figure 6.4.

Significant decreases were found for several amino acids (glutamate, aspartate, glycine, alanine, *β*-alanine, and threonine), ATP, choline-containing compounds (phosphocholine and glycerophosphocholine), and others (*myo*-inositol, betaine, and pantothenate). Among these variations, aspartate, phosphocholine, and glycerophosphocholine, presented particularly high decreases, varying more than 44% in relation to controls. The highest concentration of AgNPs (IC_{20}) caused additional decreases (although not significant) in the levels of fumarate and ADP, which did not vary upon exposure to the IC_5.

AgNPs appeared to cause very little effect on the lipid composition of RAW 264.7 macrophages; the only significant change was the 7% decrease in phosphatidylethanolamine (Figure 6.3c). Nonetheless, other non-significant variations were

observed. Total unsaturated fatty acyl chains decreased by 8%, and free cholesterol was increased by 9%, upon exposure to the IC_{20} of AgNPs, in relation to controls.

As citrate was used to coat and suspend the nanoparticles, its effect on the cells metabolome was also assessed, after 24 h exposure to 69 µM (the concentration estimated to be present when the IC_{20} concentration of Cit30 was administered to cells). As observed in Figure 6.3b, a few changes were noted in the intracellular composition of citrate-exposed cells in relation to controls. Interestingly, these variations were clearly different from AgNPs-induced effects. Variations in opposite directions include fumarate (that was decreased upon AgNPs exposure, but increased with citrate), serine, GSH and choline (decreased upon citrate exposure). Metabolites varying in the same direction but to different extents in cells exposed to Cit30 AgNPs or citrate include lactate, succinate, itaconate, aspartate, glycine, glycerophosphocholine, *myo*-inositol and betaine. Concerning lipophilic extracts, there were hardly any changes, with a small (6%) non-significant decrease being noted for the plasmenyl form of phosphatidylethanolamine.

6.6. Metabolic variations induced by Ag^+ in RAW 264.7 macrophages

The impact of Ag^+ (from $AgNO_3$) on the metabolism of RAW 264.7 macrophages has been evaluated through NMR analysis of culture medium supernatants, and of cell extracts (polar and lipophilic).

The changes in the exometabolome of cells exposed for 24 h to Ag^+ (at respective IC_5 and IC_{20}), are summarised in Figure 6.3a and Supplementary Table S6.1. Ag^+ had a noticeable influence in substrate consumption and metabolite excretion. Specifically, several metabolites were less consumed by RAW 264.7 macrophages in the presence of Ag^+ (glucose, glutamine, choline, methionine, and branched chain amino acids), while others, such as pyruvate, lactate, citrate, itaconate, fumarate, alanine, keto-acids (resulting from lower consumption of branched chain amino acids), and formate, were less released. Compared to the extracellular variations induced by AgNPs, Ag^+ had a much stronger impact; also some qualitative differences could be noticed. For instance, while the consumption of glucose and the excretion of lactate and citrate were increased in AgNPs exposed cells, the opposite effect was seen in cells exposed to Ag^+. It should also be noted that the above changes were not seen in acellular medium to which Ag^+ was added, and are thus not expected to result from interactions between Ag^+ and medium components.

The intracellular composition of RAW 264.7 macrophages was also greatly affected by Ag^+. However, in this case, we found larger biological variability within the assays, as reflected on the multivariate analysis results (Figure 6.5a and b, showing high dispersion between exposed samples), and confirmed by the poorer validation achieved through MCCV and permutation testing (Supplementary Figure S6.2). Still, together with the PLS-DA loadings (Figure 6.5c), individual metabolite integrals allowed the most relevant variations in polar compounds to be highlighted and compared to those induced by Cit30 AgNPs (Figure 6.3b and Supplementary Table S6.2).

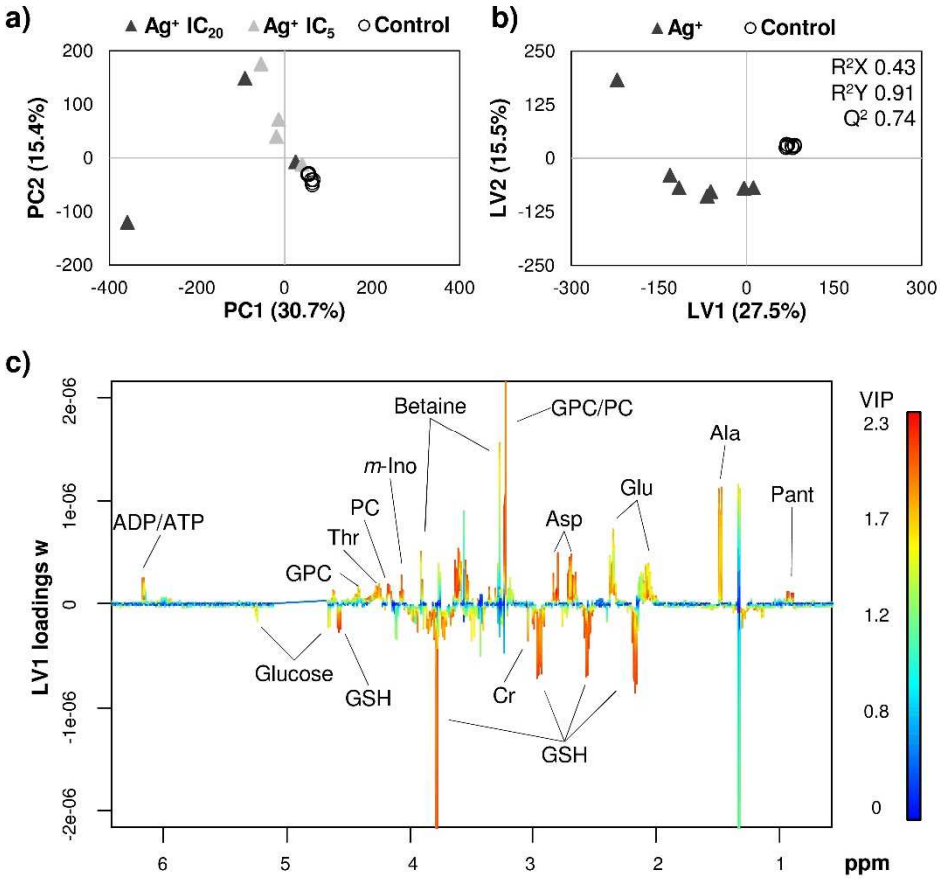

Figure 6.5. Multivariate analysis of ^{1}H NMR spectra from polar extracts of control and Ag^+-exposed RAW 264.7 cells: a) PCA, b) PLS-DA scores scatter plots, and c) LV1 loadings *w*, coloured as a function of variable importance to the projection (VIP). Pant, pantothenate; for other metabolite codes, *vide* legend of Figure 6.4.

Several consistent variations were identified in Ag^+-exposed cells, in relation to controls. The largest variation was in glucose levels, with an increase of 475% in IC_{20}-exposed cells (170% at the IC_5). Other marked increases were seen for lactate, succinate, serine, (phospho)creatine, GSH, choline and taurine. Interestingly, some of these increases

were clearly less intense than those induced by AgNPs, namely in the case of succinate and creatine/phosphocreatine. Additionally, while itaconate was markedly increased in AgNPs-exposed cells, it was decreased or unaltered in cells exposed to Ag^+. On the other hand, fumarate was more markedly decreased upon exposure to Ag^+ than to AgNPs. Other metabolites with decreased levels in exposed cells (compared to controls) included several amino acids, phosphocholine, *myo*-inositol and betaine, similarly to what has been found in AgNPs-exposed cells. Additionally, Ag^+ caused significant decreases in NAD^+, not seen with AgNPs, while the levels of ATP and glycerophosphocholine, significantly depleted upon exposure to AgNPs, remained unaltered in Ag^+-treated cells.

Analysis of lipophilic extracts showed that Ag^+ had a greater influence on the lipid composition of RAW 264.7 macrophages than Cit30 AgNPs (Figure 6.3c). In addition to a significant and more pronounced decrease in total unsaturated fatty acyl chains, Ag^+ caused decreases in cholesterol (total and free), phosphatidylcholine, and sphingomyelin. Other differences comprised the increased levels of polyunsaturated fatty acyl chains, and of phosphatidylethanolamine in the plasmenyl form.

6.7. Metabolic variations induced by H_2O_2 in RAW 264.7 macrophages

Exposure to H_2O_2 at concentrations causing approximately 5 and 20% reduction in cell viability (IC_5 and IC_{20}, respectively) had a much weaker impact on the RAW 264.7 cells metabolome than exposures to Cit30 AgNPs or Ag^+. Indeed, few changes were noted in extracellular metabolites, most of which were dose-dependent (Figure 6.3a). Decreased consumption of glucose and of glutamine, together with decreased excretion of lactate, were seen in IC_5-exposed cells, while increased excretion of glutamate and decreased consumption of leucine and choline were clearer at the IC_{20}.

The weaker impact of H_2O_2 in the metabolism of RAW 264.7 macrophages, in comparison to Cit30 or Ag^+, was also clearly demonstrated through multivariate analysis of polar extracts (Figure 6.6). Even though there was a trend for class distinction in the PCA scores scatter plot (Figure 6.7a), and an apparent good separation between classes along LV1 in the PLS-DA scores plot (Figure 6.6b), MCCV and permutation testing failed to validate the results (Supplementary Figure S6.3). Nonetheless, the combined interpretation of the PLS-DA loadings plot and integration results (Figures 6.6c and 6.3b, respectively)

revealed relevant changes (with absolute effect size greater than 0.8) in 7 intracellular metabolites at the IC_5 exposure and in 15 metabolites at the IC_{20} exposure. These comprised minor increases in *β*-alanine and betaine, only at the IC_5, and moderate increases in lactate, itaconate, succinate, serine, creatine, phosphocreatine and taurine, only at the IC_{20}. Both concentrations caused increased levels of glycine and alanine, and decreased levels of aspartate, phosphocholine and glycerophosphocholine. At the IC_{20} exposure, further decreases were observed for GSH, *myo*-inositol, and pantothenate. It should also be noted that glycine, alanine, GSH and betaine presented opposite variations in H_2O_2-exposed cells in comparison to those observed after exposure to Cit30 or Ag^+.

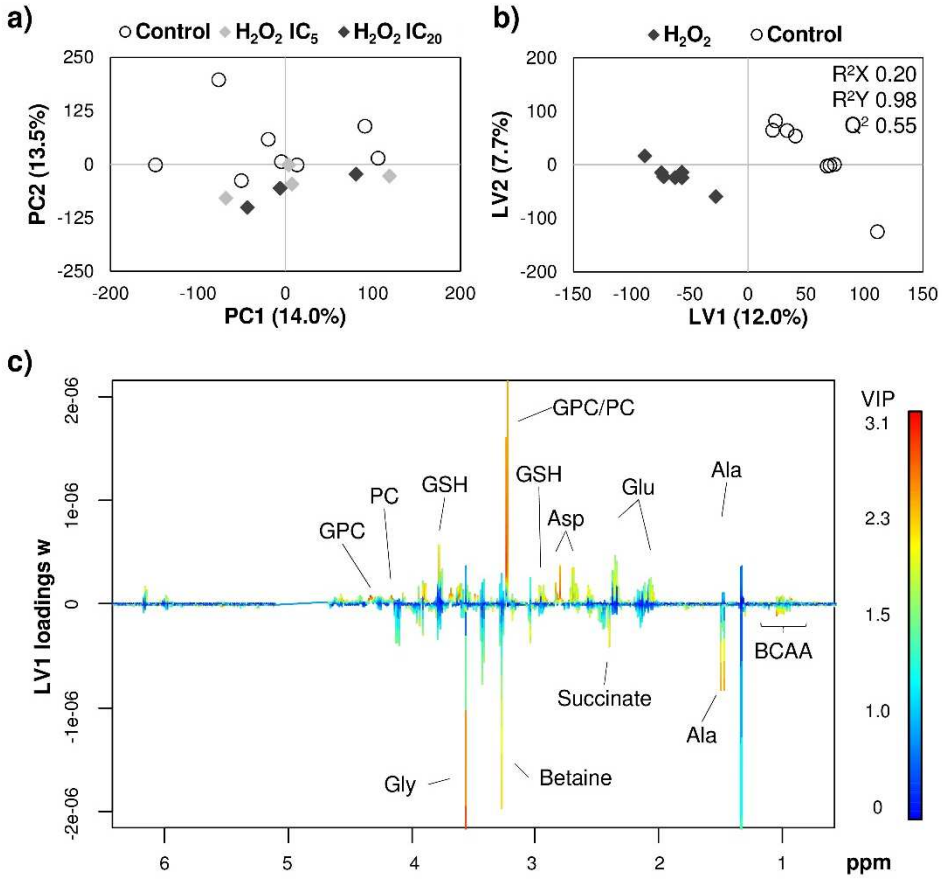

Figure 6.6. Multivariate analysis of ^{1}H NMR spectra from polar extracts of control and H_2O_2-exposed RAW 264.7 cells: a) PCA, b) PLS-DA scores scatter plots, and c) LV1 loadings *w*, coloured as a function of variable importance to the projection (VIP). BCAA, branched chain amino acids; for other metabolite codes, *vide* legend of Figure 6.4.

The lipid composition of RAW 264.7 cells was only slightly affected by H_2O_2 (Figure 6.3c). Main variations were below 10% and included decreased cholesterol levels and increased phosphatidylethanolamine (both forms, acyl and plasmenyl), in opposition to the effects induced by Cit30 AgNPs.

6.8. Discussion of metabolic variations in RAW 264.7 macrophages

The basal metabolic activity and intracellular composition of RAW 264.7 macrophages were clearly altered after exposure to 30 nm citrate-coated AgNPs (Cit30), even at non-toxic or sub-toxic concentrations. Interestingly, some effects were common to those induced by Ag^+ (given to cells as $AgNO_3$, at concentrations inducing equivalent decreases in cell viability), while others were clearly distinct, as discussed in the following paragraphs.

The IC_5 concentration of Cit30 (but not the IC_{20}) appeared to induce an increase in the glycolytic activity of RAW 264.7 cells, as suggested by increased glucose consumption and increased lactate production and excretion. Increased glycolysis in macrophages has also been observed after exposure to ultrasmall superparamagnetic particles of iron oxide (Feng *et al.*, 2011a), airborne particulate matter (Santini *et al.*, 2004), or bacterial LPS (Meiser *et al.*, 2016). On the other hand, opposite variations in glucose consumption and in lactate excretion, together with decreased excretion of alanine (glycolytic product), were apparent in cells exposed to the IC_{20} concentration of Ag^+, suggesting downregulation of glycolysis. Furthermore, exposure to Ag^+ reduced the consumption of several medium substrates, namely glutamine, methionine, branched chain amino acids, and choline.

AgNPs and Ag^+ also appeared to have distinct effects on the TCA cycle, as schematically illustrated in Figure 6.7. AgNPs-exposed cells displayed increased release of citrate and very high increases in intracellular itaconate and succinate. The latter metabolites have been found elevated in LPS-stimulated macrophages, and are considered markers of a pro-inflammatory (M1) state (Strelko *et al.*, 2011; Meiser *et al.*, 2016). LPS-activated macrophages have been described to present mitochondrial dysfunction, associated with a defective TCA cycle, with breakpoints at isocitrate dehydrogenase (IDH), the enzyme that converts isocitrate to *α*-ketoglutarate, and at succinate dehydrogenase (SDH), the enzyme that catalyses the oxidation of succinate to fumarate (Jha *et al.*, 2015). While the breakpoint at SDH could forthrightly explain the increased levels of succinate, the reduced IDH activity results in a redirection of the TCA cycle flow towards the decarboxylation of *cis*-aconitate, inducing increased itaconate synthesis, and avoiding isocitrate accumulation (Michelucci *et al.*, 2013; Jha *et al.*, 2015). Furthermore, inhibition of SDH can also affect energy production through oxidative phosphorylation, since this enzyme constitutes complex II of the respiratory chain (El Kasmi and Stenmark, 2015). In the event of impaired respiration, substrate-level phosphorylation has a critical role in preventing ATP depletion; however, it has been shown that excessive itaconate abolishes

mitochondrial substrate-level phosphorylation in LPS-activated macrophages (Németh *et al.*, 2015). Hence, the decreased ATP levels observed in RAW 264.7 cells after exposure to AgNPs, may be the combined result of SDH inhibition and increased itaconate synthesis. Macrophages exposed to sub-toxic concentrations of Cit30 additionally showed significantly decreased levels of aspartate and glutamate. The decreased levels of these metabolites could indicate that they were used in the aspartate-argininosuccinate shunt, which has been proven to have an anaplerotic role to replenish the TCA cycle of M1 macrophages, and thus overcome the breakpoint at SDH (Jha *et al.*, 2015).

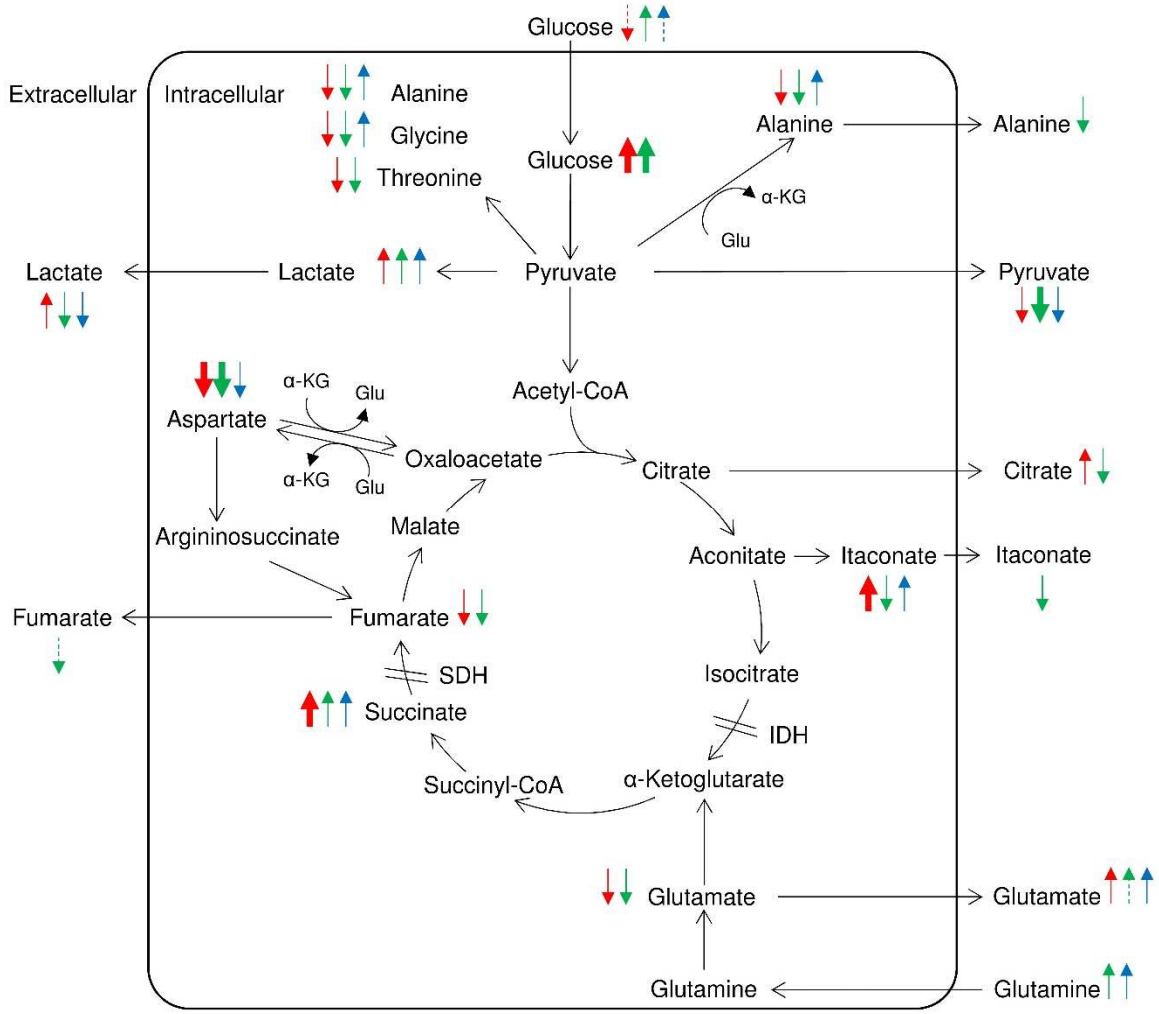

Figure 6.7. Schematic diagram of the putative effects of Cit30 (red arrows), Ag^+ (green arrows), and H_2O_2 (blue arrows), on glycolysis and the TCA cycle. Dashed arrows indicate |% variation| < 10%; thick arrows indicate |% variation| > 50%.

On the other hand, upon exposure to Ag^+, cells decreased the release of citrate and the production and excretion of itaconate and fumarate. These variations are suggestive of a simple downregulation of the TCA cycle activity, distinct from the specific effects induced

by AgNPs. The observed decrease in NAD^+ further supports the downregulation of glycolysis and the TCA cycle. Moreover, Ag^+ did not alter intracellular ATP levels.

The levels of several amino acids (glutamate, aspartate, glycine, alanine and threonine) were markedly decreased upon exposure to both Cit30 and Ag^+. At the same time, intracellular glucose increased significantly in exposed macrophages, while the excretion of pyruvate decreased. A possible explanation to these observations could be the activation of gluconeogenesis (Figure 6.8). In fact, FBP1, the enzyme that catalyses the hydrolysis of fructose-1,6-bisphosphate to form fructose-6-phosphate, has been found upregulated in human macrophages differentiated under the influence of granulocyte macrophage colony-stimulating factor (GM-CSF), i.e. in M1-activated macrophages, but not in those exposed to macrophage colony-stimulating factor (M-CSF), i.e. in M2-activated macrophages (Reales-Calderon *et al.*, 2014). In that study, the authors proposed FBP1 as a metabolic target for modulating macrophage polarisation, since it was one of the most differentially expressed proteins between M1 and M2 macrophages.

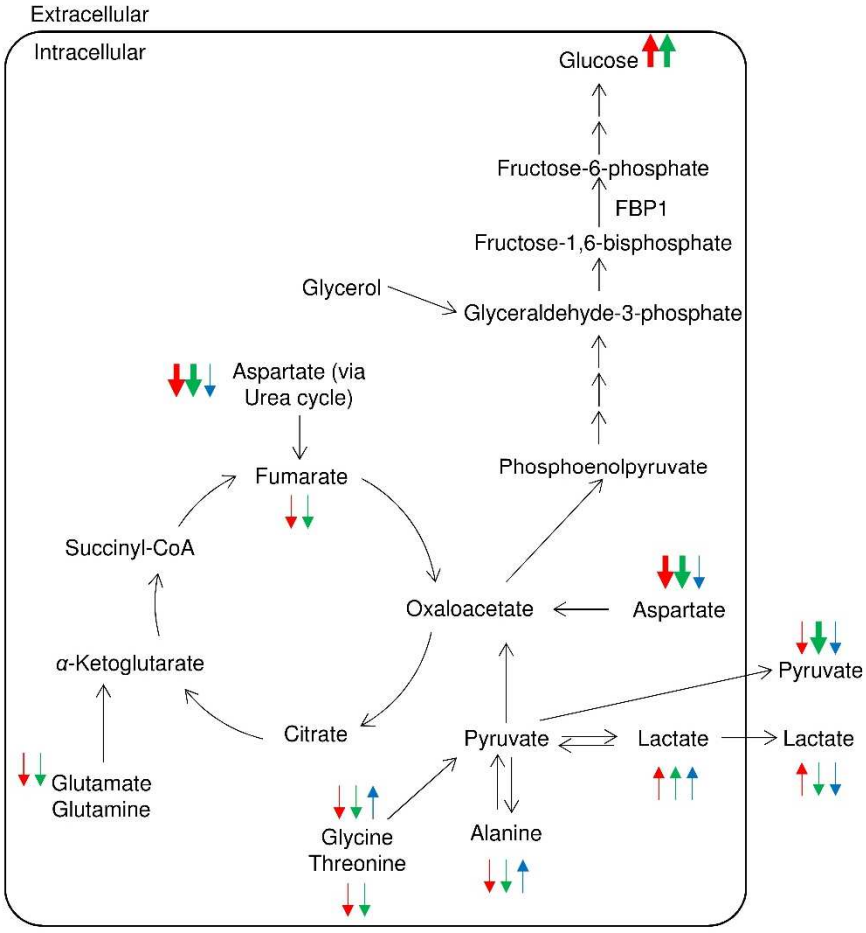

Figure 6.8. Schematic diagram of the putative effects of Cit30 (red arrows), Ag^+ (green arrows), and H_2O_2 (blue arrows), on gluconeogenesis and the TCA cycle. Thick arrows indicate |% variation| > 50%.

Furthermore, we have observed increased levels of creatine and phosphocreatine in response to both Cit30 and Ag^+, but with a much higher magnitude in the case of nanoparticle-exposed cells. These metabolites were also reported to increase in RAW 264.7 cells exposed to other nanoparticles (Feng *et al.*, 2011a; Saborano *et al.*, 2016). It is known that differentiated macrophages contain a phosphocreatine pool that functions as a high energy phosphate reservoir to replenish ATP levels (Loike *et al.*, 1984; Wallimann *et al.*, 1992). As such, it is possible that the accumulation of creatine and phosphocreatine in RAW 264.7 cells after exposure to AgNPs, is a consequence of the increased energy requirements, to compensate for the decreased ATP levels. The maintenance of such phosphocreatine pool is likely dependent on the creatine available in the extracellular medium since macrophages have been reported to be incapable of synthesising creatine *de novo* (from guanidinoacetate and glycine) (Loike *et al.*, 1984).

Upon exposure to both Cit30 and Ag^+, the levels of GSH increased in RAW 264.7 cells. This is in contrast with the reported decrease in GSH levels of RAW 264.7 macrophages exposed to 0.2-1.6 ppm of AgNPs sized ~69 nm (Park *et al.*, 2010). Conversely, a proteomic study on the effects of copper-based nanoparticles in the same cell line, revealed increased glutathione biosynthesis, which was suggested to be a critical factor for cell survival under stress (Triboulet *et al.*, 2013). The GSH-mediated cellular antioxidant capacity is modulated by different processes. Serine *de novo* biosynthesis has been recognised as one of these processes, namely in tumour cells (Amelio *et al.*, 2014), according to the reactions schematically shown in Figure 6.9. A possible hypothesis is that exposed cells are synthesising serine *de novo*, through a glycolysis-diverting pathway, to sustain the production of GSH, needed to neutralise ROS. Correlation analysis between serine and GSH provided some support to this hypothesis (r 0.79, $p < 0.05$, for Ag^+-treated cells). Additionally, significant negative correlations were found between serine and lactate (r -0.95, $p < 0.005$), and between serine and alanine (r -0.92, $p < 0.005$). Since lactate and alanine are glycolytic products, this observation supports the hypothesis of glycolysis diversion towards serine biosynthesis.

Choline and choline-containing compounds were also greatly affected by the presence of Cit30 AgNPs; while choline was non-significantly increased by ~27-33%, phosphocholine (PC) and glycerophosphocholine (GPC) were significantly decreased by ~44-58%, in nanoparticle-exposed cells, compared to controls. Similar decreases in these choline-containing metabolites have been observed in RAW 264.7 macrophages exposed to ultrasmall superparamagnetic particles of iron oxide (Feng *et al.*, 2011a). These compounds are associated with the structural components of cell membranes and their

altered levels in exposed-macrophages are probably related to cell membrane modification. Interestingly, Ag^+ induced similar changes in choline and PC but no change in GPC, while the lipid composition assessed by NMR of lipophilic extracts was found to be more greatly affected by Ag^+ than by AgNPs. Indeed, in addition to the decreased consumption of choline (which was not altered in cells exposed to AgNPs), Ag^+-treated cells showed decreased levels of sphingomyelin and phosphatidylcholine, not observed in nanoparticle-exposed cells. This could reflect direct membrane damage by silver ions. Also, previous studies have reported that, upon stimulation, macrophages produce lipid mediators, important in the response to inflammation, from polyunsaturated fatty acids present in membrane glycerophospholipids (Rouzer *et al.*, 2007; Biswas and Mantovani, 2012). This process involves the hydrolysis of the ester bond linking the fatty acids to the glycerol backbone, leading to membrane remodelling. Thus, the observed decreases in sphingomyelin and phosphatidylcholine could also result from increased lipid mediator biosynthesis.

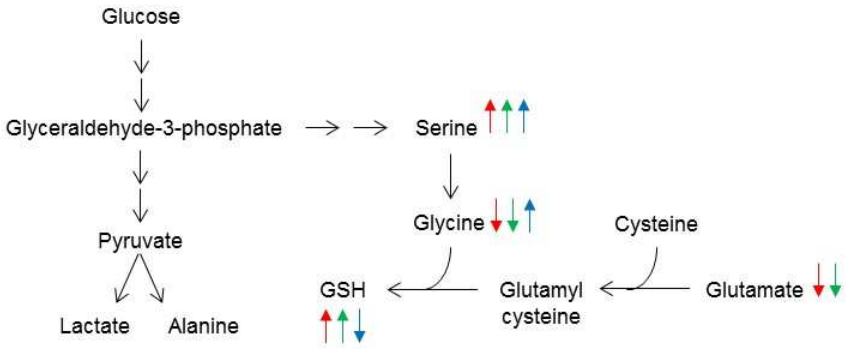

Figure 6.9. Schematic diagram of glycolysis diversion into serine synthesis to support GSH production. Effects of Cit30, Ag^+, and H_2O_2, are represented by red, green, and blue arrows, respectively. Thick arrows indicate |% variation| > 50%.

Other effects common to Cit30 and Ag^+ in RAW 264.7 cells were the decreased levels of *myo*-inositol and betaine. These two metabolites are important organic osmolytes that help cells to maintain their volume (Friedrich *et al.*, 2006). Following cell swelling or shrinkage, volume regulatory mechanisms are activated so that intracellular osmolarity is either decreased, through osmolyte release, or increased, through osmolyte generation and/or accumulation. Cell swelling has been previously observed in RAW 264.7 cells upon AgNPs exposure (Hashimoto *et al.*, 2014). Thus, the observed decreases in intracellular levels of *myo*-inositol and betaine could be related to their release in order to regulate osmolarity. Indeed, the osmoregulatory role of betaine in RAW 264.7 cells has been previously demonstrated (Warskulat *et al.*, 1995). As for *myo*-inositol, the mRNA for the

sodium/myo-inositol co-transporter (SMIT) was not detected in these cells, questioning the role of this metabolite as an osmolyte in RAW 264.7 macrophages (Warskulat *et al.*, 1997). It is also possible that *myo*-inositol variations reflect its role in cell signalling through the phosphatidylinositol cycle (Santini *et al.*, 2004).

The macrophage metabolome was much less affected by H_2O_2 than by AgNPs or Ag^+, as immediately revealed in the heatmaps in Figure 6.3. In addition to having affected fewer metabolites, H_2O_2 caused an inverse or less pronounced effect in some pathways found to be disturbed by AgNPs/Ag^+. For example, H_2O_2 caused reduced glucose consumption and lactate release, suggesting downregulation of glycolysis, contrarily to the effect suggested for AgNPs. As for TCA cycle intermediates, H_2O_2-exposed cells showed moderate increases in itaconate and succinate, in contrast with the huge increases in AgNPs-exposed cells. Thus, TCA cycle reprogramming does not seem to be exclusively mediated by ROS generation. Another clear difference in cells treated with H_2O_2 was that, unlike AgNPs/Ag^+-exposed cells, there was no evidence for activated gluconeogenesis. Intracellular glucose did not increase and gluconeogenic substrates (e.g. alanine, glycine, threonine, glutamate) did not decrease after H_2O_2-exposure. Furthermore, GSH showed a distinct response in H_2O_2-exposed cells, by showing unaltered or decreased levels, which is in accordance with its greater utilisation, to detoxify the increased ROS levels (Figure 6.2).

Finally, the cellular response to the addition of citrate (used as a stabiliser for AgNPs) also deserves a comment. When exposing cells to excess citrate, it is possible that this metabolite is accumulated within the mitochondria, potentiating the TCA cycle and promoting pyruvate/citrate cycling (Figure 6.10) (Guay *et al.*, 2007). The upregulation of the TCA cycle would explain the increased levels of itaconate and fumarate, and the decrease in aspartate. Furthermore, at excessive levels, mitochondrial citrate is exported into the cytosol, where it is converted to pyruvate, through oxaloacetate and malate. This could explain the increased levels of lactate.

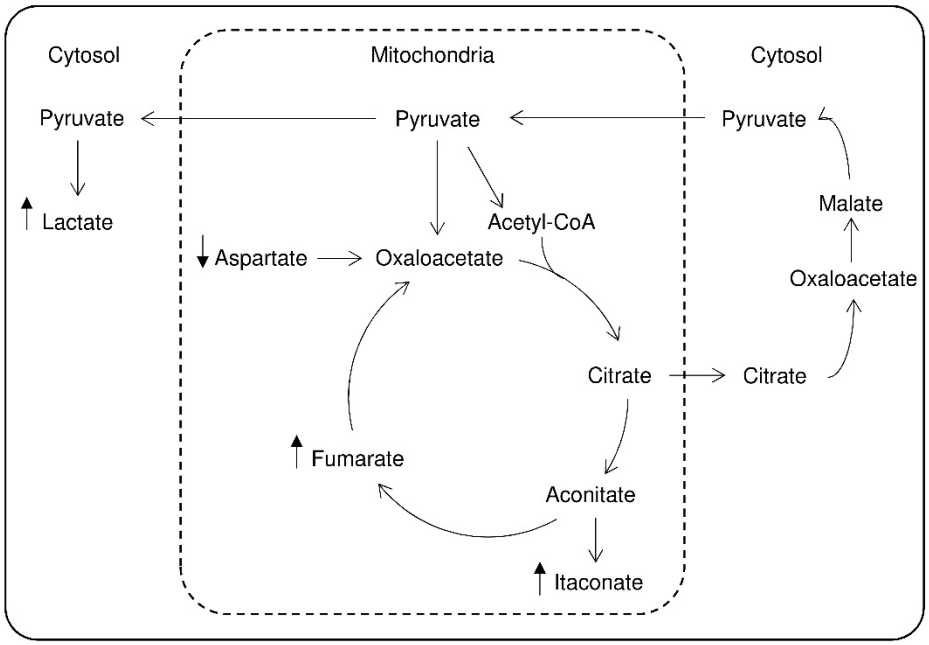

Figure 6.10. Schematic diagram of the putative effects of excess citrate (full arrows) on pyruvate/citrate cycling. Adapted from (Guay *et al.*, 2007).

Supplementary information to Chapter 6

Table S6.1. Main metabolite variations in culture medium of RAW 264.7 cells exposed to Cit30, Ag^+, and H_2O_2, at the IC_5 and IC_{20}, in relation to culture media from control cells, expressed as % variation (%var) and respective error (±), effect size (ES), *p*-value (*p*), and FDR-adjusted *p*-value (FDR). The variations with |ES| < 0.8 (or standard error > |ES|, or mean error > |% variation|) were considered null.

		Cit30		Citrate	Ag^+		H_2O_2	
		IC_5	IC_{20}		IC_5	IC_{20}	IC_5	IC_{20}
Glucose	%var	-8.45	0	0	0	13.55	9.51	0
	±	5.27				6.32	6.62	
	ES	-0.97	0	0	0	1.33	0.91	0
	p	0.1497				0.1025	0.2313	
	FDR	0.5952				0.1974	0.6397	
Pyruvate	%var	-34.35	-41.50	0	-43.71	-55.81	-21.80	-15.62
	±	4.87	4.74		10.52	15.18	20.81	5.55
	ES	-3.84	-4.73	0	-3.29	-3.31	-0.86	-1.60
	p	2.17E-05	4.72E-06		0.0068	0.0128	0.3327	0.0183
	FDR	0.0007	0.0002		0.0666	0.0713	0.6397	0.2018
Lactate	%var	21.27	0	0	0	-36.85	-24.22	0
	±	12.49				19.64	20.26	
	ES	0.93	0	0	0	-1.39	-0.87	0
	p	0.1656				0.0873	0.2554	
	FDR	0.5952				0.1902	0.6397	
Citrate	%var	34.90	45.26	57.22	0	-14.59	0	5.48
	±	2.66	2.60	2.44		8.54		2.54
	ES	6.97	8.99	12.00	0	-1.36	0	1.18
	p	3.84E-05	1.08E-05	4.58E-07		0.1617		0.0725
	FDR	0.0007	0.0002	1.79E-05		0.2426		0.2570
Itaconate	%var	0	0	0	-16.31	-28.81	0	0
	±				8.58	14.92		
	ES	0	0	0	-1.08	-1.43	0	0
	p				0.0792	0.0927		
	FDR				0.1715	0.1902		
Fumarate	%var	0	0	0	-4.79	-6.50	0	0
	±				2.86	3.05		
	ES	0	0	0	-1.00	-1.31	0	0
	p				0.1390	0.0754		
	FDR				0.2710	0.1885		
Glutamine	%var	0	0	0	19.75	32.15	16.23	0
	±				7.88	10.13	12.10	
	ES	0	0	0	1.29	1.78	0.83	0
	p				0.0509	0.0367	0.2680	
	FDR				0.1417	0.1300	0.6397	
Glutamate	%var	20.45	20.49	0	7.42	0	0	13.10
	±	4.43	4.49		4.14			4.85
	ES	2.19	2.18	0	0.83	0	0	1.37
	p	0.0022	0.0025		0.1150			0.0327
	FDR	0.0290	0.0322		0.2361			0.2127
Alanine	%var	-3.56	-3.63	0	-12.78	-15.20	0	3.86
	±	2.46	2.78		2.62	3.63		2.41
	ES	-0.88	-0.84	0	-3.11	-3.00	0	0.95
	p	0.1961	0.2452		0.0031	0.0110		0.1706
	FDR	0.5952	0.4347		0.0666	0.0713		0.4436

		Cit30		Citrate	Ag^+		H_2O_2	
		IC_5	IC_{20}		IC_5	IC_{20}	IC_5	IC_{20}
Methionine	%var	4.23	4.97	0	19.11	14.27	0	4.63
	±	2.84	3.49		3.49	3.05		1.98
	ES	0.86	0.89	0	3.31	2.72	0	1.10
	p	0.1930	0.2230		0.0049	0.0059		0.0473
	FDR	0.5952	0.4142		0.0666	0.0464		0.2135
Isoleucine	%var	3.36	4.39	0	5.68	9.61	5.93	3.85
	±	1.85	2.10		1.73	2.10	3.02	1.31
	ES	1.02	1.24	0	1.78	2.69	1.31	1.36
	p	0.1198	0.0904		0.0143	0.0058	0.1273	0.0179
	FDR	0.5952	0.2287		0.0724	0.0464	0.6397	0.2018
Leucine	%var	0	5.38	0	8.71	11.83	5.57	5.52
	±		2.64		2.52	3.34	4.50	2.09
	ES	0	1.18	0	1.95	2.21	0.85	1.36
	p		0.0938		0.0149	0.0232	0.2953	0.0322
	FDR		0.2287		0.0724	0.0906	0.6397	0.2127
Valine	%var	3.25	4.40	0	3.58	7.54	4.57	4.52
	±	2.05	2.41		2.21	1.93	2.28	1.58
	ES	0.85	1.06	0	0.90	2.02	1.14	1.32
	p	0.1594	0.1238		0.1566	0.0053	0.0935	0.0207
	FDR	0.5952	0.2683		0.2909	0.0464	0.6397	0.2018
2-Oxoisoleucine	%var	0	-3.06	3.28	-6.76	-9.83	0	0
	±		0.75	1.99	2.39	4.49		
	ES	0	-2.45	1.80	-2.21	-1.78	0	0
	p		0.0068	0.0672	0.0578	0.1063		
	FDR		0.0666	0.6556	0.1456	0.1974		
α-Ketovaline	%var	0	-4.45	0	-9.08	-15.82	0	0
	±		2.00		3.50	5.62		
	ES	0	-1.17	0	-1.76	-2.17	0	0
	p		0.0524		0.0502	0.0483		
	FDR		0.2043		0.1417	0.1480		
Choline	%var	0	4.77	0	16.08	17.12	6.04	8.42
	±		2.96		4.03	3.01	4.10	3.27
	ES	0	0.84	0	2.35	2.93	0.89	1.40
	p		0.1524		0.0129	0.0009	0.2072	0.0423
	FDR		0.3062		0.0724	0.0352	0.6397	0.2135
Allantoin	%var	0	0	0	-8.58	0	9.95	0
	±				3.52		6.21	
	ES	0	0	0	-1.26	0	1.03	0
	p				0.0335		0.1925	
	FDR				0.1304		0.6397	
Formate	%var	0	0	0	-16.40	-30.53	-15.01	0
	±				6.54	11.88	14.87	
	ES	0	0	0	-1.87	-2.19	-0.82	0
	p				0.0597	0.0576	0.3609	
	FDR				0.1456	0.1604	0.6397	

Table S6.2. Main metabolite variations in polar extracts of RAW 264.7 cells exposed to Cit30, Ag^+, and H_2O_2, at the IC_5 and IC_{20}, in relation to controls, expressed as % variation (%var) and respective error (±), effect size (ES), *p*-value (*p*), and FDR-adjusted *p*-value (FDR). The variations with |ES| < 0.8 (or standard error > |ES|, or mean error > |% variation|) were considered null.

		Cit30		Citrate	Ag^+		H_2O_2	
		IC_5	IC_{20}		IC_5	IC_{20}	IC_5	IC_{20}
Glucose	%var	250.47	396.40	0	170.12	474.51	0	0
	±	19.22	24.24		14.57	104.78		
	ES	5.35	5.66	0	4.96	2.20	0	0
	p	0.0036	0.0049		0.0014	0.1867		
	FDR	0.0164	0.0150		0.0214	0.3272		
Lactate	%var	36.39	29.38	24.04	24.63	0	0	24.67
	±	17.66	20.87	11.05	12.35			13.25
	ES	1.13	0.84	0.89	0.91	0	0	0.89
	p	0.1262	0.2639	0.0739	0.0997			0.1339
	FDR	0.2149	0.3372	0.3356	0.1765			0.4734
Itaconate	%var	229.72	288.37	31.11	-23.86	0	0	33.62
	±	19.73	27.84	15.35	11.29			16.42
	ES	5.14	4.31	1.28	-1.14	0	0	1.35
	p	0.0053	0.0120	0.1566	0.0488			0.1612
	FDR	0.0188	0.0291	0.4879	0.1309			0.4734
Succinate	%var	63.39	77.53	9.28	11.52	0	0	34.16
	±	13.53	15.79	6.55	8.36			5.98
	ES	3.01	3.11	0.85	0.88	0	0	3.15
	p	0.0258	0.0266	0.2445	0.2514			0.0072
	FDR	0.0539	0.0510	0.6616	0.3212			0.0828
Fumarate	%var	0	-22.46	26.20	-29.49	-43.99	0	0
	±		11.32	6.24	12.69	27.47		
	ES	0	-1.24	1.62	-1.56	-1.67	0	0
	p		0.0772	0.0035	0.0480	0.1961		
	FDR		0.1262	0.0406	0.1309	0.3272		
Glutamate	%var	-26.33	-28.82	0	-18.15	-32.86	0	0
	±	5.86	6.00		6.41	11.94		
	ES	-2.30	-2.51	0	-1.52	-2.26	0	0
	p	0.0007	0.0004		0.0163	0.0637		
	FDR	0.0034	0.0018		0.0831	0.3150		
Aspartate	%var	-57.79	-57.36	-32.52	-56.90	-65.01	-20.53	-43.07
	±	8.50	7.88	8.28	9.91	18.03	7.40	11.26
	ES	-3.66	-3.70	-1.94	-3.44	-3.20	-1.30	-2.43
	p	8.19E-06	1.04E-05	0.0027	0.0001	0.0251	0.0141	0.0096
	FDR	0.0001	0.0001	0.0406	0.0026	0.2306	0.3232	0.0828
Glycine	%var	-11.48	-18.50	-6.63	-2.90	-11.89	14.04	20.03
	±	1.65	1.51	2.99	2.19	6.85	1.17	3.86
	ES	-4.15	-7.02	-1.90	-0.89	-1.87	5.62	4.65
	p	0.0004	3.97E-06	0.1303	0.2469	0.2099	1.50E-06	0.0319
	FDR	0.0026	0.0001	0.4626	0.3212	0.3307	0.0001	0.1834
Alanine	%var	-22.95	-31.24	0	-33.87	-41.07	10.71	13.81
	±	6.76	6.75		9.52	16.38	5.87	7.11
	ES	-1.97	-2.71	0	-2.51	-2.48	0.93	1.14
	p	0.0078	0.0011		0.0112	0.0890	0.1196	0.1384
	FDR	0.0238	0.0044		0.0738	0.3150	0.7862	0.4734
β-Alanine	%var	0	-14.16	0	-21.50	-34.24	5.36	0
	±		4.71		10.24	20.08	3.21	
	ES	0	-1.92	0	-1.74	-1.99	0.84	0
	p		0.0247		0.0993	0.1968	0.1398	
	FDR		0.0494		0.1765	0.3272	0.8037	

		Cit30		Citrate	Ag^+		H_2O_2	
		IC_5	IC_{20}		IC_5	IC_{20}	IC_5	IC_{20}
Threonine	%var	-12.43	-14.47	0	-17.76	-22.70	0	0
	±	3.69	3.19		3.75	8.21		
	ES	-1.99	-2.47	0	-2.85	-2.63	0	0
	p	0.0124	0.0016		0.0023	0.0829		
	FDR	0.0300	0.0057		0.0263	0.3150		
Isoleucine	%var	0	11.06	-3.92	0	0	0	0
	±		4.99	3.75				
	ES	0	1.62	-0.83	0	0	0	0
	p		0.1115	0.3802				
	FDR		0.1655	0.7680				
Valine	%var	0	7.35	0	-6.86	-3.67	0	3.02
	±		5.06		5.53	1.38		1.77
	ES	0	1.16	0	-1.05	-1.83	0	1.34
	p		0.2488		0.2916	0.0717		0.2048
	FDR		0.3270		0.3626	0.3150		0.4797
Serine	%var	20.49	30.47	-17.42	32.00	39.04	0	12.62
	±	8.31	9.26	6.80	11.56	14.26		7.53
	ES	1.38	1.91	-1.32	1.74	2.12	0	0.92
	p	0.0664	0.0341	0.0348	0.0680	0.1117		0.1749
	FDR	0.1272	0.0627	0.2000	0.1563	0.3272		0.4734
Tyrosine	%var	18.50	64.66	0	0	0	0	0
	±	11.63	12.90					
	ES	0.80	2.51	0	0	0	0	0
	p	0.1774	0.0088					
	FDR	0.2632	0.0239					
Creatine	%var	208.73	252.06	0	26.08	25.63	0	26.13
	±	4.79	4.53		7.02	12.99		12.71
	ES	18.91	22.37	0	2.47	1.85	0	1.92
	p	3.46E-05	2.10E-05		0.0307	0.1992		0.1873
	FDR	0.0004	0.0002		0.1179	0.3272		0.4787
Phosphocreatine	%var	117.06	124.88	0	13.61	0	0	12.03
	±	6.36	8.46		7.71			3.41
	ES	9.53	8.01	0	1.18	0	0	1.53
	p	0.0003	0.0011		0.1693			0.0090
	FDR	0.0025	0.0044		0.2686			0.0828
ADP	%var	0	-38.88	0	0	-31.80	0	0
	±		21.95			17.17		
	ES	0	-1.07	0	0	-0.91	0	0
	p		0.0796			0.0773		
	FDR		0.1262			0.3150		
ATP	%var	-26.89	-26.41	0	0	0	0	0
	±	8.45	9.79					
	ES	-1.66	-1.55	0	0	0	0	0
	p	0.0063	0.0196					
	FDR	0.0209	0.0430					
NAD^+	%var	0	0	0	-14.01	-16.37	0	0
	±				5.76	4.97		
	ES	0	0	0	-1.48	-1.84	0	0
	p				0.0453	0.0181		
	FDR				0.1309	0.2306		
GSH	%var	31.42	29.49	-12.28	43.55	40.27	0	-6.31
	±	6.78	6.91	11.55	8.70	8.83		5.37
	ES	3.19	2.96	-1.11	3.46	4.03	0	-0.93
	p	0.0191	0.0240	0.3805	0.0191	0.0479		0.3297
	FDR	0.0439	0.0494	0.7680	0.0878	0.3147		0.5417

		Cit30		Citrate	Ag^+		H_2O_2	
		IC_5	IC_{20}		IC_5	IC_{20}	IC_5	IC_{20}
Choline	%var	26.67	33.20	-13.68	15.24	0	0	0
	±	12.60	11.63	5.90	7.54			
	ES	1.34	1.73	-0.98	1.03	0	0	0
	p	0.1244	0.0602	0.0394	0.0952			
	FDR	0.2149	0.1025	0.2016	0.1765			
Phosphocholine	%var	-44.18	-50.75	0	-38.90	-42.91	-5.57	-17.21
	±	3.58	3.11		7.62	11.86	2.97	4.73
	ES	-7.46	-9.06	0	-4.25	-3.99	-0.96	-2.58
	p	6.64E-07	3.38E-09		0.0055	0.0478	0.0904	0.0291
	FDR	1.53E-05	1.55E-07		0.0424	0.3147	0.7862	0.1834
Glycero-phosphocholine	%var	-51.61	-57.60	-28.26	0	0	-15.82	-16.04
	±	3.98	4.50	5.48			6.59	4.14
	ES	-6.18	-6.74	-2.97	0	0	-1.51	-1.76
	p	6.16E-07	3.56E-08	0.0024			0.0493	0.0033
	FDR	1.53E-05	8.18E-07	0.0406			0.5665	0.0828
myo-Inositol	%var	-28.49	-32.50	-15.27	-39.25	-39.22	0	-13.00
	±	5.84	6.13	7.18	9.73	10.67		7.55
	ES	-2.47	-2.79	-1.22	-2.82	-2.83	0	-1.02
	p	0.0003	0.0002	0.0803	0.0053	0.0250		0.1445
	FDR	0.0025	0.0010	0.3356	0.0424	0.2306		0.4734
Taurine	%var	0	0	0	11.44	0	0	9.97
	±				5.24			2.95
	ES	0	0	0	1.24	0	0	1.25
	p				0.0848			0.0108
	FDR				0.1695			0.0828
Betaine	%var	-26.93	-35.91	-19.51	-13.88	-17.03	6.51	-4.34
	±	3.87	3.78	3.25	3.90	4.16	2.33	3.44
	ES	-4.74	-6.51	-3.78	-2.37	-3.03	1.36	-0.82
	p	0.0007	0.0001	0.0034	0.0155	0.0240	0.0244	0.2816
	FDR	0.0034	0.0007	0.0406	0.0831	0.2306	0.3741	0.4797
Pantothenate	%var	-22.56	-23.84	0	-24.69	-22.04	0	-8.07
	±	5.27	3.14		3.34	4.19		3.51
	ES	-3.29	-4.72	0	-4.75	-4.02	0	-1.55
	p	0.0112	0.0002		0.0003	0.0126		0.0929
	FDR	0.0286	0.0010		0.0072	0.2306		0.4734

Table S6.3. Main metabolite variations in lipophilic extracts of RAW 264.7 cells exposed to Cit30, Ag^+, and H_2O_2, at the IC_5 and IC_{20}, in relation to controls, expressed as % variation (%var) and respective error (±), effect size (ES), *p*-value (*p*), and FDR-adjusted *p*-value (FDR). The variations with |ES| < 0.8 (or standard error > |ES|, or mean error > |% variation|) were considered null.

		Cit30		Citrate	Ag^+		H_2O_2	
		IC_5	IC_{20}		IC_5	IC_{20}	IC_5	IC_{20}
Total cholesterol	%var	0	0	0	-20.23	-28.08	0	-6.10
	±				7.98	14.20		3.42
	ES	0	0	0	-1.84	-1.98	0	-0.81
	p				0.0503	0.1509		0.1064
	FDR				0.1417	0.3094		0.3800
Free cholesterol	%var	0	9.13	0	0	-12.45	-8.97	0
	±		4.55			6.12	5.71	
	ES	0	0.87	0	0	-1.06	-0.80	0
	p		0.0896			0.0751	0.1390	
	FDR		0.3201			0.3094	0.8539	
PTC	%var	0	0	0	-15.35	-19.05	0	0
	±				6.69	8.90		
	ES	0	0	0	-1.55	-1.80	0	0
	p				0.0624	0.1223		
	FDR				0.1417	0.3094		
PTE	%var	-3.89	-7.40	0	2.75	0	0	5.20
	±	1.15	0.77		2.26			1.25
	ES	-2.17	-5.19	0	0.89	0	0	2.97
	p	0.0202	7.52E-06		0.3064			0.0276
	FDR	0.5061	0.0002		0.3685			0.3445
PTE plasmalogen	%var	0	0	-5.78	13.38	0	0	9.19
	±			5.60	3.83			2.26
	ES	0	0	-0.96	2.37	0	0	2.50
	p			0.3944	0.0334			0.0191
	FDR			0.8805	0.1391			0.3445
SM	%var	0	0	0	-13.94	-25.27	0	0
	±				6.09	14.88		
	ES	0	0	0	-1.57	-1.74	0	0
	p				0.0666	0.1991		
	FDR				0.1417	0.3094		
Total unsaturated fatty acyl chains	%var	0	-7.72	0	-16.29	-20.92	0	0
	±		6.05		5.71	10.00		
	ES	0	-0.82	0	-1.82	-1.85	0	0
	p		0.2467		0.0254	0.1320		
	FDR		0.6377		0.1391	0.3094		
Polyunsaturated fatty acyl chains	%var	0	0	0	16.36	13.84	0	5.28
	±				4.21	7.63		3.72
	ES	0	0	0	2.32	1.52	0	0.85
	p				0.0154	0.2061		0.2342
	FDR				0.1281	0.3094		0.5458

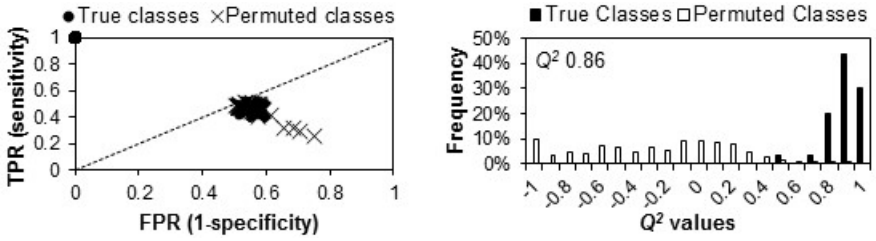

Figure S6.1. ROC space (left) and Q^2 histogram (right) obtained by MCCV and permutation testing of the PLS-DA models of polar extracts, corresponding to Cit30 exposure (sensitivity 100%, specificity 100%, classification rate 100%). TPR: true positive rate; FPR: false positive rate.

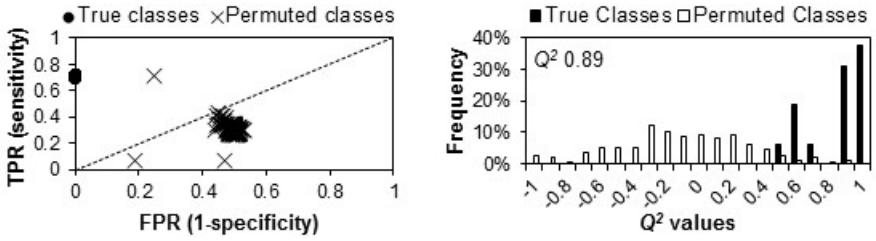

Figure S6.2. ROC space (left) and Q^2 histogram (right) obtained by MCCV and permutation testing of the PLS-DA models of polar extracts, corresponding to Ag^+ exposure (sensitivity 70.0%, specificity 100%, classification rate 86.0%). TPR: true positive rate; FPR: false positive rate.

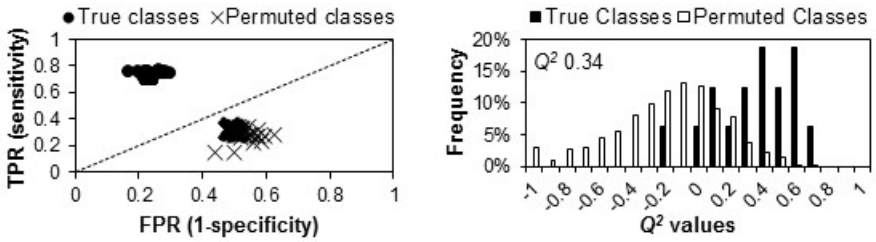

Figure S6.3. ROC space (left) and Q^2 histogram (right) obtained by MCCV and permutation testing of the PLS-DA models of polar extracts, corresponding to H_2O_2 exposure (sensitivity 74.3%, specificity 72.5%, classification rate 73.3%). TPR: true positive rate; FPR: false positive rate.

Chapter 7. Integrated discussion and conclusions

In this work, the metabolic responses of cultured mammalian cells to silver nanoparticles (AgNPs) were evaluated through NMR metabolomics, with a view to improve current knowledge on the (sub)toxic effects of these relevant and widely disseminated nanoparticles. The cell lines used were epidermis keratinocytes (HaCaT), liver hepatoma cells (HepG2) and blood macrophages (RAW 264.7), selected to represent important sites of AgNPs entry, accumulation and interaction within the organism. Purified, well-characterised AgNPs were used to enable meaningful relationships between nanoparticle properties and biological outcomes to be established. The exposure conditions for metabolomic profiling of AgNPs-induced effects were chosen after careful dose-response studies of cell viability, conducted for each cell type. Furthermore, the metabolic signatures of cell exposures to ionic silver and hydrogen peroxide were also characterised to assess the role of silver ions and oxidative stress on the biological impact of AgNPs.

Silver nanoparticles were found to elicit profound alterations in the metabolic activity and intracellular composition of the three cell types studied, even at concentrations causing minimal (≤ 20%) decreases in cell viability. By measuring consistent changes in metabolite levels upon exposure to AgNPs, multiple effects in pathways used by cells for purposes like energy production, biosynthesis, antioxidant protection, membrane remodelling or osmoregulation, could be proposed. The great advantage of this approach was that it enabled the simultaneous, comprehensive screening of unpredicted effects, without making *a priori* assumptions. Compared to conventional cytotoxicity studies typically based on a single pre-established endpoint, this achievement has great potential for providing new mechanistic insights. On the other hand, one should be aware that metabolite levels reflect pools resulting from the interplay between different biochemical processes, and as such, it is hard to derive definite information based only on metabolic variations. Instead, metabolic profiling can be viewed as an initial step in the quest for mechanistic answers, which should be followed by more targeted investigations to confirm the hypotheses generated. That said, this thesis is believed to represent an important contribute towards the revelation of a more complete picture of AgNPs biological effects.

The three cell types tested showed both common and distinct responses to AgNPs-exposure. To aid this comparative analysis, the main variations resulting from 24 h exposure

of each cell line to citrate-coated AgNPs with a core diameter of 30 nm at the IC_{20} concentration are summarised in Figure 7.1. Overall, HaCaT cells showed the least altered metabolic profile under these exposure conditions. Note, however, that some effects (seen for the other cell types) were also noticed in HaCaT cells exposed to a higher AgNPs concentration (IC_{50}) or for a longer period (48 h). Thus, the complete sets of data were taken into consideration for the integrated discussion presented in the following paragraphs.

The uptake and conversion of glucose into lactate through glycolysis and lactic acid fermentation was suggested to be moderately intensified in HaCaT cells exposed to the smaller (10 nm) AgNPs and in RAW 264.7 macrophages exposed to the IC_5 concentration. However, there were generally no strong evidences for altered glycolytic activity. In HepG2 cells, the lack of effect could be influenced by the medium supplementation with pyruvate (used as the main substrate). Glutamine was another major substrate used by cells and its variations suggested increased glutaminolytic activity in AgNPs-exposed HaCaT cells and in HepG2 cells exposed to the biogenic GS30 AgNPs; again, this was a cell- and material-dependent effect.

The TCA cycle emerged as an important target of AgNPs effects in all tested cell lines. Common variations relating to intermediates of this pathway included increased citrate excretion, decreased levels of several anaplerotic substrates (mainly amino acids like glutamate or aspartate), and increased intracellular succinate and/or decreased fumarate. This latter effect suggests altered activity for the enzyme succinate dehydrogenase (SDH), which catalyses the oxidation of succinate to fumarate; thus, this is an example of a specific enzymatic step deserving further investigation. Exposed macrophages additionally showed very high levels of the metabolite itaconate, known to be produced from aconitate after a TCA cycle breakpoint at isocitrate dehydrogenase (IDH), in response to a pro-inflammatory stimulus. Overall, exposed cells seemed to maintain an active, reprogrammed TCA cycle, with RAW macrophages showing the more profound changes in this pathway.

Another distinctive feature of the macrophages response to AgNPs, not seen in the other cell types, regarded the increase in intracellular glucose, which, together with decreased levels of gluconeogenic substrates, suggested activation of gluconeogenesis. Assessing the expression and/or activity of the enzymes involved in this pathway, such as the rate-limiting enzyme fructose-1,6-bisphosphatase 1 (FBP1), should be pursued to confirm this hypothesis and to evaluate the functional significance of this change.

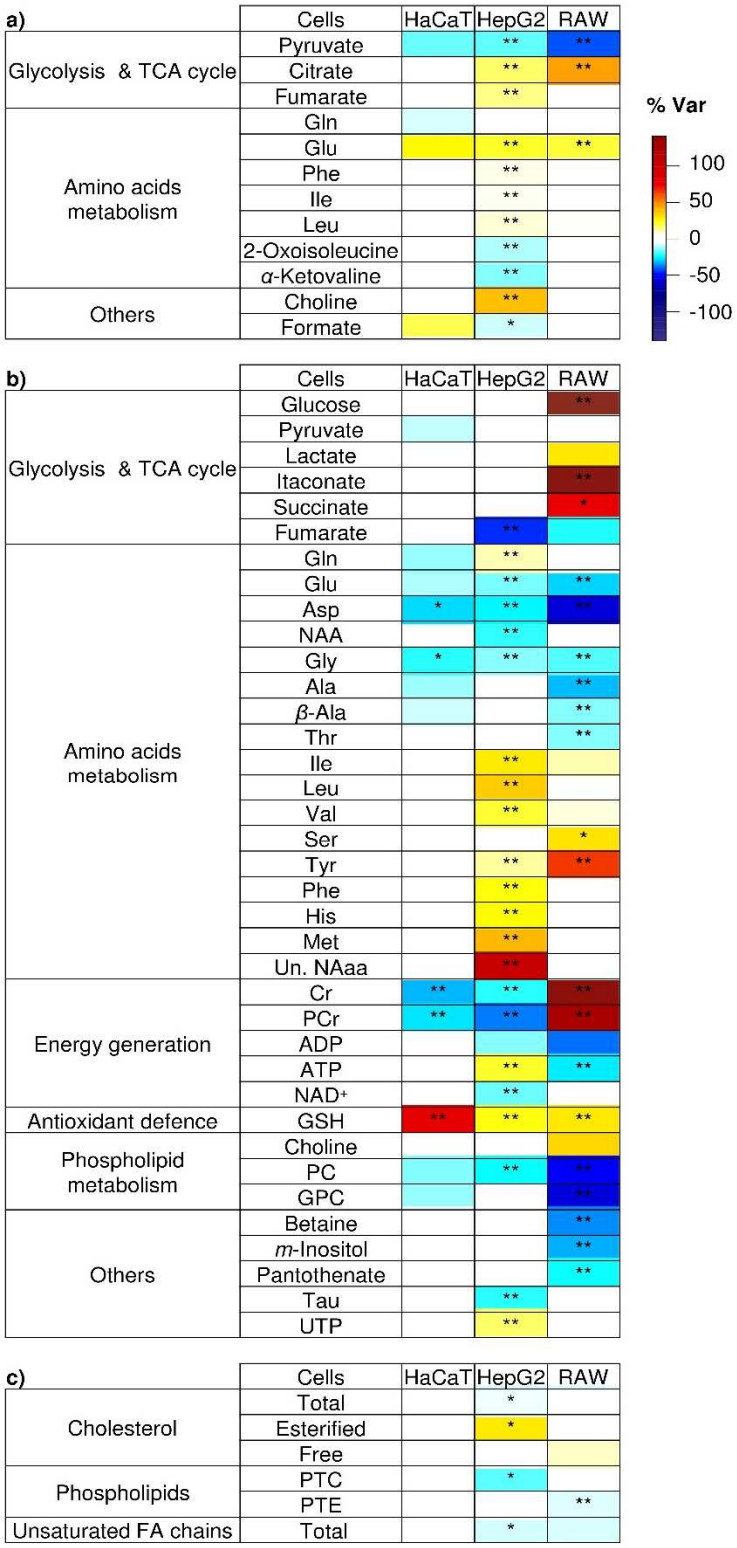

Figure 7.1. Heatmap of the main variations in a) culture media, b) polar extracts, and c) lipophilic extracts, of HaCaT, HepG2, and RAW 264.7 cells exposed to Cit30 AgNPs, at IC_{20} concentrations, for 24 h, coloured according to % variation in relation to controls. * Uncorrected *p*-value < 0.05; ** FDR-corrected *p*-value < 0.05. Three letter code used for amino acids; NAA, *N*-acetylaspartate; Un. NAaa, unidentified *N*-acetylated amino acid; Cr, creatine; PCr, phosphocreatine; ADP/ATP, adenosine di/triphosphate; NAD^+, nicotinamide adenine dinucleotide; GSH, reduced glutathione; PC, phosphocholine; GPC, glycerophosphocholine; UTP, uridine triphosphate; PTC, phosphatidylcholine; PTE, phosphatidylethanolamine; FA, fatty acyl.

TCA cycle reprogramming is expected to affect oxidative phosphorylation and energy production. Interestingly, the variation in ATP levels was clearly cell-dependent. Upon exposure to AgNPs, HaCaT cells maintained their ATP levels unchanged, HepG2 cells presented an increased ATP pool and RAW 264.7 macrophages showed ATP depletion. We have hypothesised that HepG2 cells have enhanced their metabolic activity, including ATP production, as a protective mechanism to cope with the presence of AgNPs. As for the RAW 264.7 macrophages, the profound reprogramming of the TCA cycle could have directly resulted in ATP depletion, through inhibition of SDH (complex II of the respiratory chain) and downregulation of substrate-level phosphorylation (by excess itaconate). Another striking energy-related change regarded the levels of creatine and phosphocreatine; these metabolites decreased in HaCaT and HepG2 cells exposed to AgNPs (compared to their respective controls), while exposed macrophages displayed marked increases in both compounds. In times of high metabolic demand, cells use phosphocreatine to obtain ATP through an enzymatic reaction catalysed by creatine kinase, whereby creatine is formed. Thus, the decrease in phosphocreatine could reflect the higher energetic needs of AgNPs-exposed cells (namely HaCaT and HepG2 cells). This was however not accompanied by the expected increase in creatine, possibly indicating its use by another reaction. As for RAW 264.7 macrophages, the opposite effect was observed, with exposed cells building up a large pool of creatine and phosphocreatine. Whether this alteration reflects an attempt to compensate for inhibited ATP production or it has another functional significance remains to be clarified. In future studies, it would be interesting to assess the expression of creatine kinase isoforms and of creatine transporter molecules, as well as to evaluate the activation state and metabolic profile of macrophages upon blockage of the creatine/phosphocreatine shuttle system.

The intracellular levels of the antioxidant tripeptide glutathione (GSH) were seen to increase in the three cell lines upon exposure to AgNPs, with the exception of HaCaT cells exposed to the smallest (10 nm) nanoparticles, which displayed unaltered or decreased GSH levels compared to controls. When comparing the same NP type and exposure conditions, HaCaT cells registered the largest increase in GSH levels, in agreement with the strong antioxidant capacity of skin keratinocytes. We have thus postulated that cells activated GSH *de novo* synthesis, as supported by decreased amounts of precursor amino acids and, in the case of macrophages, by the increased production of serine through a glycolysis-diverting pathway. This preservation of the GSH-mediated defence against reactive oxygen species generated in AgNPs-exposed cells could have played a crucial role in avoiding major oxidative damage. Future work should entail the assessment of enzymes

involved in GSH synthesis, namely glutamate cysteine ligase (GCL) and GSH synthetase, as well as the quantitative measurement of both GSH and GSSG by alternative biochemical methods.

Based on the increased levels of several amino acids, autophagy was proposed as an additional protective mechanism which appeared to be activated mainly in HepG2 cells, and, to a lesser extent, in HaCaT cells. Further metabolic variations comprised prominent decreases in *myo*-inositol (HaCaT and RAW 264.7 cells), taurine (HepG2 cells) and betaine (RAW 264.7 cells), possibly in relation to the osmoregulatory role of these metabolites. Additionally, the significant decreases in phosphocholine (common to the three cell lines) and glycerophosphocholine (seen in HaCaT and RAW 264.7 cells), pointed to changes in cell membrane composition and/or turnover.

Analysis of lipophilic extracts was expected to provide complementary insight into AgNPs-induced alterations in lipid composition. The NMR-derived lipophilic profiles showed dominant contributions from membrane components, such as cholesterol and different phospholipid classes (phosphatidylcholine, phosphatidylethanolamine and sphingomyelin), and smaller contributions from neutral lipids (especially noticeable in HepG2 cells). However, the impact of AgNPs on those lipid profiles was found to be much smaller than that observed for polar metabolites. The few AgNPs-induced alterations which could be suggested based on the lipid metabolome comprised downregulation of phospholipid synthesis and storage of fatty acids in the form of cholesterol esters in HepG2 cells, and membrane damage and/or the possible use of phospholipids for the production of inflammatory mediators in RAW 264.7 macrophages. However, these hypotheses were rather speculative, requiring further confirmation. The use of alternative analytical methods to characterise lipid components could be helpful in this respect. Indeed, the ^{1}H NMR analysis of lipids has important limitations, such as the large signal width resulting from the lower molecular mobility of bigger molecules (thus giving rise to broad, poorly resolved signals), and the high degree of spectral overlap between different lipid species (e.g. phospholipids with different fatty acids in their composition). Thus, other methods like liquid chromatography coupled to mass spectrometry (LC/MS), more commonly used in lipidomic studies, would be recommended; this technique not only has the ability to provide more detailed information on lipids structural diversity, as it is more sensitive than NMR, potentially allowing changes in minor lipid metabolites, present at submicromolar concentrations, to be detected.

It has been widely reported that the different physicochemical properties of AgNPs (such as size or coating) can influence the way they interact with cells. As such, a panel of six AgNP types with different diameters (10, 30 or 60 nm) and coatings (citrate, polyethylene glycol (PEG) or bovine serum albumin (BSA)) were tested in HaCaT cells, to assess the influence of nanoparticle size and surface on the cytotoxic and metabolic effects produced. Although several metabolic variations were commonly seen across all tested AgNPs, the smallest (10 nm) particles, coated either with citrate or PEG, produced the most distinct effects, namely in regard to glycolysis and GSH production/utilisation. Additionally, in HepG2 cells, a comparison was established between citrate-stabilised (Cit30) and phytosynthesised (GS30) AgNPs. Again, the two nanoparticle types induced many common effects; still, Cit30 AgNPs, which were slightly more cytotoxic to liver cells than GS30 AgNPs, appeared to produce a greater impact on the TCA cycle and protein degradation. On the other hand, GS30 AgNPs apparently elicited higher glutaminolytic activity and a stronger downregulation of phospholipid synthesis. The detection of such differences suggests that the fine tuning of AgNPs properties may be used to modulate the cellular metabolic responses and, thus, the biological outcomes achieved.

The role of silver ion release in AgNPs-mediated effects has been addressed in this work by exposing cells to a soluble silver salt ($AgNO_3$) at concentrations causing equivalent decreases in cell viability. Metabolic profiling revealed remarkably similar effects for AgNPs and Ag^+, especially in HaCaT and HepG2 cells. Still, some differences could be noted. In HaCaT cells, extracellular Ag^+ ions appeared to cause a lower impact on the TCA cycle and glutaminolysis and to differently affect phosphocreatine levels, possibly in relation to energetic recovery. Moreover, Ag^+ elicited much stronger changes in cellular lipids, such as the more prominent decreases in cholesterol and membrane phospholipids. In the case of HepG2 cells, differences like the less pronounced increases in GSH and ATP and the release of allantoin, suggested that cells treated with extracellular Ag^+ were less capable of dealing with oxidative stress than those exposed to AgNPs. As for the RAW 264.7 macrophages, although there were common features in the metabolic responses to AgNPs and Ag^+ (e.g. activated gluconeogenesis, upregulated GSH synthesis), several pathways appeared to be distinctly affected. For instance, the TCA cycle was suggested to be exquisitely reprogrammed in AgNPs-treated cells, likely to sustain an inflammatory response, while in Ag^+-exposed cells it appeared to be simply downregulated; also, ATP depletion was not seen upon exposure to extracellular Ag^+ and the build-up of a creatine/phosphocreatine pool was much less significant. On the other hand, Ag^+ produced

a clearly stronger impact on cellular lipids, which could be related to cell membrane damage and/or the synthesis of inflammatory mediators.

The excessive production of reactive oxygen species (ROS) has been advocated as a major cause of AgNPs damaging effects on cells. Thus, to assess the role of oxidative stress in the metabolic signature of AgNPs, exposure to hydrogen peroxide (H_2O_2) has been performed and the resulting effects on the cellular metabolome have been evaluated. Clearly, many of the effects attributed to AgNPs were not exclusively mediated by ROS. Comparatively to AgNPs, H_2O_2 (at concentrations causing similar decreases in cell viability) caused a lower impact on the TCA cycle and did not appear to upregulate glutaminolysis or GSH synthesis. Additionally, in RAW 264.7 macrophages, there was no evidence of activated gluconeogenesis as seen upon exposure to AgNPs/Ag^+. Also, in HaCaT cells, H_2O_2 was suggested to cause membrane degradation, in contrast with the lower turnover postulated for AgNPs-exposed keratinocytes. Another contrasting effect regarded the inhibition of glycolysis, which emerged as a common response of the three cell lines to H_2O_2 but not to AgNPs. On the other hand, in HaCaT and HepG2 cells, H_2O_2 induced similar or even more intense increases in some amino acids (as compared to AgNPs), suggesting that the proposed autophagic protein degradation was a ROS-mediated effect.

As a final conclusion, we can state that metabolic reprogramming in cells exposed to AgNPs took place independently of direct cytotoxic effects. In fact, some of the observed changes were possibly linked to protective mechanisms that conferred cells functional advantages to cope with the presence of foreign particles (and/or the ions/molecules released from their surface). Other effects, on the other hand, were likely related to adverse outcomes, providing novel insights into toxicity mechanisms of AgNPs.

Overall, the work hereby presented has proven that NMR metabolomics is a powerful tool for the untargeted screening of the biochemical effects of AgNPs in mammalian cells. It is believed that this approach can be extended for establishing the biosafety of other existing and new nanomaterials, providing an invaluable complementary platform for their tailored design and risk-benefit assessment.

Bibliography

Adosraku, R.K., Choi, G.T., Constantinou-Kokotos, V., Anderson, M.M. and Gibbons, W.A., 1994. NMR lipid profiles of cells, tissues, and body fluids: proton NMR analysis of human erythrocyte lipids. *Journal of Lipid Research*, 35(11): 1925-31.

Agnihotri, S., Mukherji, S. and Mukherji, S., 2014. Size-controlled silver nanoparticles synthesized over the range 5-100 nm using the same protocol and their antibacterial efficacy. *RSC Advances*, 4(8): 3974-83.

Ahlberg, S., Meinke, M.C., Werner, L., Epple, M., Diendorf, J., Lademann, J., Blume-Peytavi, U., Vogt, A. and Rancan, F., 2014. Production of reactive oxygen species and toxic effects of silver nanoparticles towards the human keratinocyte cell line HaCaT. *Experimental Dermatology*, 23(3): e8.

Aldossari, A.A., Shannahan, J.H., Podila, R. and Brown, J.M., 2015. Scavenger receptor B1 facilitates macrophage uptake of silver nanoparticles and cellular activation. *Journal of Nanoparticle Research*, 17(7): 313, 14 pages.

Alia, M., Ramos, S., Mateos, R., Bravo, L. and Goya, L., 2005. Response of the antioxidant defense system to tert-butyl hydroperoxide and hydrogen peroxide in a human hepatoma cell line (HepG2). *Journal of Biochemical and Molecular Toxicology*, 19(2): 119-28.

Amelio, I., Cutruzzolá, F., Antonov, A., Agostini, M. and Melino, G., 2014. Serine and glycine metabolism in cancer. *Trends in Biochemical Sciences*, 39(4): 191-8.

Arora, S., Jain, J., Rajwade, J.M. and Paknikar, K.M., 2009. Interactions of silver nanoparticles with primary mouse fibroblasts and liver cells. *Toxicology and Applied Pharmacology*, 236(3): 310-8.

Asharani, P.V., Low Kah Mun, G., Hande, M.P. and Valiyaveettil, S., 2009. Cytotoxicity and genotoxicity of silver nanoparticles in human cells. *ACS Nano*, 3(2): 279-90.

Aslund, M.L.W., Mcshane, H., Simpson, M.J., Simpson, A.J., Whalen, J.K., Hendershot, W.H. and Sunahara, G.I., 2012. Earthworm sublethal responses to titanium dioxide nanomaterial in soil detected by ^{1}H NMR metabolomics. *Environmental Science & Technology*, 46(2): 1111-8.

Aude-Garcia, C., Villiers, F., Collin-Faure, V., Pernet-Gallay, K., Jouneau, P.H., Sorieul, S., Mure, G., Gerdil, A., Herlin-Boime, N., Carriere, M. and Rabilloud, T., 2016. Different in vitro exposure regimens of murine primary macrophages to silver nanoparticles induce different fates of nanoparticles and different toxicological and functional consequences. *Nanotoxicology*, 10(5): 586-96.

Austin, L.A., Kang, B., Yen, C.W. and El-Sayed, M.A., 2011. Nuclear targeted silver nanospheres perturb the cancer cell cycle differently than those of nanogold. *Bioconjugate Chemistry*, 22(11): 2324-31.

Avalos, A., Haza, A.I., Mateo, D. and Morales, P., 2014. Cytotoxicity and ROS production of manufactured silver nanoparticles of different sizes in hepatoma and leukemia cells. *Journal of Applied Toxicology*, 34(4): 413-23.

Babich, H., Liebling, E.J., Burger, R.F., Zuckerbraun, H.L. and Schuck, A.G., 2009. Choice of DMEM, formulated with or without pyruvate, plays an important role in assessing the *in vitro* cytotoxicity of oxidants and prooxidant nutraceuticals. *In Vitro Cellular & Developmental Biology - Animal*, 45(5): 226-33.

Baram-Pinto, D., Shukla, S., Perkas, N., Gedanken, A. and Sarid, R., 2009. Inhibition of herpes simplex virus type 1 infection by silver nanoparticles capped with mercaptoethane sulfonate. *Bioconjugate Chemistry*, 20(8): 1497-502.

Bastos, V., Ferreira-De-Oliveira, J.M.P., Carrola, J., Daniel-Da-Silva, A.L., Duarte, I.F., Santos, C. and Oliveira, H., 2016. Coating independent cytotoxicity of citrate- and PEG-coated silver nanoparticles on a human hepatoma cell line. *Journal of Environmental Sciences*: in Press.

Bayet-Robert, M., Loiseau, D., Rio, P., Demidem, A., Barthomeuf, C., Stepien, G. and Morvan, D., 2010. Quantitative two-dimensional HRMAS ^{1}H-NMR spectroscopy-based metabolite profiling of human cancer cell lines and response to chemotherapy. *Magnetic Resonance in Medicine*, 63(5): 1172-83.

Beer, C., Foldbjerg, R., Hayashi, Y., Sutherland, D.S. and Autrup, H., 2012. Toxicity of silver nanoparticles - nanoparticle or silver ion? *Toxicology Letters*, 208(3): 286-92.

Benjamini, Y. and Hochberg, Y., 1995. Controlling the false discovery rate: a practical and powerful approach to multiple testing. *Journal of the Royal Statistical Society Series B*, 57(1): 289-300.

Berben, L., Sereika, S.M. and Engberg, S., 2012. Effect size estimation: methods and examples. *International Journal of Nursing Studies*, 49(8): 1039-47.

Berg, J.M., Tymoczko, J.L. and Stryer, L. 2002. *Biochemistry*5th edition*,* New York, W H Freeman.

Bharti, S.K. and Roy, R., 2012. Quantitative ^{1}H NMR spectroscopy. *Trends in Analytical Chemistry*, 35: 5-26.

Bhattacharjee, S., Rietjens, I.M., Singh, M.P., Atkins, T.M., Purkait, T.K., Xu, Z., Regli, S., Shukaliak, A., Clark, R.J., Mitchell, B.S., Alink, G.M., Marcelis, A.T., Fink, M.J., Veinot, J.G., Kauzlarich, S.M. and Zuilhof, H., 2013. Cytotoxicity of surface-functionalized silicon and germanium nanoparticles: the dominant role of surface charges. *Nanoscale*, 5(11): 4870-83.

Biswas, S.K. and Mantovani, A., 2012. Orchestration of metabolism by macrophages. *Cell Metabolism*, 15(4): 432-7.

Blaske, F., Stork, L., Sperling, M. and Karst, U., 2013. Adduct formation of ionic and nanoparticular silver with amino acids and glutathione. *Journal of Nanoparticle Research*, 15(9): 1928, 10 pages.

Bo, Y., Jin, C.Y., Liu, Y.M., Yu, W.J. and Kang, H.Z., 2014. Metabolomic analysis on the toxicological effects of TiO_2 nanoparticles in mouse fibroblast cells: from the perspective of perturbations in amino acid metabolism. *Toxicology Mechanisms and Methods*, 24(7): 461-9.

Boca, S.C., Potara, M., Gabudean, A.M., Juhem, A., Baldeck, P.L. and Astilean, S., 2011. Chitosan-coated triangular silver nanoparticles as a novel class of biocompatible, highly effective photothermal transducers for *in vitro* cancer cell therapy. *Cancer Letters*, 311(2): 131-40.

Bolea, E., Jimenez-Lamana, J., Laborda, F., Abad-Alvaro, I., Blade, C., Arola, L. and Castillo, J.R., 2014. Detection and characterization of silver nanoparticles and dissolved species of silver in culture medium and cells by AsFlFFF-UV-Vis-ICPMS: application to nanotoxicity tests. *Analyst*, 139(5): 914-22.

Bonilla, J.J.A., Guerrero, D.J.P., Suarez, C.I.S., Lopez, C.C. and Saez, R.G.T., 2015. *In vitro* antifungal activity of silver nanoparticles against fluconazole-resistant *Candida* species. *World Journal of Microbiology & Biotechnology*, 31(11): 1801-9.

Bordbar, A., Mo, M.L., Nakayasu, E.S., Schrimpe-Rutledge, A.C., Kim, Y.M., Metz, T.O., Jones, M.B., Frank, B.C., Smith, R.D., Peterson, S.N., Hyduke, D.R., Adkins, J.N. and Palsson, B.O., 2012. Model-driven multi-omic data analysis elucidates metabolic immunomodulators of macrophage activation. *Molecular Systems Biology*, 8: Article number 558, 12 pages.

Boukamp, P., Petrussevska, R.T., Breitkreutz, D., Hornung, J., Markham, A. and Fusenig, N.E., 1988. Normal keratinization in a spontaneously immortalized aneuploid human keratinocyte cell line. *The Journal of Cell Biology*, 106(3): 761-71.

Bouwmeester, H., Poortman, J., Peters, R.J., Wijma, E., Kramer, E., Makama, S., Puspitaninganindita, K., Marvin, H.J.P., Peijnenburg, A. and Hendriksen, P.J.M., 2011. Characterization of translocation of silver nanoparticles and effects on whole-genome gene expression using an *in vitro* intestinal epithelium coculture model. *ACS Nano*, 5(5): 4091-103.

Boyles, M.S.P., Ranninger, C., Reischl, R., Rurik, M., Tessadri, R., Kohlbacher, O., Duschl, A. and Huber, C.G., 2016. Copper oxide nanoparticle toxicity profiling using untargeted metabolomics. *Particle and Fibre Toxicology*, 13: 49, 20 pages.

Brand, A., Leibfritz, D. and Richter-Landsberg, C., 1999. Oxidative stress-induced metabolic alterations in rat brain astrocytes studied by multinuclear NMR spectroscopy. *Journal of Neuroscience Research*, 58(4): 576-85.

Braun, N.J., Comfort, K.K., Schlager, J.J. and Hussain, S.M., 2013. Partial recovery of silver nanoparticle-induced neural cytotoxicity through the application of a static magnetic field. *BioNanoScience*, 3(4): 367-77.

Bu, Q., Yan, G.Y., Deng, P.C., Peng, F., Lin, H.J., Xu, Y.Z., Cao, Z.X., Zhou, T., Xue, A.Q., Wang, Y.L., Cen, X.B. and Zhao, Y.L., 2010. NMR-based metabonomic study of the sub-acute toxicity of titanium dioxide nanoparticles in rats after oral administration. *Nanotechnology*, 21(12): 12 pages.

Buesen, R., Landsiedel, R., Sauer, U.G., Wohlleben, W., Groeters, S., Strauss, V., Kamp, H. and Van Ravenzwaay, B., 2014. Effects of SiO_2, ZrO_2, and $BaSO_4$ nanomaterials with or without surface functionalization upon 28-day oral exposure to rats. *Archives of Toxicology*, 88(10): 1881-906.

Butler, K.S., Peeler, D.J., Casey, B.J., Dair, B.J. and Elespuru, R.K., 2015. Silver nanoparticles: correlating nanoparticle size and cellular uptake with genotoxicity. *Mutagenesis*, 30(4): 577-91.

Caballero-Diaz, E., Pfeiffer, C., Kastl, L., Rivera-Gil, P., Simonet, B., Valcarcel, M., Jimenez-Lamana, J., Laborda, F. and Parak, W.J., 2013. The toxicity of silver nanoparticles depends on their uptake by cells and thus on their surface chemistry. *Particle & Particle Systems Characterization*, 30(12): 1079-85.

Calzolai, L., Gilliland, D. and Rossi, F., 2012. Measuring nanoparticles size distribution in food and consumer products: a review. *Food Additives & Contaminants: Part A*, 29(8): 1183-93.

Carrola, J., Bastos, V., Ferreira De Oliveira, J.M., Oliveira, H., Santos, C., Gil, A.M. and Duarte, I.F., 2016a. Insights into the impact of silver nanoparticles on human keratinocytes metabolism through NMR metabolomics. *Archives of Biochemistry and Biophysics*, 589: 53-61.

Carrola, J., Bastos, V., Jarak, I., Oliveira-Silva, R., Malheiro, E., Daniel-Da-Silva, A.L., Oliveira, H., Santos, C., Gil, A.M. and Duarte, I.F., 2016b. Metabolomics of silver nanoparticles toxicity in HaCaT cells: structure-activity relationships and role of ionic silver and oxidative stress. *Nanotoxicology*, 10(8): 1105-17.

Casu, M., Anderson, G.J., Choi, G. and Gibbons, W.A., 1991. NMR lipid profiles of cells, tissues and body fluids. I - 1D and 2D proton NMR of lipids from rat liver. *Magnetic Resonance in Chemistry*, 29(6): 594-602.

Chairuangkitti, P., Lawanprasert, S., Roytrakul, S., Aueviriyavit, S., Phummiratch, D., Kulthong, K., Chanvorachote, P. and Maniratanachote, R., 2013. Silver nanoparticles induce toxicity in A549 cells via ROS-dependent and ROS-independent pathways. *Toxicology in Vitro*, 27(1): 330-8.

Chang, Y.F. and Carman, G.M., 2008. CTP synthetase and its role in phospholipid synthesis in the yeast *Saccharomyces cerevisiae*. *Progress in Lipid Research*, 47(5): 333-9.

Chatterjee, N., Yang, J., Kim, S., Joo, S.W. and Choi, J., 2016. Diameter size and aspect ratio as critical determinants of uptake, stress response, global metabolomics and epigenetic alterations in multi-wall carbon nanotubes. *Carbon*, 108: 529-40.

Chen, Q.Q., Xue, Y. and Sun, J., 2013. Kupffer cell-mediated hepatic injury induced by silica nanoparticles *in vitro* and *in vivo*. *International Journal of Nanomedicine*, 8: 1129-40.

Chen, X., Zhong, Z., Xu, Z., Chen, L. and Wang, Y., 2011. No protective effect of curcumin on hydrogen peroxide-induced cytotoxicity in HepG2 cells. *Pharmacological Reports*, 63(3): 724-32.

Chen, Y., Wang, Z., Xu, M., Wang, X., Liu, R., Liu, Q., Zhang, Z., Xia, T., Zhao, J., Jiang, G., Xu, Y. and Liu, S., 2014. Nanosilver incurs an adaptive shunt of energy metabolism mode to glycolysis in tumor and nontumor cells. *ACS Nano*, 8(6): 5813-25.

Chichova, M., Shkodrova, M., Vasileva, P., Kirilova, K. and Doncheva-Stoimenova, D., 2014. Influence of silver nanoparticles on the activity of rat liver mitochondrial ATPase. *Journal of Nanoparticle Research*, 16(2): 2243, 14 pages.

Choi, O. and Hu, Z., 2008. Size dependent and reactive oxygen species related nanosilver toxicity to nitrifying bacteria. *Environmental Science & Technology*, 42(12): 4583-8.

Chow, J.-M., Shen, S.-C., Huan, S.K., Lin, H.-Y. and Chen, Y.-C., 2005. Quercetin, but not rutin and quercitrin, prevention of H_2O_2-induced apoptosis via anti-oxidant activity and heme oxygenase 1 gene expression in macrophages. *Biochemical Pharmacology*, 69(12): 1839-51.

Chunyan, W. and Valiyaveettil, S., 2013. Correlation of biocapping agents with cytotoxic effects of silver nanoparticles on human tumor cells. *RSC Advances*, 3(34): 14329-38.

Cloarec, O., Dumas, M.E., Craig, A., Barton, R.H., Trygg, J., Hudson, J., Blancher, C., Gauguier, D., Lindon, J.C., Holmes, E. and Nicholson, J., 2005. Statistical total correlation spectroscopy: an exploratory approach for latent biomarker identification from metabolic ^{1}H NMR data sets. *Analytical Chemistry*, 77(5): 1282-9.

Cohen, J. 1988. *Statistical power analysis for the behavioral sciences,* Hillsdale, N.J., L. Erlbaum Associates.

Colussi, C., Albertini, M.C., Coppola, S., Rovidati, S., Galli, F. and Ghibelli, L., 2000. H_2O_2-induced block of glycolysis as an active ADP-ribosylation reaction protecting cells from apoptosis. *The FASEB Journal*, 14(14): 2266-76.

Comfort, K.K., Braydich-Stolle, L.K., Maurer, E.I. and Hussain, S.M., 2014. Less is more: long-term *in vitro* exposure to low levels of silver nanoparticles provides new insights for nanomaterial evaluation. *ACS Nano*, 8(4): 3260-71.

Costa, C.S., Ronconi, J.V., Daufenbach, J.F., Goncalves, C.L., Rezin, G.T., Streck, E.L. and Paula, M.M., 2010. *In vitro* effects of silver nanoparticles on the mitochondrial respiratory chain. *Molecular and Cellular Biochemistry*, 342(1-2): 51-6.

Cronholm, P., Karlsson, H.L., Hedberg, J., Lowe, T.A., Winnberg, L., Elihn, K., Wallinder, I.O. and Moller, L., 2013. Intracellular uptake and toxicity of Ag and CuO nanoparticles: a comparison between nanoparticles and their corresponding metal ions. *Small*, 9(7): 970-82.

Čuperlović-Culf, M., Barnett, D.A., Culf, A.S. and Chute, I., 2010. Cell culture metabolomics: applications and future directions. *Drug Discovery Today*, 15(15–16): 610-21.

D'errico, M., Lemma, T., Calcagnile, A., Santis, L.P.D. and Dogliotti, E., 2007. Cell type and DNA damage specific response of human skin cells to environmental agents. *Mutation Research/Fundamental and Molecular Mechanisms of Mutagenesis*, 614(1–2): 37-47.

Dailey, L.A., Hernandez-Prieto, R., Casas-Ferreira, A.M., Jones, M.C., Riffo-Vasquez, Y., Rodriguez-Gonzalo, E., Spina, D., Jones, S.A., Smith, N.W., Forbes, B., Page, C. and Legido-Quigley, C., 2015. Adenosine monophosphate is elevated in the bronchoalveolar lavage fluid of mice with acute respiratory toxicity induced by nanoparticles with high surface hydrophobicity. *Nanotoxicology*, 9(1): 106-15.

David, L., Moldovan, B., Vulcu, A., Olenic, L., Perde-Schrepler, M., Fischer-Fodor, E., Florea, A., Crisan, M., Chiorean, I., Clichici, S. and Filip, G.A., 2014. Green synthesis, characterization and anti-inflammatory activity of silver nanoparticles

using European black elderberry fruits extract. *Colloids and Surfaces B-Biointerfaces*, 122: 767-77.

De Matteis, V., Malvindi, M.A., Galeone, A., Brunetti, V., De Luca, E., Kote, S., Kshirsagar, P., Sabella, S., Bardi, G. and Pompa, P.P., 2015. Negligible particle-specific toxicity mechanism of silver nanoparticles: the role of Ag^+ ion release in the cytosol. *Nanomedicine*, 11(3): 731-9.

Dettmer, K., Nurnberger, N., Kaspar, H., Gruber, M.A., Almstetter, M.F. and Oefner, P.J., 2011. Metabolite extraction from adherently growing mammalian cells for metabolomics studies: optimization of harvesting and extraction protocols. *Analytical and Bioanalytical Chemistry*, 399(3): 1127-39.

Dibrov, P., Dzioba, J., Gosink, K.K. and Hase, C.C., 2002. Chemiosmotic mechanism of antimicrobial activity of Ag^+ in *Vibrio cholerae*. *Antimicrobial Agents and Chemotherapy*, 46(8): 2668-70.

Dietmair, S., Timmins, N.E., Gray, P.P., Nielsen, L.K. and Kromer, J.O., 2010. Towards quantitative metabolomics of mammalian cells: development of a metabolite extraction protocol. *Analytical Biochemistry*, 404(2): 155-64.

Dong, X., Mattingly, C.A., Tseng, M.T., Cho, M.J., Liu, Y., Adams, V.R. and Mumper, R.J., 2009. Doxorubicin and paclitaxel-loaded lipid-based nanoparticles overcome multidrug resistance by inhibiting P-glycoprotein and depleting ATP. *Cancer Research*, 69(9): 3918-26.

Duarte, I.F., 2011. Following dynamic biological processes through NMR-based metabonomics: A new tool in nanomedicine? *Journal of Controlled Release*, 153(1): 34-9.

Duarte, I.F., Lamego, I., Rocha, C. and Gil, A.M., 2009a. NMR metabonomics for mammalian cell metabolism studies. *Bioanalysis*, 1(9): 1597-614.

Duarte, I.F., Marques, J., Ladeirinha, A.F., Rocha, C., Lamego, I., Calheiros, R., Silva, T.M., Marques, M.P., Melo, J.B., Carreira, I.M. and Gil, A.M., 2009b. Analytical approaches toward successful human cell metabolome studies by NMR spectroscopy. *Analitical Chemistry*, 81(12): 5023-32.

Dziendzikowska, K., Gromadzka-Ostrowska, J., Lankoff, A., Oczkowski, M., Krawczynska, A., Chwastowska, J., Sadowska-Bratek, M., Chajduk, E., Wojewodzka, M., Dusinska, M. and Kruszewski, M., 2012. Time-dependent biodistribution and excretion of silver nanoparticles in male Wistar rats. *Journal of Applied Toxicology*, 32(11): 920-8.

Eckhardt, S., Brunetto, P.S., Gagnon, J., Priebe, M., Giese, B. and Fromm, K.M., 2013. Nanobio silver: its interactions with peptides and bacteria, and its uses in medicine. *Chemical Reviews*, 113(7): 4708-54.

El Badawy, A.M., Silva, R.G., Morris, B., Scheckel, K.G., Suidan, M.T. and Tolaymat, T.M., 2011. Surface charge-dependent toxicity of silver nanoparticles. *Environmental Science & Technology*, 45(1): 283-7.

El Kasmi, K.C. and Stenmark, K.R., 2015. Contribution of metabolic reprogramming to macrophage plasticity and function. *Seminars in Immunology*, 27(4): 267-75.

Elechiguerra, J.L., Burt, J.L., Morones, J.R., Camacho-Bragado, A., Gao, X., Lara, H.H. and Yacaman, M.J., 2005. Interaction of silver nanoparticles with HIV-1. *Journal of Nanobiotechnology*, 3: 6, 10 pages.

Feng, J., Liu, H., Zhang, L., Bhakoo, K. and Lu, L., 2010. An insight into the metabolic responses of ultra-small superparamagnetic particles of iron oxide using metabonomic analysis of biofluids. *Nanotechnology*, 21(39): 395101, 14 pages.

Feng, J., Zhao, J., Hao, F., Chen, C., Bhakoo, K. and Tang, H., 2011a. NMR-based metabonomic analyses of the effects of ultrasmall superparamagnetic particles of iron oxide (USPIO) on macrophage metabolism. *Journal of Nanoparticle Research*, 13(5): 2049-62.

Feng, J.H., Li, J.Q., Wu, H.F. and Chen, Z., 2013. Metabolic responses of HeLa cells to silica nanoparticles by NMR-based metabolomic analyses. *Metabolomics*, 9(4): 874-86.

Feng, J.H., Liu, H.L., Bhakoo, K.K., Lu, L.H. and Chen, Z., 2011b. A metabonomic analysis of organ specific response to USPIO administration. *Biomaterials*, 32(27): 6558-69.

Ferreira De Oliveira, J.M., Costa, M., Pedrosa, T., Pinto, P., Remedios, C., Oliveira, H., Pimentel, F., Almeida, L. and Santos, C., 2014. Sulforaphane induces oxidative stress and death by p53-independent mechanism: implication of impaired glutathione recycling. *PLoS One*, 9(3): e92980, 11 pages.

Fiehn, O., 2002. Metabolomics - the link between genotypes and phenotypes. *Plant Molecular Biology*, 48(1-2): 155-71.

Foldbjerg, R., Dang, D.A. and Autrup, H., 2011. Cytotoxicity and genotoxicity of silver nanoparticles in the human lung cancer cell line, A549. *Archives of Toxicology*, 85(7): 743-50.

Foldbjerg, R., Irving, E.S., Hayashi, Y., Sutherland, D.S., Thorsen, K., Autrup, H. and Beer, C., 2012. Global gene expression profiling of human lung epithelial cells after exposure to nanosilver. *Toxicological Sciences*, 130(1): 145-57.

Foldbjerg, R., Jiang, X., Miclaus, T., Chen, C., Autrup, H. and Beer, C., 2015. Silver nanoparticles - wolves in sheep's clothing? *Toxicology Research*, 4(3): 563-75.

Foldbjerg, R., Olesen, P., Hougaard, M., Dang, D.A., Hoffmann, H.J. and Autrup, H., 2009. PVP-coated silver nanoparticles and silver ions induce reactive oxygen species, apoptosis and necrosis in THP-1 monocytes. *Toxicology Letters*, 190(2): 156-62.

Franci, G., Falanga, A., Galdiero, S., Palomba, L., Rai, M., Morelli, G. and Galdiero, M., 2015. Silver nanoparticles as potential antibacterial agents. *Molecules*, 20(5): 8856-74.

Friedrich, B., Matskevich, I. and Lang, F., 2006. Cell volume regulatory mechanisms. *Contributions to Nephrology*, 152: 1-8.

Fujii, J., Ito, J.I., Zhang, X. and Kurahashi, T., 2011. Unveiling the roles of the glutathione redox system in vivo by analyzing genetically modified mice. *Journal of Clinical Biochemistry and Nutrition*, 49(2): 70-8.

Galdiero, S., Falanga, A., Vitiello, M., Cantisani, M., Marra, V. and Galdiero, M., 2011. Silver nanoparticles as potential antiviral agents. *Molecules*, 16(10): 8894-918.

Gao, Q. and Goodman, J.M., 2015. The lipid droplet - a well-connected organelle. *Frontiers in Cell and Developmental Biology*, 3: 49, 12 pages.

Garcia-Canaveras, J.C., Donato, M.T., Castell, J.V. and Lahoz, A., 2011. A comprehensive untargeted metabonomic analysis of human steatotic liver tissue by RP and HILIC chromatography coupled to mass spectrometry reveals important metabolic alterations. *Journal of Proteome Research*, 10(10): 4825-34.

Garcia-Contreras, R., Sugimoto, M., Umemura, N., Kaneko, M., Hatakeyama, Y., Soga, T., Tomita, M., Scougall-Vilchis, R.J., Contreras-Bulnes, R., Nakajima, H. and Sakagami, H., 2015. Alteration of metabolomic profiles by titanium dioxide nanoparticles in human gingivitis model. *Biomaterials*, 57: 33-40.

Ge, L., Li, Q., Wang, M., Ouyang, J., Li, X. and Xing, M.M.Q., 2014. Nanosilver particles in medical applications: synthesis, performance, and toxicity. *International Journal of Nanomedicine*, 9: 2399-407.

Gioria, S., Vicente, J.L., Barboro, P., La Spina, R., Tomasi, G., Urban, P., Kinsner-Ovaskainen, A., Francois, R. and Chassaigne, H., 2016. A combined proteomics and metabolomics approach to assess the effects of gold nanoparticles *in vitro*. *Nanotoxicology*, 10(6): 736-48.

Giovanni, M., Yue, J., Zhang, L., Xie, J., Ong, C.N. and Leong, D.T., 2015. Pro-inflammatory responses of RAW264.7 macrophages when treated with ultralow concentrations of silver, titanium dioxide, and zinc oxide nanoparticles. *Journal of Hazardous Materials*, 297: 146-52.

Gliga, A.R., Skoglund, S., Wallinder, I.O., Fadeel, B. and Karlsson, H.L., 2014. Size-dependent cytotoxicity of silver nanoparticles in human lung cells: the role of cellular uptake, agglomeration and Ag release. *Particle and fibre toxicology*, 11: 11, 7 pages.

Greulich, C., Diendorf, J., Simon, T., Eggeler, G., Epple, M. and Köller, M., 2011. Uptake and intracellular distribution of silver nanoparticles in human mesenchymal stem cells. *Acta Biomaterialia*, 7(1): 347-54.

Grosse, S., Evje, L. and Syversen, T., 2013. Silver nanoparticle-induced cytotoxicity in rat brain endothelial cell culture. *Toxicology in Vitro*, 27(1): 305-13.

Guay, C., Madiraju, S.R.M., Aumais, A., Joly, É. and Prentki, M., 2007. A role for ATP-citrate lyase, malic enzyme, and pyruvate/citrate cycling in glucose-induced insulin secretion. *Journal of Biological Chemistry*, 282(49): 35657-65.

Guo, D.W., Dou, D.D., Ge, L., Huang, Z.H., Wang, L.P. and Gu, N., 2015. A caffeic acid mediated facile synthesis of silver nanoparticles with powerful anti-cancer activity. *Colloids and Surfaces B-Biointerfaces*, 134: 229-34.

Gurunathan, S., Lee, K.J., Kalishwaralal, K., Sheikpranbabu, S., Vaidyanathan, R. and Eom, S.H., 2009. Antiangiogenic properties of silver nanoparticles. *Biomaterials*, 30(31): 6341-50.

Gurunathan, S., Park, J.H., Han, J.W. and Kim, J.H., 2015. Comparative assessment of the apoptotic potential of silver nanoparticles synthesized by *Bacillus tequilensis* and *Calocybe indica* in MDA-MB-231 human breast cancer cells: targeting p53 for anticancer therapy. *International Journal of Nanomedicine*, 10: 4203-22.

Haase, A., Tentschert, J., Jungnickel, H., Graf, P., Mantion, A., Draude, F., Plendl, J., Goetz, M.E., Galla, S., Mašić, A., Thuenemann, A.F., Taubert, A., Arlinghaus, H.F. and Luch, A., 2011. Toxicity of silver nanoparticles in human macrophages: uptake, intracellular distribution and cellular responses. *Journal of Physics: Conference Series*, 304(1): 012030, 14 pages.

Haase, H., Fahmi, A. and Mahltig, B., 2014. Impact of silver nanoparticles and silver ions on innate immune cells. *Journal of Biomedical Nanotechnology*, 10(6): 1146-56.

Hadrup, N., Lam, H.R., Loeschner, K., Mortensen, A., Larsen, E.H. and Frandsen, H., 2012. Nanoparticulate silver increases uric acid and allantoin excretion in rats, as identified by metabolomics. *Journal of Applied Toxicology*, 32(11): 929-33.

Halliwell, B., 2008. Are polyphenols antioxidants or pro-oxidants? What do we learn from cell culture and *in vivo* studies? *Archives of Biochemistry and Biophysics*, 476(2): 107-12.

Hansen, U. and Thunemann, A.F., 2015. Characterization of silver nanoparticles in cell culture medium containing fetal bovine serum. *Langmuir*, 31(24): 6842-52.

Hashimoto, M., Toshima, H., Yonezawa, T., Kawai, K., Narushima, T., Kaga, M. and Endo, K., 2014. Responses of RAW264.7 macrophages to water-dispersible gold and silver nanoparticles stabilized by metal-carbon sigma-bonds. *Journal of Biomedical Materials Research Part A*, 102(6): 1838-49.

Hassellov, M., Readman, J.W., Ranville, J.F. and Tiede, K., 2008. Nanoparticle analysis and characterization methodologies in environmental risk assessment of engineered nanoparticles. *Ecotoxicology*, 17(5): 344-61.

He, W., Zhou, Y.-T., Wamer, W.G., Boudreau, M.D. and Yin, J.-J., 2012. Mechanisms of the pH dependent generation of hydroxyl radicals and oxygen induced by Ag nanoparticles. *Biomaterials*, 33(30): 7547-55.

Henderson, W.M., Bouchard, D., Chang, X.J., Al-Abed, S.R. and Teng, Q., 2016. Biomarker analysis of liver cells exposed to surfactant-wrapped and oxidized multi-walled carbon nanotubes (MWCNTs). *Science of the Total Environment*, 565: 777-86.

Hsin, Y.H., Chen, C.F., Huang, S., Shih, T.S., Lai, P.S. and Chueh, P.J., 2008. The apoptotic effect of nanosilver is mediated by a ROS- and JNK-dependent mechanism involving the mitochondrial pathway in NIH3T3 cells. *Toxicology Letters*, 179(3): 130-9.

Huang, S.M., Zuo, X.B., Li, J.J., Li, S.F.Y., Bay, B.H. and Ong, C.N., 2012. Metabolomics studies show dose-dependent toxicity Induced by SiO_2 nanoparticles in MRC-5 human fetal lung fibroblasts. *Advanced Healthcare Materials*, 1(6): 779-84.

Huk, A., Izak-Nau, E., Reidy, B., Boyles, M., Duschl, A., Lynch, I. and Dusinska, M., 2014. Is the toxic potential of nanosilver dependent on its size? *Particle and Fibre Toxicology*, 11: 65, 16 pages.

Hwang, I.S., Lee, J., Hwang, J.H., Kim, K.J. and Lee, D.G., 2012. Silver nanoparticles induce apoptotic cell death in *Candida albicans* through the increase of hydroxyl radicals. *The FEBS Journal*, 279(7): 1327-38.

Iravani, S., 2011. Green synthesis of metal nanoparticles using plants. *Green Chemistry*, 13(10): 2638-50.

Irfan, A., Cauchi, M., Edmands, W., Gooderham, N.J., Njuguna, J. and Zhu, H.J., 2014. Assessment of temporal dose-toxicity relationship of fumed silica nanoparticle in human lung A549 cells by conventional cytotoxicity and ^{1}H-NMR-based extracellular metabonomic assays. *Toxicological Sciences*, 138(2): 354-64.

Jain, J., Arora, S., Rajwade, J.M., Omray, P., Khandelwal, S. and Paknikar, K.M., 2009. Silver nanoparticles in therapeutics: development of an antimicrobial gel formulation for topical use. *Molecular Pharmaceutics*, 6(5): 1388-401.

Jang, S., Park, J.W., Cha, H.R., Jung, S.Y., Lee, J.E., Jung, S.S., Kim, J.O., Kim, S.Y., Lee, C.S. and Park, H.S., 2012. Silver nanoparticles modify VEGF signaling pathway and mucus hypersecretion in allergic airway inflammation. *International Journal of Nanomedicine*, 7: 1329-43.

Jha, A.K., Huang, S.C., Sergushichev, A., Lampropoulou, V., Ivanova, Y., Loginicheva, E., Chmielewski, K., Stewart, K.M., Ashall, J., Everts, B., Pearce, E.J., Driggers, E.M. and Artyomov, M.N., 2015. Network integration of parallel metabolic and transcriptional data reveals metabolic modules that regulate macrophage polarization. *Immunity*, 42(3): 419-30.

Jiang, J.Y., Yu, S.N., Jiang, Z.C., Liang, C.H., Yu, W.B., Li, J., Du, X.D., Wang, H.L., Gao, X.H. and Wang, X., 2014. N-Acetyl-serotonin protects HepG2 cells from oxidative stress injury induced by hydrogen peroxide. *Oxidative Medicine and Cellular Longevity*: Article ID 310504, 15 pages.

Jiang, P. and Mizushima, N., 2014. Autophagy and human diseases. *Cell Research*, 24(1): 69-79.

Jiang, X., Foldbjerg, R., Miclaus, T., Wang, L., Singh, R., Hayashi, Y., Sutherland, D., Chen, C., Autrup, H. and Beer, C., 2013. Multi-platform genotoxicity analysis of silver nanoparticles in the model cell line CHO-K1. *Toxicology Letters*, 222(1): 55-63.

Jiao, Z.H., Li, M., Feng, Y.X., Shi, J.C., Zhang, J. and Shao, B., 2014. Hormesis effects of silver nanoparticles at non-cytotoxic doses to human hepatoma cells. *PloS One*, 9(7): e102564, 12 pages.

Jin, C.Y., Liu, Y.M., Sun, L.M., Chen, T.L., Zhang, Y.N., Zhao, A.H., Wang, X.Y., Cristau, M., Wang, K.S. and Jia, W., 2013. Metabolic profiling reveals disorder of carbohydrate metabolism in mouse fibroblast cells induced by titanium dioxide nanoparticles. *Journal of Applied Toxicology*, 33(12): 1442-50.

Johnston, H.J., Hutchison, G., Christensen, F.M., Peters, S., Hankin, S. and Stone, V., 2010. A review of the *in vivo* and *in vitro* toxicity of silver and gold particulates: particle attributes and biological mechanisms responsible for the observed toxicity. *Critical Reviews in Toxicology*, 40(4): 328-46.

Jung, H., Kwak, H.-K. and Hwang, K.T., 2014. Antioxidant and antiinflammatory activities of cyanidin-3-glucoside and cyanidin-3-rutinoside in hydrogen peroxide and lipopolysaccharide-treated RAW264.7 cells. *Food Science and Biotechnology*, 23(6): 2053-62.

Kalinowski, P. and Fidler, F., 2010. Interpreting significance: the differences between statistical significance, effect size, and practical importance. *Newborn and Infant Nursing Reviews*, 10(1): 50-4.

Kanehisa, M., Sato, Y., Kawashima, M., Furumichi, M. and Tanabe, M., 2016. KEGG as a reference resource for gene and protein annotation. *Nucleic Acids Research*, 44(D1): D457-62.

Kang, S.J., Lee, Y.J., Lee, E.K. and Kwak, M.K., 2012. Silver nanoparticles-mediated G2/M cycle arrest of renal epithelial cells is associated with NRF2-GSH signaling. *Toxicology Letters*, 211(3): 334-41.

Kaur, J. and Tikoo, K., 2013. Evaluating cell specific cytotoxicity of differentially charged silver nanoparticles. *Food and Chemical Toxicology*, 51: 1-14.

Kawata, K., Osawa, M. and Okabe, S., 2009. *In vitro* toxicity of silver nanoparticles at noncytotoxic doses to HepG2 human hepatoma cells. *Environmental Science & Technology*, 43(15): 6046-51.

Keeler, J. 2010. *Understanding NMR spectroscopy*1st edition, Wiley.

Kelts, J.L., Cali, J.J., Duellman, S.J. and Shultz, J., 2015. Altered cytotoxicity of ROS-inducing compounds by sodium pyruvate in cell culture medium depends on the location of ROS generation. *SpringerPlus*, 4(1): 1-8.

Kennedy, D.C., Orts-Gil, G., Lai, C.H., Muller, L., Haase, A., Luch, A. and Seeberger, P.H., 2014. Carbohydrate functionalization of silver nanoparticles modulates cytotoxicity and cellular uptake. *Journal of Nanobiotechnology*, 12(59): 8 pages.

Khoo, S.H. and Al-Rubeai, M., 2007. Metabolomics as a complementary tool in cell culture. *Biotechnology and Applied Biochemistry*, 47(2): 71-84.

Kim, H.R., Kim, M.J., Lee, S.Y., Oh, S.M. and Chung, K.H., 2011a. Genotoxic effects of silver nanoparticles stimulated by oxidative stress in human normal bronchial epithelial (BEAS-2B) cells. *Mutation Research*, 726(2): 129-35.

Kim, J.-S., Kim, E.-J., Kim, H.-J., Yang, J.-Y., Hwang, G.-S. and Kim, C.-W., 2011b. Proteomic and metabolomic analysis of H_2O_2-induced premature senescent human mesenchymal stem cells. *Experimental Gerontology*, 46(6): 500-10.

Kim, J., Kuk, E., Yu, K., Kim, J., Park, S. and Lee, H., 2007. Antimicrobial effects of silver nanoparticles. *Nanomedicine: Nanotechnology, Biology and Medicine*, 3: 95-101.

Kim, K.J., Sung, W.S., Suh, B.K., Moon, S.K., Choi, J.S., Kim, J.G. and Lee, D.G., 2009a. Antifungal activity and mode of action of silver nano-particles on *Candida albicans*. *Biometals*, 22(2): 235-42.

Kim, S., Choi, J.E., Choi, J., Chung, K.H., Park, K., Yi, J. and Ryu, D.Y., 2009b. Oxidative stress-dependent toxicity of silver nanoparticles in human hepatoma cells. *Toxicology in Vitro*, 23(6): 1076-84.

Kim, S., Kim, S., Lee, S., Kwon, B., Choi, J., Hyun, J.W. and Kim, S., 2011c. Characterization of the effects of silver nanoparticles on liver cell using HR-MAS NMR spectroscopy. *Bulletin of the Korean Chemical Society*, 32(6): 2021-6.

Kim, S. and Ryu, D.-Y., 2013. Silver nanoparticle-induced oxidative stress, genotoxicity and apoptosis in cultured cells and animal tissues. *Journal of Applied Toxicology*, 33(2): 78-89.

Kim, T.H., Kim, M., Park, H.S., Shin, U.S., Gong, M.S. and Kim, H.W., 2012. Size-dependent cellular toxicity of silver nanoparticles. *Journal of Biomedical Materials Research Part A*, 100(4): 1033-43.

Kitchin, K.T., Grulke, E., Robinette, B.L. and Castellon, B.T., 2014. Metabolomic effects in HepG2 cells exposed to four TiO_2 and two CeO_2 nanomaterials. *Environmental Science: Nano*, 1(5): 466-77.

Klaper, R., Arndt, D., Bozich, J. and Dominguez, G., 2014. Molecular interactions of nanomaterials and organisms: defining biomarkers for toxicity and high-throughput screening using traditional and next-generation sequencing approaches. *Analyst*, 139(5): 882-95.

Knijn, A., Brisdelli, F., Ferretti, A., Iorio, E., Marcheggiani, D. and Bozzi, A., 2005. Metabolic alterations in K562 cells exposed to taxol and tyrphostin AG957: ^{1}H NMR and biochemical studies. *Cell Biology International*, 29(11): 890-7.

Krishnasamy, L., Masilamaniselvam, M. and Jayanthi, K., 2015. Demonstration of anticancer effect by apoptosis exhibited by biotechnologically synthesized silver nanoparticle of *Indigofera aspalathoids* leaf extract. *Research Journal of Biotechnology*, 10(1): 72-5.

Kuehne, A., Emmert, H., Soehle, J., Winnefeld, M., Fischer, F., Wenck, H., Gallinat, S., Terstegen, L., Lucius, R., Hildebrand, J. and Zamboni, N., 2015. Acute activation of oxidative pentose phosphate pathway as first-line response to oxidative stress in human skin cells. *Molecular Cell*, 59(3): 359-71.

Kumar, G., Degheidy, H., Casey, B.J. and Goering, P.L., 2015. Flow cytometry evaluation of *in vitro* cellular necrosis and apoptosis induced by silver nanoparticles. *Food and Chemical Toxicology*, 85: 45-51.

Lamego, I., Duarte, I.F., Marques, M.P.M. and Gil, A.M., 2014. Metabolic markers of MG-63 osteosarcoma cell line response to doxorubicin and methotrexate treatment: comparison to cisplatin. *Journal of Proteome Research*, 13(12): 6033-45.

Lamour, S.D., Choi, B.S., Keun, H.C., Muller, I. and Saric, J., 2012. Metabolic characterization of *Leishmania major* infection in activated and nonactivated macrophages. *Journal of Proteome Research*, 11(8): 4211-22.

Lankadurai, B.P., Nagato, E.G., Simpson, A.J. and Simpson, M.J., 2015. Analysis of *Eisenia fetida* earthworm responses to sub-lethal C60 nanoparticle exposure using ^{1}H-NMR based metabolomics. *Ecotoxicology and Environmental Safety*, 120: 48-58.

Lara, H., Romero-Urbina, D., Pierce, C., Lopez-Ribot, J., Arellano-Jimenez, M. and Jose-Yacaman, M., 2015. Effect of silver nanoparticles on *Candida albicans* biofilms: an ultrastructural study. *Journal of Nanobiotechnology*, 13(1): 91, 12 pages.

Lara, H.H., Ayala-Nunez, N.V., Ixtepan-Turrent, L. and Rodriguez-Padilla, C., 2010. Mode of antiviral action of silver nanoparticles against HIV-1. *Journal of Nanobiotechnology*, 8(1): 10 pages.

Le Ouay, B. and Stellacci, F., 2015. Antibacterial activity of silver nanoparticles: a surface science insight. *Nano Today*, 10(3): 339-54.

Lee, M.J., Lee, S.J., Yun, S.J., Jang, J.-Y., Kang, H., Kim, K., Choi, I.-H. and Park, S., 2016a. Silver nanoparticles affect glucose metabolism in hepatoma cells through production of reactive oxygen species. *International Journal of Nanomedicine*, 11: 55-68.

Lee, S.H., Wang, T.Y., Hong, J.H., Cheng, T.J. and Lin, C.Y., 2016b. NMR-based metabolomics to determine acute inhalation effects of nano- and fine-sized ZnO particles in the rat lung. *Nanotoxicology*, 10(7): 924-34.

Lei, R., Wu, C., Yang, B., Ma, H., Shi, C., Wang, Q., Yuan, Y. and Liao, M., 2008. Integrated metabolomic analysis of the nano-sized copper particle-induced hepatotoxicity and nephrotoxicity in rats: a rapid *in vivo* screening method for nanotoxicity. *Toxicology and Applied Pharmacology*, 232(2): 292-301.

León, Z., García-Cañaveras, J.C., Donato, M.T. and Lahoz, A., 2013. Mammalian cell metabolomics: experimental design and sample preparation. *Electrophoresis*, 34(19): 2762-75.

Leonardi, R., Zhang, Y.M., Rock, C.O. and Jackowski, S., 2005. Coenzyme A: back in action. *Progress in Lipid Research*, 44(2-3): 125-53.

Li, J.Q., Zhao, Z.H., Feng, J.H., Gao, J.H. and Chen, Z., 2013. Understanding the metabolic fate and assessing the biosafety of MnO nanoparticles by metabonomic analysis. *Nanotechnology*, 24(45): 455102, 14 pages.

Li, J.Q., Zhou, Z.J., Feng, J.H., Cai, S.H., Gao, J.H. and Chen, Z., 2014a. NMR-based metabonomic analysis of MnO-embedded iron oxide nanoparticles as potential dual-modal contrast agents. *Journal of Nanoparticle Research*, 16(5): 2411, 16 pages.

Li, L., Wu, H., Ji, C., Van Gestel, C.a.M., Allen, H.E. and Peijnenburg, W.J.G.M., 2015a. A metabolomic study on the responses of *daphnia magna* exposed to silver nitrate and coated silver nanoparticles. *Ecotoxicology and Environmental Safety*, 119: 66-73.

Li, L., Wu, H., Peijnenburg, W.J.G.M. and Van Gestel, C.a.M., 2015b. Both released silver ions and particulate Ag contribute to the toxicity of AgNPs to earthworm Eisenia fetida. *Nanotoxicology*, 9(6): 792-801.

Li, X., Lenhart, J.J. and Walker, H.W., 2010. Dissolution-accompanied aggregation kinetics of silver nanoparticles. *Langmuir*, 26(22): 16690-8.

Li, X., Lenhart, J.J. and Walker, H.W., 2012. Aggregation kinetics and dissolution of coated silver nanoparticles. *Langmuir*, 28(2): 1095-104.

Li, X.B., Zhang, C.C., Zhang, X., Wang, S.Z., Meng, Q.T., Wu, S.S., Yang, H.B., Xia, Y.K. and Chen, R., 2016. An acetyl-L-carnitine switch on mitochondrial dysfunction and rescue in the metabolomics study on aluminum oxide nanoparticles. *Particle and Fibre Toxicology*, 13: 4, 19 pages.

Li, Z., Sun, J., Lan, J. and Qi, Q., 2014b. Effect of a denture base acrylic resin containing silver nanoparticles on *Candida albicans* adhesion and biofilm formation. *Gerodontology*, 13(2): 209-16.

Li, Z., Zheng, L., Shi, J., Zhang, G., Lu, L., Zhu, L., Zhang, J. and Liu, Z., 2015c. Toxic markers of matrine determined using ^{1}H-NMR-based metabolomics in cultured cells *in vitro* and rats *in vivo*. *Evidence-based Complementary and Alternative Medicine*, 2015: Article ID 598412, 11 pages.

Lin, B., Zhang, H., Lin, Z., Fang, Y., Tian, L., Yang, H., Yan, J., Liu, H., Zhang, W. and Xi, Z., 2013. Studies of single-walled carbon nanotubes-induced hepatotoxicity by NMR-based metabonomics of rat blood plasma and liver extracts. *Nanoscale Research Letters*, 8: 236, 11 pages.

Lin, G., Troy, H., Andrejeva, G., Fong, A.-C.L.W.T., Koh, D.-M., Robinson, S.P., Judson, I.R., Griffiths, J.R., Leach, M.O. and Chung, Y.-L., 2016. Abstract B56: Treatment-induced autophagy increases amino acid uptake and switches glucose addiction to amino acid catabolism in cancer. *Molecular Cancer Research*, 14(1 Supplement): B56-B.

Lin, J., Huang, Z., Wu, H., Zhou, W., Jin, P., Wei, P., Zhang, Y., Zheng, F., Zhang, J., Xu, J., Hu, Y., Wang, Y., Li, Y., Gu, N. and Wen, L., 2014. Inhibition of autophagy enhances the anticancer activity of silver nanoparticles. *Autophagy*, 10(11): 2006-20.

Lindon, J.C. and Nicholson, J.K., 2008. Spectroscopic and statistical techniques for information recovery in metabonomics and metabolomics. *Annual Review of Analytical Chemistry*, 1: 45-69.

Liu, L., Xie, H., Chen, X., Shi, W., Xiao, X., Lei, D. and Li, J., 2012a. Differential response of normal human epidermal keratinocytes and HaCaT cells to hydrogen peroxide-induced oxidative stress. *Clinical and Experimental Dermatology*, 37(7): 772-80.

Liu, W., Wu, Y., Wang, C., Li, H.C., Wang, T., Liao, C.Y., Cui, L., Zhou, Q.F., Yan, B. and Jiang, G.B., 2010. Impact of silver nanoparticles on human cells: effect of particle size. *Nanotoxicology*, 4(3): 319-30.

Liu, X.L., Hao, W., Lok, C.N., Wang, Y.C., Zhang, R.Z. and Wong, K.K.Y., 2014. Dendrimer encapsulation enhances anti-inflammatory efficacy of silver nanoparticles. *Journal of Pediatric Surgery*, 49(12): 1846-51.

Liu, Y., Cheng, Y., Chen, T., Zhang, Y., Wang, X., Zhao, A., Jia, W., Bo, Y. and Jin, C., 2012b. GC/TOFMS analysis of endogenous metabolites in mouse fibroblast cells and its application in TiO_2 nanoparticle-induced cytotoxicity study. *Chromatographia*, 75(21-22): 1301-10.

Liz-Marzán, L.M., 2006. Tailoring surface plasmons through the morphology and assembly of metal nanoparticles. *Langmuir*, 22(1): 32-41.

Loike, J.D., Kozler, V.F. and Silverstein, S.C., 1984. Creatine kinase expression and creatine phosphate accumulation are developmentally regulated during differentiation of mouse and human monocytes. *The Journal of Experimental Medicine*, 159(3): 746-57.

Loiseau, D., Morvan, D., Chevrollier, A., Demidem, A., Douay, O., Reynier, P. and Stepien, G., 2009. Mitochondrial bioenergetic background confers a survival advantage to HepG2 cells in response to chemotherapy. *Molecular Carcinogenesis*, 48(8): 733-41.

Lok, C.N., Ho, C.M., Chen, R., He, Q.Y., Yu, W.Y., Sun, H., Tam, P.K., Chiu, J.F. and Che, C.M., 2006. Proteomic analysis of the mode of antibacterial action of silver nanoparticles. *Journal of Proteome Research*, 5(4): 916-24.

Long, L.H., Hoi, A. and Halliwell, B., 2010. Instability of, and generation of hydrogen peroxide by, phenolic compounds in cell culture media. *Archives of Biochemistry and Biophysics*, 501(1): 162-9.

Longhi, C., Santos, J.P., Morey, A.T., Marcato, P.D., Duran, N., Pinge-Filho, P., Nakazato, G., Yamada-Ogatta, S.F. and Yamauchi, L.M., 2015. Combination of fluconazole with silver nanoparticles produced by *Fusarium oxysporum* improves antifungal effect against planktonic cells and biofilm of drug-resistant *Candida albicans*. *Medical Mycology*, 54(4): 428-32.

Lu, L., Sun, R.W.-Y., Chen, R., Hui, C.-K., Ho, C.-M., Luk, J.M., Lau, G.K.K. and Che, C.-M., 2008. Silver nanoparticles inhibit hepatitis B virus replication. *Antiviral Therapy*, 13(2): 253-62.

Lu, R.Q., Yang, D.P., Cui, D.X., Wang, Z.Y. and Guo, L., 2012. Egg white-mediated green synthesis of silver nanoparticles with excellent biocompatibility and enhanced radiation effects on cancer cells. *International Journal of Nanomedicine*, 7: 2101-7.

Lu, W., Senapati, D., Wang, S., Tovmachenko, O., Singh, A.K., Yu, H. and Ray, P.C., 2010. Effect of surface coating on the toxicity of silver nanomaterials on human skin keratinocytes. *Chemical Physics Letters*, 487(1-3): 92-6.

Lu, X.Y., Ji, C., Jin, T.T. and Fan, X.H., 2015. The effects of size and surface modification of amorphous silica particles on biodistribution and liver metabolism in mice. *Nanotechnology*, 26(17): 75101, 15 pages.

Lu, X.Y., Tian, Y., Zhao, Q.Q., Jin, T.T., Xiao, S. and Fan, X.H., 2011. Integrated metabonomics analysis of the size-response relationship of silica nanoparticles-induced toxicity in mice. *Nanotechnology*, 22(5): 055101, 16 pages.

Luo, C., Zhang, Y., Zeng, X., Zeng, Y. and Wang, Y., 2005. The role of poly(ethylene glycol) in the formation of silver nanoparticles. *Journal of Colloid and Interface Science*, 288(2): 444-8.

Lutz, N.W., Franks, S.E., Frank, M.H., Pomer, S. and Hull, W.E., 2005. Investigation of multidrug resistance in cultured human renal cell carcinoma cells by ^{31}P-NMR spectroscopy and treatment survival assays. *Magma*, 18(3): 144-61.

Lv, M.Y., Huang, W.Q., Chen, Z.P., Jiang, H.L., Chen, J.Q., Tian, Y., Zhang, Z.J. and Xu, F.G., 2015. Metabolomics techniques for nanotoxicity investigations. *Bioanalysis*, 7(12): 1527-44.

Maccuspie, R.I., 2011. Colloidal stability of silver nanoparticles in biologically relevant conditions. *Journal of Nanoparticle Research*, 13(7): 2893-908.

Maier, K., Hofmann, U., Reuss, M. and Mauch, K., 2010. Dynamics and control of the central carbon metabolism in hepatoma cells. *BMC Systems Biology*, 4(1): 1-28.

Manikandan, R., Manikandan, B., Raman, T., Arunagirinathan, K., Prabhu, N.M., Basu, M.J., Perumal, M., Palanisamy, S. and Munusamy, A., 2015. Biosynthesis of silver nanoparticles using ethanolic petals extract of *Rosa indica* and characterization of its antibacterial, anticancer and anti-inflammatory activities. *Spectrochimica Acta Part A: Molecular and Biomolecular Spectroscopy*, 138: 120-9.

Mannina, L., Sobolev, A.P., Capitani, D., Iaffaldano, N., Rosato, M.P., Ragni, P., Reale, A., Sorrentino, E., D'amico, I. and Coppola, R., 2008. NMR metabolic profiling of organic and aqueous sea bass extracts: implications in the discrimination of wild and cultured sea bass. *Talanta*, 77(1): 433-44.

Martineau, E., Tea, I., Loaec, G., Giraudeau, P. and Akoka, S., 2011. Strategy for choosing extraction procedures for NMR-based metabolomic analysis of mammalian cells. *Analytical and Bioanalytical Chemistry*, 401(7): 2133-42.

Matsuno, T. and Goto, I., 1992. Glutaminase and glutamine synthetase activities in human cirrhotic liver and hepatocellular carcinoma. *Cancer Research*, 52(5): 1192-4.

Mazurek, S. 2007. Tumor cell energetic metabolome. *Molecular System Bioenergetics.* Wiley-VCH Verlag GmbH & Co. KGaA.

Meiser, J., Krämer, L., Sapcariu, S.C., Battello, N., Ghelfi, J., D'herouel, A.F., Skupin, A. and Hiller, K., 2016. Pro-inflammatory macrophages sustain pyruvate oxidation through pyruvate dehydrogenase for the synthesis of itaconate and to enable cytokine expression. *The Journal of Biological Chemistry*, 291(8): 3932-46.

Mfouo-Tynga, I., El-Hussein, A., Abdel-Harith, M. and Abrahamse, H., 2014. Photodynamic ability of silver nanoparticles in inducing cytotoxic effects in breast and lung cancer cell lines. *International Journal of Nanomedicine*, 9: 3771-80.

Miccheli, A., Tomassini, A., Puccetti, C., Valerio, M., Peluso, G., Tuccillo, F., Calvani, M., Manetti, C. and Conti, F., 2006a. Metabolic profiling by ^{13}C-NMR spectroscopy: [1,2-^{13}C2]glucose reveals a heterogeneous metabolism in human leukemia T cells. *Biochimie*, 88(5): 437-48.

Miccheli, A.T., Miccheli, A., Di Clemente, R., Valerio, M., Coluccia, P., Bizzarri, M. and Conti, F., 2006b. NMR-based metabolic profiling of human hepatoma cells in relation to cell growth by culture media analysis. *Biochimica et Biophysica Acta*, 1760(11): 1723-31.

Michelucci, A., Cordes, T., Ghelfi, J., Pailot, A., Reiling, N., Goldmann, O., Binz, T., Wegner, A., Tallam, A., Rausell, A., Buttini, M., Linster, C.L., Medina, E., Balling, R. and Hiller, K., 2013. Immune-responsive gene 1 protein links metabolism to immunity by catalyzing itaconic acid production. *PNAS, Proceedings of the National Academy of Sciences*, 110(19): 7820-5.

Milic, M., Leitinger, G., Pavicic, I., Avdicevic, M.Z., Dobrovic, S., Goessler, W. and Vrcek, I.V., 2015. Cellular uptake and toxicity effects of silver nanoparticles in mammalian kidney cells. *Journal of Applied Toxicology*, 35(6): 581-92.

Mills, E.L. and O'neill, L.A., 2016. Reprogramming mitochondrial metabolism in macrophages as an anti-inflammatory signal. *European Journal of Immunology*, 46(1): 13-21.

Mishra, A.R., Zheng, J., Tang, X. and Goering, P.L., 2016. Silver nanoparticle-induced autophagic-lysosomal disruption and NLRP3-inflammasome activation in HepG2 cells is size-dependent. *Toxicological Sciences*, 150(2): 473-87.

Monteiro-Riviere, N.A., Samberg, M.E., Oldenburg, S.J. and Riviere, J.E., 2013. Protein binding modulates the cellular uptake of silver nanoparticles into human cells: Implications for *in vitro* to *in vivo* extrapolations? *Toxicology Letters*, 220(3): 286-93.

Mori, Y., Ono, T., Miyahira, Y., Vinh Quang, N., Matsui, T. and Ishihara, M., 2013. Antiviral activity of silver nanoparticle/chitosan composites against H1N1 influenza A virus. *Nanoscale Research Letters*, 8(1): 93, 6 pages.

Morones, J.R., Elechiguerra, J.L., Camacho, A., Holt, K., Kouri, J.B., Ramirez, J.T. and Yacaman, M.J., 2005. The bactericidal effect of silver nanoparticles. *Nanotechnology*, 16(10): 2346-53.

Mosmann, T., 1983. Rapid colorimetric assay for cellular growth and survival: application to proliferation and cytotoxicity assays. *Journal of Immunological Methods*, 65(1-2): 55-63.

Mukherjee, S.G., O'claonadh, N., Casey, A. and Chambers, G., 2012. Comparative *in vitro* cytotoxicity study of silver nanoparticle on two mammalian cell lines. *Toxicology in Vitro*, 26(2): 238-51.

Munusamy, P., Wang, C.M., Engelhard, M.H., Baer, D.R., Smith, J.N., Liu, C.X., Kodali, V., Thrall, B.D., Chen, S., Porter, A.E. and Ryan, M.P., 2015. Comparison of 20nm silver nanoparticles synthesized with and without a gold core: structure, dissolution in cell culture media, and biological impact on macrophages. *Biointerphases*, 10(3): 031003, 16 pages.

Murphy, M., Ting, K., Zhang, X.L., Soo, C. and Zheng, Z., 2015. Current development of silver nanoparticle preparation, investigation, and application in the field of medicine. *Journal of Nanomaterials*, 2015: Article ID 696918, 12 pages.

Nadworny, P.L., Wang, J.F., Tredget, E.E. and Burrell, R.E., 2008. Anti-inflammatory activity of nanocrystalline silver in a porcine contact dermatitis model. *Nanomedicine-Nanotechnology Biology and Medicine*, 4(3): 241-51.

nanoComposix. 2016a. Available: http://nanocomposix.eu/pages/silver-nanoparticles-physical-properties [Accessed October 27 2016].

nanoComposix. 2016b. *Handbooks* [Online]. Available: http://nanocomposix.eu/pages/handbooks [Accessed October 27 2016].

Nelson, D.L. and Cox, M.M. 2004. *Lehninger Principles of Biochemistry, Fourth Edition*Fourth Edition edition.

Németh, B., Doczi, J., Csete, D., Kacso, G., Ravasz, D., Adams, D., Kiss, G., Nagy, A.M., Horvath, G., Tretter, L., Mócsai, A., Csépányi-Kömi, R., Iordanov, I., Adam-Vizi, V. and Chinopoulos, C., 2015. Abolition of mitochondrial substrate-level phosphorylation by itaconic acid produced by LPS-induced Irg1 expression in cells of murine macrophage lineage. *The FASEB Journal*, 30(1): 286-300.

Newsholme, P., Costa Rosa, L.F., Newsholme, E.A. and Curi, R., 1996. The importance of fuel metabolism to macrophage function. *Cell Biochemistry and Function*, 14(1): 1-10.

Newsholme, P., Gordon, S. and Newsholme, E.A., 1987. Rates of utilization and fates of glucose, glutamine, pyruvate, fatty acids and ketone bodies by mouse macrophages. *Biochemical Journal*, 242(3): 631-6.

Newsholme, P., Lima, M.M.R., Procopio, J., Pithon-Curi, T.C., Doi, S.Q., Bazotte, R.B. and Curi, R., 2003. Glutamine and glutamate as vital metabolites. *Brazilian Journal of Medical and Biological Research*, 36: 153-63.

Nicholson, J.K., Lindon, J.C. and Holmes, E., 1999. 'Metabonomics': understanding the metabolic responses of living systems to pathophysiological stimuli via multivariate statistical analysis of biological NMR spectroscopic data. *Xenobiotica*, 29(11): 1181-9.

Nishanth, R.P., Jyotsna, R.G., Schlager, J.J., Hussain, S.M. and Reddanna, P., 2011. Inflammatory responses of RAW 264.7 macrophages upon exposure to nanoparticles: role of ROS-NFkappaB signaling pathway. *Nanotoxicology*, 5(4): 502-16.

Nobbmann, U. 2014. *Polydispersity – what does it mean for DLS and chromatography?* [Online]. Malvern. Available: http://www.materials-talks.com/blog/2014/10/23/polydispersity-what-does-it-mean-for-dls-and-chromatography/ [Accessed October 27 2016].

O'neill, L.A., Kishton, R.J. and Rathmell, J., 2016. A guide to immunometabolism for immunologists. *Nature Reviews Immunology*, 16(9): 553-65.

Oberdorster, G., Oberdorster, E. and Oberdorster, J., 2005. Nanotoxicology: An emerging discipline evolving from studies of ultrafine particles. *Environmental Health Perspectives*, 113(7): 823-39.

Oh, H.M., Kang, Y.J., Lee, Y.S., Park, M.K., Kim, S.H., Kim, H.J., Seo, H.G., Lee, J.H. and Chang, K.C., 2006. Protein kinase G-dependent heme oxygenase-1 induction by

Agastache rugosa leaf extract protects RAW264.7 cells from hydrogen peroxide-induced injury. *Journal of Ethnopharmacology*, 103(2): 229-35.

Oostendorp, M., Engelke, U.F.H., Willemsen, M. and Wevers, R.A., 2006. Diagnosing inborn errors of lipid metabolism with proton nuclear magnetic resonance spectroscopy. *Clinical Chemistry*, 52(7): 1395-405.

Orlowski, P., Krzyzowska, M., Zdanowski, R., Winnicka, A., Nowakowska, J., Stankiewicz, W., Tomaszewska, E., Celichowski, G. and Grobelny, J., 2013. Assessment of *in vitro* cellular responses of monocytes and keratinocytes to tannic acid modified silver nanoparticles. *Toxicology in Vitro*, 27(6): 1798-808.

Orlowski, P., Tomaszewska, E., Gniadek, M., Baska, P., Nowakowska, J., Sokolowska, J., Nowak, Z., Donten, M., Celichowski, G., Grobelny, J. and Krzyzowska, M., 2014. Tannic acid modified silver nanoparticles show antiviral activity in herpes simplex virus type 2 infection. *PloS One*, 9(8): e104113, 15 pages.

Pal, S., Tak, Y.K. and Song, J.M., 2007. Does the antibacterial activity of silver nanoparticles depend on the shape of the nanoparticle? A study of the gram-negative bacterium *Escherichia coli*. *Applied and Environmental Microbiology*, 73(6): 1712-20.

Panacek, A., Kolar, M., Vecerova, R., Prucek, R., Soukupova, J., Krystof, V., Hamal, P., Zboril, R. and Kvitek, L., 2009. Antifungal activity of silver nanoparticles against *Candida spp*. *Biomaterials*, 30(31): 6333-40.

Park, E.J., Yi, J., Kim, Y., Choi, K. and Park, K., 2010. Silver nanoparticles induce cytotoxicity by a Trojan-horse type mechanism. *Toxicology in Vitro*, 24(3): 872-8.

Park, H.J., Kim, J.Y., Kim, J., Lee, J.H., Hahn, J.S., Gu, M.B. and Yoon, J., 2009. Silver-ion-mediated reactive oxygen species generation affecting bactericidal activity. *Water research*, 43(4): 1027-32.

Park, M., Neigh, A.M., Vermeulen, J.P., De La Fonteyne, L.J.J., Verharen, H.W., Briede, J.J., Van Loveren, H. and De Jong, W.H., 2011. The effect of particle size on the cytotoxicity, inflammation, developmental toxicity and genotoxicity of silver nanoparticles. *Biomaterials*, 32(36): 9810-7.

Parveen, A., Rizvi, S.H.M., Gupta, A., Singh, R., Ahmad, I., Mahdi, F. and Mahdi, A.A., 2012. NMR-based metabonomics study of sub-acute hepatotoxicity induced by silica nanoparticles in rats after intranasal exposure. *Cellular and Molecular Biology*, 58(1): 196-203.

Paul, A., Ju, H., Rangasamy, S., Shim, Y. and Song, J.M., 2015. Nanosized silver (II) pyridoxine complex to cause greater inflammatory response and less cytotoxicity to RAW264.7 macrophage cells. *Nanoscale Research Letters*, 10: 140, 10 pages.

Piao, M.J., Kang, K.A., Lee, I.K., Kim, H.S., Kim, S., Choi, J.Y., Choi, J. and Hyun, J.W., 2011. Silver nanoparticles induce oxidative cell damage in human liver cells through inhibition of reduced glutathione and induction of mitochondria-involved apoptosis. *Toxicology Letters*, 201(1): 92-100.

Pinto, R.J.B., Nasirpour, M., Carrola, J., Oliveira, H., Freire, C.S.R. and Duarte, I.F. 2017. Antimicrobial properties and therapeutic applications of silver nanoparticles and nanocomposites. *In:* Grumezescu, A.M. (ed.) *Antimicrobial Nanoarchitectonics.* Elsevier.

Prasad, R.Y., Mcgee, J.K., Killius, M.G., Suarez, D.A., Blackman, C.F., Demarini, D.M. and Simmons, S.O., 2013. Investigating oxidative stress and inflammatory responses elicited by silver nanoparticles using high-throughput reporter genes in HepG2 cells: effect of size, surface coating, and intracellular uptake. *Toxicology in Vitro*, 27(6): 2013-21.

Pratsinis, A., Hervella, P., Leroux, J.C., Pratsinis, S.E. and Sotiriou, G.A., 2013. Toxicity of silver nanoparticles in macrophages. *Small*, 9(15): 2576-84.

Rai, M.K., Deshmukh, S.D., Ingle, A.P. and Gade, A.K., 2012. Silver nanoparticles: the powerful nanoweapon against multidrug-resistant bacteria. *Journal of Applied Microbiology*, 112(5): 841-52.

Rajan, R., Chandran, K., Harper, S.L., Yun, S.-I. and Kalaichelvan, P.T., 2015. Plant extract synthesized silver nanoparticles: an ongoing source of novel biocompatible materials. *Industrial Crops and Products*, 70: 356-73.

Ramanauskienė, K., Stelmakiene, A. and Majienė, D., 2015. Assessment of lemon balm (*Melissa officinalis* L.) hydrogels: quality and bioactivity in skin cells. *Evidence-based Complementary and Alternative Medicine*, 2015: Article ID 635975, 7 pages.

Rao, C.N.R. and Biswas, K., 2009. Characterization of nanomaterials by physical methods. *Annual Review of Analytical Chemistry*, 2: 435-62.

Ratnasekhar, C., Sonane, M., Satish, A. and Mudiam, M.K., 2015. Metabolomics reveals the perturbations in the metabolome of *Caenorhabditis elegans* exposed to titanium dioxide nanoparticles. *Nanotoxicology*, 9(8): 994-1004.

Rauwel, P., Kuunal, S., Ferdov, S. and Rauwel, E., 2015. A review on the green synthesis of silver nanoparticles and their morphologies studied via TEM. *Advances in Materials Science and Engineering*, 2015: Article ID 682749, 9 pages.

Reales-Calderon, J.A., Aguilera-Montilla, N., Corbi, A.L., Molero, G. and Gil, C., 2014. Proteomic characterization of human proinflammatory M1 and anti-inflammatory M2 macrophages and their response to *Candida albicans*. *Proteomics*, 14(12): 1503-18.

Ren, C., Hu, X., Li, X. and Zhou, Q., 2016. Ultra-trace graphene oxide in a water environment triggers Parkinson's disease-like symptoms and metabolic disturbance in zebrafish larvae. *Biomaterials*, 93: 83-94.

Rizzello, L. and Pompa, P.P., 2014. Nanosilver-based antibacterial drugs and devices: mechanisms, methodological drawbacks, and guidelines. *Chemical Society Reviews*, 43(5): 1501-18.

Rodriguez-Prados, J.C., Traves, P.G., Cuenca, J., Rico, D., Aragones, J., Martin-Sanz, P., Cascante, M. and Bosca, L., 2010. Substrate fate in activated macrophages: a comparison between innate, classic, and alternative activation. *The Journal of Immunology*, 185(1): 605-14.

Ross, A., Schlotterbeck, G., Dieterle, F. and Senn, H. 2007. Chapter 3 - NMR spectroscopy techniques for application to metabonomics. *The Handbook of Metabonomics and Metabolomics.* Amsterdam: Elsevier Science B.V.

Rouzer, C.A., Ivanova, P.T., Byrne, M.O., Brown, H.A. and Marnett, L.J., 2007. Lipid profiling reveals glycerophospholipid remodeling in zymosan-stimulated macrophages. *Biochemistry*, 46(20): 6026-42.

Rui, L., 2014. Energy metabolism in the liver. *Comprehensive Physiology*, 4(1): 177-97.

Ruiz-Aracama, A., Peijnenburg, A., Kleinjans, J., Jennen, D., Van Delft, J., Hellfrisch, C. and Lommen, A., 2011. An untargeted multi-technique metabolomics approach to studying intracellular metabolites of HepG2 cells exposed to 2,3,7,8-tetrachlorodibenzo-p-dioxin. *BMC Genomics*, 12(1): 1-19.

Saborano, R., Wongpinyochit, T., Johnston, B.F., Seib, F.P. and Duarte, I.F., 2016. Metabolic reprogramming of macrophages exposed to silk, poly(lactic-co-glycolic acid) and silica nanoparticles. *submitted*.

Sadeghi, B., Garmaroudi, F.S., Hashemi, M., Nezhad, H.R., Nasrollahi, A., Ardalan, S. and Ardalan, S., 2012. Comparison of the anti-bacterial activity on the nanosilver shapes: nanoparticles, nanorods and nanoplates. *Advanced Powder Technology*, 23(1): 22-6.

Sahu, S.C., Njoroge, J., Bryce, S.M., Zheng, J. and Ihrie, J., 2016. Flow cytometric evaluation of the contribution of ionic silver to genotoxic potential of nanosilver in human liver HepG2 and colon Caco2 cells. *Journal of Applied Toxicology*, 36(4): 521-31.

Sahu, S.C., Zheng, J.W., Yourick, J.J., Sprando, R.L. and Gao, X.G., 2015. Toxicogenomic responses of human liver HepG2 cells to silver nanoparticles. *Journal of Applied Toxicology*, 35(10): 1160-8.

Sambale, F., Wagner, S., Stahl, F., Khaydarov, R.R., Scheper, T. and Bahnemann, D., 2015. Investigations of the toxic effect of silver nanoparticles on mammalian cell lines. *Journal of Nanomaterials*, 2015: Article ID 136765, 9 pages.

Santini, M.T., Rainaldi, G., Ferrante, A., Romano, R., Clemente, S., Motta, A., De Berardis, B., Balduzzi, M., Paoletti, L. and Indovina, P.L., 2004. Environmental fine particulate matter (PM 2.5) activates the RAW 264.7 macrophage cell line even at very low concentrations as revealed by ^{1}H NMR. *Chemical Research in Toxicology*, 17(1): 63-74.

Santos, S.a.O., Pinto, R.J.B., Rocha, S.M., Marques, P.a.a.P., Neto, C.P., Silvestre, A.J.D. and Freire, C.S.R., 2014. Unveiling the chemistry behind the green synthesis of metal nanoparticles. *ChemSusChem*, 7(9): 2704-11.

Sardi, J.C.O., Scorzoni, L., Bernardi, T., Fusco-Almeida, A.M. and Giannini, M., 2013. *Candida* species: current epidemiology, pathogenicity, biofilm formation, natural antifungal products and new therapeutic options. *Journal of Medical Microbiology*, 62: 10-24.

Satapathy, S.R., Mohapatra, P., Das, D., Siddharth, S. and Kundu, C.N., 2015. The apoptotic effect of plant based nanosilver in colon cancer cells is a p53 dependent process involving ROS and JNK cascade. *Pathology & Oncology Research*, 21(2): 405-11.

Schlattner, U., Tokarska-Schlattner, M. and Wallimann, T., 2006. Mitochondrial creatine kinase in human health and disease. *Biochimica et Biophysica Acta*, 1762(2): 164-80.

Selvaraj, M., Pandurangan, P., Ramasami, N., Rajendran, S.B., Sangilimuthu, S.N. and Perumal, P., 2014. Highly potential antifungal activity of quantum-sized silver nanoparticles against *Candida albicans*. *Applied Biochemistry and Biotechnology*, 173(1): 55-66.

Shannahan, J.H., Lai, X.Y., Ke, P.C., Podila, R., Brown, J.M. and Witzmann, F.A., 2013. Silver nanoparticle protein corona composition in cell culture media. *PloS One*, 8(9): e74001, 10 pages.

Sheline, C.T., Behrens, M.M. and Choi, D.W., 2000. Zinc-induced cortical neuronal death: contribution of energy failure attributable to loss of NAD^{+} and inhibition of glycolysis. *Journal of Neuroscience*, 20(9): 3139-46.

Shi, J., Sun, X., Zou, X. and Zhang, H., 2014. Amino acid-dependent transformations of citrate-coated silver nanoparticles: impact on morphology, stability and toxicity. *Toxicology Letters*, 229(1): 17-24.

Shin, S.H. and Ye, M.K., 2012. The effect of nano-silver on allergic rhinitis model in mice. *Clinical and Experimental Otorhinolaryngology*, 5(4): 222-7.

Snyder, N.W., Tombline, G., Worth, A.J., Parry, R.C., Silvers, J.A., Gillespie, K.P., Basu, S.S., Millen, J., Goldfarb, D.S. and Blair, I.A., 2015. Production of stable isotope-labeled acyl-coenzyme A thioesters by yeast stable isotope labeling by essential nutrients in cell culture. *Analytical Biochemistry*, 474: 59-65.

Song, X.L., Li, B., Xu, K., Liu, J., Ju, W., Wang, J., Liu, X.D., Li, J. and Qi, Y.F., 2012. Cytotoxicity of water-soluble mPEG-SH-coated silver nanoparticles in HL-7702 cells. *Cell Biology and Toxicology*, 28(4): 225-37.

Song, Y., Zhao, R., Hu, Y., Hao, F., Li, N., Nie, G., Tang, H. and Wang, Y., 2015. Assessment of the biological effects of a multifunctional nano-drug-carrier and its encapsulated drugs. *Journal of Proteome Research*, 14(12): 5193-201.

Speshock, J.L., Murdock, R.C., Braydich-Stolle, L.K., Schrand, A.M. and Hussain, S.M., 2010. Interaction of silver nanoparticles with Tacaribe virus. *Journal of Nanobiotechnology*, 8: 19, 9 pages.

Stoehr, L.C., Gonzalez, E., Stampfl, A., Casals, E., Duschl, A., Puntes, V. and Oostingh, G.J., 2011. Shape matters: effects of silver nanospheres and wires on human alveolar epithelial cells. *Particle and Fibre Toxicology*, 8: 36, 15 pages.

Straadt, I.K., Young, J.F., Petersen, B.O., Duus, J.O., Gregersen, N., Bross, P., Oksbjerg, N., Theil, P.K. and Bertram, H.C., 2010. Oxidative stress-induced metabolic changes in mouse C2C12 myotubes studied with high-resolution ^{13}C, ^{1}H, and ^{31}P NMR spectroscopy. *Journal of Agricultural and Food Chemistry*, 58(3): 1918-26.

Strelko, C.L., Lu, W., Dufort, F.J., Seyfried, T.N., Chiles, T.C., Rabinowitz, J.D. and Roberts, M.F., 2011. Itaconic acid is a mammalian metabolite induced during macrophage activation. *Journal of the American Chemical Society*, 133(41): 16386-9.

Stuckey, D.J., Anthony, D.C., Lowe, J.P., Miller, J., Palm, W.M., Styles, P., Perry, V.H., Blamire, A.M. and Sibson, N.R., 2005. Detection of the inhibitory neurotransmitter GABA in macrophages by magnetic resonance spectroscopy. *Journal of Leukocyte Biology*, 78(2): 393-400.

Sujitha, V., Murugan, K., Paulpandi, M., Panneerselvam, C., Suresh, U., Roni, M., Nicoletti, M., Higuchi, A., Madhiyazhagan, P., Subramaniam, J., Dinesh, D., Vadivalagan, C., Chandramohan, B., Alarfaj, A.A., Munusamy, M.A., Barnard, D.R. and Benelli, G., 2015. Green-synthesized silver nanoparticles as a novel control tool against dengue virus (DEN-2) and its primary vector *Aedes aegypti*. *Parasitology Research*, 114(9): 3315-25.

Suliman, Y.A., Ali, D., Alarifi, S., Harrath, A.H., Mansour, L. and Alwasel, S.H., 2015. Evaluation of cytotoxic, oxidative stress, proinflammatory and genotoxic effect of silver nanoparticles in human lung epithelial cells. *Environmental Toxicology*, 30(2): 149-60.

Sun, L., Singh, A.K., Vig, K., Pillai, S.R. and Singh, S.R., 2008. Silver nanoparticles inhibit replication of respiratory syncytial virus. *Journal of Biomedical Nanotechnology*, 4(2): 149-58.

Suresh, A.K., Pelletier, D.A., Wang, W., Morrell-Falvey, J.L., Gu, B.H. and Doktycz, M.J., 2012. Cytotoxicity induced by engineered silver nanocrystallites is dependent on surface coatings and cell types. *Langmuir*, 28(5): 2727-35.

Swanner, J., Mims, J., Carroll, D.L., Akman, S.A., Furdui, C.M., Torti, S.V. and Singh, R.N., 2015. Differential cytotoxic and radiosensitizing effects of silver nanoparticles on triple-negative breast cancer and non-triple-negative breast cells. *International Journal of Nanomedicine*, 10: 3937-53.

Szmyd, R., Goralczyk, A.G., Skalniak, L., Cierniak, A., Lipert, B., Filon, F.L., Crosera, M., Borowczyk, J., Laczna, E., Drukala, J., Klein, A. and Jura, J., 2012. Effect of silver nanoparticles on human primary keratinocytes. *Biological Chemistry*, 394(1): 113-23.

Tang, M., Zhang, T., Xue, Y.Y., Wang, S., Huang, M.M., Yang, Y., Lu, M.Y., Lei, H., Kong, L., Wang, Y.Q. and Pu, Y.P., 2011. Metabonomic studies of biochemical changes in the serum of rats by intratracheally instilled TiO_2 nanoparticles. *Journal of Nanoscience and Nanotechnology*, 11(4): 3065-74.

Teng, Q., Huang, W., Collette, T.W., Ekman, D.R. and Tan, C., 2008. A direct cell quenching method for cell-culture based metabolomics. *Metabolomics*, 5(2): 199-208.

Teodoro, J.S., Simoes, A.M., Duarte, F.V., Rolo, A.P., Murdoch, R.C., Hussain, S.M. and Palmeira, C.M., 2011. Assessment of the toxicity of silver nanoparticles *in vitro*: a mitochondrial perspective. *Toxicology in Vitro*, 25(3): 664-70.

ThomsonReuters[tm]. 2016. *Web of Science*[TM] [Online]. Available: http://apps.webofknowledge.com/ [Accessed September 30 2016].

Tolaymat, T.M., El Badawy, A.M., Genaidy, A., Scheckel, K.G., Luxton, T.P. and Suidan, M., 2010. An evidence-based environmental perspective of manufactured silver nanoparticle in syntheses and applications: a systematic review and critical appraisal of peer-reviewed scientific papers. *Science of The Total Environment*, 408(5): 999-1006.

Tran, Q.H., Nguyen, V.Q. and Le, A.T., 2013. Silver nanoparticles: synthesis, properties, toxicology, applications and perspectives. *Advances in Natural Sciences-Nanoscience and Nanotechnology*, 4(3): 033001, 20 pages.

Trefry, J.C. and Wooley, D.P., 2013. Silver nanoparticles inhibit *Vaccinia virus* infection by preventing viral entry through a macropinocytosis-dependent mechanism. *Journal of Biomedical Nanotechnology*, 9(9): 1624-35.

Triba, M.N., Starzec, A., Bouchemal, N., Guenin, E., Perret, G.Y. and Le Moyec, L., 2010. Metabolomic profiling with NMR discriminates between biphosphonate and doxorubicin effects on B16 melanoma cells. *NMR in Biomedicine*, 23(9): 1009-16.

Triboulet, S., Aude-Garcia, C., Carriere, M., Diemer, H., Proamer, F., Habert, A., Chevallet, M., Collin-Faure, V., Strub, J.M., Hanau, D., Van Dorsselaer, A., Herlin-Boime, N. and Rabilloud, T., 2013. Molecular responses of mouse macrophages to copper and copper oxide nanoparticles inferred from proteomic analyses. *Molecular & Cellular Proteomics*, 12(11): 3108-22.

Trygg, J., Holmes, E. and Lundstedt, T., 2007. Chemometrics in metabonomics. *Journal of Proteome Research*, 6: 469-79.

Tucci, P., Porta, G., Agostini, M., Dinsdale, D., Iavicoli, I., Cain, K., Finazzi-Agro, A., Melino, G. and Willis, A., 2013. Metabolic effects of TiO_2 nanoparticles, a common component of sunscreens and cosmetics, on human keratinocytes. *Cell Death & Disease*, 4: e549, 11 pages.

Ulrich, E.L., Akutsu, H., Doreleijers, J.F., Harano, Y., Ioannidis, Y.E., Lin, J., Livny, M., Mading, S., Maziuk, D., Miller, Z., Nakatani, E., Schulte, C.F., Tolmie, D.E., Kent Wenger, R., Yao, H. and Markley, J.L., 2008. BioMagResBank. *Nucleic Acids Research*, 36(suppl 1): D402-D8.

Valverde, D., Quintero, M.R., Candiota, A.P., Badiella, L., Cabañas, M.E. and Arús, C., 2006. Analysis of the changes in the ^{1}H NMR spectral pattern of perchloric acid extracts of C6 cells with growth. *NMR in Biomedicine*, 19(2): 223-30.

Vazquez-Munoz, R., Avalos-Borja, M. and Castro-Longoria, E., 2014. Ultrastructural analysis of *Candida albicans* when exposed to silver nanoparticles. *PloS One*, 9(10): e108876, 10 pages.

Veselkov, K.A., Lindon, J.C., Ebbels, T.M.D., Crockford, D., Volynkin, V.V., Holmes, E., Davies, D.B. and Nicholson, J.K., 2009. Recursive segment-wise peak alignment of biological ^{1}H NMR spectra for improved metabolic biomarker recovery. *Analytical Chemistry*, 81(1): 56-66.

Vogt, A., Rancan, F., Ahlberg, S., Nazemi, B., Choe, C.S., Darvin, M.E., Hadam, S., Blume-Peytavi, U., Loza, K., Diendorf, J., Epple, M., Graf, C., Rühl, E., Meinke, M.C. and Lademann, J., 2014. Interaction of dermatologically relevant nanoparticles with skin cells and skin. *Beilstein Journal of Nanotechnology*, 5: 2363-73.

Vrček, I.V., Žuntar, I., Petlevski, R., Pavičić, I., Dutour Sikirić, M., Ćurlin, M. and Goessler, W., 2016. Comparison of *in vitro* toxicity of silver ions and silver nanoparticles on human hepatoma cells. *Environmental Toxicology*, 31(6): 679-92.

Wallimann, T., Wyss, M., Brdiczka, D., Nicolay, K. and Eppenberger, H.M., 1992. Intracellular compartmentation, structure and function of creatine kinase isoenzymes in tissues with high and fluctuating energy demands: the 'phosphocreatine circuit' for cellular energy homeostasis. *Biochemical Journal*, 281(Pt 1): 21-40.

Wang, X., Ji, Z., Chang, C.H., Zhang, H., Wang, M., Liao, Y.-P., Lin, S., Meng, H., Li, R., Sun, B., Winkle, L.V., Pinkerton, K.E., Zink, J.I., Xia, T. and Nel, A.E., 2014. Use of coated silver nanoparticles to understand the relationship of particle dissolution and bioavailability to cell and lung toxicological potential. *Small*, 10(2): 385-98.

Warskulat, U., Weik, C. and Häussinger, D., 1997. *myo*-Inositol is an osmolyte in rat liver macrophages (Kupffer cells) but not in RAW 264.7 mouse macrophages. *Biochemical Journal*, 326(1): 289-95.

Warskulat, U., Wettstein, M. and Häussinger, D., 1995. Betaine is an osmolyte in RAW 264.7 mouse macrophages. *FEBS Letters*, 377(1): 47-50.
Wei, L., Lu, J., Xu, H., Patel, A., Chen, Z.-S. and Chen, G., 2015. Silver nanoparticles: synthesis, properties, and therapeutic applications. *Drug Discovery Today*, 20(5): 595-601.
Wen, Z.-S., Liu, L.-J., Qu, Y.-L., Ouyang, X.-K., Yang, L.-Y. and Xu, Z.-R., 2013. Chitosan nanoparticles attenuate hydrogen peroxide-induced stress injury in mouse macrophage RAW264.7 cells. *Marine Drugs*, 11(10): 3582-600.
Westerhuis, J.A., Hoefsloot, H.C.J., Smit, S., Vis, D.J., Smilde, A.K., Van Velzen, E.J.J., Van Duijnhoven, J.P.M. and Van Dorsten, F.A., 2008. Assessment of PLSDA cross validation. *Metabolomics*, 4(1): 81-9.
Wishart, D.S., Jewison, T., Guo, A.C., Wilson, M., Knox, C., Liu, Y., Djoumbou, Y., Mandal, R., Aziat, F., Dong, E., Bouatra, S., Sinelnikov, I., Arndt, D., Xia, J., Liu, P., Yallou, F., Bjorndahl, T., Perez-Pineiro, R., Eisner, R., Allen, F., Neveu, V., Greiner, R. and Scalbert, A., 2013. HMDB 3.0 - The human metabolome database in 2013. *Nucleic Acids Research*, 41(D1): D801-D7.
Wiśniewski, J.R., Vildhede, A., Norén, A. and Artursson, P., 2016. In-depth quantitative analysis and comparison of the human hepatocyte and hepatoma cell line HepG2 proteomes. *Journal of Proteomics*, 136: 234-47.
Wong, K.K., Cheung, S.O., Huang, L., Niu, J., Tao, C., Ho, C.M., Che, C.M. and Tam, P.K., 2009. Further evidence of the anti-inflammatory effects of silver nanoparticles. *ChemMedChem*, 4(7): 1129-35.
Xiang, D.-X., Chen, Q., Pang, L. and Zheng, C.-L., 2011. Inhibitory effects of silver nanoparticles on H1N1 influenza A virus *in vitro*. *Journal of Virological Methods*, 178(1-2): 137-42.
Xiang, D., Zheng, Y., Duan, W., Li, X., Yin, J., Shigdar, S., O'connor, M.L., Marappan, M., Zhao, X., Miao, Y., Xiang, B. and Zheng, C., 2013. Inhibition of A/Human/Hubei/3/2005 (H3N2) influenza virus infection by silver nanoparticles *in vitro* and *in vivo*. *International Journal of Nanomedicine*, 8: 4103-13.
Xiu, Z.M., Zhang, Q.B., Puppala, H.L., Colvin, V.L. and Alvarez, P.J., 2012. Negligible particle-specific antibacterial activity of silver nanoparticles. *Nano Letters*, 12(8): 4271-5.
Xu, B., Chen, M.J., Ji, X.L., Mao, Z.L., Zhang, X.M., Wang, X.R. and Xia, Y.K., 2014. Metabolomic profiles delineate the potential role of glycine in gold nanorod-induced disruption of mitochondria and blood-testis barrier factors in TM-4 cells. *Nanoscale*, 6(14): 8265-73.
Xu, H., Qu, F., Lai, W., Andrew Wang, Y., Aguilar, Z.P. and Wei, H., 2012. Role of reactive oxygen species in the antibacterial mechanism of silver nanoparticles on *Escherichia coli* O157:H7. *Biometals*, 25(1): 45-53.
Xu, Q.S. and Liang, Y.Z., 2001. Monte Carlo cross validation. *Chemometrics and Intelligent Laboratory Systems*, 56(1): 1-11.
Xu, T., Zhang, N., Nichols, H.L., Shi, D. and Wen, X., 2007. Modification of nanostructured materials for biomedical applications. *Materials Science and Engineering: C*, 27(3): 579-94.
Xue, Y., Zhang, T., Zhang, B., Gong, F., Huang, Y. and Tang, M., 2016. Cytotoxicity and apoptosis induced by silver nanoparticles in human liver HepG2 cells in different dispersion media. *Journal of Applied Toxicology*, 36(3): 352-60.
Xue, Y.Y., Zhang, S.S., Huang, Y.M., Zhang, T., Liu, X.R., Hu, Y.Y., Zhang, Z.Y. and Tang, M., 2012. Acute toxic effects and gender-related biokinetics of silver nanoparticles following an intravenous injection in mice. *Journal of Applied Toxicology*, 32(11): 890-9.
Yan, G.Y., Huang, Y.N., Bu, Q., Lv, L., Deng, P.C., Zhou, J.Q., Wang, Y.L., Yang, Y.Z., Liu, Q.Q., Cen, X.B. and Zhao, Y.L., 2012. Zinc oxide nanoparticles cause nephrotoxicity

and kidney metabolism alterations in rats. *Journal of Environmental Science and Health, Part A: Toxic/Hazardous Substances and Environmental Engineering*, 47(4): 577-88.

Yilma, A.N., Singh, S.R., Dixit, S. and Dennis, V.A., 2013. Anti-inflammatory effects of silver-polyvinyl pyrrolidone (Ag-PVP) nanoparticles in mouse macrophages infected with live *Chlamydia trachomatis*. *International Journal of Nanomedicine*, 8: 2421-32.

Yu, K.N., Yoon, T.J., Minai-Tehrani, A., Kim, J.E., Park, S.J., Jeong, M.S., Ha, S.W., Lee, J.K., Kim, J.S. and Cho, M.H., 2013a. Zinc oxide nanoparticle induced autophagic cell death and mitochondrial damage via reactive oxygen species generation. *Toxicology in Vitro*, 27(4): 1187-95.

Yu, S.J., Chao, J.B., Sun, J., Yin, Y.G., Liu, J.F. and Jiang, G.B., 2013b. Quantification of the uptake of silver nanoparticles and ions to HepG2 cells. *Environmental Science & Technology*, 47(7): 3268-74.

Zabirnyk, O., Yezhelyev, M. and Seleverstov, O., 2007. Nanoparticles as a novel class of autophagy activators. *Autophagy*, 3(3): 278-81.

Zanette, C., Pelin, M., Crosera, M., Adami, G., Bovenzi, M., Larese, F.F. and Florio, C., 2011. Silver nanoparticles exert a long-lasting antiproliferative effect on human keratinocyte HaCaT cell line. *Toxicology in Vitro*, 25(5): 1053-60.

Zanin, H., Hollanda, L.M., Ceragioli, H.J., Ferreira, M.S., Machado, D., Lancellotti, M., Catharino, R.R., Baranauskas, V. and Lobo, A.O., 2014. Carbon nanoparticles for gene transfection in eukaryotic cell lines. *Materials Science & Engineering C-Materials for Biological Applications*, 39: 359-70.

Zerbe, O. and Jurt, S. 2014. *Applied NMR spectroscopy for chemists and life scientists*, Wiley-VCH.

Zhang, H.Y., Wang, X., Wang, M.Y., Li, L.J., Chang, C.H., Ji, Z.X., Xia, T. and Nel, A.E., 2015a. Mammalian cells exhibit a range of sensitivities to silver nanoparticles that are partially explicable by variations in antioxidant defense and metallothionein expression. *Small*, 11(31): 3797-805.

Zhang, L.M., Wang, L.M., Hu, Y.L., Liu, Z.G., Tian, Y., Wu, X.C., Zhao, Y.L., Tang, H.R., Chen, C.Y. and Wang, Y.L., 2013. Selective metabolic effects of gold nanorods on normal and cancer cells and their application in anticancer drug screening. *Biomaterials*, 34(29): 7117-26.

Zhang, S.W., Liu, X.L., Wang, H.L., Peng, J. and Wong, K.K.Y., 2014a. Silver nanoparticle-coated suture effectively reduces inflammation and improves mechanical strength at intestinal anastomosis in mice. *Journal of Pediatric Surgery*, 49(4): 606-13.

Zhang, T.L., Wang, L.M., Chen, Q. and Chen, C.Y., 2014b. Cytotoxic potential of silver nanoparticles. *Yonsei Medical Journal*, 55(2): 283-91.

Zhang, W., Yao, Y., Sullivan, N. and Chen, Y., 2011. Modeling the primary size effects of citrate-coated silver nanoparticles on their ion release kinetics. *Environmental Science & Technology*, 45(10): 4422-8.

Zhang, X., Xu, Y., Zhou, L., Zhang, C., Meng, Q., Wu, S., Wang, S., Ding, Z., Chen, X., Li, X. and Chen, R., 2015b. Sex-dependent depression-like behavior induced by respiratory administration of aluminum oxide nanoparticles. *International Journal of Environmental Research and Public Health*, 12(12): 15692-705.

Zhao, F., Zhao, Y., Liu, Y., Chang, X. and Chen, C., 2011. Cellular uptake, intracellular trafficking, and cytotoxicity of nanomaterials. *Small*, 7(10): 1322-37.

Zheng, J.-F., Lu, J., Wang, X.-Z., Guo, W.-H. and Zhang, J.-X., 2015. Comparative metabolomic profiling of hepatocellular carcinoma cells treated with sorafenib monotherapy vs. sorafenib-everolimus combination therapy. *Medical Science Monitor*, 21: 1781-91.

Zook, J.M., Long, S.E., Cleveland, D., Geronimo, C.L.A. and Maccuspie, R.I., 2011. Measuring silver nanoparticle dissolution in complex biological and environmental

matrices using UV-visible absorbance. *Analytical and Bioanalytical Chemistry*, 401(6): 1993-2002.